Multi-Axis Differential Optical Absorption Spectroscopy Measurements in Polluted Environments

Roman Sinreich

Dissertation
submitted to the
Combined Faculties for the Natural Sciences and for Mathematics
of the Ruperto-Carola University of Heidelberg, Germany
for the degree of
Doctor of Natural Sciences

presented by: Roman Sinreich
born in: Saarbrücken

oral examination: 23.1.2008

Multi-Axis Differential Optical Absorption Spectroscopy Measurements in Polluted Environments

Referees: Prof. Dr. Ulrich Platt
Prof. Dr. Thomas Wagner

Zusammenfassung

In dieser Arbeit werden die Ergebisse von MAX-DOAS Messungen während zweier umfangreicher Meßkampagnen vorgestellt. Eine Meßkampagne fand im Sommer 2004 im Nordosten der USA statt (ICARTT), die andere im Frühling 2006 in Mexiko Stadt (MILAGRO). In beiden Meßkampagnen wurden mehrere MAX-DOAS Instrumente an verschiedenen Orten aufgestellt und Zeitserien von NO_2, SO_2, HONO, HCHO, CHOCHO und O_4 sowie von Aerosolextinktion gewonnen. Die räumliche und zeitliche Variation dieser Messungen wurden untersucht, um die entsprechenden Emissionsquellen, die chemischen Transformationsprozesse und die Transportwege zu charakterisieren und zu quantifizieren. Insgesamt erfüllten sich die diesabezüglichen Vermutungen. In einigen Fällen konnten Wochengänge in den Zeitserien beobachtet werden, was eine klare zeitliche Verknüpfung zwischen den Rhythmen der Emissionen und den gemessenen Spurengasen bedeutet. In den meisten Fällen konnten die gemessenen Spurengase eindeutig bestimmten Emissionsquellen zugeordnet werden. Ein weiteres interessantes Ergebnis war die weitgehende Übereinstimmung der Zeitserien von Aerosolextinktion und der von Spurengasen. Als Entdeckung können die erstmaligen Messungen sowohl von Glyoxal als auch von schwefliger Säure mit der MAX-DOAS Methode angeführt werden. Beide Messungen ergaben teilweise unerwartete Erkenntnisse, was die sehr starken Absorptionen von schwefliger Säure in Mexiko Stadt und die von Glyoxal im Golf von Maine betreffen. Daher sollten die Forschungen in dieser Richtung weitergeführt werden. In dieser Arbeit wurden auch Inversionstechniken entwickelt, die einen quantitativen Vergleich von mit MAX-DOAS gemessenen Daten mit anderen Messungen von z. B. in-situ oder durch Satelliten ermöglichen. Aufgrund der erfahrungen dieser beiden Meßkampagnen wird die Gründung eines globalen Netzwerks von automatisierten MAX-DOAS Instrumenten empfohlen.

Abstract

In this thesis, results of MAX-DOAS measurements performed during two extensive measurement campaigns are presented. One measurement campaign took place in the north-east of the USA in summer 2004 (ICARTT) and another in Mexico City in spring 2006 (MILAGRO). During both campaigns, an extended network of MAX-DOAS instruments was operated and time series of NO_2, SO_2, HONO, HCHO, CHOCHO and O_4 as well as aerosol extinction were analyzed. The spatial and temporal variation of these observations was investigated in order to characterize and quantify the respective emission sources, chemical transformation and transport pathways. Overall, the existing expectations on these processes could be confirmed. In some cases, a weekly cycle was discovered in the time series indicating a clear relationship between the temporal pattern of emissions and observed concentrations. In most cases, also a clear attribution to specific emission sources was possible. Another interesting example was that the time series of the aerosol extinction in general agrees well with those of the trace gases. Also new discoveries could be made, especially the first detection of glyoxal and nitrous acid by MAX-DOAS measurements. Both observations led to partly unexpected results, namely very high absorptions of nitrous acid in Mexico City and very high absorptions of glyoxal over the Gulf of Maine. Both findings should be investigated in more detail in future research. In this thesis, also new inversion techniques were developed which allow the quantitative comparison of the retrieved data sets of MAX-DOAS measurements with other observations like in-situ measurements or satellite observations. Based on the experience gained during both campaigns the foundation of a global network of automated MAX-DOAS instruments is recommended.

Contents

1 Introduction

Pollution of the environment caused by human activity is getting more and more a public concern. Especially, anthropogenic emissions in the atmosphere are in discussion nowadays due to increase of greenhouse gases. These gases are strongly suspected to be causative for the increase in the global mean temperature in the last decades and hence for climate change [IPCC, 2007]. The contribution of large cities to local and global pollution is increasing strongly because more people are moving from rural areas to cities. Since about this year more people have lived in cities than in the countryside[1]. This implies that existing cities are growing. The number of megacities (cities of more than 10 million inhabitants) increases continuously. This involves more health problems and a higher mortality rate for people exposed to air pollution [Molina and Molina, 2002]. Thus, the investigation of air pollution in urban areas, its transport and chemical processes is of high importance in order to improve air quality.

As part of this work, measurements of trace gases of mainly anthropogenic origin were conducted during two measurement campaigns. The first measurement campaign was performed in the north-east of the USA in summer 2004 in the framework of the International Consortium for Atmospheric Research on Transport and Transformation (ICARTT) study. This region of the USA is often called the tailpipe of the USA due to the large amounts of emissions which stream out of the American continent prevailingly in north-east direction. The focus of ICARTT was the investigation of sources, sinks, chemical transformations and transport of ozone, aerosols and their precursors to and over the North Atlantic Ocean. A network of 6 measurement devices on the mainland and an additional on a research vessel which cruised through the Gulf of Maine was set up within this thesis. The second measurement campaign took place in Mexico City in 2006 in the framework of the Megacity Initiative: Local and Global Research Observations (MILAGRO) 2006 field campaign. Its goal was to observe and quantify anthropogenic pollutants emitted from Mexico City which is the world's second largest city with more than 20 million inhabitants and accordingly high air pollution.

The Multi-Axis Differential Optical Absorption Spectroscopy (MAX-DOAS) method was applied to retrieve several trace gases of interest. DOAS is a well established technique for the detection of trace gases [Platt, 1994]. The position and optical density of narrow band absorption features (<5 nm width) in spectra of

---

[1] see http://www.un.org/esa/population/publications/wup2003/WUP2003.htm and http://esa.un.org/unup/index.asp?panel=1

UV-Visible scattered sunlight are analyzed to detect and quantify trace gases by applying Lambert-Beer law. The DOAS technique identifies particular molecules by their characteristic absorption structures and is a self-calibrating and remote sensing method [Platt, 1999]. During the last decades, the application of the DOAS technique at various platforms has allowed to detect a variety of trace gases, such as NO_2, O_3, SO_2, HCHO, NO_3, BrO and OClO. Recently, also observations in the so called MAX-DOAS viewing geometry were introduced. MAX-DOAS observes scattered sunlight from different viewing directions. Observations performed at directions slightly above the horizon increase the sensitivity to trace gases close to the surface. Thus, MAX-DOAS is a suitable technique to retrieve trace gases in the lowest layer of the atmosphere.

In this work, tropospheric columns analyzed during both measurement campaigns are presented. Thereby, two species, glyoxal (CHOCHO) and nitrous acid (HONO), were measured for the first time by the MAX-DOAS technique. Comparisons with in-situ measurements and meteorolgical data were performed. Furthermore, trace gas height profiles could be derived by using radiative transfer modeling which accounts for different light path distributions in the atmosphere.

2 Chemistry in the Troposphere

2.1 Nitrogen Dioxide

Nitrogen dioxide (NO_2) forms part of a family of gases which are often expressed by NO_x (=NO_2+NO) since NO_2 and NO rapidly convert into each other in the atmosphere. NO_x is of large importance for chemical processes in the atmosphere: They have a strong impact on the oxidative capacity of the atmosphere because they influence the abundance and partitioning of HO_x radicals (HO_x=OH+HO_2). Furthermore, they act as a catalysator in the formation of ozone (O_3) in the troposphere. However in the stratosphere, NO_x enhance the degradation of the ozone layer. NO_x is mostly removed from the atmosphere in form of nitric acid (HNO_3) which is, besides sulfuric acid (H_2SO_4), an important component of acid rain.

The effective lifetime of NO_2 depends on the solar radiation, and ranges between 33 hours in winter times and 12 hours in summer times [Beirle et al., 2003]. There are many sources for nitrogen oxides: The largest source is the anthropogenic fossil fuel combustion in industrial activities and traffic. Thus, the NO_x values are much higher in urban areas than in rural regions. Also air traffic whose exhaust gases are emitted mostly in the upper troposphere must not be ignored as NO_x source. Furthermore NO_x is generated by the burning of biomass e.g. during forest fires as well as clearings of forest by fire. Moreover, emissions from soil owing to fertilizer and microbiological processes, like e.g. putrefraction, contribute to the NO_x budget. Also thunderstorms are an important source in the production of NO_x because air which is exposed to lightnings is strongly heated up. Finally, NO_x diffuses from the stratosphere into the troposphere. Table 2.1 lists the most important NO_x sources as well as their amounts of emission and uncertainties [Lee et al., 1997].

The relatively high uncertainties in Table 2.1 show, that the understanding of the processes which generates NO_x is still in progress [Leue et al., 2001; Beirle et al., 2003]. Yet, it can easily be seen that more as the half of the emissions have anthropogenic origin. Such sources are concentrated on small spots. Thus, in especially high polluted areas, mixing ratios in the order of magnitude of 100 ppb[1] can occur. In contrast, natural NO_x sources are distributed more equally over the Earth. Figure 2.1 shows the tropospheric mean repartition of NO_2 retrieved from satellite measurements during 18 months. Large cities can easily be recognized by significant larger NO_2 column densities.

---

[1] 1 ppb = 1 part per billion = 10^{-9} mixing ratio

Table 2.1: *NO_x emissions sorted by sources [Lee et al., 1997].*

Emission source	Emission [mt]	Uncertainty [mt]
Industry and traffic	22	13-31
Biomass burning	7,9	3-15
Soil emissions	7	4-12
Thunderstorms	5	2-20
Air traffic	0,8	0,6-1
Stratospheric diffusion	0,6	0,4-1

Nitrogen oxides are produced in the atmosphere whenever air is heated to temperatures higher than 2000 K, e.g. in combustion processes. In this case, the thermal energy is high enough to dissociate O_2 into atomic oxygen which reacts with molecular nitrogen to form NO:

$$\mathrm{O} + \mathrm{N_2} \longrightarrow \mathrm{NO} + \mathrm{N} \tag{2.1}$$

Another byproduct is N_2O can be generated. In the troposphere, N_2O is inert (lifetime of about 120 years) and thus, does not play a chemical role. However in the stratosphere, the strong UV radiation can dissociate N_2O (at $\lambda < 298$ nm) yielding atomic oxygen for further reactions.

NO, as it is produced in reaction 2.1, is rapidly oxidized by ozone to NO_2:

$$\mathrm{O_3} + \mathrm{NO} \longrightarrow \mathrm{NO_2} + \mathrm{O_2} \tag{2.2}$$

NO_2 mostly yielded from reaction (2.2) can be photolyzed by UV radiation of the sun below 420 nm generating ozone (see reaction (2.3)). Under direct sun exposure at noon, this happens fast and the mean lifetime of NO_2 only accounts to several minutes.

$$\mathrm{NO_2} \xrightarrow{\mathrm{h}\nu\ (\lambda<420\ \mathrm{nm})} \mathrm{NO} + \mathrm{O(^3P)} \tag{2.3}$$

where $O(^3P)$ reacts rapidly with O_2 to ozone:

$$\mathrm{O(^3P)} + \mathrm{O_2} + \mathrm{M} \longrightarrow \mathrm{O_3} + \mathrm{M} \tag{2.4}$$

with M as required collision partner (e.g. N_2 or O_2) due to conversation of energy and spin momentum. Since other reactions with $O(^3P)$ can be neglected, each NO_2 molecule leads to the generation of an ozone and NO molecule. However, according to reaction (2.2), NO and O_3 form NO_2 again. Finally, a photostationary state arises between NO_2 and NO which is referred to as the Leighton ratio [Leighton, 1961]:

$$\frac{[\mathrm{NO}]}{[\mathrm{NO_2}]} = \frac{j_{\mathrm{NO_2}}}{k_{\mathrm{NO}} \cdot [\mathrm{O_3}]} \tag{2.5}$$

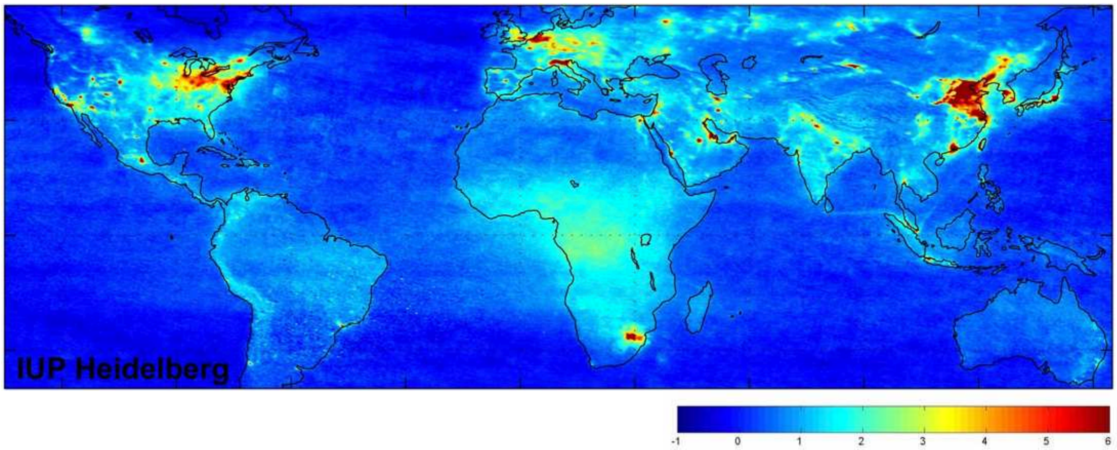

Figure 2.1: *Mean repartition of tropospheric NO_2 in 10^{15} molecules/cm^2 retrieved by the satellite instrument SCIAMACHY during 18 months. Large cities can easily be recognized by significant larger NO_2 column densities.*

with j_{NO_2} as photolysis frequency of NO_2 and k_{NO} as rate constant of the reaction of ozone with NO (reaction (2.2)). The photolysis frequency j_{NO_2} depends on the solar radiation and thus change over the day. Yet, the rate constant k_{NO} is temperature dependent and accounts to 1.8×10^{-14} cm^3 molecule^{-1} s^{-1} at 298 K [Atkinson et al., 2004]. Typically, the Leighton ratio in the lower troposphere is between 0.5 and 1 depending on the ozone concentration and the photolysis frequency. With increasing height the ratio increases due to higher photolysis frequency of NO_2.

In the photostationary state, on average ozone neither is formed nor destroyed. Net ozone production is observed if NO_x is sufficiently abandant to react with peroxy radicals, HO_2 and RO_2. In this case, the following reaction can occur:

$$\mathrm{NO} + \mathrm{HO_2} \longrightarrow \mathrm{NO_2} + \mathrm{OH} \tag{2.6}$$

whereby the peroxy radicals are generated from oxidation of volatile organic compounds (VOCs), which are abundant in urban areas. To a very small amount ($\approx 0.1\,\%$), it is assumed that also other products, such as HNO_3, can be produced in this reaction.

Thus, ozone is produced by reaction (2.3) and (2.4), but not degraded by NO in the same extent. This can lead to the so-called photosmog with large amounts of ozone, oxidized VOCs and organic aerosols. However, peroxy radicals also can react with ozone to molecular oxygen and OH. But this only plays a role if the concentrations of NO_x are very low:

$$\mathrm{O_3} + \mathrm{HO_2} \longrightarrow 2\,\mathrm{O_2} + \mathrm{OH} \tag{2.7}$$

Thus, it depends on the different abundances of NO_x and VOCs if more ozone is produced by reactions (2.3) and (2.4) or destroyed by reaction (2.7). This is illustrated in Figure 2.2 where ozone mixing ratio isopleths are plotted.

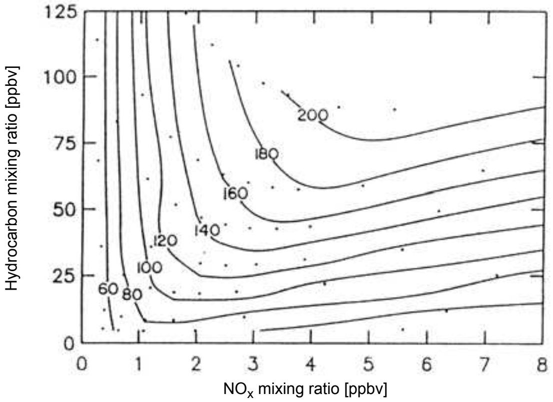

Figure 2.2: *Ozone mixing ratio isopleths (in ppb) derived from simulations [Sillman et al., 1990]. In the top left of the diagram the ozone production is limited by the mixing ratio of* NO_x*, in the bottom right by the mixing ratio of VOCs.*

The decomposition product of NO_2 is mostly nitric acid (HNO_3) which is generated by the reaction with OH:

$$NO_2 + OH + M \longrightarrow HNO_3 + M \tag{2.8}$$

Hence, this reaction is not only a sink for NO_2, but also for OH. Thus, NO_2 contributes to the degradation of the concentration of the hydroxyl radical.

NO_2 can also be further oxidized toNO_3:

$$NO_2 + O_3 \longrightarrow NO_3 + O_2 \tag{2.9}$$

However during daylight, NO_3 is degraded by photolysis within several seconds in two ways:

$$NO_3 \xrightarrow{h\nu} NO + O_2 \tag{2.10}$$

$$NO_3 \xrightarrow{h\nu} NO_2 + O \tag{2.11}$$

and furthermore, by the rapid reaction with NO:

$$NO_3 + NO \longrightarrow 2\,NO_2 \tag{2.12}$$

At day, the photolysis and the NO concentrations prevent a significant level of NO_3 concentration. Yet by night, when no photolysis occurs so that also NO concentrations are low, NO_3 can accumulate in the atmosphere.

Additionally, NO_3 can react with NO_2 yielding N_2O_5:

$$\mathrm{NO_3 + NO_2 + M \longleftrightarrow N_2O_5 + M} \tag{2.13}$$

NO_3, NO_2 and N_2O_5 are in a thermodynamic equilibrium which depends strongly on temperature [Finlayson-Pitts and Pitts jr., 2000]. N_2O_5 is degraded mainly by reaction on water (droplet) surfaces [Mentel et al., 1996], and is an important process of NO_x on local and global scales.

2.2 Nitrous Acid

Nitrous acid (HONO) plays an important role in the atmosphere due to its capability to form hydroxyl radicals (OH) at daytime [Platt et al., 1980; Calvert et al., 1994; Lammel and Cape, 1996; Alicke et al., 2003], which acts as a strong oxidant in the atmosphere. Thereby, HONO is photolysed to NO and OH at wavelengths between 300 and 405 nm:

$$\mathrm{HONO \xrightarrow{h\nu\ (300nm<\lambda<405nm)} OH + NO} \tag{2.14}$$

Especially in the morning when HONO has been accumulated in the planetary boundary layer over night, HONO can be the most important source of the OH production. For instance, in spring 2003 during the Mexico City Metropolitan Area (MCMA)-2003 field campaign it was found that at 7am HONO contributed almost 50 % to the OH production - more than through O_3 or HCHO [Volkamer et al., 2007].

The photolytic reaction (2.14) is the main degradation process of HONO. Furthermore, a few percent of HONO is destroyed by gas phase reaction with OH to H_2O and NO_2:

$$\mathrm{HONO + OH \longrightarrow H_2O + NO_2} \tag{2.15}$$

Also other HONO degrading gas phase reactions have been discussed, but none of them seems to be fast enough to reduce the concentration of HONO noticeable. Furtermore, HONO can be removed by wet deposition when it is washed out by rain as well as dry deposition when it agglomerates on aerosols and ground.

Nitrous acid (HONO) belongs to the group of NO_y which contains all kinds of nitrogen oxides, such as e.g. NO_x, NO_3, HNO_3, N_2O_5, HONO, peroxyacetyl nitrate (PAN). The different NO_y species have in common that they are mostly generated from NO emissions by chemical transformations. Thus, nitrous acid can often be found in polluted areas and proportional to the strength of pollution. Therefore, it can be used as an indicator for the pollution present in the atmosphere. However, unexpected high values of HONO measurements in unpolluted environments indicate that the formation processes of HONO is still not fully understood [e.g. Acker et al., 2006].

Although the formation processes of HONO are still not well known the following various sources can be specified:

HONO can be emitted directly from combustion sources [Kessler and Platt, 1984]. In contrast to NO which is produced at high temperatures ($>2000\,\mathrm{K}$) HONO is formed immediately after the combustion gas has left the combustion area and is cooling down. This process happens e.g. in a tailpipe of a combustion engine (of a car). Therefore, several studies have been performed to investigate the output of HONO during the operation of such an engine [Kessler and Platt, 1984; Pitts et al., 1984; Calvert et al., 1994; Kirchstetter et al., 1996; Kurtenbach et al., 2001]. It turned out that the HONO emissions ranged mostly between 0 and 1 % of those of NO_x, but also reached up to 1.8 %. In high traffic areas, this can arise a significant amount of nitrous acid in the ambient air. The different studies also revealed the behaviour of different engine types. So, the HONO-to-NO_x ratio for diesel engines of heavy trucks was significantly higher than for gasoline engines of cars (without catalytic converter) [Kessler and Platt, 1984]. This is most likely due to formation of nitrous acid on the soot surface in the tailpipe which is explained later. Furthermore, the state of the engine has an impact on the emission amount of HONO. A cold engine operation, bad-maintained engine or an older catalytic converter cause HONO tailpipe emissions to increase [Pitts et al., 1984; Calvert et al., 1994].

The significance of direct emissions of HONO could also be shown in a study of Winer and Biermann [1994]. They did not investigate the exhaust of engines, but measured the concentrations of HONO and NO_2 in the ambient air. This was done between sunset and midnight during six periods in the fall of 1987 in Los Angeles. Thereby, no correlations between the concentrations of HONO and NO_2 or the square of the NO_2 could be observed. In contrast, CO and NO which both are directly emitted from combustion sources correlate with HONO which indicates HONO as a primary emission product as well. The HONO emissions were deduced to be about 0.8 % of the NO_x emissions and a rate of conversion of NO_2 to HONO to be about 1 % per hour.

Indoor combustion processes like gas heating and cooking also emits HONO and can lead to high peak concentrations inside buildings. Brauer et al. [1990] measured 24 h averaged mixing ratios of 40 ppb and peaks of up to 100 ppb. The indoor HONO values correlate with indoor NO_x values and correlate inversely with indoor O_3 [Lee et al., 2002]. Furthermore, comparable high HONO concentrations were measured in tabacco smoke [Eatough et al., 1989]. Since HONO is harmful for the human health such high concentrations can lead to severe health problems. HONO has mutagenic and carcinogenic properties and can affect the lung function as well as irritate eyes.

Generally, direct emissions of HONO are too small to explain the measured concentrations of HONO in the atmosphere [Platt, 1986]. But nevertheless their contribution must not be neglected.

Nitrous acid can also be formed by homogeneous gas phase reactions. Various potential reactions could be identified whereby most of them were found to be of minor importance as a source of HONO. Yet, the recombination of the hydroxyl radical (OH) with nitrogen monoxide (NO) yields significant amounts of HONO:

$$\mathrm{OH + NO + M \longrightarrow HONO + M} \tag{2.16}$$

This HONO source becomes important during daytime under conditions of high pollution with corresponding amounts of NO. Then, NO and OH are formed by photolysis of HONO (see reaction (2.14)). Hence, reaction (2.16) does not represent a net source but rather a secondary source of HONO. Between NO, OH and HONO an equillibrium is established where the HONO present in the atmosphere is photolysed to the reactants of the gas phase reaction (2.16). This happens relatively fast typically within 10 minutes. However, this gas phase reaction cannot explain the nighttime production of HONO because at night, both NO and OH concentrations are generally very low [Geyer et al., 2003]. Furthermore, the amounts of the produced HONO are relatively small [Trick, 2004].

Recently, Bejan et al. [2006] found out that HONO is also generated in the gas phase because of the photolysis of ortho-nitrophenols. In this case, the HONO formation is initiated by intramolecular hydrogen transfer from the phenolic OH group to the nitro group. Again, this can only occur at daytime and yield HONO only in the same order of magnitude as reaction (2.16).

Furthermore, homogeneous three-body reactions of H_2O with NO_x yield nitrous acid. Thereby, the two following reactions can form HONO:

$$\mathrm{2\,NO_2 + H_2O \longrightarrow HONO + HNO_3} \tag{2.17}$$

$$\mathrm{NO + NO_2 + H_2O \longrightarrow 2\,HONO} \tag{2.18}$$

where a disproportionation of NO_x takes place. In contrast to reaction (2.16), the photolysis of HONO formed by reactions (2.17) and (2.18) represent a net source of OH. However, both gas phase reactions can be regarded as relatively unlikely because the reactions are based on three-body collisions.

Thus, also the gas phase reactions can be assumed to be too slow to explain the HONO production, especially at nighttime.

Nitrous acid was found to be generated also heterogeneously, for instance, on humid surfaces like on aerosols, buildings as well as ground [e.g. Platt, 1986; Calvert et al., 1994; Ammann et al., 1998]. Nowadays, heterogeneous formation presumably is the main source of HONO. Thereby, the reactions of NO_x with H_2O (see reactions (2.17) and (2.18)) are important [e.g. Kleffmann et al., 1998; Pitts et al., 1984]:

$$\mathrm{2\,NO_2(g) + H_2O(liq) \xrightarrow{surface} HONO(g) + HNO_3(g)} \tag{2.19}$$

$$NO(g) + NO_2(g) + H_2O(liq) \xrightarrow{\text{surface}} 2\,HONO(g) \tag{2.20}$$

The heterogenity of these reactions was derived by experiments which showed that the reactivity increased with a higher surface-to-volume ratio. Nevertheless, the exact heterogeneous formation process is still in discussion. For instance, the assumption in which N_2O_4 serves as intermediate product in reaction (2.19) resulted in too low calculated HONO yields than actually measured in experiments under atmospheric conditions [Kleffmann et al., 1998]. Thus, the exact HONO contribution of reaction (2.19) is not known as well. However, it is assumed that significant amounts of HONO are produced by this reaction pathway. In contrast, reaction (2.20) seems not to be significant for the formation of HONO in the atmosphere. Several laboratory and field studies found an independence from NO for the HONO formation [e.g. Alicke, 2000; Kleffmann et al., 1998; Pitts et al., 1984]. However, it becomes important in the presence of huge amounts of NO. Notholt and Raes [1992] observed this for foggy episodes of high NO, NO_2 and aerosol concentrations.

Excited NO_2^* which is produced in daylight at wavelengths larger than 420 nm could also play an important role in the HONO formation. In reaction with liquid H_2O, additional OH would be generated:

$$NO_2^*(g) + H_2O(liq) \xrightarrow{\text{surface}} HONO(g) + OH(g) \tag{2.21}$$

Further studies have to check how far this daytime reaction provide significant amounts of HONO.

Further heterogeneous reactions yielding HONO were in discussion, e.g. the reaction of NO_x with sulfuric acid [Svensson et al., 1987]:

$$NO + NO_2 + 2\,H_2SO_4 \longrightarrow 2\,HSO_4NO + H_2O \tag{2.22}$$

$$HSO_4NO + H_2O \longrightarrow H_2SO_4 + HONO \tag{2.23}$$

as well as the reaction of from surface adsorbed nitric acid and NO [e.g. Saliba et al., 2000]:

$$HNO_3(\text{adsorbed}) + NO(g) \xrightarrow{\text{surface}} NO_2(g) + HONO(g) \tag{2.24}$$

However, both reaction pathways are much too slow or at least unimportant in terms of HONO production [Kleffmann et al., 1998, 2004]

Furthermore, Ammann et al. [1998] suggested that HONO is generated heterogeneously from NO_2 exposed to a reducing soot surface:

$$NO_2 + \text{surface}_{\text{red}} \xrightarrow{H_2O} HONO + \text{surface}_{\text{ox}} \tag{2.25}$$

However, only a very small fraction of the soot particles acts reducing (a few percent of a monolayer) and this fraction decreases towards zero within several minutes or less. Thus, the HONO production through the reduction reaction of NO_2 on soot particles saturates and can be most probably regarded as subordinate [Aumont et al., 1999]. This is different when fresh soot is continuously available, like e.g. in tailpipes. Also, an irradiation of soot particles with light could recycle the particle surface reactivity [Gerecke et al., 1998]. Thus, at daytime this source could become important.

The heterogeneous reduction of NO_2 can also take place on adsorbed hydrocarbons HC, such as alkenes, phenols or aromatic amines, which, in turn, are oxidzed:

$$NO_2 + HC_{red}(\text{adsorbed}) \longrightarrow HONO + HC_{ox}(\text{adsorbed}) \tag{2.26}$$

This reaction is very efficient and can explain the nighttime formation of HONO [Vogel et al., 2003]. At daytime, this reaction assumably occurs much faster (1-2 orders of magnitude) owing to photoenhancement with high yields of HONO up to 100 %. This was observed in recent studies where aromatic hydrocarbons and humic acid were photochemically activated in order to form HONO [George et al., 2005; Stemmler et al., 2006]. In the presence of high NO_2 concentrations, also the HONO formation at daytime could be explained in the lower few 100 m of the planetary boundary layer. However, this does not apply to rural regions with very low NO_2.

Finally, it seems nowadays that reaction (2.19) of NO_2 and H_2O as well as reaction (2.26) of the (photoenhanced) reduction of NO_2 by hydrocarbons are the main sources for HONO and additionally, that the latter are much faster at daytime. However, little is known about the vertical distribution of HONO at higher altitudes. It is still controversial if the formation of HONO on surfaces of aerosols or on ground surfaces is larger. While some studies concluded from the coincidence of HONO formation and aerosols that aerosols are the major source [e.g. Notholt and Raes, 1992; Reisinger, 2000], others concluded that the occurence of a vertical gradient of HONO is an indication for a dominant ground source [e.g. Veitel et al., 2002; Kleffmann et al., 2003].

The typical diurnal cycle of HONO in an urban boundary layer shows a strong decrease of HONO amounts after sunrise. So, HONO which was accumulated over night is degraded photochemically. The lifetime of HONO accounts to less than 10 minutes under clear sky and at noon. Over the day, HONO does not disappear at all, but a steady small amount of HONO in the boundary layer is indicative of a steady HONO source as well. While in rural and medium polluted areas, this was found to be less than 100 ppt[2] in polluted areas mixing ratios of about 200 ppt can be measured [e.g. Reisinger, 2000; Veitel, 2002; Alicke et al., 2003]. After sunset, the degradation by photolysis does not take place any more and the concentration of HONO can increase over night.

---

[2] 1 ppt = 1 part per trillion

2.3 Formaldehyde

Formaldehyde (HCHO) is an important intermediate in the oxidation of hydrocarbons (e.g. alkanes and aromatics), especially of methane, in the troposphere [Meller and Moortgat, 2000]. Formaldehyde is a carcinogenic trace gas, irritates the respiratory tract and can induce cancer [WHO, 2000]. Moreover, it entails the formation of other air toxics like ozone.

HCHO can be found both in rural remote regions and industrialised polluted air masses. The mixing ratio of HCHO in rural remote regions is usually below 0.5 ppb while in urban areas it typically accounts for 1-20 ppb. Highly polluted air masses can contain even significantly higher values [e.g. Grosjean, 1991]. In Figure 2.3 the 8 year mean distribution of formaldehyde from satellite measurements (GOME) is shown.

HCHO is a primary emission product mainly in biomass burning [Carlier et al., 1986] and fossil fuel combustion (primary HCHO) [Anderson et al., 1996; Altshuller, 1993]. Furthermore, it is emitted directly into the atmosphere from industrial activity and from vegetation [Kesselmeier et al., 1997]. But predominantly, HCHO is generated as a secondary product of the oxidation of volatile organic compounds (VOCs) (secondary HCHO) [e.g. Altshuller, 1993; Carlier et al., 1986] to which hydrocarbons belong. Generally, many hydrocarbons can form HCHO. Thus, HCHO is an important indicator of tropospheric emissions of hydrocarbons as well as photochemical reactions and photosmog, respectively [Chance et al., 2000]. There are too many individual reaction paths to be mentioned here. But since in regions remote from industrial activity, methane (CH_4) is the most dominant reactant yielding HCHO the following description of the reaction path is confined to methane.

Methane has an averaged mixing ratio of about 1.7 ppm and has a relatively long lifetime of about 10 years, which leads to a constant distribution up to a height of 15-20 km [Finlayson-Pitts and Pitts jr., 2000]. Thus, methane causes a steady source of formaldehyde. Thereby, two main reactions of methane contribute to HCHO [Logan et al., 1981]. Firstly, CH_4 can be oxidised photochemically below a wavelength of 340 nm. There the molecular oxygen (O_2) can be photolytically dissociated to oxygen atoms:

$$\mathrm{CH_4 + O_2 \xrightarrow{h\nu\ (\lambda<340\ nm)} HCHO + H_2O} \tag{2.27}$$

Secondly, CH_4 also reacts with OH and HO_2:

$$\mathrm{CH_4 + OH + HO_2 \longrightarrow HCHO + 2\,H_2O} \tag{2.28}$$

In presence of NO in the atmosphere, which is typical in urban and polluted areas, photochemical oxidation also of non methane hydrocarbons (NMHCs) can occur yielding HCHO [Atkinson et al., 1995]. Thereby, NO is converted to NO_2 (see

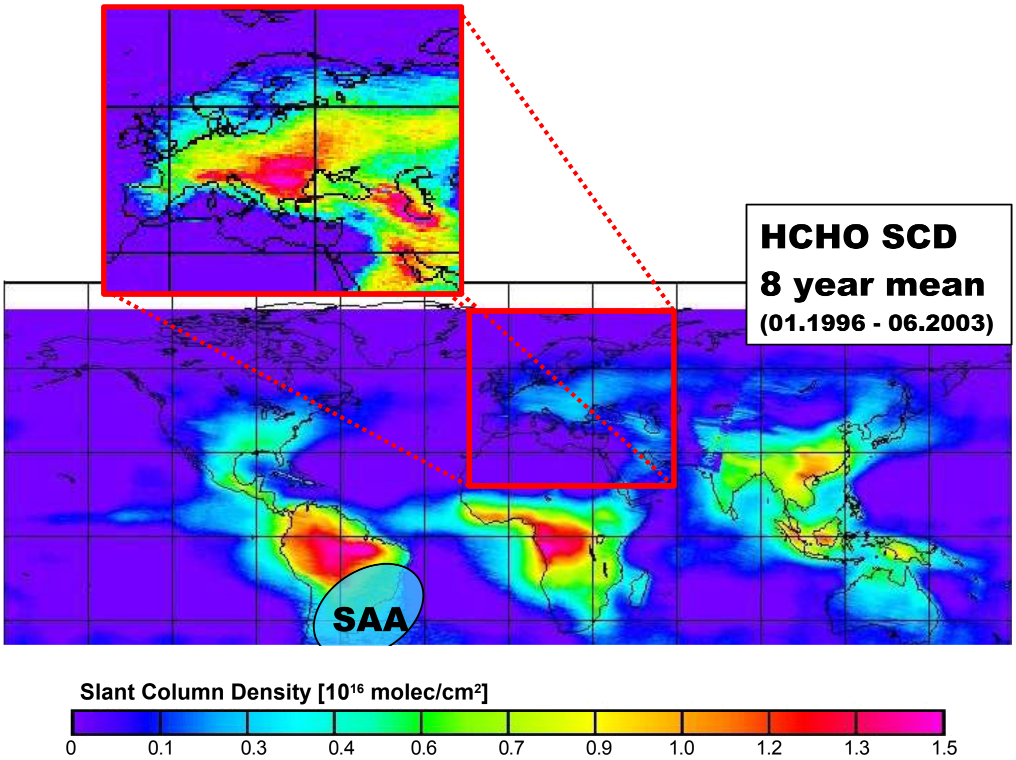

Figure 2.3: *Mean distribution of formaldehyde from satellite measurements (GOME) [Marbach et al., 2007].*

reaction (2.31)). The following reaction path (2.29 - 2.32) is also valid for higher hydrocarbons, but is shown for methane as instance:

$$CH_4 + OH \longrightarrow CH_3 + H_2O \tag{2.29}$$

$$CH_3 + O_2 + M \longrightarrow CH_3O_2 + M \tag{2.30}$$

where M is a required collision partner (e.g. N_2 or O_2) due to conversation of energy and spin momentum.

$$CH_3O_2 + NO \longrightarrow CH_3O + NO_2 \tag{2.31}$$

$$CH_3O + O_2 \longrightarrow HCHO + HO_2 \tag{2.32}$$

HO_2 can further react with NO to NO_2 or with O_3 to two O_2 forming the hydroxyl radical (OH) that is initially consumed in 2.29. Besides, NO_2 is photolytically dissociated at wavelengths below 400 nm and can form O_3 in reaction with O_2.

At daylight, formaldehyde is degraded by photolysis and reaction with OH. Thereby, the lifetime of HCHO is relatively short and accounts for several hours [Logan et al.,

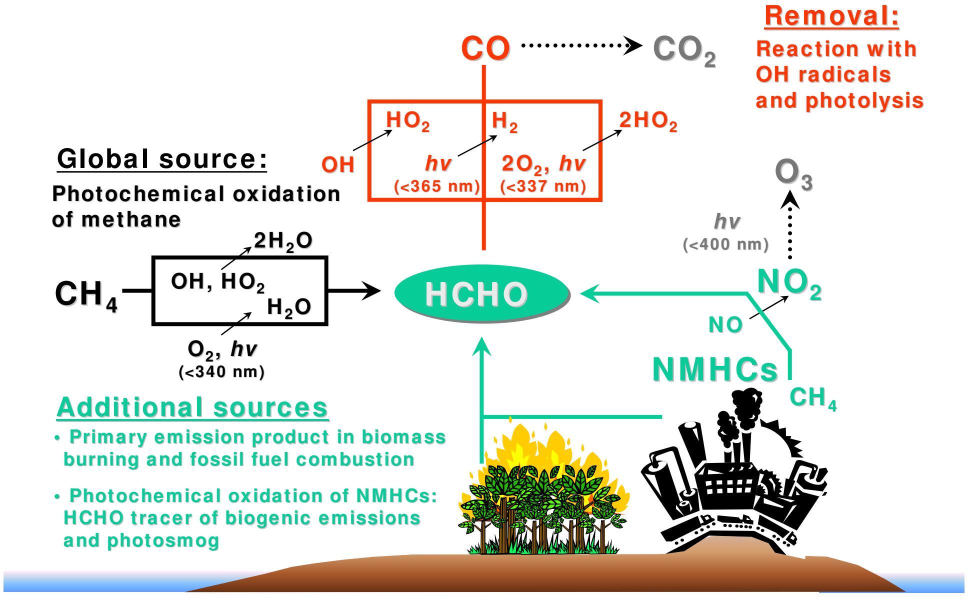

Figure 2.4: *Daylight cycle of formaldehyde in the troposphere [adapted from Marbach et al., 2007].*

1981; Hak, 2006]. Two photolysis paths are possible whereby photolysis path 2.33 dominates for wavelength greater than 325 nm and photolysis path 2.34 at shorter wavelengths:

$$\mathrm{HCHO} \xrightarrow{\mathrm{h}\nu\ (\lambda<365\ \mathrm{nm})} \mathrm{H_2} + \mathrm{CO} \tag{2.33}$$

$$\mathrm{HCHO} \xrightarrow{\mathrm{h}\nu\ (\lambda<337\ \mathrm{nm})} \mathrm{H} + \mathrm{HCO} \tag{2.34}$$

The products of the latter photolysis react rapidly further:

$$\mathrm{H} + \mathrm{O_2} + \mathrm{M} \longrightarrow \mathrm{HO_2} + \mathrm{M} \tag{2.35}$$

$$\mathrm{HCO} + \mathrm{O_2} \longrightarrow \mathrm{HO_2} + \mathrm{CO} \tag{2.36}$$

The reaction of HCHO with OH forms H_2O and HCO which yield with reaction 2.36 HO_2 and CO:

$$\mathrm{HCHO} + \mathrm{OH} \longrightarrow \mathrm{H_2O} + \mathrm{HCO} \tag{2.37}$$

Therefore, all three degradation paths of HCHO result in the production of CO which can be converted to CO_2. The full daylight cycle is outlined in Figure 2.4.

At nighttime, the chemical degradation takes place by the reaction with the nitrate radical (NO_3, see reaction 2.38) which is a relatively slow reaction (the lifetime of HCHO is several orders longer than at daylight) [Altshuller, 1993].

$$\mathrm{HCHO} + \mathrm{NO_3} \longrightarrow \mathrm{HNO_3} + \mathrm{HCO} \tag{2.38}$$

2.4 Glyoxal

Glyoxal (CHOCHO) is the smallest α-dicarbonyl (see Figure 2.5). In the atmosphere, it is generated by oxidation of numerous volatile organic compounds (VOCs) [Calvert et al., 2000; Volkamer et al., 2001; Calvert et al., 2002]. Aromatics, such as benzene, toluene and p-xylene, yield CHOCHO in reaction with OH and are the predominant source for CHOCHO in urban air [Volkamer et al., 2007]. But also the oxidation of some alkenes via O_3 and OH, respectively, produce CHOCHO. On global scales, biogenic VOCs are the largest source for glyoxal. In minor amounts, glyoxal is also emitted from automobile tailpipes. Recent satellite measurements from space (see Figure 2.6) indicate that CHOCHO is released from biomass burning. Additionally, significant CHOCHO concentrations over oceans were measured [Wittrock et al., 2006; Beirle et al., 2006]. It is noteworthy that trace amounts of CHOCHO can be found in butter and in fermented food, such as wine, brandy, beer, yoghurt, cheese and vinegar [Volkamer et al., 2005].

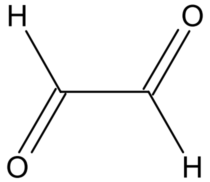

Figure 2.5: *Chemical structure of glyoxal.*

Similarly to formaldehyde, glyoxal is degraded by photolysis and reaction with OH-radicals in many different reaction pathways, which can lead to the formation of H_2, CO, HCHO and HCO. Furthermore, CHOCHO can be removed from atmosphere by dry and wet deposition as well as by adsorption to aerosols. Volatile CHOCHO is suspected to contribute to secondary organic aerosol (SOA) formation which would explain a missing sink of CHOCHO and cannot be observed with HCHO [Volkamer et al., 2007]. However, the atmospheric relevance of CHOCHO uptake on aerosols is presently not clear. At nighttime, another loss pathway possibly is the reaction with NO_3 radicals.

Due to the rapid photolysis and reaction with OH radicals, the atmospheric residence time of CHOCHO accounts to about 1.3 h for overhead sun conditions [Volkamer et al., 2005]. CHOCHO can reach mixing ratios up to a few ppb at peak values around noon.

CHOCHO measurements provide an useful indicator to constrain VOC oxidation processes [Volkamer et al., 2005] and enable an improved source apportionment of formaldehyde in urban air [García et al., 2006].

In high concentrations, CHOCHO may irritate the skin, the respiratory tract or

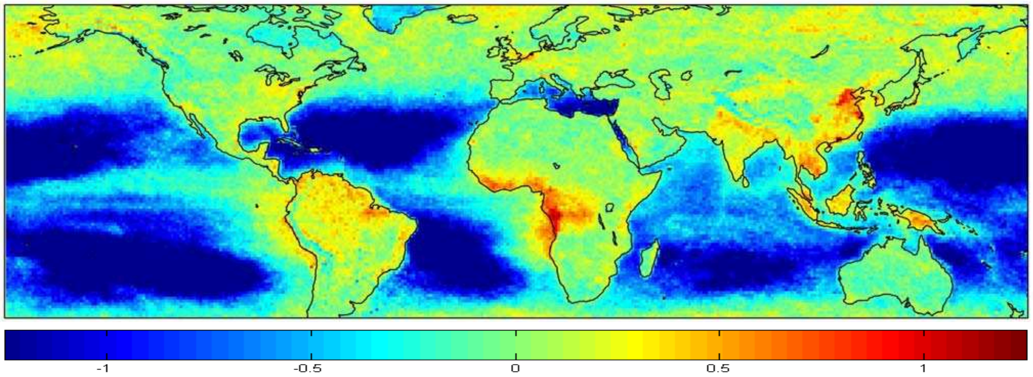

Figure 2.6: *Mean distribution of glyoxal (CHOCHO) slant column densities from satellite measurements (SCIAMACHY) from 2003 to 2005. The values are given in* 10^{15} *molec/cm*^{2} *[Beirle et al., 2006].*

the eyes. the potential health effects of particulate bound CHOCHO are likely very different than that of gas-phase glyoxal, and are presently not yet studied.

2.5 Sulfur Dioxide

Sulfur dioxide SO_2 plays an important role in regional air quality acid rain formation, and the climate. It is generated both naturally (0.05 % of the Earth's crust consists of sulfur) and by human activity. SO_2 emissions can lead to winter smog, like in London 1952. Converted to sulfuric acid (H_2SO_4), it causes acid rain with its adverse effects on soil, trees, lakes, rivers and the involved animals. In high concentrations, it can also be harmful for the human's health due to its toxicity.

More as the half of SO_2 emissions are from antropogenic sources [Brasseur et al., 1999], such as the combustion of sulfur containing fossil fuel. Thus, due to the adverse effects on the performance of catalysts and also on health and environment, desulfurized fuel is used increasingly. Furthermore, the metal ore smelting industry generates SO_2 when producing as pure as possible metals by smelting. Additionally, in the oil production and refinery as well as during coal fires, which could also occur naturally, SO_2 is released because crude oil and coal contain a lot of sulfur. Burning of biomass also produces SO_2 and can be both antropogenic (clearings of forest by fire) and natural (e.g. forest fires due to lightning strokes). As definite natural source, volcanos emit significant amounts of SO_2. Finally, oceans and wetlands release reduced sulfur species which are rapidly oxidized by OH yielding SO_2. Such species are hydrogen sulfide (H_2S), carbonyl sulfide (COS) and dimethyl sulfide (DMS, CH_3SCH_3) as well as carbon disulfide (CS_2) which is additionally emitted from volcanos, forests and industry [Watts, 2000; Ulshöfer et al., 1995].

Sulfur dioxide is oxidized reaction with OH-radicals and removed from the atmosphere by dry deposition on the ground. Yet, the degradation by oxidation is more likely whereby the most important reaction chain is the following [Stockwell and Calvert, 1983]:

$$\mathrm{SO_2 + OH + M \longrightarrow HSO_3 + M} \tag{2.39}$$

$$\mathrm{HSO_3 + O_2 \longrightarrow SO_3 + HO_2} \tag{2.40}$$

$$\mathrm{SO_3 + H_2O + M \longrightarrow H_2SO_4 + M} \tag{2.41}$$

where about 30 % of the total SO_2 is degraded. Thereby, the oxidative capacity of the atmosphere does not change. Since SO_2 is a polar molecule it is water soluble. It also reacts with liquid water e.g. in clouds yielding an equilibrium of SO_2 in gas phase and SO_3^{2-} in aqueous phase:

$$\mathrm{SO_2(g) + H_2O \longleftrightarrow H_2SO_3(aq)} \tag{2.42}$$

$$\mathrm{H_2SO_3(aq) \longleftrightarrow HSO_3^-(aq) + H^+(aq)} \tag{2.43}$$

$$\mathrm{HSO_3^-(aq) \longleftrightarrow SO_3^{2-}(aq) + H^+(aq)} \tag{2.44}$$

$H_2SO_3^-$ and SO_3^{2-} in aqueous phase can also be oxidized to H_2SO_4, e.g. by reaction with hydrogen peroxide (H_2O_2). The oxidation processes finally leads to sulfate (SO_4^{2-}) which conglomerate to particles. These can serve as cloud condensation nuclei facilitating the formation of cloud droplets. Then, the sulfate particles are removed from atmosphere by wet deposition (rain-out).

SO_2 can affect the Earth's radiative budget and climate in two ways:

Firstly, as serving as cloud condensation nuclei, it leads to more clouds and moreover, to more and hence smaller cloud droplets within the cloud since the water in the atmosphere has to be distributed to more droplets. Both mostly increase the albedo compared to ground and clouds with larger droplets which are darker. In 1987, the CLAW hypothesis was introduced which claims a self-regulation of the climate due to higher biological emissions of sulfur (via DMS) in warmer periods. This sulfur, in turn, cools the climate owing to the then higher albedo so that it serves as a kind of thermistat [Charlson et al., 1987; Bates et al., 1987]. However, the CLAW hypothesis has been discussed controversy.

Secondly, the sulfate particles reflect more sunlight back to space than thermal radiation back to Earth. This occurs especially in higher altitudes, hence the stratosphere, and induce a cooling effect to climate. Therefore, Crutzen [2006] discussed to emit additional sulfur to atmosphere to compensate for the antropogenic green house effect. Also, this has led to a heated debate.

3 Differential Optical Absorption Spectroscopy

3.1 DOAS Overview

Differential Optical Absorption Spectroscopy (DOAS) is a very sensitive and widely used measurement technique used in order to detect trace gases in the atmosphere [Perner and Platt, 1979; Platt, 1994]. It was introduced by Platt et al. [1979] when measuring atmospheric trace gases with an artificial light source. Since then, DOAS has been applied to measure concentrations of many trace gases for the first time, e.g. OH by Perner et al. [1976], HONO by Perner and Platt [1979] and Platt and Perner [1980], NO_3 by Platt et al. [1980], BrO in the stratosphere by Sanders et al. [1988] and BrO in the troposphere by Hausmann and Platt [1994], IO by Alicke et al. [1999], and CHOCHO by Volkamer et al. [2005]. A variety of other trace gases absorbing in the UV and the visible wavelength region can be detected as well, e.g. NO_2, ClO, O_3, SO_2, CS_2, HCHO, OClO, H_2O, and NH_3 [Platt, 1994]. Most recently, CH_4 could be measured in the near-IR wavelength region from satellite [Frankenberg et al., 2005] and from a ground-based device [Woyde, 2007].

DOAS is based on the absorption of light traversing a gas volume and being attenuated characteristically for each trace gas in this volume. From the spectral position and strength of these absorbing lines, the trace gases can be identified and quantified. Because DOAS is capable of measuring the composition of ambient air in the open atmosphere without any interactions caused by measurement processes, it can also detect highly reactive species, such as the free radicals OH, NO_3, NO_2, BrO, ClO and IO. Furthermore, DOAS is able to measure several trace gases simultaneously, which reduces measurement time and allows the analyse of different chemical components in the observed air mass.

Generally, DOAS can be performed actively, using artificial light sources, as well as passively with natural, extraterrestrial light sources. As passive light source, most commonly the sun is used owing to its high intensity in comparison, for instance, to the moon. Passive DOAS can be divided into scattered light measurements pointing somewhere into the sky and direct light measurements, which point directly into the sun or moon. Active setups often use high pressure Xe-arc lamps, but most recently light emitting diodes (LEDs) were also introduced [Kern et al., 2006; Sihler, 2007]. They need far less power, have a much longer lifetime, are easier to handle, and have less spectral structures as well as stray light in the spectrograph than the traditional

Xe-arc lamps. However their wavelength range is much more limited. The following list gives an overview of the most common DOAS applications:

Multi-AXis(MAX)- and Zenith-Sky-DOAS measure scattered sunlight mostly from the ground and provide information on the concentration of trace gases in the atmosphere integrated along the light path. Zenith-Sky-DOAS instruments only point into the zenith and are suitable for investigating stratospheric absorbers. In contrast, MAX-DOAS measurements, on which this work is based, vary the viewing direction, are sensitive to trace gases in the troposphere and can deliver information on the altitude profile of trace gases (see chapter 3.6). MAX-DOAS devices are easy to maintain and are also suited for conducting long term measurements.
Recently, these devices have been installed on different platforms, such as airplanes (AMAX-DOAS), vessels (SMAX-DOAS) and cars (Auto-MAX-DOAS). Thus, it is possible to observe atmospheric gases along these respective tracks.

Long path DOAS uses artificial light sources. Typically, light is sent out by a Newton telescope and is reflected by a retro-reflector array usually at a distance of several kilometers away, before it is received again. Thus, the measurement is constrained to the lowermost atmosphere. In contrast to scattered light instruments, the derivation of concentrations and mixing ratios is easier and measurements by night are also possible. However, it is adverse that the operation of long path DOAS devices requires a relatively large effort. By using several long path instruments together, tomography measurements can provide information on spatial distributions of trace gases. Multiple reflection cells (White Cells) convolve the light path many times and, therefore, can measure trace gases of a small air mass parcel. The recently developed method Cavity Enhanced Absorption Spectroscopy (CEAS) uses this principle.

Satellite borne DOAS enables the retrieval of a global picture of the spatial distribution of atmospheric trace gases. Instruments such as the Global Ozone Monitoring Instrument (GOME) onboard the satellite ERS-2, the SCanning Imaging Absorbtion SpectroMeter for Atmospheric CHartographY (SCIAMACHY) onboard Envisat, the Ozone Monitoring Instrument (OMI) onboard NASA/EOS AURA, and finally, GOME2 onboard METOP, measure reflected and in the Earth's atmosphere scattered sunlight (Nadir mode) and direct sunlight traversed the Earth's atmosphere (Limb mode), respectively.

Imaging DOAS enables the retrieval of two-dimensional images of the distribution of trace gases. It has been applied to exhaust gas plumes from power plants and volcanic plumes.

Balloon borne DOAS measurements use either scattered or direct sunlight. The latter requires a good alignment with the sun even in atmospheric turbulence. They are able to provide altitude profiles of atmospheric trace gases up until the stratosphere.

3.2 The Lambert-Beer Law

The Lambert-Beer Law (see equation (3.1)), on which absorption spectroscopy is based, describes how light is absorbed by matter. Three parameters determine the attenuation of light: the concentration c of the absorbing material, its cross section σ (i.e. the probability of absorption) and the length L of the light path through the absorbing material:

$$I(\lambda, L) = I_0(\lambda) \cdot e^{-c \cdot \sigma \cdot L} \tag{3.1}$$

In this work, the light source consists of the sun, and the matter is the Earth's atmosphere. The sunlight traversing the atmosphere is scattered and absorbed by the different trace gases i in the atmosphere. Scattering processes can be both Mie and Rayleigh scattering, which are described in detail in section 4.2. One portion of the incident light finally reaches the Earth's surface with the intensity $I(\lambda, L)$:

$$I(\lambda, L) = I_0(\lambda) \cdot e^{-\int_0^L [\sum_j \sigma_j(\lambda,T,p) \cdot c_j(l) + \epsilon_M(\lambda,l) + \epsilon_R(\lambda,l)] dl} \tag{3.2}$$

where $I(\lambda, L)$ and $I_0(\lambda)$ denote the wavelength dependent intensities after and before, respectively, passing the atmosphere. $I(\lambda, L)$ is also dependent on the length of the light path, assuming that more absorbing and scattering processes take place when the light path through the atmosphere is longer. $\sigma_j(\lambda, T, p)$ are the cross sections of the different trace gases, which are dependent on the wavelength λ, the temperature T, and to a minor degree, the pressure p. $c_j(l)$ are the concentrations of the different trace gases j along the light path. $\epsilon_M(\lambda, l)$ and $\epsilon_R(\lambda, l)$ stand for the extinction coefficients of the Mie and Rayleigh scattering respectively, which both are also wavelength dependent.

The logarithm of the ratio of the initial and attenuated intensity is defined as the optical density $\tau(\lambda)$:

$$\tau(\lambda) := \ln\left(\frac{I_0(\lambda)}{I(\lambda, L)}\right) \tag{3.3}$$

However, the calculation of τ requires the knowledge of $I(\lambda, L)$ and $I_0(\lambda)$. While $I(\lambda, L)$ can be determined easily at the Earth's surface, in most cases $I_0(\lambda)$ is not known and would have to be measured simultaneously from space. Furthermore, the scattering processes mentioned above are overlaid onto the absorption structure of the trace gases and disturb the retrieval of the absorption structures. Both

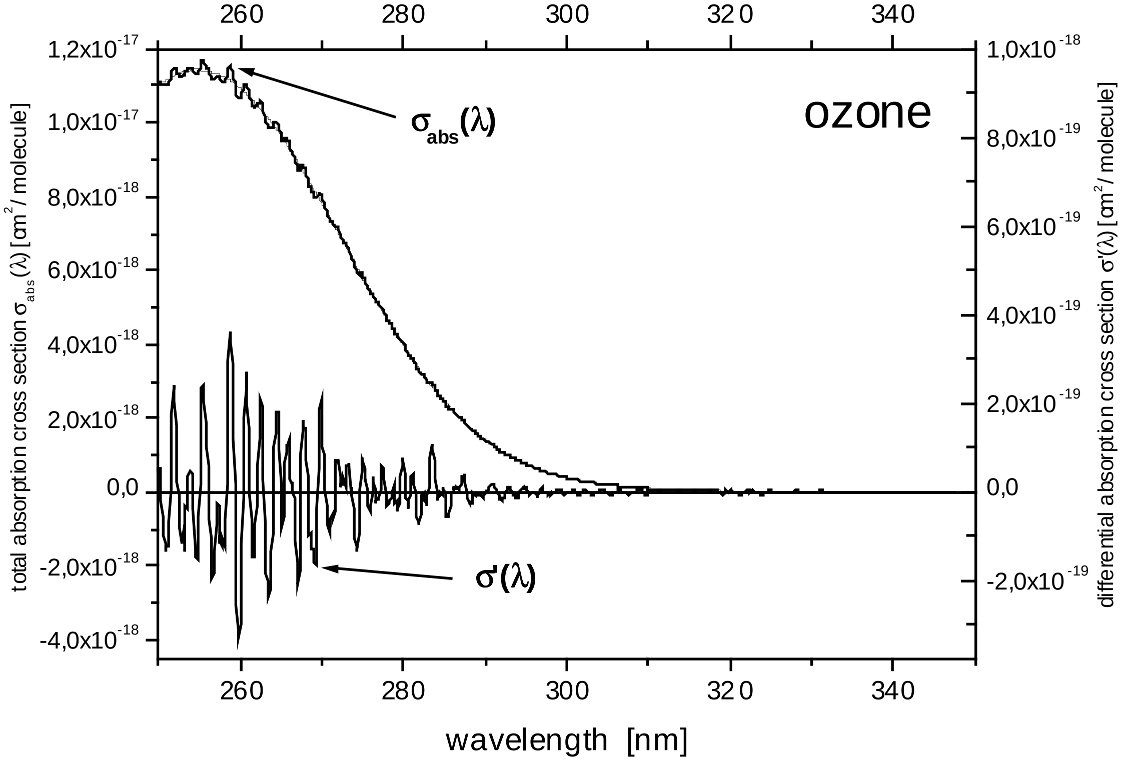

Figure 3.1: *Absolute cross section* $\sigma_{abs}(\lambda)$ *and narrow band (differential) cross section* $\sigma'(\lambda)$ *of ozone as instance.* $\sigma'(\lambda)$ *can be extracted by subtracting the broad band part of the cross section from* $\sigma_{abs}(\lambda)$ *which is mathematically the application of a high pass filter.*

restrictions can be overcome by separating the absorption cross section $\sigma(\lambda, T, p)$ into a narrow and a broad band part, $\sigma'(\lambda, T, p)$ and $\sigma^B(\lambda, T, p)$, respectively:

$$\sigma_{abs}(\lambda, T, p) := \sigma'(\lambda, T, p) + \sigma^B(\lambda, T, p) \tag{3.4}$$

Figure 3.1 illustrates the extraction of the narrow band (differential) part from the absolute cross section of ozone. With equation (3.4) the Lambert-Beer Law for n trace gases can now be written as:

$$\begin{aligned} I(\lambda, L) &= I_0(\lambda) \cdot e^{-\int_0^L [\sum\limits_{j=0}^{n} (\sigma'_j(\lambda,T,p)+\sigma^B_j(\lambda,T,p))\cdot c_j(l)+\epsilon_M(\lambda,l)+\epsilon_R(\lambda,l)]dl} \\ &= I'_0(\lambda) \cdot e^{-\int_0^L [\sum\limits_{j=0}^{n} (\sigma'_j(\lambda,T,p))\cdot c_j(l)]dl} \end{aligned} \tag{3.5}$$

where $I'_0(\lambda)$ contains the initial intensity as well as the broad band absorption part of the trace gases and the Mie and Rayleigh scattering, which are both also

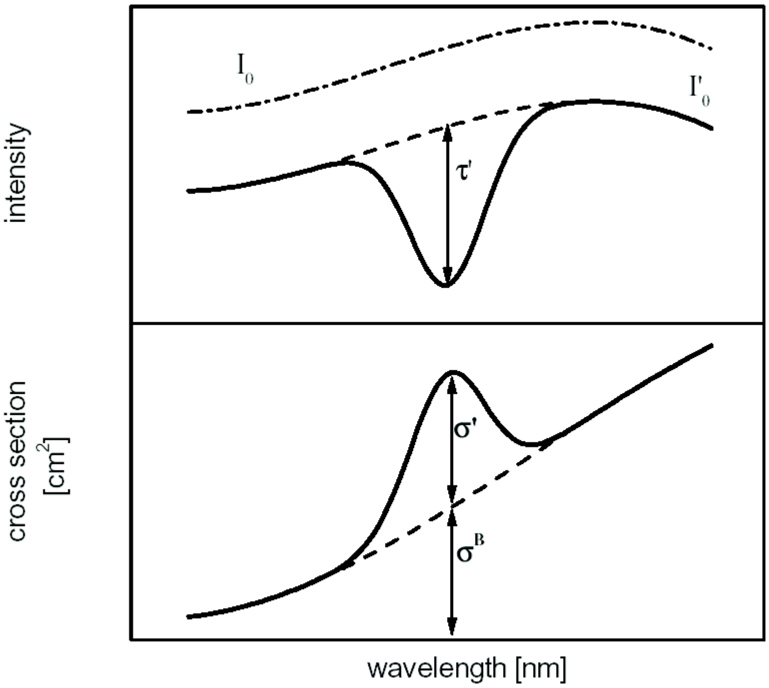

Figure 3.2: *Above: The differential optical density* τ' *which is derived from* I_0'*. Below: Dispartment of the absolute cross section* σ_{abs} *into a broad band part* σ^B *and a narrow band part* σ'*.*

broad banded. $I_0'(\lambda)$ can be computed from the measured spectrum $I(\lambda, L)$ by applying a low pass filter. Mathematically, the differential absorption cross sections $\sigma_j'(\lambda, T, p)$ can be yielded by applying a high pass filter to the absorption cross sections $\sigma_j(\lambda, T, p)$.

Similarly, from (3.3) and (3.5) the differential optical density $\tau'(\lambda)$ is derived, which is sketched in Figure 3.2:

$$\tau'(\lambda) = \ln\left(\frac{I_0'(\lambda)}{I(\lambda, L)}\right) \tag{3.6}$$

Since DOAS uses only differential cross sections, no absolute calibration of $I_0(\lambda)$ is necessary. The trace gas can be measured by merely observing differential values.

The primary quantity of a DOAS measurement is the slant column density (SCD) S, which is the integrated concentration c along the light path l, and is given in the unit of molecules per cm^2:

$$S = \int_0^L c\, dl \tag{3.7}$$

Comparing equation (3.6) with equation (3.7) and taking into account equation (3.3), the slant column density becomes:

$$S = \frac{\tau'(\lambda)}{\sigma'(\lambda, T, p)} \tag{3.8}$$

Since for scattered light measurements the DOAS analysis is applied to the ratio of the measured spectrum $I(\lambda)$ and the reference spectrum $I_0(\lambda)$ which also contains a certain amount of trace gas absorption, the actual quantity of the DOAS measurement is the differential slant column density (dSCD), i.e. the difference between the actual SCD and the SCD of the reference spectrum.

3.3 The Measurement Procedure

In Figure 3.3 the measurement procedure of a simplified DOAS setup is illustrated. Light with the initial intensity $I_0(\lambda)$ traverses the observing air mass (atmosphere). Along the light path L, it is affected by extinction owing to absorption as well as scattering processes by molecules and aerosol particles before $I(\lambda, L)$ is collected by a telescope (see Figure 3.3a). In this example, only one absorber, namely formaldehyde, is considered. The telescope focuses the light onto an entrance slit of a grating spectrograph with a detector which records the spectrum of the dispersed light. Owing to the limited resolution of the spectrograph (determined by the entrance slit and the grating properties), the spectral resolution of spectrum $I(\lambda, L)$ is degraded (see Figure 3.3b). The mathematical description of this process is a convolution with the instrument function H yielding $I^*(\lambda, L)$ as it is projected by the spectrograph on the detector:

$$I^*(\lambda, L) = H * I(\lambda, L) = \int I(\lambda') \cdot H(\lambda - \lambda') d\lambda' \tag{3.9}$$

Via the multi-channel detector the wavelength range is mapped into n discrete pixels, numbered i, each integrating the light in a small wavelength range between λ_i and λ_{i+1} (see Figure 3.3c):

$$I'(i) = \int_{\lambda_i}^{\lambda_{i+1}} I^*(\lambda', L) d\lambda' \tag{3.10}$$

These channels are read out and the spectra are stored and logarithmized yielding $J(i)$ by a connected PC. The correlation between wavelengths and channels of the spectrograph can usually be approximated by a polynomial:

$$\lambda(i) = \sum_{k=0}^{q} \gamma_k \cdot i^k \tag{3.11}$$

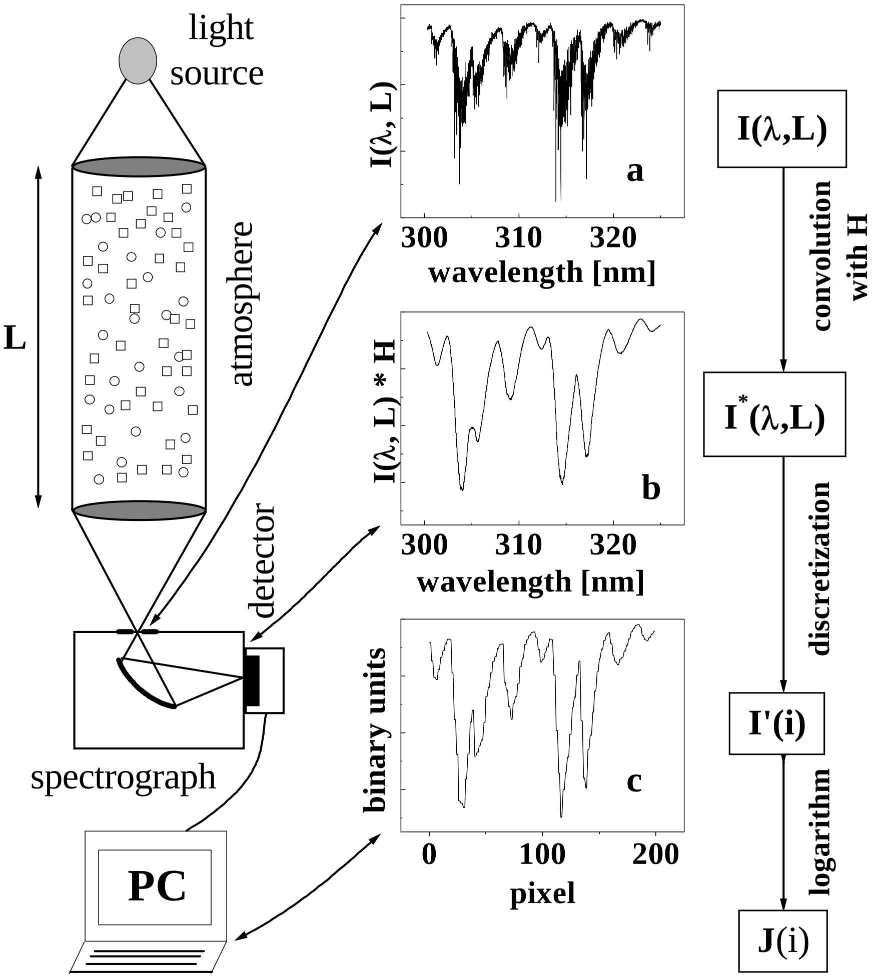

Figure 3.3: *The components of a simplified DOAS setup. Light traverses an air mass and is attenuated by an absorber, characteristically for the trace gas in the atmosphere (in this example formaldehyde). (a) shows the respective spectrum with the absorption structure of formaldehyde. In (b) the light was convolved by the spectrograph and (c) shows the mapping by the detector. Afterwards the spectrum consisting of discrete pixels is stored in a connected PC [Stutz and Platt, 1996].*

where the mapping of the pixel i to the wavelength $\lambda(i)$ is given by γ_k and is referred to as wavelength-pixel-mapping or wavelength calibration. γ_0 denotes a spectral shift of the spectrum, while γ_1 stands for a spectral squeeze or stretch of the entire spectrum. A parameter γ_k with $k \geq 2$ indicates a distortion of the spectrum and an unequal spectral pixel width. In contrast, a linear wavelength-pixel-mapping yields a constant spectral pixel width. The parameter vector (γ_k) changes easily if the measurement conditions are not stable. For instance, a varying temperature of the spectrograph usually leads to a shift in the wavelength calibration. This has to be either avoided or later corrected accordingly.

After having derived the suitable wavelength calibration it also has to be applied to the differential trace gas cross sections $\sigma'_j(\lambda, T, p)$ so that the wavelength-pixel-mapping of the measured spectrum and the cross sections are the same. Furthermore, $\sigma'_j(\lambda, T, p)$ have to be converted to the same resolution as the spectrograph. If the cross sections are measured with the same spectrograph, both restrictions are already inherently fulfilled. However, often cross sections are used which are measured in the laboratory with a different measurement device and which have a much higher resolution. Thus, subsequently they have to be convolved with the instrument function H:

$$\sigma^*(\lambda, T, p) = H * \sigma(\lambda, T, p) = \int \sigma(\lambda', T, p) \cdot H(\lambda - \lambda') d\lambda' \tag{3.12}$$

In Figure 3.4, the high resolution cross sections which are used in this work are shown between 290 and 460 nm. In the spectral analysis, which is a numerical process and which is described in the following section, up to ten trace gases can be identified simultaneously in one single spectrum [Platt, 1994].

3.4 The Spectral Analysis

3.4.1 The Analysis Procedure

The aim of the spectral analysis is the retrieval of the slant column densities of trace gases in the observed air mass. For that, the Lambert-Beer Law from equation (3.5) is taken and logarithmized:

$$\begin{aligned} \ln(I(\lambda, L)) = \ln(I_0(\lambda)) - \\ \int_0^L \left(\sum_{j=0}^{n} (\sigma'_j(\lambda, T, p) + \sigma_j^B(\lambda, T, p)) \cdot c_j(l) + \epsilon_M(\lambda, l) + \epsilon_R(\lambda, l) \right) dl \end{aligned} \tag{3.13}$$

Mathematically, the separation of the narrow and broad band part can be achieved by merging all broad banded spectral components, namely the broad band part of the trace gas absorption cross sections $\sigma_j^B(\lambda, T, p)$, the Mie scattering $\epsilon_M(\lambda, l)$ and the

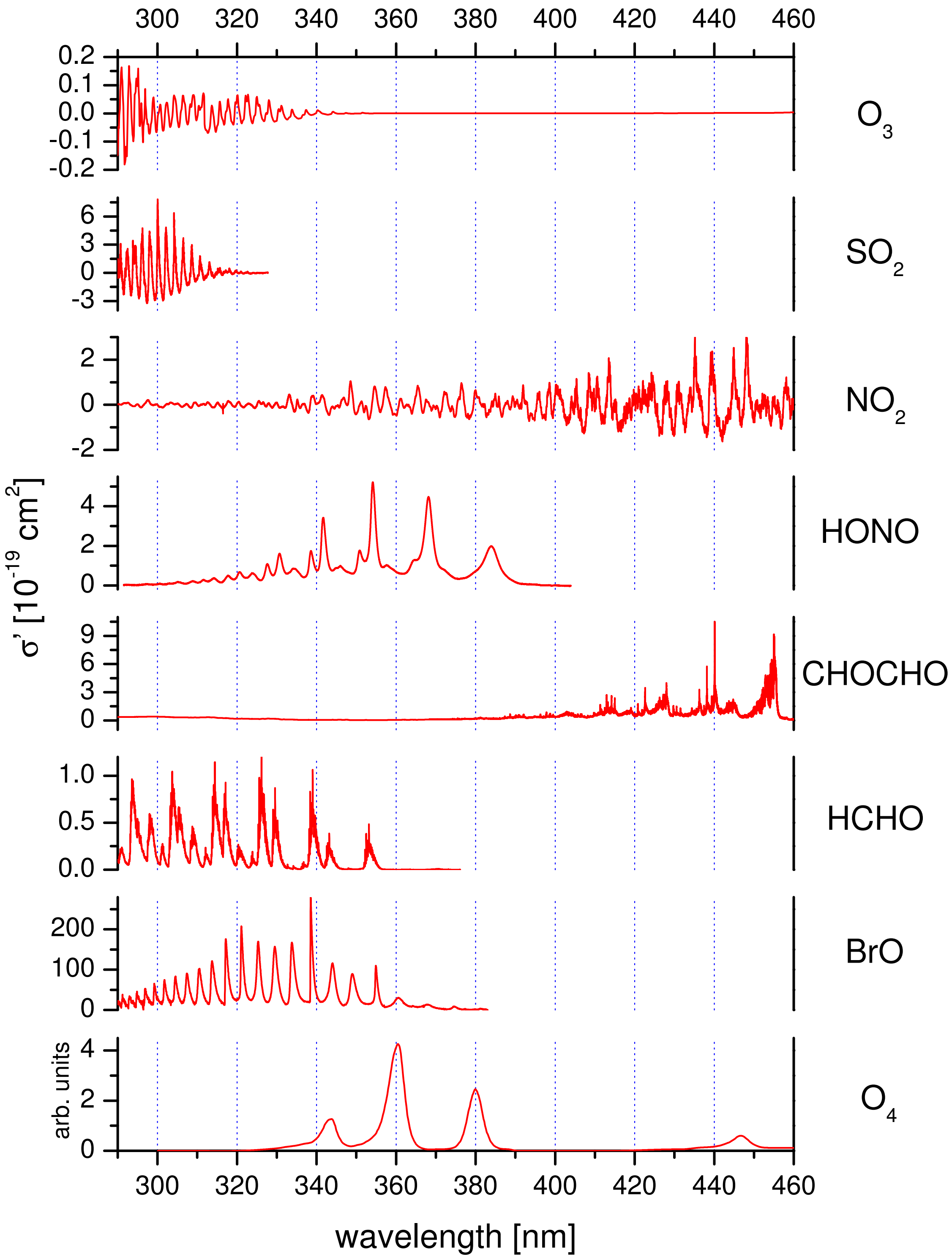

Figure 3.4: *High resolution cross sections from literature in the wavelength range from 290 to 460 nm. From top to down:* O_3 *[Bogumil et al., 2003],* SO_2 *[Vandaele et al., 1994],* NO_2 *[Vandaele et al., 1998], HONO [Stutz et al., 2000], CHOCHO [Volkamer et al., 2005], HCHO [Meller and Moortgat, 2000] as well as BrO [Wilmouth et al., 1999] all in* 10^{-19} *cm*^{2}*, and* O_4 *[Greenblatt et al., 1990] in arbitrary units.*

Rayleigh scattering $\epsilon_R(\lambda, l)$, into one polynomial [Platt et al., 1979]. Consequently, the differential trace gas cross sections $\sigma'_j(\lambda, T, p)$ remain:

$$\ln(I(\lambda, L)) = \ln(I_0(\lambda)) - \int_0^L \left(\sum_{j=0}^{n} \sigma'_j(\lambda, T, p) \cdot c_j(l) + \sum_{m=0}^{p} \alpha_m \cdot \lambda^m \right) dl \qquad (3.14)$$

with the polynomial $\sum\limits_{m=0}^{p} \alpha_m \cdot \lambda^m$ of the degree p, which has to be chosen according to the broad banded shape. A higher polynomial degree than required could affect the retrieval of the differential structures.

Since the differential trace gas cross sections $\sigma'_j(\lambda, T, p)$ and the polynomial do not depend on the light path through the observed air mass they can be excluded from the integral (regarding T and p to be constant in the investigated air mass):

$$\ln(I(\lambda, L)) = \ln(I_0(\lambda)) - \left(\sum_{j=0}^{n} \sigma'_j(\lambda, T, p) \cdot \int_0^L c_j(l) dl + \sum_{m=0}^{p} \alpha_m \cdot \lambda^m \right) \qquad (3.15)$$

With equation (3.7), it can also be written as:

$$\ln(I(\lambda, L)) = \ln(I_0(\lambda)) - \left(\sum_{j=0}^{n} \sigma'_j(\lambda, T, p) \cdot S_j + \sum_{m=0}^{p} \alpha_m \cdot \lambda^m \right) \qquad (3.16)$$

The solution of equation (3.16) delivers the values for S_j and can be retrieved by a least squares fit [Gomer et al., 1993; Stutz and Platt, 1996]. Thereby, a combination of a linear least squares fit [Albritton et al., 1976; Bevington, 1969] and the non-linear Levenberg-Marquardt method [Levenberg, 1944; Marquardt, 1963] is applied. The latter is an iterative procedure starting with the linear solution of the least squares fit.

The linear least squares fit procedure simulates numerically $\ln(I(\lambda, L))$ as exact as possible by means of the slant column densities S_j and the polynomial so that the difference χ^2 between $\ln(I(\lambda, L))$ and the fit (i.e. the right side of equation (3.16)) becomes minimal. Thereby, $\sigma'_j(\lambda, T, p)$, n, and p are fixed parameters:

$$\chi^2 := \int_{\lambda_1}^{\lambda_2} \left(\ln(I(\lambda, L)) - \ln(I_0(\lambda)) + \sum_{j=0}^{n} \sigma'_j(\lambda, T, p) \cdot S_j + \sum_{m=0}^{p} \alpha_m \cdot \lambda^m \right)^2 d\lambda \xrightarrow{!} min \qquad (3.17)$$

where λ_1 and λ_2 determine the limits of the wavelength range in which the analysis should be performed. The wavelength range should include suitably strong differential absorption features of the trace gas of interest. Since the output of the measurement is not a continuous spectrum but discrete pixels, the integral over the wavelength can be replaced by a sum:

$$\chi^2 := \sum_{k=k_{\lambda_1}}^{k_{\lambda_2}} \left(\ln(I(k,L)) - \ln(I_0(k)) + \sum_{j=0}^{n} \sigma'_j(k,T,p) \cdot S_j + \sum_{m=0}^{p} \alpha_m \cdot k^m \right)^2 \overset{!}{\rightarrow} min \tag{3.18}$$

with k_{λ_1} and k_{λ_2} as the pixel numbers of the start and the end wavelengths of the investigated wavelength range, respectively. For condition (3.18) the analytical solution can be derived by obtaining the partial derivations of χ^2 with respect to the free parameters S_j and α_m.

In practice, this condition cannot be totally fulfilled in the way that the minimum becomes zero. This is due to inevitable noise during the measurement procedure. Even when using a light source with a constant intensity, noise is still present because the number of detected photons vary around a mean value. Besides this photon noise, instrument noise also occurs. That means that in the electronics statistical variations are superimposed onto the measured signal. Thus, a residual R remains which is the difference between $\ln(I(k,L))$ and the fitted logarithm of the intensity:

$$R_k = \ln(I(k,L)) - \ln(I_0(k)) + \sum_{j=0}^{n} \sigma'_j(k,T,p) \cdot S_j + \sum_{m=0}^{p} \alpha_m \cdot k^m \tag{3.19}$$

The root mean square (RMS) χ of the residual is a measure of the quality of a trace gas retrieval. The lower the RMS, the better the spectral analysis can be considered. An ideal spectral analysis leads to an unstructured residual, containing noise only. However, a misalignment of the wavelength calibration, an inclusion of inaccurate cross sections, or additional absorbers not considered could easily cause systematic structures to appear in the residual.

The described linear fitting procedure inherently cannot include non linear effects, e.g. a change in the wavelength calibration. The spectral analysis is very sensitive to changes in the wavelength calibration, especially for absorbers with small optical densities. Even wavelength shifts of only a few percentage of a pixel can lead to strong systematic structures in the residual. Allowing for a shift and a squeeze/stretch of a spectrum can compensate for the changing of the wavelength calibration of a spectrum. This can be done by adding an additional polynomial to the original wavelength grid with λ_k creating a new wavelength grid with λ'_k:

$$I(\lambda_k) \rightarrow I(\lambda'_k) \quad \text{with} \quad \lambda'_k = \lambda_k + s_0 + s_1(\lambda_k - \lambda_c) + s_2(\lambda_k - \lambda_c)^2 \tag{3.20}$$

where λ_c denotes the centre wavelength of the investigating wavelength range (see equation (3.18)), s_0 the shift parameter, and s_1 and s_2 the squeeze/stretch parameters.

Furthermore, an artificial signal can be overlaid onto the spectra's intensities. This can be due to stray light in the housing of the spectrograph, a nonlinearity between the signal of the detector and the light intensity or unstable detector electronics. Normally these additional signals vary only slowly with wavelength so that a polynomial which is added to the intensity is able to compensate for them:

$$I(\lambda) \rightarrow I(\lambda') = I(\lambda) - P_{add} \tag{3.21}$$

P_{add} is referred to as an additive or prelogarithmic polynomial and is not related to the polynomial introduced in equation (3.14), which, in turn, accounts for the broad banded part of the measured sunlight.

These non-linear effects are solved with the Levenberg-Marquardt algorithm, which varies the wavelength calibration and the additive polynomial numerically in order to achieve the best fit for the slant column densities in the measured spectrum.

3.4.2 Validity Considerations

The linear least squares fit in the spectral analysis provides the best results and accounts for the most errors if the following assumptions are valid:

- *The errors of the pixels must have a finite variance* [Albritton et al., 1976]. Since the dominant source of noise is normally photon noise, for which the error distribution accords with the Poisson statistics, this assumption is fulfilled.

- The least squares fit normally presumes that *the intensity errors of the individual pixels are independent* [Albritton et al., 1976; Bevington, 1969]. However, the instrument function of the measurement instrument ranges over several pixels. Thus, adjacent pixels cannot be regarded as strictly independent so that this presumption is not strictly valid.
  This can lead, despite high diligence, to statistical structures in the residual which are not caused by noise. In most cases, these structures occur randomly and vary continuously. In a residual containing noise only, the width of any structure would be only one pixel, hence indicating independent pixel intensities. But here, groups of adjacent pixel intensities seem to change simultaneously in the residuals in a random way. In order to quantify the statistical effect of residual structures on the DOAS retrieval error, an approach based on simple Monte Carlo methods [Hausmann et al., 1997, 1999] can be applied. Alternatively, the fit errors can be multiplied with the appropriate factor for the respective spectral analysis [Stutz and Platt, 1996]. In any case, such structures must be evaluated carefully in terms of spectral fit quality and uncertainty estimation.

In contrast, stable residual structures cannot be described by statistical methods and are caused by systematic errors in the analysis, such as an additional, not considered absorber or neglected special features of the instrument.

- *The systematic error of the pixel is zero* [Albritton et al., 1976]. It depends on the measurement instrument if this is given. The different pixels of various detectors do not have the same sensitivity so that systematic pixel-to-pixel variabilities can occur. For correction, these can be measured by a broad-banded light source with smooth wavelength dependency.

- *The finite spectral resolution of the measurement instrument has a negligible effect on the spectral analysis.* In practice, the typical spectral resolution of a DOAS instrument is in the order of tenths to several nanometers in the UV-Vis range. This is much larger than the natural band width of atmospheric absorptions. In the spectral analysis, this mismatch is overcome by convolving the absorption cross sections $\sigma(\lambda, T, p)$. This means that $H * \sigma(\lambda, T, p)$ is calculated yielding $\sigma^*(\lambda, T, p)$ (see equation (3.12)), with H being the instrument function.
However, as described in section 3.3, in the measurement process the lower resolution originates in the spectrograph (determined by the entrance slit and the grating) and actually affects the intensity (see equation (3.9)):

$$I^*(\lambda, L) = H * I(\lambda, L) = H * (I_0(\lambda) \cdot e^{-\sigma(\lambda,T,p)\cdot S}) \tag{3.22}$$

for the simplified case of only one absorber and no broad band features. From equation (3.22), $\tau(\lambda)$ can be written as:

$$\tau(\lambda) = \ln\left(\frac{H * I_0(\lambda)}{H * (I_0(\lambda) \cdot e^{-\sigma(\lambda,T,p)\cdot S})}\right) \tag{3.23}$$

For weak absorbers ($\tau(\lambda) \ll 1$), the logarithm can be approximated by the first two terms of the Taylor expansion so that the convolution and the logarithm function can be exchanged:

$$\begin{aligned}\tau(\lambda) \approx H * ln\left(\frac{I_0(\lambda)}{I_0(\lambda) \cdot e^{-\sigma(\lambda,T,p)\cdot S}}\right) &= H * \sigma(\lambda, T, p) \cdot S \\ &= \sigma^*(\lambda, T, p) \cdot S \qquad (3.24)\end{aligned}$$

which complies with the mathematical operation mentioned above. However, for optically thick absorbers the convolution and the logarithm cannot be exchanged even by approximation. In this case, the slant column densities cannot be retrieved directly, but iterative methods, such as that used in Frankenberg et al. [2005] have to be applied.
Therefore, the finite spectral resolution of the instrument can have an effect

on the spectral analysis. But for most cases, including this work, the optical densities are so small that the presumption above is valid. However, it should be referred to the I_0-Effect (section 3.5.3), which arises when the light source features fine structures (compared to the resolution of the instrument). In this case, additional corrections have to be applied.

3.5 Passive DOAS Characteristics

3.5.1 Fraunhofer Lines

For passive DOAS measurements the Sun is commonly the light source. The shape of the solar spectrum at the top of the atmosphere is given by the individual physical processes of the Sun. As a first approximation, the solar spectrum can be considered as an emission spectrum of a black body with a surface temperature of roughly 5800 K. This continuous spectrum is overlaid by many strong absorption lines which arise from the discrete absorption and re-emission of radiation in the Sun's photosphere (see Figure 3.5a). These respective absorption structures are referred to as Fraunhofer lines (first discovered by Josef Fraunhofer, 1787 - 1826) and produce strong variations in the intensity of the solar spectrum. The Fraunhofer lines are not constant in shape and strength. They vary rather slightly over time and change depending on the observation of different regions of the solar disc. This plays an important role in direct sun observations. In scattered light measurements however, this can be neglected and averages out.

In the UV-Vis wavelength range, the optical densities of the Fraunhofer lines are typically two to three orders of magnitude higher than the optical densities of the trace gases in the Earth's atmosphere. Accordingly, the Fraunhofer lines can easily distort the measurement values if they are not thoroughly removed in the spectral analysis. Thus, a Fraunhofer reference spectrum (FRS) has to be included, which also serves as I_0 spectrum. The FRS would have to be measured from space so that it was not influenced by absorptions in the Earth's atmosphere. However, on one hand the effort required to send a measurement device into space may be considered too large when only the FRS is measured. Meanwhile, the Fraunhofer lines would also have to be averaged over the solar disc as well. Consequently, in practice, the FRS is acquired from the measurement site at times and at measurement geometries where the absorptions in the Earth's atmosphere are assumed to be the lowest. This procedure accepts that the retrieved absorption signal of the trace gases is reduced by a small amount which is included in the FRS itself. Although the Langley plot (see section 4.22) is sometimes able to quantify this amount, the FRS has to be chosen carefully from the measured spectra.

3.5.2 The Ring Effect

The Ring Effect (named after Grainger and Ring [1962]) leads to a reduction of the observed optical densities of the Fraunhofer lines and is based on the inelastic rotational Raman scattering (see section 4.2.2) of photons with air molecules [Bussemer, 1993; Fish and Jones, 1995; Burrows et al., 1996]. Such scattering processes cause a change in the photon's wavelength due to the interaction between a rotating molecule and an oscillating electric field [Brinkmann, 1968]. As a result of the low light intensity in the wavelength ranges of the Fraunhofer lines compared to adjacent wavelengths, there is a larger probability of photon scattering into the wavelength range of a Fraunhofer line from the outside rather than vice versa. This is why the depth (i.e. intensity) of solar Fraunhofer lines in scattered light is less than in extraterrestrial observations. Therefore, the Ring effect is also called ”filling-in”.

This effect has to be thoroughly corrected when applying the DOAS method because the atmospheric absorptions can be as much as one to two orders of magnitude smaller than the Ring effect. The magnitude of the Ring effect increases with longer light paths and accordingly with higher solar zenith angles. Therefore, the Ring effect has to be accounted for accurately and a so called Ring reference spectrum (or Ring spectrum) has to be included into the fitting process when scattered sunlight is measured (see Figure 3.5c).

The scattered sunlight intensity I_{meas} observed by DOAS measurements is composed of the elastic Rayleigh and Mie scattering processes, $I_{Rayleigh}$ and I_{Mie}, as well as by Raman scattering I_{Raman}:

$$I_{meas} = I_{Rayleigh} + I_{Mie} + I_{Raman} = I_{elastic} + I_{Raman} \tag{3.25}$$

As described in section 3.2, the logarithm of the measured spectrum has to be taken for the DOAS analysis:

$$\begin{aligned} ln(I_{meas}) &= \ln(I_{elastic} + I_{Raman}) \\ &= \ln(I_{elastic}) + \ln\left(1 + \frac{I_{Raman}}{I_{elastic}}\right) \\ &\approx \ln(I_{elastic}) + \frac{I_{Raman}}{I_{elastic}} \end{aligned} \tag{3.26}$$

whereby the Ring spectrum I_{Ring} can be found as:

$$I_{Ring} = \frac{I_{Raman}}{I_{elastic}} \tag{3.27}$$

There are two approaches used in order to determine the Ring spectrum. It can be either measured or modelled:

Measured Ring spectrum: The Ring spectrum can be measured by using the different properties of the scattering processes in terms of polarization. While Rayleigh

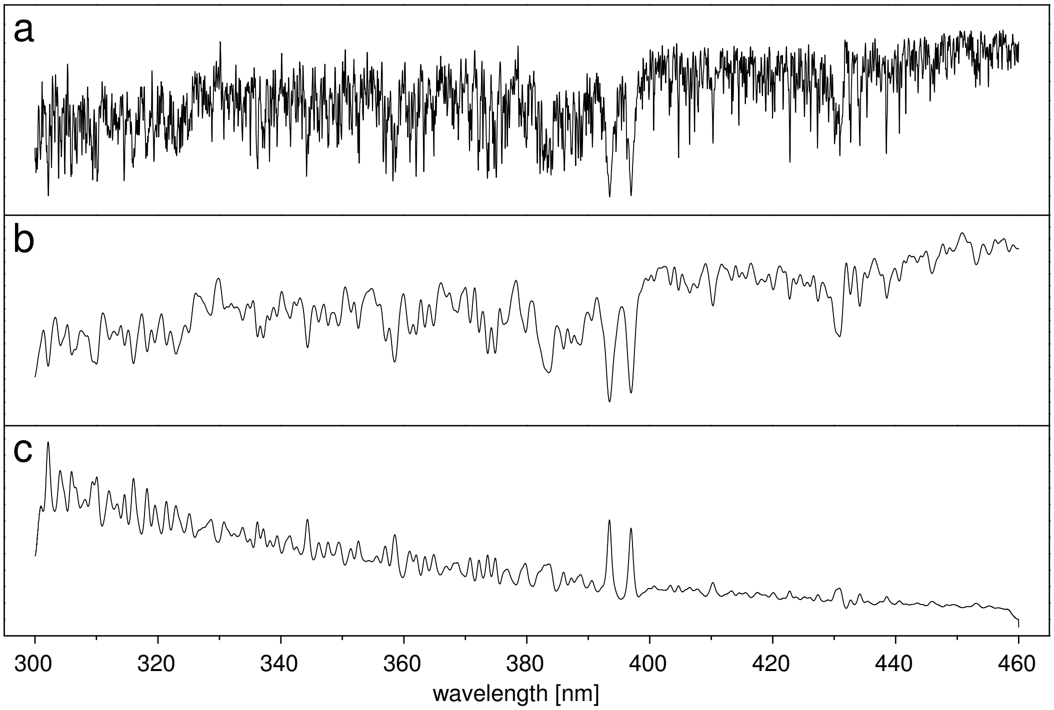

Figure 3.5: *(a): High resolution solar spectrum in the wavelength range from 300 to 460 nm. The continuous spectrum is overlaid by Fraunhofer lines. (b): The same as in (a), but convolved with a Gaussian instrument function with 0.7 nm full width at half maximum, which is a typical resolution for DOAS measurements. (c): Ring spectrum modelled from (b). When the solar spectrum has dips, the Ring spectrum features peaks and vice versa, which illustrates the "filling-in" process.*

scattering on molecules highly polarizes light for scattering angles around 90° (see section 4.2.1), this occurs only weakly for rotational Raman scattering. By measuring spectra at different polarisation orientations, the Raman scattered intensity and hence a Ring spectrum can be measured [Solomon et al., 1987]. However, scattering on aerosols (Mie scattering) also has a weak wavelength dependence and contributes to the depolarized light fraction. Thus, the Ring spectrum also contains structures caused by Mie scattering, which actually do not belong to the Ring spectrum. Accordingly, the measurement would have to be conducted in the absence of aerosols in order to achieve good accuracy, which, under normal conditions, is quite an unrealistic precondition. A further adverse effect is that the light path through the atmosphere depends on the polarisation direction. This can lead to trace gas absorption structures in the measured Ring spectrum [Wagner, 1999].

Modelled Ring spectrum: The spectrum of inelastically scattered light can be modelled by using the known rotational states of oxygen and nitrogen [Bussemer, 1993; Fish and Jones, 1995; Chance and Spurr, 1997], which are the two main constitutes of the atmosphere. The modeling of the Ring spectrum can overcome the shortcomings of the measurement and show very good agreement with highly resolved atmospheric observations [Aben et al., 2001]. It can be performed either on the basis of a measured solar spectrum from the data set to be analyzed, or on the basis of a high resolution solar spectrum [Kurucz et al., 1984], which still has to be convolved with the instrument function H to match the spectral resolution.

In this work, modeled Ring spectra were used for the spectral analysis. Thereby, it turned out that the Ring spectra modeled from measured spectra provided better results with smaller and less structured residuals than those modeled from high resolution solar spectrum. The calculation of the Ring spectra was performed with the software DOASIS [Kraus, 2004].

3.5.3 The Solar $\mathrm{I_0}$ Effect

The denotation Solar $\mathrm{I_0}$ Effect is derived from the highly structured solar $\mathrm{I_0}$ spectrum, whose strong variations in the intensity caused by the Fraunhofer lines (see section 3.5.1) affects the DOAS analysis [Platt et al., 1997; Richter, 1997; Van Roozendael et al., 1999]. Since the typical spectral resolution of a DOAS instrument is in the order of tenths to several nanometers in the UV-Vis range, the Fraunhofer lines cannot be resolved (see Figure 3.5a and b). Therefore, discrepancies between the absorption structures of a trace gas when observing scattered sunlight and its (convolved) absorption cross section, which was usually generated in the lab with an unstructured light source, can occur. Hence, errors in the spectral analysis can arise.

In order to account for the Solar $\mathrm{I_0}$ Effect, the absorption cross sections must be calculated considering these effects, yielding $\mathrm{I_0}$ corrected absorption cross sections $\sigma^*_{\mathrm{I_0}}(\lambda, T, p)$ [Johnston, 1996]:

$$\sigma^*_{\mathrm{I_0}}(\lambda, T, p, S) = -\ln\left(\frac{I^*(\lambda)}{I_0^*(\lambda)}\right) \cdot \frac{1}{S} \tag{3.28}$$

S denotes the slant column density of the respective trace gas and should be in the order of magnitude that is typically expected in the measurement. $I_0^*(\lambda)$ is a high resolution solar spectrum $I_0(\lambda)$, e.g. from Kurucz et al. [1984], convolved with the instrument function H. $I^*(\lambda)$ is a convolved synthetic absorption spectrum calculated from the high resolution solar spectrum $I_0(\lambda)$ and the absorption of the trace gas in the magnitude according to S:

$$I^*(\lambda) = H * I(\lambda) = H * \left(I_0(\lambda) \cdot e^{-\sigma(\lambda,T,p)\cdot S}\right) \tag{3.29}$$

whereby $\sigma(\lambda, T, p)$ is the respective highly resolved absorption cross section.

The $\mathrm{I_0}$ corrected absorption cross section $\sigma^*_{\mathrm{I_0}}(\lambda, T, p)$ perfectly matches the absorptions in the measured spectrum only if the assumed SCD agrees with the measured SCD. However, slight deviations between them do not have a significant effect.

Generally, the Solar $\mathrm{I_0}$ Effect is strongest for strong absorbers, such as ozone. In this case, the retrieved SCD of weak absorbers can be significantly affected if the Solar $\mathrm{I_0}$ Effect is not corrected. But for trace gases which are weak absorbers and do not exhibit high resolution spectral features, the Solar $\mathrm{I_0}$ Effect is very small and can be neglected. In this work, the absorption cross sections of NO_2 and O_3 were $\mathrm{I_0}$ corrected with typical slant column densities of 2.5×10^{16}, and 1×10^{20}, respectively. All other cross sections were convolved conventionally as described in section 3.3.

3.6 Multi-Axis-DOAS

"Traditional" scattered light DOAS setups point only at the zenith and are most sensitive to trace gases located in the stratosphere. In order to increase the sensitivity to trace gases close to the surface, the Multi-AXis-DOAS (MAX-DOAS) technique has been recently developed. MAX-DOAS instruments observe scattered sunlight from different viewing directions. The special advantage of this technique occurs when measuring trace gases close to the ground at directions slightly above the horizon. In such cases, high sensitivities for trace gases close to the ground are obtained because the longer light path through these trace gas layers yields significantly higher slant column densities [Hönninger and Platt, 2002; Leser et al., 2003; van Roozendael et al., 2003; Wittrock et al., 2004; Hönninger et al., 2004; Wagner et al., 2004; Heckel et al., 2005; von Friedeburg et al., 2005; Frieß et al., 2006; Sinreich et al., 2007].

This is illustrated in Figure 3.6 with a simplified MAX-DOAS measurement sketch. The sunlight enters the Earth's atmosphere at a given angle, which is referred to as the solar zenith angle ϑ (SZA). It is defined as the angle from the direction of the sun to the zenith. The sunlight is scattered (red points) in the line of sight of the different elevation angles α, which are defined as the angles between the horizon and the pointing direction of the measurement device. In this Figure, the single scattering case is assumed, i.e. each photon is scattered only once in the atmosphere. But in reality, multiple scattering can also occur. Finally, the scattered light is collected by the telescope of the measurement device. The green areas signify atmospheric absorbers in the stratosphere and troposphere, respectively. It can clearly be seen that, in the troposphere, higher slant column densities are yielded when the elevation angle is lower.

The sensitivity difference between the troposphere and the stratosphere can be explained by the different measurement approach of MAX-DOAS. In section 3.2 the differential slant column density dSCD was introduced as the difference between the

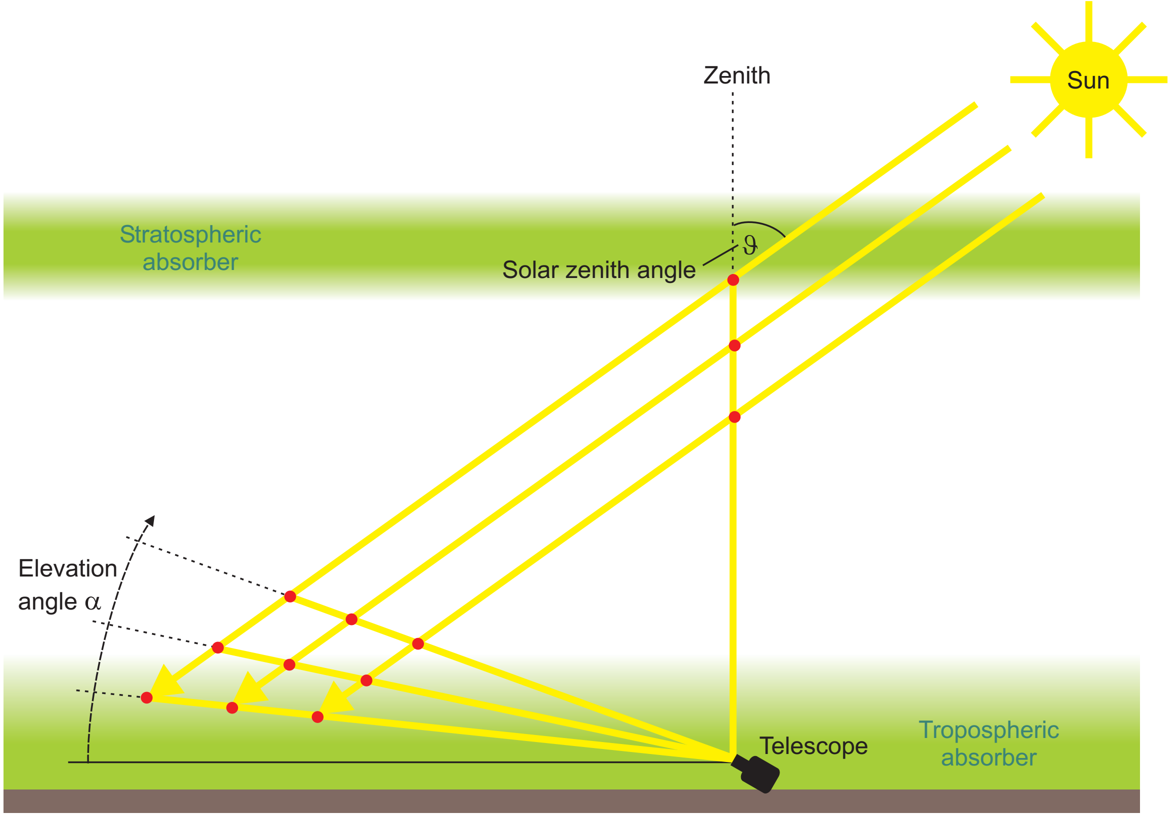

Figure 3.6: *Sketch of a MAX-DOAS measurement in the single scattering case. The telescope points at different elevation angles including the zenith in order to collect scattered light. The red points indicate scattering events along the line of sight of the elevation angles.*

actual SCD and the SCD of the reference spectrum. On the one hand, the reference spectrum can be chosen with respect to the solar zenith angle ϑ:

$$dS(\vartheta, \alpha) = S(\vartheta, \alpha) - S(\vartheta_{Ref}, \alpha_{Ref}) \tag{3.30}$$

where ϑ_{Ref} should be chosen to be lowest and α_{Ref} highest so that the absorption in the reference is correspondingly low. In this case, the stratospheric absorption contributes to the slant column density. On the other hand, the reference can be chosen with respect to the elevation angle α (as in the MAX-DOAS technique) to yield ΔS:

$$\Delta S(\vartheta, \alpha) = S(\vartheta, \alpha) - S(\vartheta, 90^\circ) \tag{3.31}$$

where the reference points to zenith and is measured at approximately the same solar zenith angle ϑ as the measurement at the elevation angle α. The slant column density can be separated into a tropospheric part S_{trop} and a stratospheric part S_{strat} so that equation (3.31) can be written as:

$$\Delta S(\vartheta, \alpha) = (S_{trop}(\vartheta, \alpha) + S_{strat}(\vartheta, \alpha)) - (S_{trop}(\vartheta, 90^\circ) + S_{strat}(\vartheta, 90^\circ)) \quad (3.32)$$

Since the scattering objects, i.e. molecules and aerosols (see section 4.2), are located predominantly in the lower atmosphere, the scattering events also occur predominantly there. Therfore, $S_{strat}(\vartheta, \alpha) \approx S_{strat}(\vartheta, 90^\circ)$ at a fixed solar zenith angle ϑ. In this case, the light path through the stratosphere is almost the same independently of the viewing direction so that the following approximation can be made:

$$\Delta S(\vartheta, \alpha) \approx S_{trop}(\vartheta, \alpha) - S_{trop}(\vartheta, 90^\circ) \quad (3.33)$$

Thus, when changing the elevation angle α, MAX-DOAS is mainly sensitive towards tropospheric absorbers. In practice however, the instrument often points sequentially at different elevation angles including the zenith so that the presumption of the same solar zenith angle is not accurately fulfilled. This can usually be neglected since a measurement sequence does not take very long and the slight change in SZA causes no significant effect. However, in the morning and evening when the SZA changes rapidly with time, and in the UV wavelength range where ozone absorbs strongly, it can influence the ΔSCD significantly.

Since the slant column density is defined as the concentration along the light path and, in a first approach, the randomly occurring scattering events usually cannot be retraced, quantitative conclusions cannot be made from the slant column density. Thus, the vertical slant column density (VCD) V is introduced, and is defined as the integrated concentration $c(z)$ along the height z:

$$V = \int c(z) dz \quad (3.34)$$

The VCD does not depend on wavelength, the light path, or the observation geometry, so that it can be used for comparison of measurements. From Figure 3.6, the VCD can be derived. For a trace gas located near the ground the following geometrical approximation can be made:

$$V \approx sin(\alpha) \cdot S_{trop}(\alpha) \quad (3.35)$$

In contrast, the geometrical approximation is altered when considering trace gases in the stratosphere:

$$V \approx cos(\vartheta) \cdot S_{strat}(\vartheta) \quad (3.36)$$

Combining both approximations, the connection between $S(\vartheta, \alpha)$ and V can be written as [Hönninger, 2002]:

$$S(\vartheta, \alpha) \approx \left(a \cdot \frac{1}{sin(\alpha)} + (1 - a) \cdot \frac{1}{cos(\vartheta)} \right) \cdot V \quad (3.37)$$

with a as the fraction of the total vertical trace gas column located below the scattering altitude. It should be noted that this approximation is only valid for elevation angles α larger than around 20° and solar zenith angles ϑ smaller than around 70°. Otherwise, the single scattering assumption is not even approximately fulfilled because scattering occurs also within the trace gas layer. In this case, radiative transfer calculations may lead to more accurate conversions between $S(\vartheta, \alpha)$ and V (see section 4.5).

MAX-DOAS with its simple setup has many properties of the desired uncomplicated tropospheric monitoring instrument. However, a shortcoming is the need for precise knowledge regarding the atmospheric radiative transfer (see chapter 4), which, in turn, is largely determined by the aerosol load. Recently, inverse models based on radiative transport models have been developed which allow to infer some degree of vertical resolution from MAX-DOAS measurements. In particular, when assuming a well mixed tropospheric trace gas layer (e.g. within the planetary boundary layer), its vertical extent can be determined with good accuracy (e.g. [Hönninger, 2002; Wittrock et al., 2004; Sinreich et al., 2005; Heckel et al., 2005; Frieß et al., 2006; Sinreich et al., 2007], see section 4.6). This is generally not possible with Zenith-Sky-DOAS or active DOAS measurements.

4 Radiative Transfer in the Atmosphere

4.1 Parameters of the Radiative Transfer

The radiative transfer in the atmosphere is a very complex interaction of many factors. It depends on several parameters which represent the current atmospheric conditions:

The vertical temperature profile is required because the absorption cross sections of the trace gases present in the atmosphere are temperature dependent.

The vertical pressure profile has to be known since the Rayleigh scattering events (see section 4.2.1) increase with pressure. The air pressure amounts to around 1 bar at sea level and decreases approximately exponentially with height.

The vertical profile of ozone. Owing to the Chappuis and the Huggins absorption bands, ozone is a strong absorber in the UV and has a large impact on the radiative transfer in this wavelength range. The maximum of the ozone concentration is located in the stratosphere at a height between 20 and 25 km.

The aerosol extinction profile affects significantly the light path in the atmosphere due to scattering (see section 4.2.3) and absorption. Aerosols are small particles or droplets in the atmosphere with diameters from about 0.01 to 10 micrometers. They can be originated from natural sources being sea salt particles, mineral dust or particles emitted from volcanos and bush fires. Aerosols from anthropogenic sources are fine dust, nitrates, sulfates and soot. Furthermore, aerosols can grow if they hit together, accumulate non volatile compounds or serve as condensation nuclei. It is distinguished between primary aerosols which are emitted directly into the atmosphere (e.g. sea salt particles) and secondary aerosols which are formed owing to physical or chemical processes of gases (e.g. sulfates or nitrates).

The aerosol extinction depends on the kind and the amount of the aerosols present in the atmosphere. It is the most crucial parameter because it can generally vary far more than the other three parameters, which, in turn, are known approximately. Since direct aerosol extinction measurements are not performed usually together with MAX-DOAS measurements, the uncertainties in the vertical profile can lead to large errors. However, the aerosol extinction profile can be estimated by combining the MAX-DOAS measurements with radiative transfer modeling (see sections 4.5 and 4.6).

4.2 Scattering Processes

4.2.1 Rayleigh Scattering

Elastic scattering of electromagnetic radiation by matter when the wavelength of the incident light is much larger than the dimension of the particles is called Rayleigh scattering. In the scattering process, physically, an oscillating dipole is induced by electromagnetic radiation in a polarisable particle, e.g. air molecules [e.g. Van de Hulst, 1981].

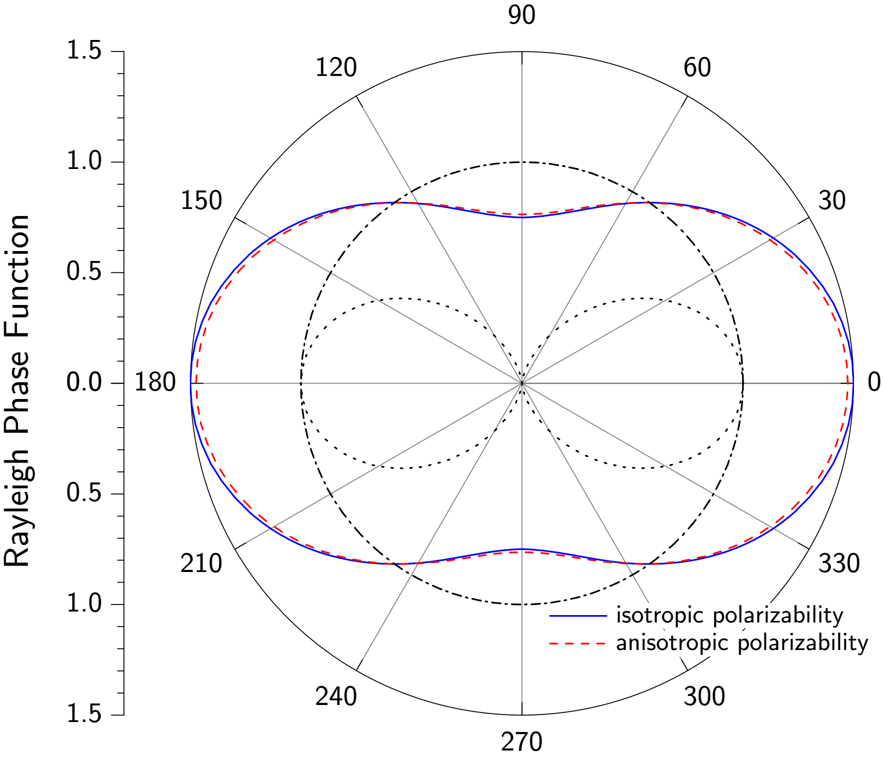

Figure 4.1: *Rayleigh scattering phase function $\Phi_R(\theta)$ and its contributions (see text). Adapted from Hönninger [2002].*

The Rayleigh scattering phase function $\Phi_R(\theta)$ shown in Figure 4.1 describes the relative intensity of the scattered light. Thereby, θ is the scattering angle between the incident propagation direction and the direction after the scattering event. The dotted black line is the contribution of light polarised parallel to the scattering plane which indicates the $\sim \sin^2\theta'$ dependence of a Hertz dipole (where $\theta' = \frac{\pi}{2} - \theta$ is the angle between dipole axis and Poynting vector of the incident light). In contrast, the dash dotted line shows the contribution of light polarised perpendicular to the scattering plane which does not feature a dependence on θ. Finally, the blue line indicates the Rayleigh scattering phase function - the superimposition of both contributions - for unpolarised incident light which is given by:

$$\Phi_R(\cos(\theta)) = \frac{3}{4} \cdot (1 + \cos^2(\theta)) \tag{4.1}$$

If the anisotropy of the polarizability is taken into account (red dashed line, see Penndorf [1957]), equation (4.1) changes slightly to:

$$\Phi_R(\cos(\theta)) = 0.7629 \cdot (1 + 0.9324 \cdot \cos^2(\theta)) \tag{4.2}$$

An important feature of the Rayleigh scattering is its strong wavelength dependency which is approximately:

$$\sigma_R \propto \frac{1}{\lambda^4} \tag{4.3}$$

where σ_R as the Rayleigh cross section. The exact value for σ_R is calculated with [Penndorf, 1957]:

$$\sigma_R = \frac{3.9993 \cdot 10^{-32} \cdot x^4}{1 - 1.069 \cdot 10^{-2} \cdot x^2 - 6.681 \cdot 10^{-5} \cdot x^4} \cdot m^2 \tag{4.4}$$

where $x = \frac{10^{-6} m}{\lambda}$. For blue light the scattering probability is one order of magnitude larger than for red light. This explains the "blue" sky over the day when the sun stands high and the red light in the dawn and dusk when the light path through the atmosphere is extraordinarily long. However, over the day, the maximum of the scattered light spectrum is located in the UV wavelength range which is not visible for the human eye.

4.2.2 Raman Scattering

Raman scattering denotes inelastic scattering on air molecules. With respect to Rayleigh scattering, Raman scattering accounts to a few per cent depending on the wavelength [haug1996]. It can be described as light interacting with an air molecule that changes its excitation state during the scattering process. The photon either transfers part of its energy to the molecule (Stokes lines, $\Delta J = +2$, S-branch) or takes over part of the molecule's excitation energy (Anti-Stokes, $\Delta J = -2$, O-branch). If only the rotational excitation is affected ($\Delta\nu = 0$) it is called rotational Raman scattering (RRS). If also the vibrational state changes the term rotational-vibrational Raman scattering (RVRS) is used ($\Delta\nu = \pm 1$). Only discrete amounts of energy given by the difference between the discrete excitation levels can be transferred between the photon and the molecule. For air molecules (mainly oxygen and nitrogen) RRS frequency shifts of up to ±200 cm^{-1} occur, which corresponds to several nanometers in the UV/Vis wavelength range. In case of RVRS a vibrational shift of ±2331 cm^{-1} for nitrogen and ±1555 cm^{-1} for oxygen has to be added [Burrows et al., 1996; Haug, 1996; Sioris and Evans, 1999]. Since the RRS is one order of magnitude stronger then the RVRS, it dominates the Raman scattering and the RVRS can be neglected for the calculation of the Ring spectrum (see section 3.5.2).

While in terms of the Ring spectrum the consideration of Raman scattering is indispensable, the specific attributes of Raman scattering do not play an important role in the radiative transfer. Thus, they are not taken into account in the calculation of air mass factors (see section 4.4) and the modeling of the radiative transfer.

4.2.3 Mie Scattering

Mie scattering occurs if light is scattered on aerosols whose dimensions are similar or larger than the wavelength of the incident light (for a short description of aerosols see section 4.1). During the scattering process, the components of the aerosol are excited coherently and radiate themselves. The scattered light features interference properties owing to comparable dimensions with the incident light and minima as well as maxima in the intensity of the scattered light depending on the scattering angle θ occur (see Figure 4.2 left column). Furthermore, Mie scattering generally prefers the forward scattering direction. Actually, Mie scattering only refers to spherical aerosols and there are other theories for non-spherical particles. However, also the non-spherical cases can mostly be well approximated by the spherical description of the Mie scattering.

Aerosols differ naturally strongly in shape and size so that the determination of the Mie scattering cross section can be very complex. This problem is addressed by the Mie theory, which includes a variety of numerical models to calculate scattering phase functions and extinction coefficients for given aerosol types and particle size distributions [Van de Hulst, 1981; Wiscombe, 1980]. The scattering phase function, which determines the direction and the strength of the scattered light, depends on the aerosol size parameter x:

$$x = \frac{2 \cdot \pi \cdot r}{\lambda} \tag{4.5}$$

with r being the radius of the aerosol and λ being the wavelength of the light. In Figure 4.2 Mie scattering phase functions $\Phi_M(\theta)$ at 550 nm wavelength for water droplets with size parameters x = 1, x = 3 and x = 10 are shown [Sanghavi, 2003]. Obviously, the larger the particle size, the more dominant is the forward scattering direction.

Aerosols with different aerosol size parameters exhibit different wavelength dependencies. The wavelength dependence is expressed by the Ångström coefficient

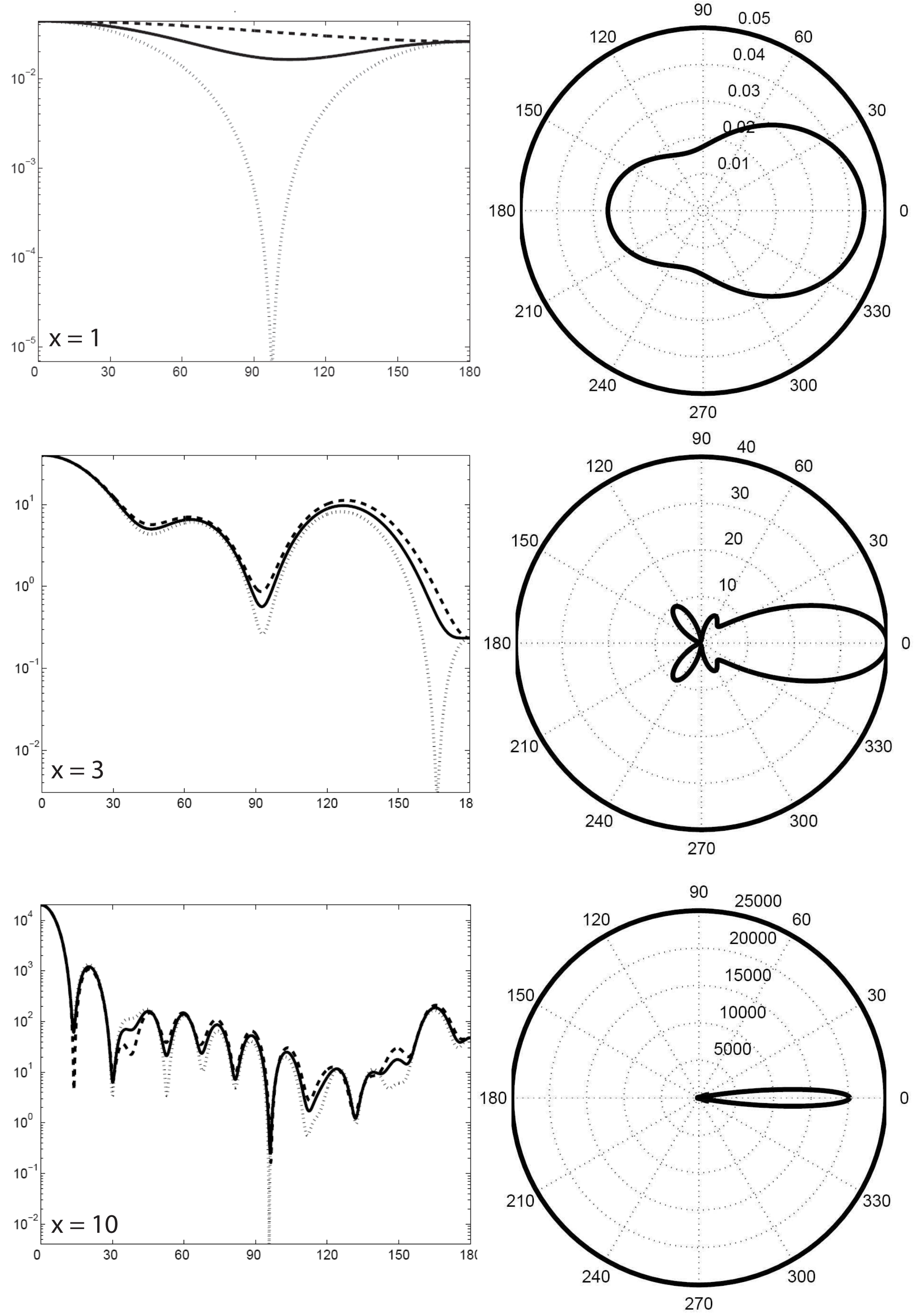

Figure 4.2: *Mie scattering phase functions at 550 nm wavelength for water droplets with size parameters $x = 1$ (top), $x = 3$ (middle) and $x = 10$ (bottom) [Sanghavi, 2003] on logarithmic scale (left) and linear scale (right).*

α. For the Mie scattering cross section σ_M follows:

$$\sigma_M \approx \frac{1}{\lambda^\alpha} \tag{4.6}$$

whereby α is larger for smaller aerosol size parameters. Rayleigh scattering can be regarded as a special case of Mie scattering reaching $\alpha = 4$ (for $x \to 0$). For typical atmospheric aerosols the Ångström coefficient is around 1.3 which indicates a small wavelength dependence.

In reality, aerosols of different size and chemical composition are present simultaneously in the atmosphere. By integrating the individual scattering properties of aerosols over their whole size distribution and considering the different chemical types, bulk scattering properties can be derived. In doing so, an asymmetry coefficient g is often introduced describing the averaged cosine of the scattering angle θ. The asymmetry coefficient is a measure for the degree of forward-peakedness and parameterizes the rate of discrepancy to the Rayleigh scattering behaviour whereby the value 0 indicates a totally isotropic scattering behaviour and the value 1 scattering events solely in forward direction. In urban regions, the asymmetry coefficient ranges typically around 0.7. Very common is the Henyey-Greenstein phase function approximation [Henyey and Greenstein, 1941] utilizing the asymmetry coefficient g:

$$\Phi_{HG}(\theta) = \frac{1 - g^2}{\sqrt{(1 + g^2 - 2g\cos(\theta))^3}} \tag{4.7}$$

with θ being the scattering angle. The Henyey-Greenstein approximation underestimates slightly the backward scattering, but its advantage is the easy calculation.

Aerosols not only scatter but also absorb light depending on the surface of the aerosol. This is described by the single scattering albedo (SSA) ω (as well as by the imaginary part of the complex refractive index) which is the scattering fraction of the aerosol extinction ϵ_M.

$$\omega = \frac{\epsilon_{M_{scatt}}}{\epsilon_M} = \frac{\epsilon_{M_{scatt}}}{\epsilon_{M_{scatt}} + \epsilon_{M_{abs}}} \tag{4.8}$$

where $\epsilon_{M_{scatt}}$ and $\epsilon_{M_{abs}}$ are the scattering and absorbing fractions of ϵ_M, respectively. $\omega = 0$ means that only absorption and no scattering occurs when light hitting an aerosol which can be assumed from soot. $\omega = 1$ stands for the contrary case where only scattering and no absorption takes place as it is approximately for e.g. sea salt. While in the visible wavelength range, the SSA for urban aerosols amounts to nearly 1, in the UV range, it can decrease significantly.

4.3 Visibility

The visibility is determined by the radiative transfer in the atmosphere and is connected with the extinction of light. Extinction, hence scattering and absorption, can happen by both molecules and aerosls. However, in reality the molecule extinction is that weak that, in presence of aerosols, the aerosol extinction dominates. Thus, the visibility can be utilized as a first approximation of the aerosol extinction. It can be determined from the contrast C between a laminar object and its background if there is no limitation due to the resolution of the human's eye:

$$C = \left| \frac{H - H_0}{H_0} \right| \tag{4.9}$$

where H and H_0 are the brightness of the object and the background felt by the human's eye, respectively. Without glare, a contrast of about 2 % is normally sufficient to distinguish between the object and the background.

Applying the Lambert-Beer law, H can be expressed by the extinction coefficient K of the atmosphere:

$$H = H_0 \cdot \left(1 - e^{-K \cdot d}\right), \tag{4.10}$$

with d as the distance between the human's eye and the object. Combining the equations (4.9) and (4.10) yields

$$C = e^{-K \cdot d} \tag{4.11}$$

If d corresponds to the maximum visibility R the contrast C has to amount to 0.02 as explained above. Thus, equation (4.11) can be written as

$$R = \frac{3,9}{K} \tag{4.12}$$

This relation is just a rough approximation, but under normal conditions without glare the extinction coefficient derived from the maximum visibility can be retrieved in good accuracy [Roedel, 2000].

4.4 The Air Mass Factor Concept

As introduced in chapter 3, the primary quantity of a DOAS measurement analysis is the slant column density S, which is the integrated concentration along the light (see equation 3.7). The slant column density depends on several parameters. These are the wavelength λ, the solar zenith angle ϑ, the elevation angel α and the relative azimuth angle ϕ which is the horizontal angle between the telescope direction and the sun. Thus, the slant column density is generally hard to evaluate. In contrast, the vertical column density V is the integrated concentration along the height (see equation 3.34) and is independent of the wavelength of the measurement geometry. V is fully determined by the trace gas profile. The Air Mass Factor (AMF) A

connects both quantities and is defined as [Noxon et al., 1979; Solomon et al., 1987; Marquard et al., 2000]:

$$A(\lambda, \theta, \alpha, \phi) := \frac{S(\lambda, \theta, \alpha, \phi)}{V} \tag{4.13}$$

Like the slant column density, the air mass factor A depends on the wavelength λ, the solar zenith angle ϑ, the elevation angle α and the relative azimuth angle ϕ. It is determined by the radiative transfer in the atmosphere and, hence, by its parameters. Since the air mass factor expresses the light path ratio between the slant and the vertical path through the atmosphere, it is a measure for the length of the light path in the atmosphere depending on the state of the atmosphere.

The relation between the SCD and the VCD can also be expressed by the optical density τ when sunlight passes through a concentration field $c(\vec{x})$ under the assumption that the temperature and the pressure dependency of the absorption cross section σ is small:

$$\tau(\lambda) = -ln\left(\frac{I(\lambda)}{I_0(\lambda)}\right) = \sigma(\lambda) \cdot \int_0^L c(\mathbf{x})dl = \sigma(\lambda) \cdot S(\lambda) \tag{4.14}$$

Taking equation (4.13) into account, equation (4.14) can be written as under the assumption of a well defined light path through the atmosphere:

$$A(\lambda) = \frac{\tau(\lambda)}{\sigma(\lambda) \cdot V} \tag{4.15}$$

In section 3.6, the slant column densities for absorbers close to the ground and in the stratosphere $S_{trop}(\alpha)$ and $S_{strat}(\vartheta)$, respectively, were approximated (see equations (3.35) and (3.36)). These can be applied to the respective air mass factors $A_{trop}(\alpha)$ and $A_{strat}(\vartheta)$ so that it follows:

$$A_{trop}(\alpha) = \frac{S_{trop}(\alpha)}{V} \approx \frac{S_{trop}(\alpha)}{S_{trop}(\alpha) \cdot \sin(\alpha)} = \frac{1}{\sin(\alpha)} \tag{4.16}$$

and neglecting refraction on the atmosphere

$$A_{strat}(\vartheta) = \frac{S_{strat}(\vartheta)}{V} \approx \frac{S_{strat}(\vartheta)}{S_{strat}(\vartheta) \cdot \cos(\vartheta)} = \frac{1}{\cos(\vartheta)} \tag{4.17}$$

As already mentioned in section 3.6 the approximations in equations (4.16) and (4.17) can normally only be made for elevation angles larger than around 20° and solar zenith angles smaller than around 70°. For this, it has to be assumed that light is scattered only once in the line of sight of the elevation angle. Or more precisely, in case of the tropospheric absorber the last scattering event should be above the absorber layer and, in case of the stratospheric absorber, the first scattering event should be below the absorber layer, and the photons should not be scattered back into the respective absorber layer.

In the measurement process, the observed intensity is not caused by scattered photons which all took the same light path. It is rather a sum of scattered photons which passed through the atmosphere on many different light paths which makes the description more complicated. So, a probability density function $p(k, \lambda)$ can be introduced where k describes the set of possible light paths [Marquard et al., 2000]. $p(k, \lambda)$ is regarded as the probability that a photon with wavelength λ traverses the atmosphere on a given light path $\mathbf{x}_k(l)$ from the sun to the telescope. Hence, the observed intensity is the integrated intensity over all possible light paths to the telescope, weighted with the according probability. The optical density τ can now be written as

$$\tau(\lambda) = -ln\left(\frac{I(\lambda)}{I_0(\lambda)}\right) = ln\left(\int p(k, \lambda) \cdot e^{-\sigma(\lambda)\cdot V \cdot \int \hat{c}(\mathbf{x}_k(l))dl} dk\right) \tag{4.18}$$

under the assumption that $\sigma(\lambda)$ is independent of temperature and pressure so that it can be placed outside the inner path integral. The trace gas profile $c(\mathbf{l})$ is written as the product of the vertical column density and the 'relative' profile shape $\hat{c}(\mathbf{l}) = \frac{c(\mathbf{l})}{V}$ which is independent of the trace gas amount.

Including equation (4.18) into equation (4.15), the air mass factor A for scattered light observations is

$$A(\lambda) = -\frac{1}{\sigma(\lambda) \cdot V} \cdot ln\left(\int p(k, \lambda) \cdot e^{-\sigma(\lambda)\cdot V \cdot \int \hat{c}(\mathbf{x}_k(l))dl} dk\right) \tag{4.19}$$

Equations (4.18) and (4.19) have several important implications for the interpretation of scattered light measurements:

- Equation (4.18) implies that the observed optical density is not a linear superposition of the optical densities along the individual light paths $\mathbf{x}_k$. Thus, the Lambert Beer law is only strictly fulfilled if there exists a single well defined light path $\mathbf{x}_0(l)$, i.e. when observing direct light. Then, the probability density function is delta distributed, $p(k, \lambda) = \delta(k)$. In this case, equations (4.14) and (4.18) are equivalent.

- The air mass factor for scattered light is not only a function of the relative profile shape $\hat{c}(\mathbf{l})$. Since the vertical column density cannot be divided out in equation (4.19) it also depends on the vertical column density: $A(\lambda) = A(\lambda, V)$. Therefore, the determination of the vertical column density is equivalent to the solution of the implicit relationship (see equation(4.13))

$$V = \frac{S(\lambda)}{A(\lambda, V)} \tag{4.20}$$

which can be generally solved iteratively [Marquard et al., 2000]. However, this method is very time consuming because the air mass factor has to be calculated for each iteration step.

- The air mass factor does not only depend on wavelength λ, but also on the product of the absorption cross section $\sigma(\lambda)$ and the slant column density S. The air mass factor, and therefore also the respective slant column density, is modulated with the wavelength dependency of the trace gas cross section:

  $$\tau(\lambda) = \sigma(\lambda) \cdot S(\lambda) = \sigma(\lambda) \cdot V \cdot A(\lambda, \sigma(\lambda) \cdot S) \qquad (4.21)$$

  The spectral analysis can be affected strongly since it is performed over a finite wavelength range. For strong absorbers, such as ozone in the UV, the wavelength dependence of the air mass factors leads to a modulation of the absorption structure. It can be compensated for by using $\sigma(\lambda) \cdot A(\lambda)$ instead of $\sigma(\lambda)$ as the trace gas reference spectrum [Diebel et al., 1995; Richter, 1997]. Then the VCD is determined directly by the retrieval.

- In case of a single absorber present in the atmosphere, the probability density function $p(k, \lambda)$ is determined only by Rayleigh and Mie scattering and is expected to be a broad banded function of λ. However, if additional absorbers in the considered wavelength range are present in the atmosphere, it is also a function of the cross sections and concentration fields of the additional absorbers. This amy have an significant impact on the radiative transfer.

The air mass factors can be calculated by radiative transfer models (see section 4.5). Thereby, single scattering radiative transfer models can use equation (4.19). This has the advantage to be fast and relatively easy to implement. However, this simplification can lead to significant errors. Therefore, multiple scattering radiative transfer models provide a more reliable air mass factor calculation, but need a much higher calculation effort.

Air mass factors calculated by radiative transfer modeling need to be retrieved thoroughly to fit to measured slant column densities. Since the measured slant column densities are retrieved with respect to a Fraunhofer reference spectrum, differential slant column densities $dS(\vartheta, \alpha)$ are the output of the measurement (see equation (3.30)):

$$dS(\vartheta, \alpha) = S(\vartheta, \alpha) - S_{Ref} \qquad (4.22)$$

The dependence of the air mass factor on the solar zenith angle ϑ can be used to convert the differential slant column densities $dS(\vartheta)$ into absolute slant column densities $S(\vartheta)$. With equation (4.13), equation (4.22) can be written as:

$$dS(\vartheta) = V \cdot A(\vartheta) - S_{Ref} \qquad (4.23)$$

The differential slant column density $dS(\vartheta)$ is a linear function of the air mass factor $A(\vartheta)$ if the vertical column density V does not depend on the solar zenith angle ϑ. This relationship, hence $dS(\vartheta, \alpha)$ versus $A(\vartheta, \alpha)$, can be plotted in a diagram. The slant column density of the Fraunhofer reference spectrum, S_{Ref}, is given by the negative intercept of the ordinate and the vertical column density V by the slope of the linear fit. This method is called Langley plot.

In order to separate tropospheric from stratospheric absorbers, the ΔSCD (see equation 3.31) can be plotted versus the tropospheric air mass factors $\Delta A(\alpha)$, with

$$\Delta A(\alpha) = A(\alpha) - A(90°) \approx A(\alpha) - 1 \tag{4.24}$$

where $A(90°)$ can be calculated by radiative transfer modeling (see section 4.5) or approximated by the value 1. In this case, the slant column density of the Fraunhofer reference spectrum, S_{Ref} is eliminated so that the linear fit should pass the point of origin. The Langley plot equation can now be written as:

$$\Delta S(\alpha) = V \cdot \Delta A(\alpha) \tag{4.25}$$

again with the vertical column density V as the slope of the straight line. As described in section 4.6.2, the Langley plot can be potentially used to estimate the height and concentration of a well-mixed absorber layer.

The Langley plot implies that the vertical column density is constant over the measurement period and that the air mass factors must be recalculated in case of changes in any input parameter (especially changes in the vertical profile of the absorber itself are crucial). Furthermore, the air mass factors has to be independent of the vertical column density (see equation 4.19). The Langley plot is a simplified, but efficient way to retrieve the vertical column density and the slant column density of the FRS, in case the air mass factors are calculated thoroughly.

4.5 Radiative Transfer Modeling

4.5.1 Introduction

The radiative transfer in the atmosphere is determined by interactions of radiation with the compounds of the atmosphere and with Earth's surface. These interactions are absorption, scattering, refraction, thermal emission (only relevant in the infrared wavelength range) and reflection (determined by the albedo). The Radiative Transfer Equation (RTE) describes their influences on the radiance L. The radiance L which is also denoted simplified as intensity is the radiant flux Φ per solid angle Ω and projected radiation source area A_s:

$$L = \frac{\Phi}{\Omega \cdot A_s} \tag{4.26}$$

with the radiant flux being the radiant energy E per unit time t:

$$\Phi = \frac{dE}{dt} \tag{4.27}$$

In contrast, the irradiance B is defined as the radiant flux Φ which is received by a projected illuminated area A_t:

$$B = \frac{\Phi}{A_t} \tag{4.28}$$

The radiance and the irradiance are given by the units $\left[\frac{W}{sr \cdot m^2}\right]$ and $\left[\frac{W}{m^2}\right]$, respectively.

Radiative transfer models are aimed at solving the radiative transfer equation in order to calculate the radiance acquired by a specific instrument and for a defined atmospheric scenario. For instance, a DOAS device is such an instrument which measures at a given time and location. From the radiances, the air mass factors can be calculated. However, it is not possible to analytically solve the RTE without introducing simplifications. Thus, a numerical approach usually is used which can be applied in two different ways: The RTE is either solved analytically by calculating the radiant field of a given atmospheric state or by a statistical approach, where individual photon paths are simulated for a given atmospheric scenario. The radiant field can then be derived from the photon density. Due to simplifications, e.g. concerning the sphericity of the Earth, the analytical calculation is normally faster than the simulation of the statistical approach. However, analytical solutions sometimes are difficult or even impossible to find, while the statistical approach provides reasonable results owing to many individual simulations. But generally, the results converge with each other, if both an analytical solution could be found and the statistics in the simulation is good enough.

In the following sections, the different radiative transfer models are described which were used in this work. While Tracy and Tracy-II/McArtim apply the statistical approach, Sciatran analytically calculates the radiant field.

4.5.2 The Radiative Transfer Model Tracy

Tracy (Trace gas RAdiative monte Carlo Ymplementation) is a three dimensional radiative transfer model and was developed by the Institute of Environmental Physics of the University of Heidelberg [von Friedeburg, 2003]. It is based on the backward Monte Carlo method: a photon virtually emerges from a detector in an arbitrary line of sight direction and is followed through the atmosphere along its path until it leaves the top of the atmosphere. (In a forward model instead, a multitude of photons would need to be simulated before even one photon hits the detector, which would be very time consuming.) The various possible scattering or absorption events along the path are defined by suitable probability distributions. When, for example, a photon hits an air molecule, a random number is drawn - just like a game of chance e.g. in Monte Carlo. If the number lies in a certain interval depending on the process' probability, this process occurs and the photon is e.g. scattered to a different direction of propagation. After the last scattering event and before leaving the atmosphere, the probability is calculated that the direction of the photon after this event points at the sun. Then, the probability of absorption of the photon from the location of the last scattering event to the top of the atmosphere is determined. Finally, the complete photon path weighted with all probabilities is included in the calculation of the intensity. For the modeling, the atmosphere is discretized vertically and horizontally into so-called voxels with homogeneous atmospheric properties. Therefore, a fine discretisation is necessary if parameters change strongly. Profiles of pressure, temperature, ozone, aerosols and several trace gases as well as the wavelength have to be included for the modeling, yielding air mass factors for every trace gas specified.

In Tracy, the modeling of the total air mass factor is based on calculations for optically thin absorbers, i.e. weak absorbers [Solomon et al., 1987; Perliski and Solomon, 1993; Eskes and Boersma, 2003], applying the following equation:

$$A = \frac{ln\left(\frac{I_0}{I}\right)}{\sigma(\lambda) \cdot V} \tag{4.29}$$

which is a combination of equations (4.14) and (4.15). Here $I_0(\lambda)$ denotes the measured intensity without the absorber of interest, but with the absorption of all other present absorbers, while $I(\lambda)$ is the detected intensity considering all absorbers. This formula works well as long as the impact of the absorption of the trace gas of interest on the light path distribution can be neglected. When this is not the case, e.g. for ozone in the UV, then the light paths contributing to $I(\lambda)$ are influenced by the absorption of the trace gas of interest itself and thus they differ from the light paths contributing to $I_0(\lambda)$ (see also section 4.4). In this work, this does not lead to errors because all trace gases of interest are weak absorbers.

4.5.3 The Radiative Transfer Model Tracy-II/McArtim

Tracy-II and McArtim which both are developed by Deutschmann and Wagner [2006] are almost identical, complete recompositions of Tracy with new features and improvements. Both also apply the backward Monte Carlo method at a given wavelength. However, the calculation of the photon path probability has been improved: The various possible scattering or absorption events along the path are still described by suitable probability distributions. However, here the generation of the photon paths is independent of the position of the sun. Instead at each scattering event the probability that the photon is scattered into the sun is calculated. When enough light paths are modeled, the contribution of each light path to the intensity measured at the detector is calculated by weighting the sum of the probabilities of all scattering events along the path (local estimation method [Marchuk et al., 1980]). When setting the Sun's position to a specific solar zenith angle, then a forward run of the model calculates the corresponding air mass factors and intensities, using the paths and probabilities generated in the backward run. Furthermore, Tracy-II/McArtim uses a different approach for the air mass factor calculation and calculates so-called box-AMFs A_{box} instead. When the atmosphere is divided along its vertical axis into several layers of height h, also called boxes, then A_{box_i} is the air mass factor for box i under the assumption of a horizontally homogeneous trace gas distribution in the box. The box-AMF is then defined by [Eskes and Boersma, 2003]:

$$A_{box_i} = \frac{d\left[ln\left(\frac{I_0}{I}\right)\right]}{d\left[\sigma(\lambda) \cdot V_i\right]} \tag{4.30}$$

According to equation (4.13) this can also be written as:

$$A_{box_i} = \frac{dS}{dV_i} \tag{4.31}$$

The box-AMF describes how strongly the measured SCD changes with an alteration of V_i. This expresses the sensitivity of the measurement towards changes of the vertical column density within the box i. box-AMFs (normalized to 1) are identical with weighting functions [Rodgers, 1976, 2000] which are the weights for the sensitivity of the measurement towards specific atmospheric layers. Thus, they provide information in which boxes the measurement of an absorber is most sensitive. From that, the most suitable measurement geometries can be derived when investigating an absorber with a known vertical profile.

Total AMF is calculated from the Box-AMFs A_{box_i} for each box i and the respective trace gas profile. It is the sum of the box-AMFs from the surface to the top of the atmosphere (TOA) and the corresponding partial trace gas vertical columns V_i divided by the VCD:

$$A = \frac{1}{V} \cdot \sum_i A_{box_i} \cdot V_i \tag{4.32}$$

For weak absorbers the box-AMFs are independent from the profile. Then, arbitrary trace gas profiles can be used with the same set of box-AMFs in order to derive total AMFs for different scenarios. In contrast, for strong absorbers the same height profile as used for the calculation of the respective box-AMFs must be used for the calculation of the total AMF.

Tracy-II/McArtim can also calculate the so-called normalized radiance L_n. It can be derived by modeling the radiance L, which is received by the measurement device, and the solar irradiance B:

$$L_n = \frac{L}{\pi \cdot B} \tag{4.33}$$

The normalized radiance describes which fraction of the sunlight can be detected by the measurement device. It is suited to check model runs with respect to potential errors in the settings as well as the consistency of models themselves [Wagner et al., 2007]. Furthermore, Tracy-II/McArtim can provide optical densities as well as photon path length distributions and photon scattering distances.

In Tracy-II/McArtim, the radiative transfer is modeled in a fully spherical and three-dimensional atmosphere. Three-dimensional profiles of trace gases and aerosols are considered in the calculation as well. A specific relief can be included so that significant valleys or mountains which can influence the radiative transfer are taken into account. However, refraction is not fully developed until now but is planed to be done soon. Yet, in this work, refraction has a very weak impact because this work focusses on absorbers in the troposphere.

Tracy-II and McArtim are identical except for a detail in the generation of the path through the atmosphere. In Tracy-II, paths are determined without consideration of absorption. Therefore, absorption is taking into account later in the weighting of the intensity by an additional factor. In contrast, McArtim considers absorption already in the generation of the paths. Thus, in case of strong absorptions, the path through the atmosphere can be simulated more realisticly. Furthermore, the omitting of an additional weighting factor in the intensity calculation makes McArtim one order of magnitude faster in radiative transfer modeling than Tracy-II.

4.5.4 The Radiative Transfer Model Sciatran

The analytical radiative transfer model Sciatran 1 has been developed by the Institute of Environmental Physics of the University of Bremen [Rozanov et al., 2000, 2001]. The intensity of the radiation is calculated solving the radiative transfer equation (RTE) in a spherical atmosphere in its integral form employing the characteristics method. This means that the source function is integrated along the line of sight intersecting a spherical atmosphere. The single scattering part of the source function is truly spherical and the multiple scattering part is initialized by the output of a pseudo-spherical model.

Both integro-differential radiative transfer equation in a pseudo-spherical atmosphere and spherical integral RTE are solved independently for each Fourier term of a Fourier series expansion. The weighting functions are calculated employing a solution of the adjoint RTE. Similar to the intensity, the adjoint intensity is initialized in the pseudo-spherical approximation and then used to obtain the spherical weighting functions.

The box-AMFs A_{box} are derived as follows:

$$A_{box} = -\frac{1}{I \cdot h_{box} \cdot \sigma} \cdot \frac{dI}{dc} \tag{4.34}$$

where c denotes the trace gas concentration, I the intensity of the radiance, h_{box} the height of the vertical layer and σ the trace gas cross section.

4.6 Profile Retrieval

4.6.1 Direct Comparison Approach

The direct comparison approach is based on the comparison of measured and modeled values. It is a relatively simple algorithm, which converts a set of slant column density MAX-DOAS measurements of the oxygen dimer (O_4) and of a trace gas of interest, e.g. NO_2, CHOCHO and HCHO (see sections 7.4 and 7.5), into atmospheric aerosol extinction and the absolute concentration and mixing ratio of the trace gas of interest within the atmospheric boundary layer [Sinreich et al., 2005]. In addition the height of the atmospheric boundary layer usually can be derived. The algorithm is based on radiative transfer modeling, taking into account the current aerosol scenario as determined from the O_4 measurements. Since the concentration of the oxygen dimer O_4 is proportional to the square of the O_2 concentration, the majority of O_4 is located close to the surface, and its vertical profile decreases exponentially with a scale height of approximately 4 km. The variation of the O_4 dSCD with elevation can therefore be used to quantify the aerosol extinction in the lower troposphere. Variations in the O_4 dSCDs are generally not caused by changes in concentration, but in aerosol scattering [Wagner et al., 2004; Frieß et al., 2006].

The profile retrieval is split into two steps. Firstly, sets of O_4 AMFs for a variety of aerosol scenarios are calculated and then compared with O_4 AMFs measured for a series of elevation angles in order to determine the adequate aerosol scenario. Secondly, this best-matching aerosol scenario is taken as input for AMF calculations of the trace gas of interest to derive its height profile. The details of this method are sketched in Figure 4.3 for NO_2 as the trace gas of interest.

For the retrieval of the aerosol height profile, O_4 air mass factors for several aerosol scenarios have to be calculated. Since the bulk of the aerosol is expected to be present in the lower atmosphere (in particular, in the boundary layer), box profiles (i.e. profiles with constant aerosol properties from the surface up to a certain altitude and zero extinction above) can be assumed. Aerosol profiles of this type are likely to occur in well mixed boundary layers. Yet also exponentially decreasing profiles of the aerosol extinction with altitude can be taken into account. A selection of aerosol scenarios are listed in Table 4.1, for which O_4 air mass factors were calculated with Tracy. In Figure 4.4, the air mass factors are plotted as a function of the logarithm of the elevation angle for 70° solar zenith angle. The highest O_4 air mass factors occur when no aerosols are included, and the AMF generally decreases with increasing aerosol load, except for the zenith direction. Furthermore, the O_4 AMFs of the exponentially decreasing scenarios vary less strongly with aerosol extinction than the AMFs for the box profiles with equal aerosol extinction.

In the following, the measured O_4 SCDs must be converted into AMFs using a vertical column density calculated from a typical mid-latitude air density profile. Both measured and modelled AMFs were converted to dAMFs by subtracting the

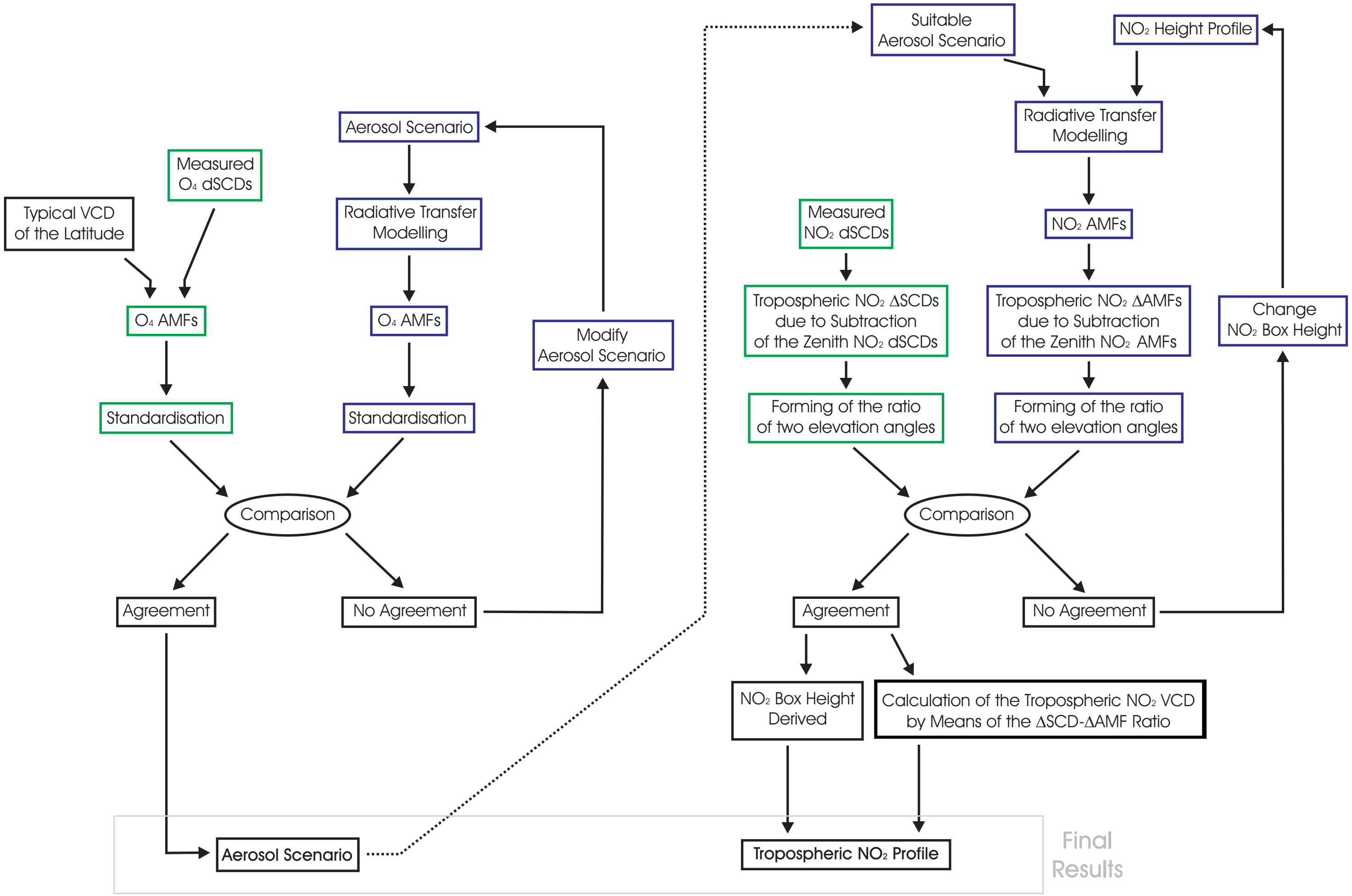

Figure 4.3: *Sketch of the retrieval process. Left: the retrieval of the aerosol scenario, right: the derivation of the tropospheric trace gas profile (here* NO_2*) is shown for which the aerosol profile must be known (dotted line). Green boxes are measurement-based, blue boxes are based on radiative transfer and preparation steps of radiative transfer modelling, respectively.*

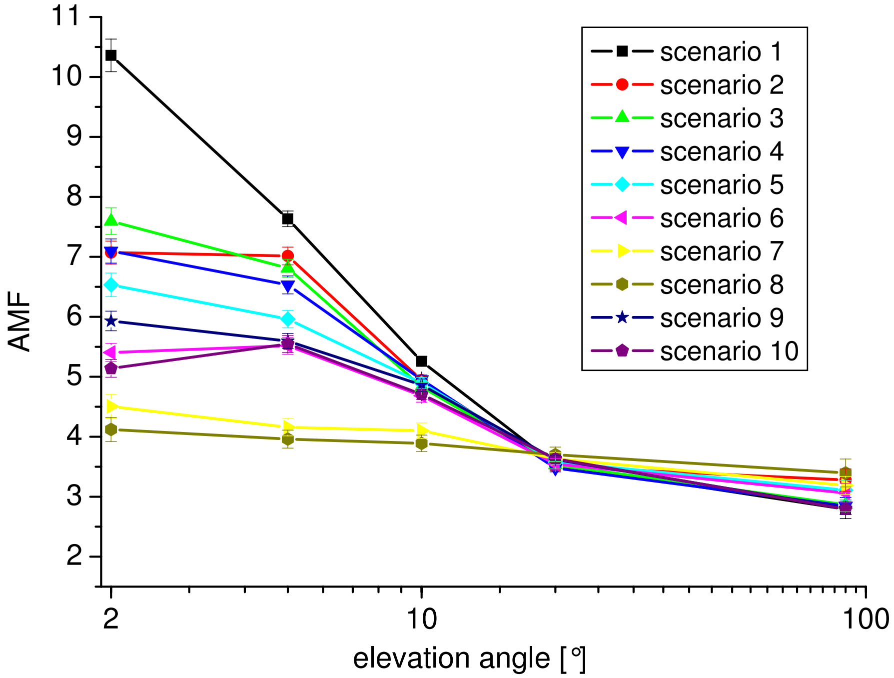

Figure 4.4: *Calculated O_4 air mass factors as a function of the logarithm of the elevation angle for 70° solar zenith angle, 440 nm and a Henyey-Greenstein phase function with an asymmetry coefficient of 0.65 [Sinreich et al., 2005]. The O_4 AMFs decrease with higher elevation angle and higher aerosol extinction.*

Table 4.1: *Applied aerosol profiles for the calculation of O_4 air mass factors.*

	Type	Aerosol extinction [km^{-1}]	Height [km]
Scenario 1	(no aerosols)	0	0
Scenario 2	box	0.025	2
Scenario 3	box	0.025	3
Scenario 4	box	0.035	2
Scenario 5	box	0.05	2
Scenario 6	box	0.1	1
Scenario 7	box	0.25	2
Scenario 8	box	0.5	1
Scenario 9	exp. decrease	0.05 (at surface)	2.7 (scale height)
Scenario 10	exp. decrease	0.1 (at surface)	2.7 (scale height)

respective zenith sky AMF at noon (which is referred to as standardisation in Figure 4.3). This procedure must be applied to all scenarios listed in Table 4.1. Afterwards, the measured dAMFs are compared with the calculated dAMFs of the different scenarios. The best matching scenario can be taken in the further calculation of the trace gas profile. Thereby, some deviations in the agreement might have to be accepted owing to the simplified aerosol profile shape or possibly other factors, e.g. an incorrect scattering phase function.

To illustrate the potential of MAX-DOAS O_4 measurements to retrieve information on the aerosol extinction profile, the ratio of 2° and 90° elevation angles of calculated O_4 AMFs as a function of aerosol extinction coefficient for a box profile with 2 km height is shown in Figure 4.5. This plot also demonstrates the strong sensitivity of O_4 AMFs to aerosols, in particular in the presence of low aerosol extinction. As shown in Figure 4.5, the MAX-DOAS measurements in this instance are sensitive to visibilities above 16 km (the visibility corresponds to approximately 3.9 times the aerosol extinction length), corresponding to aerosol extinctions lower than about 0.25 km^{-1}. This result was obtained from the ratio of AMFs at different elevations, without consideration of the information gained from the absolute values which would enhance the sensitivity even further, in particular for higher aerosol loads.

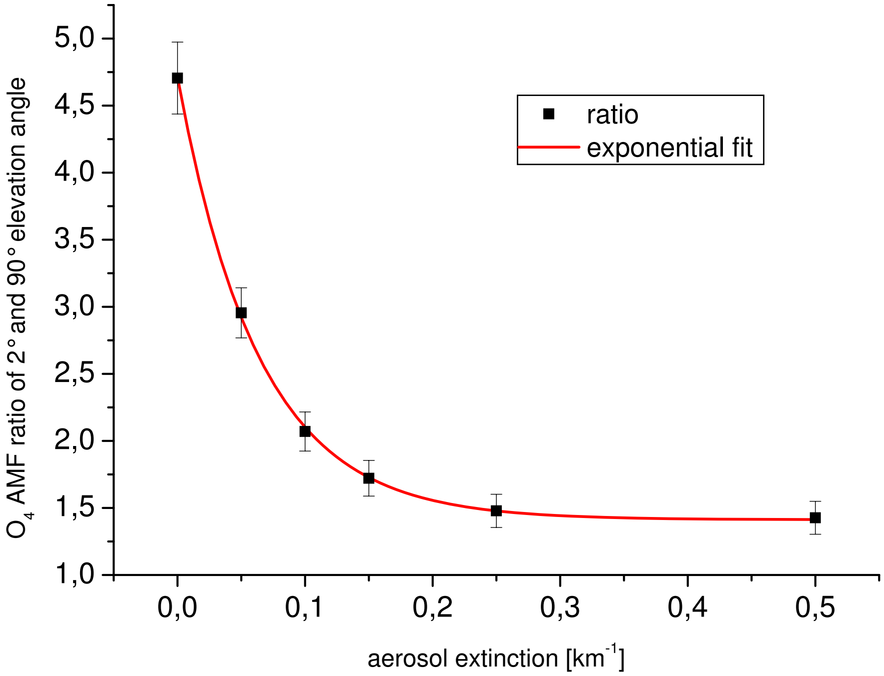

Figure 4.5: *Ratio of O_4 air mass factors calculated for 2° and 90° elevation angles versus the aerosol extinction coefficient assumed for a box profile with 2 km height. The sensitivity is remarkable up to 0.25 km^{-1} aerosol extinction (corresponding to a visibility of about 16 km).*

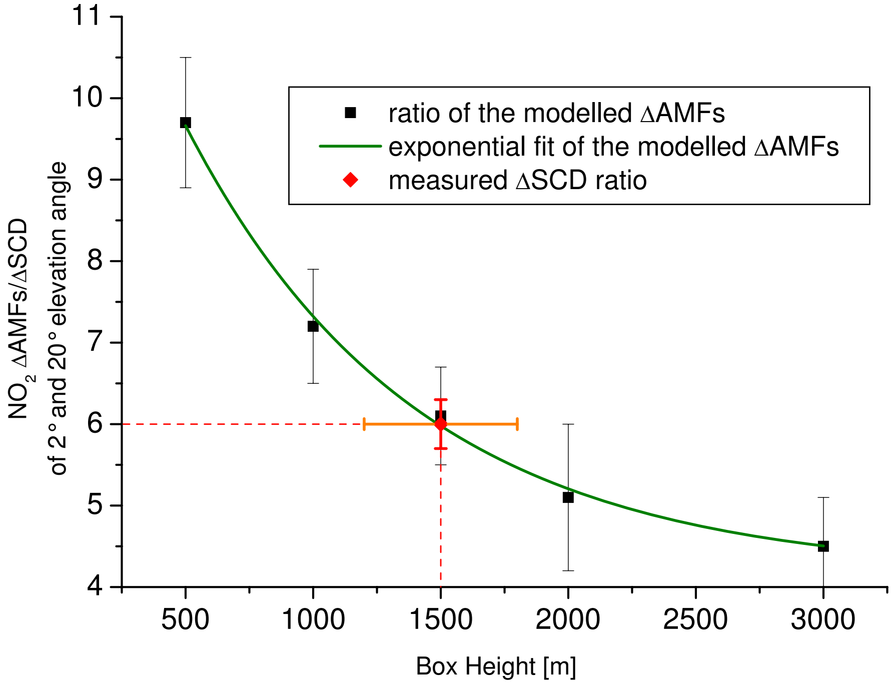

Figure 4.6: *Ratios of the modelled NO_2 ΔAMFs (black) and the measured NO_2 ΔSCD (red) of 2° and 20° elevation angle. To the modelled ratios an exponential fit (green) was applied. The orange horizontal error bar shows the inaccuracy calculated from both the modelling and the measurement error.*

The retrieval of the trace gas profile information uses a similar approach as for the retrieval of the aerosol profile described above. Trace gas ΔAMFs (hence AMFs with respect to the AMF in zenith direction) are calculated using the retrieved aerosol extinction profile and are compared to the observed MAX-DOAS ΔSCDs. The tropospheric trace gas distribution can also be represented by a box profile, and the height of the box is varied now in the course of the calculation. For a weak absorber, it is not necessary to vary the concentration in the model since, in contrast to the sensitivity of the O_4 AMF on the absolute aerosol extinction, the trace gas AMF depends only on the shape of the vertical profile and not on the absolute concentration. Therefore, the ratio of the ΔAMFs obtained from the measurements at two elevation angles provide sufficient information to derive the height of the tropospheric trace gas box. This requires that the measured ratio matches with the calculated ratio of a specific box height.

An example is shown in Figure 4.6 where the ratios of modeled NO_2 ΔAMFs at 2° and 20° elevation angle as a function of the NO_2 box height are plotted (see Sinreich et al. [2005]). An exponential fit was applied to the data. The corresponding average ratio of the measured NO_2 slant column density (NO_2 ΔSCD ratio) is 6.0 (±0.3)

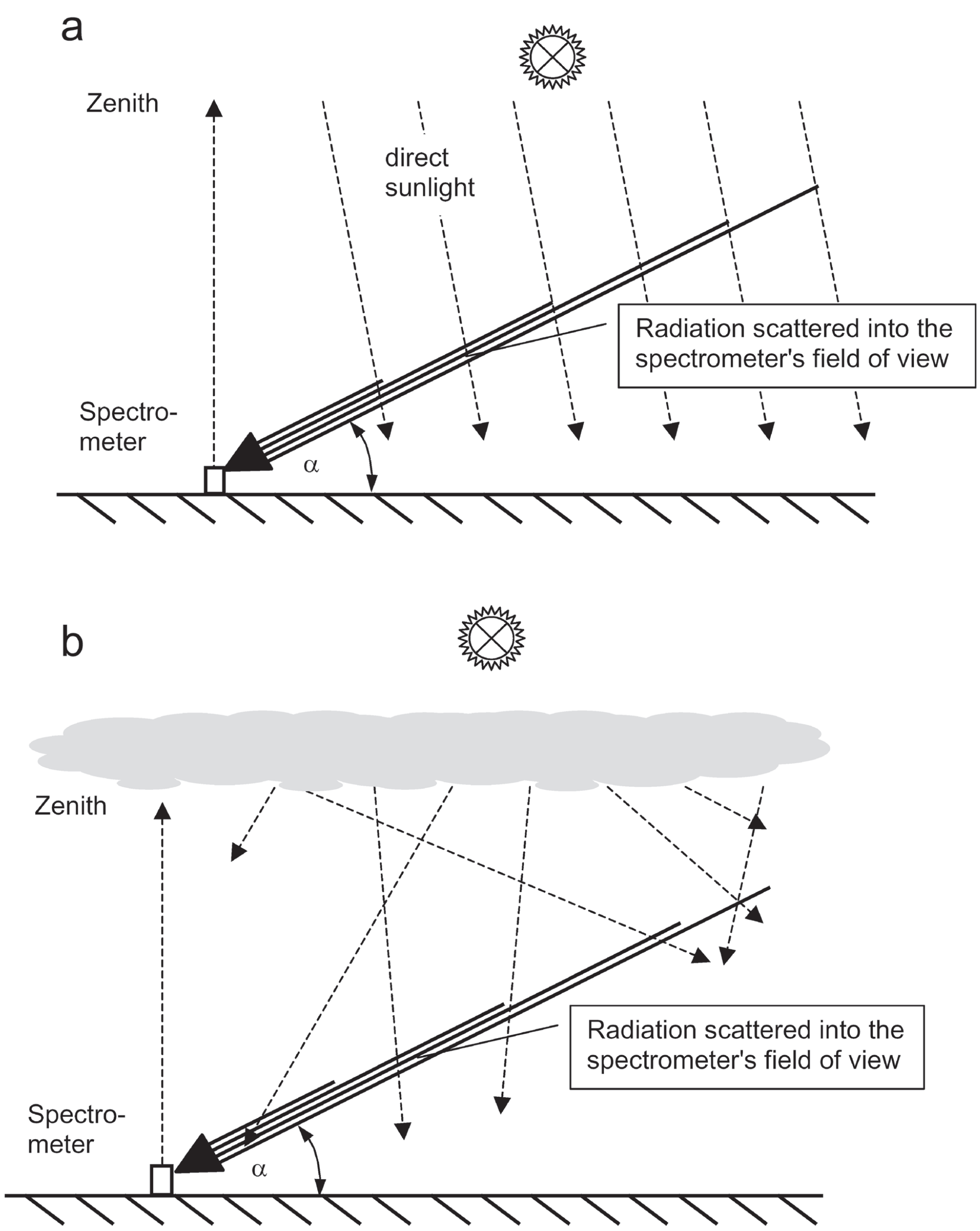

Figure 4.7: *(a) Sketch of MAX-DOAS measurement geometry under the clear sky single scattering assumption. (b) MAX-DOAS measurements under cloudy conditions. Photons from sunlight entering the lower atmosphere are successively scattered towards the instrument within the field of view of the telescope.*

(bold error bar in Figure 4.6). A comparison of this ratio to the modelled ratio leads to an NO_2 box height of 1500 (±300) m. Finally, the tropospheric trace gas concentration c_{trop} is retrieved from the calculated ΔAMFs ΔA_{calc} (at the matching height) and the measured ΔSCDs ΔS_{meas} at the two elevation angles α_1 and α_2 divided by the height h of the box:

$$c_{trop} = \frac{1}{h} \cdot \frac{\Delta S_{meas}(\alpha_1) - \Delta S_{meas}(\alpha_2)}{\Delta A_{calc}(\alpha_1) - \Delta A_{calc}(\alpha_2)} \tag{4.35}$$

This relatively simple approach implies some uncertainties:

1. fitting error of the (differential) SCDs of O_4 and trace gases,
2. errors in the radiation transfer calculation (e.g., statistical errors of the Monte-Carlo approach or due to simplifications in the Mie scattering),
3. possible oversimplification of the assumed aerosol scenario (see Table 4.1) as well as the trace gas distribution,
4. temporal variations during recording the elevation sequence, and
5. effects of clouds.

Error sources (1) and (2) are probably minor (in the order of 10 % or below), compared to the potential influence of the latter two sources of uncertainty.

Concerning uncertainty (3) the aerosol and trace gas scenarios used here are – admittedly – quite coarse in that they only assume a single homogeneous layer with fixed combinations of height and extinction or concentration. More flexible representations of the atmospheric conditions, consisting of e.g., two layers with variable height and extinction or concentration including horizontal inhomogeneities, should considerably reduce uncertainty (3). The dimension of error source (4) depends on the circumstances (e.g. time of day, changing winds in the proximity of strong aerosol or trace gas sources). Thus, temporal variations must be thoroughly considered in the evaluation of the retrieval.

In terms of error source (5), the radiative transfer under clear sky is quite well understood at present, cloudy conditions were not systematically analyzed to date. In the measurement process, photons from sunlight entering the lower atmosphere are successively scattered towards the instrument within the field of view of the telescope. While under clear sky conditions, the single scattering case can be assumed (see Figure 4.7a), under cloudy conditions (assuming the cloud layer being located above the aerosol layer(s)) diffuse light originating from the lower cloud boundary is now scattered towards the instrument (see Figure 4.7b). Clearly, this is likely to change the relative lengths of the light paths at high (i.e. zenith) and low observation elevation angles. Also the (constant) additional light path inside the cloud has to be considered. However, the general dependence of the O_4 slant column density as a function of elevation angle is likely to remain the same. Yet, the influence of clouds can be avoided by selecting cloud free periods when applying this comparison approach.

4.6.2 Langley Plot Approach

The Langley plot (see section 4.4) can also provide information on the tropospheric profile when assuming a box profile for the absorbing trace gas (i.e. profiles with a constant trace gas concentration from the surface up to a certain altitude and zero concentration above). Such a distribution scenario can be approximately found within a well mixed boundary layer.

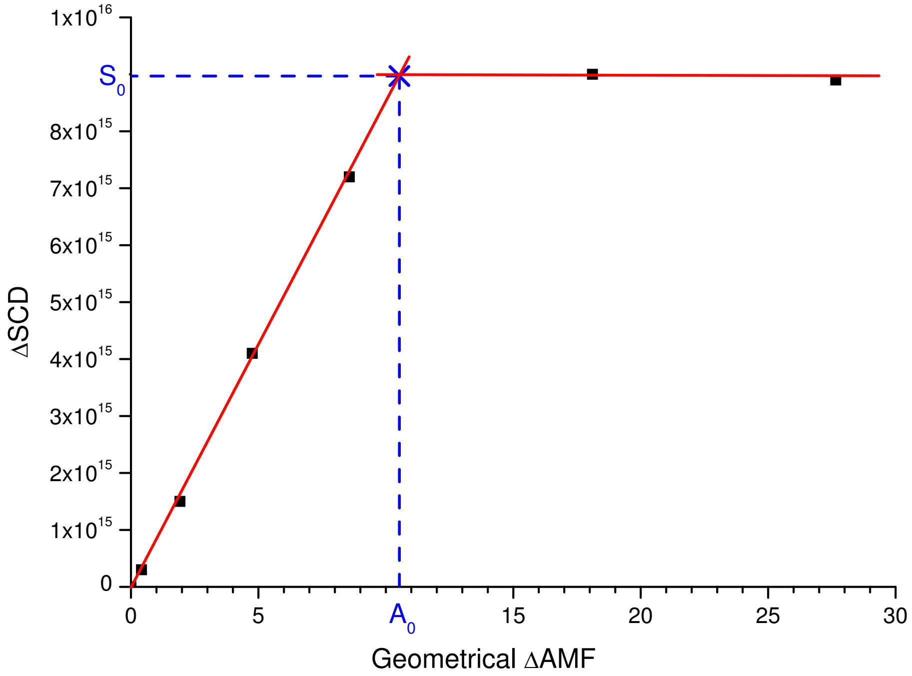

Figure 4.8: *Idealized Langley plot for a tropospheric absorber layer with synthetic values. ΔSCDs from measurements are plotted versus ΔAMFs calculated with the geometrical approximation (see also text).*

The Langley plot approach can be applied if the averaged light path length between the telescope and the (last) scattering event for the lowest elevation angles is short enough to be located within the trace gas layer. For the higher elevation angles, however, the scattering events must happen mostly outside of the trace gas layer. If the air mass factors are approximated geometrically according to the single scattering case, the Langley plot considering ΔSCDs and ΔAMFs (see equations (3.31) and (4.24)) shows a behavior like in Figure 4.8. For smaller ΔAMFs the relationship is linear to the ΔSCDs yielding the VCD. However, with higher ΔAMFs, the ΔSCDs reach a value S_0 from where they do not increase any more. Instead, they remain on a horizontal plateau because the ΔAMFs further increase since the geometrical approach is not valid any more. The corresponding air mass factor A_0 is the projection on the x-axis. Yet, it has to be noted that this an idealized plot. In reality, the border between the linear and the constant dependency will rather be smoothed out.

Since, for tropospheric absorbers in the single scattering case, the ΔAMF can be approximated by $\frac{1}{\sin(\alpha)} - 1$, the corresponding elevation angle α_0 can be determined. The angle α_0 can be considered as the angle where the averaged light path length from the last scattering event matches with the light path through the trace gas layer. For larger elevation angles, the scattering events are located mostly above the layer and, for smaller elevation angles, they are located mostly in the layer. The concentration c of the trace gas layer is given by:

$$c = \frac{S_0}{L} \tag{4.36}$$

with L as the averaged distance between the last scattering event and the telescope at the elevation angle α_0. The layer height H can be calculated from the concentration c and the ΔSCDs and ΔAMFs when the linear relation is given (values not larger than S_0 and A_0, respectively), hence e.g.:

$$H = \frac{S_0}{A_0 \cdot c} \tag{4.37}$$

With equation (4.36), this can be written as:

$$H = \frac{L}{A_0} \tag{4.38}$$

Thus, the height H of the trace gas layer can only be determined if the averaged light path length between the telescope and the last scattering event is known. However, L depends on the Rayleigh scattering as well as on the aerosol extinction.

The extinction due to Rayleigh scattering ϵ_R is calculated from the number density ρ and the Rayleigh cross section σ_R (see equation (4.4)):

$$\epsilon_R = \rho \cdot \sigma_R \tag{4.39}$$

The aerosol extinction coefficient ϵ_M can be derived from measurements forming the ratio of two ΔSCDs of O_4 from different elevation angles. Thereby, measurements from the lowest elevation angles are most sensitive for the aerosol extinction. This ratio can be compared with corresponding calculated ratios of ΔAMFs at different aerosol extinction coefficients (see also section 4.6.1). However, the height of

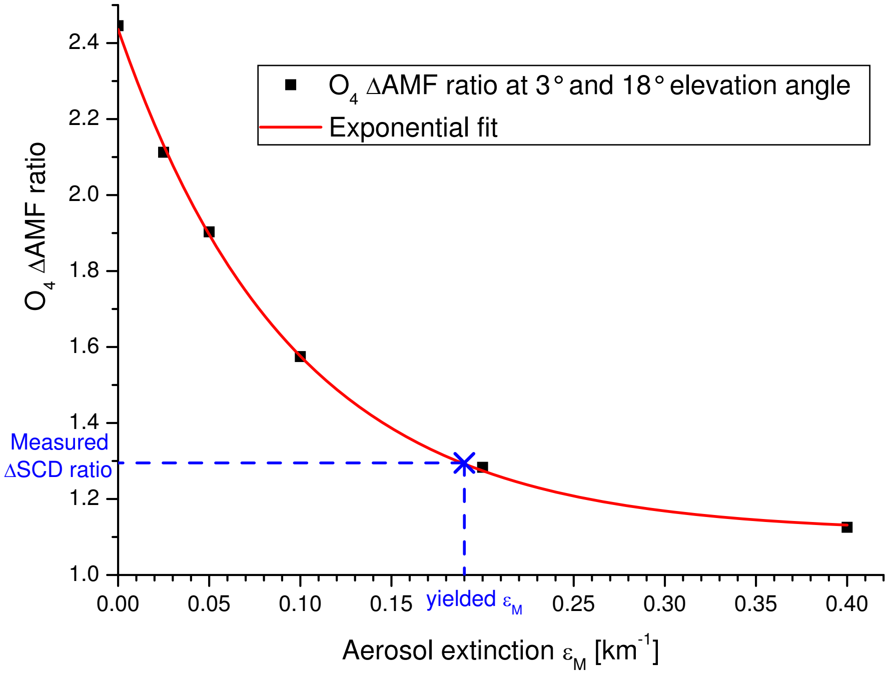

Figure 4.9: *Measured O_4 ΔAMF ratios versus the aerosol extinction ϵ_M. The projection of the measured O_4 ΔSCD ratio yields the aerosol extinction.*

the aerosol box profile has to be estimated in advance. In Figure 4.9, an example is shown for elevation angles 3° and 18° and a box height of 1 km. The ratios were calculated by Tracy-II and were fitted by an exponential function. The projection of the measured ratio on the fitted function yields the corresponding aerosol extinction coefficient.

The sum of the extinction coefficients $\epsilon_R + \epsilon_M = \epsilon_{total}$ can now be considered in the calculation of L. This was done by McArtim varying the aerosol extinction coefficient ϵ_M for the wavelength λ of 360 nm and, for instance, the elevation angle of α of 5°. The modeled scattering distances are plotted versus the different aerosol extinctions and fitted by an exponential function which is shown in Figure 4.10. For the aerosol extinction coefficient from the example in Figure 4.9, the projection of the fit yields the scattering distance L. Applying equation (4.38), now the layer height can be determined.

The Langley plot approach is a very simplified method and the uncertainties listed in the direct comparison approach (section 4.6.1) have to be considered here as well. Furthermore, an additional uncertainty arises due to the estimation of the height of the aerosol box profile. This procedure might be applied iteratively using the retrieved layer height of the trace gas as new estimated height of the aerosol layer until both layer heights match. Alternatively, the aerosol profile could be determined

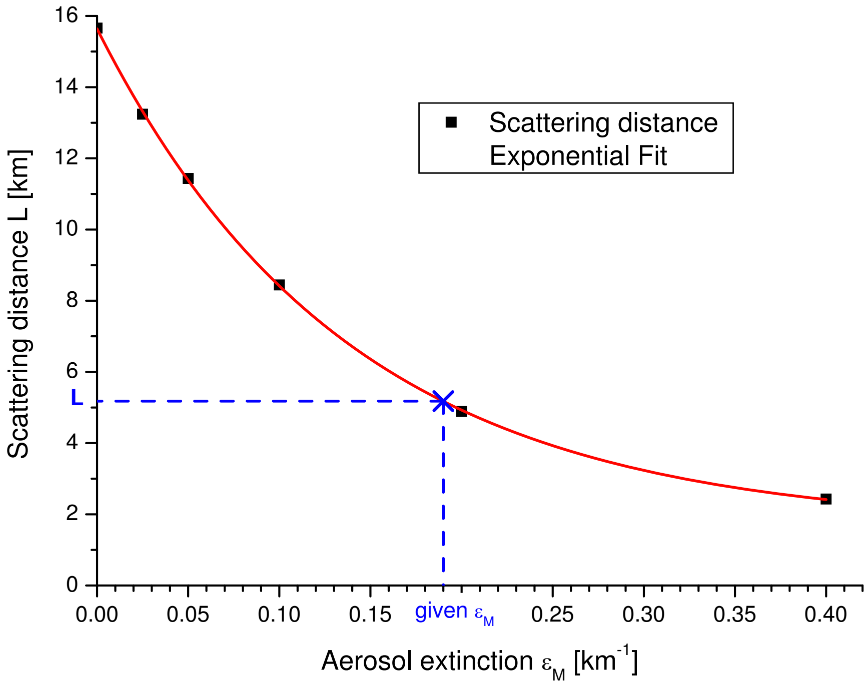

Figure 4.10: *Scattering distance L versus the aerosol extinction ϵ_M. The scattering distance can be determined from the projection of the given aerosol extinction.*

by other methods, e.g. the direct comparison approach.

Additionally, this approach can only be applied if the aerosol load is that high that the Langley plot shows the described behaviour. However, then the sensitivity resulted from the ratio of two measurements with different elevation angles is relatively low so that the potential error increase. Nevertheless, the Langley plot approach can be feasible enough to estimate the height and concentration of a well-mixed boundary layer under the described conditions.

4.6.3 Optimal Estimation

Optimal estimation is a powerful and well established technique for solving inverse problems in atmospheric remote sensing applications [Rodgers, 2000]. It has been applied to DOAS measurements of scattered sunlight [e.g. Hendrick et al., 2004; Schofield et al., 2004]. After Frieß et al. [2006] demonstrated the potential of retrieving profiles by optimal estimation using simulated MAX-DOAS measurements, also Irie et al. [2007] recently used it to retrieve aerosol properties from MAX-DOAS field measurements.

Using optimal estimation, profile retrievals can be estimated more analytical than the methods described in sections 4.6.1 and 4.6.2 so that e.g. different error components, vertical resolution or the information content can be quantified. In general, optimal estimation is based on a forward model $\mathbf{F}(\mathbf{x})$ which describes the physics of a measurement. The measurement, which is expressed by a m-element vector $\mathbf{y}$, can be calculated by $\mathbf{F}(\mathbf{x})$:

$$\mathbf{y} = \mathbf{F}(\mathbf{x}) + \epsilon \tag{4.40}$$

where ϵ describes the random and systematic errors of the measurement as well as deviations owing to simplifications made by the forward model. The n-element vector $\mathbf{x}$ contains the quantities of the state of the system. Furthermore, the forward model parameter $\mathbf{b}$ is considered which quantifies further properties of the system. These are not retrieved, but have to be determined in good accuracy. Thus, the vector $\mathbf{x}$ can now be regarded as the state of the system which is supposed to be retrieved:

$$\mathbf{y} = \mathbf{F}(\mathbf{x}, \mathbf{b}) + \epsilon \tag{4.41}$$

In the case of MAX-DOAS measurements, $\mathbf{y}$ contains differential slant column densities and, if applicable, differential intensities. Thereby, differential intensity is defined as the ratio between a measured intensity and the intensity of the reference spectrum. The forward model $\mathbf{F}(\mathbf{x}, \mathbf{b})$ is a radiative transfer model and describes the physics of the atmosphere.

The retrieval is based on a least squares fit in which the results of the forward model $\mathbf{F}(\mathbf{x}, \mathbf{b})$ should match best to the measurements $\mathbf{y}$. Since in atmospheric remote sensing applications, the information about the state of the atmosphere is often under-determined by the measurements an a priori vector $\mathbf{x_a}$ is introduced as an additional constraint. It represents an estimate of the state of the atmosphere before the measurement has been made. In the retrieval process, also the deviation of the retrieved state from the a priori state is supposed to be minimzed by least squares methods. Thus, the a priori values have to be chosen thoroughly:

$$(\mathbf{y} - \mathbf{F}(\hat{\mathbf{x}}, \mathbf{b})^T \mathbf{S}_\epsilon (\mathbf{y} - \mathbf{F}(\hat{\mathbf{x}}, \mathbf{b}) + (\hat{\mathbf{x}} - \mathbf{x}_a)^T \mathbf{S}_a (\hat{\mathbf{x}} - \mathbf{x}_a) \xrightarrow{!} min \tag{4.42}$$

where $\mathbf{S}_\epsilon$ and $\mathbf{S}_a$ are the covariance matrices of measurement and a priori, respectively. $\hat{\mathbf{x}}$ is the retrieved state vector and is called maximum a posteriori (MAP) solution. In the linear case (for which the forward model is linear, $\mathbf{F}(\mathbf{x}, \mathbf{b}) = \mathbf{K}(\mathbf{b}) \cdot \mathbf{x}$), it is given by the Gauss-Newton method as:

$$\hat{\mathbf{x}} = (\mathbf{S}_a^{-1} + \mathbf{K}^T \mathbf{S}_\epsilon^{-1} \mathbf{K})^{-1} (\mathbf{K}^T \mathbf{S}_\epsilon^{-1} \mathbf{y} + \mathbf{S}_a^{-1} \mathbf{x}_a) \tag{4.43}$$

where $\mathbf{K}$ is the weighting function matrix (Jacobi matrix). It is the matrix of partial derivatives of the forward model with respect to the state vector, which describes the sensitivity of the measurement to perturbations in the state vector, i.e. the elements of the weighting functions are:

$$K_{jk} = \frac{\partial F_j(\mathbf{x})}{\partial x_k} \tag{4.44}$$

In case of a non-linear problem, the MAP solution $\hat{\mathbf{x}}$ of an inverse problem can be determined iteratively:

$$\mathbf{x}_{i+1} = \mathbf{x}_i + (\mathbf{S}_a^{-1} + \mathbf{K}_i^T \mathbf{S}_\epsilon^{-1} \mathbf{K}_i)^{-1} [\mathbf{K}_i^T \mathbf{S}_\epsilon^{-1} (\mathbf{y} - \mathbf{F}(\mathbf{x}_i)) - \mathbf{S}_a^{-1} (\mathbf{x}_i - \mathbf{x}_a)] \tag{4.45}$$

with $\mathbf{K}_i = \mathbf{K}(\mathbf{x}_i)$.

The error of the retrieved state vector $\hat{\mathbf{S}}$ is quantified by the retrieval covariance matrix not including forward model errors and model parameter errors:

$$\hat{\mathbf{S}} = (\mathbf{K}^T \mathbf{S}_\epsilon^{-1} \mathbf{K} + \mathbf{S}_a^{-1})^{-1} \tag{4.46}$$

An important quantity for the characterization of a retrieval is the sensitivity of the retrieved state $\hat{\mathbf{x}}$ to the true state $\mathbf{x}$, which is given by the averaging kernel matrix

$$\mathbf{A} := \frac{\partial \hat{\mathbf{x}}}{\partial \mathbf{x}} = (\mathbf{S}_a^{-1} + \mathbf{K}^T \mathbf{S}_\epsilon^{-1} \mathbf{K})^{-1} \mathbf{K}^T \mathbf{S}_\epsilon^{-1} \mathbf{K} \tag{4.47}$$

For a noise free measurement, the retrieved state vector is a smoothed version of the true atmospheric state:

$$\hat{\mathbf{x}} = \mathbf{x}_a + \mathbf{A}(\mathbf{x} - \mathbf{x}_a) \tag{4.48}$$

In the case of the retrieval of atmospheric profiles, this means that the averaging kernels (rows of $\mathbf{A}$) quantify how the true profile is averaged in order to reproduce the retrieval at a particular altitude level. The averaging kernels therefore provide a measure for the vertical resolution of the measurement and the sensitivity of the retrieval to the true state at particular altitudes. The averaging kernel matrix of an ideal retrieval would be the unit matrix ($\mathbf{A} = \mathbf{I}$), yielding $\hat{\mathbf{x}} = \mathbf{x}$.

The number of independent pieces of information that can be measured is quantified by the degrees of freedom for signal d_s:

$$d_s = \mathrm{tr}(\mathbf{A}) \tag{4.49}$$

Similarly to the direct comparison approach in section 4.6.1, the profile retrieval of a trace gas is split into two steps. The first is the retrieval of the aerosol profile, for instance, by measurements of O_4. In the second step, the profile of the trace gas can be estimated.

In the retrieval of an aerosol profile using MAX-DOAS measurements, the measurements consist of dSCDs (or alternatively differential optical densities ($\mathrm{d}\tau$)) of O_4. These are observed at m different combinations $(\lambda_j, \mathbf{\Omega}_j)$ $(j = 1, \ldots, m)$. Thereby, λ_j are the different wavelengths where O_4 features absorption bands (O_4 has significant absorption bands at 360 nm, 477 nm, 577 nm, and 630nm in the UV-Vis wavelength range) and $\mathbf{\Omega}_j$ the different measurement geometries. The measurement geometry $\mathbf{\Omega} = (\alpha, \theta, \phi)$ is determined by α as the elevation angle, θ as the solar zenith angle, and ϕ as the relative azimuth angle between the measurement direction and the sun. The different combinations of measurements can be summarized in the measurement vector as

$$\mathbf{y} = \begin{pmatrix} d\tau(\lambda_1, \mathbf{\Omega}_1) \\ \vdots \\ d\tau(\lambda_m, \mathbf{\Omega}_m) \end{pmatrix} \tag{4.50}$$

Additionally, the corresponding m differential intensities relative to the reference spectrum can be taken into account, such as in Frieß et al. [2006].

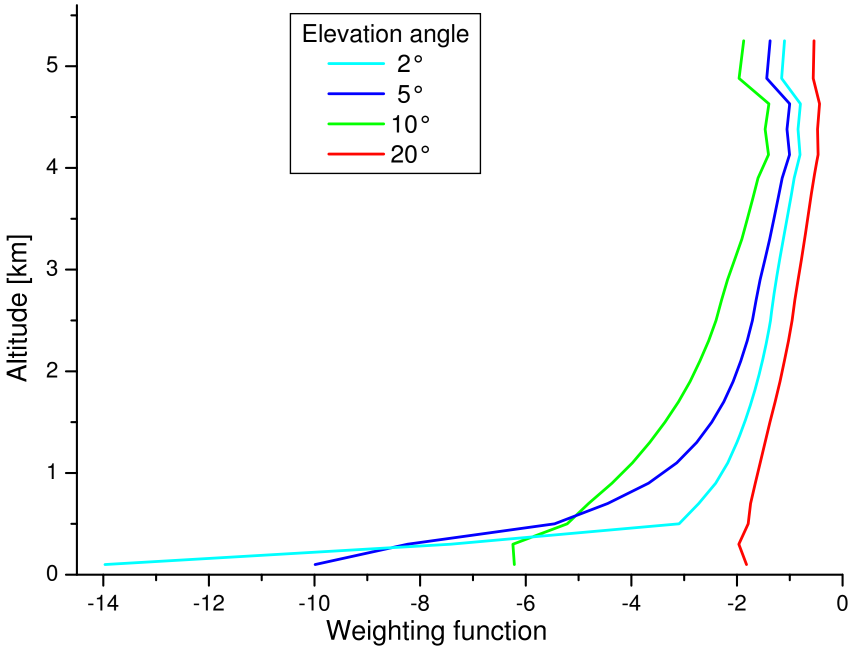

Figure 4.11: *Example of O_4 weighting functions based on simulated MAX-DOAS measurements (2°, 5°, 10° and 20° elevation angles) of O_4 at the absorption band centered around 360 nm. They are determined by the partial derivatives of the O_4 optical density with respect to the partial aerosol optical density for each height layer normalized by the vertical optical density of O_4 at 360 nm [Frieß et al., 2006]. The weighting functions show that the O_4 optical density decreases with higher aerosol optical density and that the sensitivity is highest close to the ground.*

Applying the non-linear case, aerosol extinction profiles can be retrieved. The state vector $\mathbf{x}$ contains the extinction coefficients $k(z_i)$ $(i = 1, \ldots, n)$ at n discrete layers (centered around the altitudes z_i). With different azimuth angles and including also differential intensities, optical or microphysical properties of aerosols, such as parameters of the phase function (e.g., the asymmetry parameter when using a Henyey-Greenstein phase function) and the single scattering albedo, or the particle size distribution and complex refractive index, can be retrieved. Additionally, information on the wavelength dependent surface albedo can be yielded by using several O_4 absorption bands.

The sensitivity of MAX-DOAS measurements to perturbations of the state parameters is quantified by the weighting functions K_{jk} (see equation (4.44)). An example is shown in Figure 4.11 where O_4 weighting functions are plotted for the absorption band centered around 360 nm.

In principal, the estimation of the trace gas profile is conducted in the same way now using the retrieved aerosol profile in the forward model except that, for weak absorbers, the retrieval can be assumed to be linear. In any case, the measurement vector can be written as:

$$\mathbf{y} = \begin{pmatrix} d\tau_{TG}(\lambda, \mathbf{\Omega}_1) \\ \vdots \\ d\tau_{TG}(\lambda, \mathbf{\Omega}_m) \end{pmatrix} \tag{4.51}$$

with m not being the same as in equation 4.50. $\mathrm{d}\tau_{TG}$ are the differential optical densities of the trace gas of interest at different measurement geometries $\mathbf{\Omega}_j$. The trace gas is normally evaluated only at one (optimal) wavelength λ in the measurement wavelength range. For O_3 and NO_2, also several wavelengths could be considered because they absorb over a wide wavelength range in the UV-Vis.

Combining the optimal estimation method with the Langley Plot approach in section 4.6.2 can lead to a simplified retrieval in only one step. It is assumed that both the aerosol layer and the trace gas layer are homogeneously mixed and constant until the same height, with zero above. In this case, the forward model can still be the radiative transfer model or, more simplified, a geometrical calculation. By knowing the scattering distance distribution from the last scattering event to the telescope and by assuming single scattering only within the layer into the direction of the sun, the light path through the layer can easily be calculated (see Figure 4.12). However, the scattering distance distribution still has to be modeled by radiative transfer calculations for each measurement geometry. In any case, the measurement

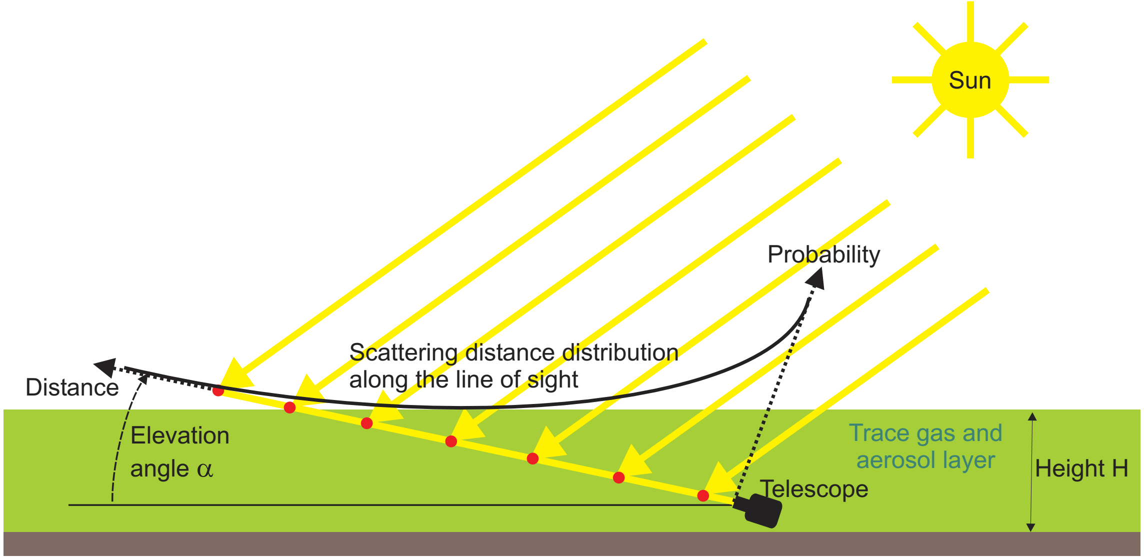

Figure 4.12: *Sketch of a DOAS measurement in the single scattering case of the Langley Plot Approach. The telescope points to the elevation angle* α *in order to collect sunlight which was scattered along the line of sight (red points). By knowing the scattering distance distribution from the last scattering event to the telescope along the line of sight, the light path through the layer can easily be calculated.*

vector would be

$$\mathbf{y} = \begin{pmatrix} d\tau_{\mathrm{O}_4}(\lambda_1, \alpha_1) \\ \vdots \\ d\tau_{\mathrm{O}_4}(\lambda_1, \alpha_s) \\ d\tau_{TG}(\lambda_2, \alpha_1) \\ \vdots \\ d\tau_{TG}(\lambda_2, \alpha_s) \end{pmatrix} \tag{4.52}$$

assuming only a changing elevation angle α_j $(j = 1, \dots, s)$ in the measurement geometry. λ_1 and λ_2 are the evaluation wavelengths of O_4 and the trace gas of interest, respectively. The state vector $\mathbf{x}$ now contains only the aerosol extinction ϵ_M and the trace gas concentration c in the layer as well as the layer height H:

$$\mathbf{x} = (\epsilon_M, c, H)^T \tag{4.53}$$

In this case, the weighting function can be written as:

$$K_{jk} = \frac{\partial F_j(\mathbf{x})}{\partial x_k} = \begin{pmatrix} \frac{\partial d\tau_{\mathrm{O}_4}(\lambda_1,\alpha_1)}{\partial \epsilon_M} & \frac{\partial d\tau_{\mathrm{O}_4}(\lambda_1,\alpha_1)}{\partial c} & \frac{\partial d\tau_{\mathrm{O}_4}(\lambda_1,\alpha_1)}{\partial H} \\ \vdots & \vdots & \vdots \\ \frac{\partial d\tau_{\mathrm{O}_4}(\lambda_1,\alpha_s)}{\partial \epsilon_M} & \frac{\partial d\tau_{\mathrm{O}_4}(\lambda_1,\alpha_s)}{\partial c} & \frac{\partial d\tau_{\mathrm{O}_4}(\lambda_1,\alpha_s)}{\partial H} \\ \frac{\partial d\tau_{TG}(\lambda_2,\alpha_1)}{\partial \epsilon_M} & \frac{\partial d\tau_{TG}(\lambda_2,\alpha_1)}{\partial c} & \frac{\partial d\tau_{TG}(\lambda_2,\alpha_1)}{\partial H} \\ \vdots & \vdots & \vdots \\ \frac{\partial d\tau_{TG}(\lambda_2,\alpha_s)}{\partial \epsilon_M} & \frac{\partial d\tau_{TG}(\lambda_2,\alpha_s)}{\partial c} & \frac{\partial d\tau_{TG}(\lambda_2,\alpha_s)}{\partial H} \end{pmatrix} \tag{4.54}$$

Since $d\tau_{\mathrm{O}_4}(\lambda_1, \alpha_1)$ does not depend on the concentration of the trace gas and

$$d\tau_{TG}(\lambda_2, \alpha) = c \cdot H \cdot \sigma \cdot dA_{TG}(\lambda_2, \alpha) \tag{4.55}$$

with σ as the absorption cross section and $dA_{TG}(\lambda_2, \alpha) = A_{TG}(\lambda_2, \alpha) - A_{TG}(\lambda_2, \alpha_{Ref})$ as the corresponding differential air mass factor, the weighting function can be rewritten:

$$K_{jk} = \begin{pmatrix} \frac{\partial d\tau_{\mathrm{O}_4}(\lambda_1,\alpha_1)}{\partial \epsilon_M} & 0 & \frac{\partial d\tau_{\mathrm{O}_4}(\lambda_1,\alpha_1)}{\partial H} \\ \vdots & \vdots & \vdots \\ \frac{\partial d\tau_{\mathrm{O}_4}(\lambda_1,\alpha_s)}{\partial \epsilon_M} & 0 & \frac{\partial d\tau_{\mathrm{O}_4}(\lambda_1,\alpha_s)}{\partial H} \\ \frac{\partial d\tau_{TG}(\lambda_2,\alpha_1)}{\partial \epsilon_M} & \sigma \cdot H \cdot dA_{TG}(\lambda_2, \alpha_1) & \sigma \cdot c \cdot dA_{TG}(\lambda_2, \alpha_1) \\ \vdots & \vdots & \vdots \\ \frac{\partial d\tau_{TG}(\lambda_2,\alpha_s)}{\partial \epsilon_M} & \sigma \cdot H \cdot dA_{TG}(\lambda_2, \alpha_s) & \sigma \cdot c \cdot dA_{TG}(\lambda_2, \alpha_s) \end{pmatrix} \tag{4.56}$$

5 Instrumentation

5.1 The Mini-MAX-DOAS Instrument

One kind of measurement instrument which was used in both measurement campaigns of this work, namely in the north-east of the USA (see chapter 7) and in Mexico City, Mexico (see chapter 8), was the Mini-MAX-DOAS instrument. This is an easily manageable and relatively small measurement device (the dimensions of the housing are about 13 cm × 19 cm × 14 cm) [Hönninger, 2002]. It is developed by the Institute of Environmental Physics of the University of Heidelberg together with Hoffmann Meßtechnik GmbH which is the manufacturer of the Mini-MAX-DOAS

Figure 5.1: *Mini-MAX-DOAS setup mounted on a tripod, in this instance at Brookhaven during ICARTT 2004 measurement field campaign (see section 7.2).*

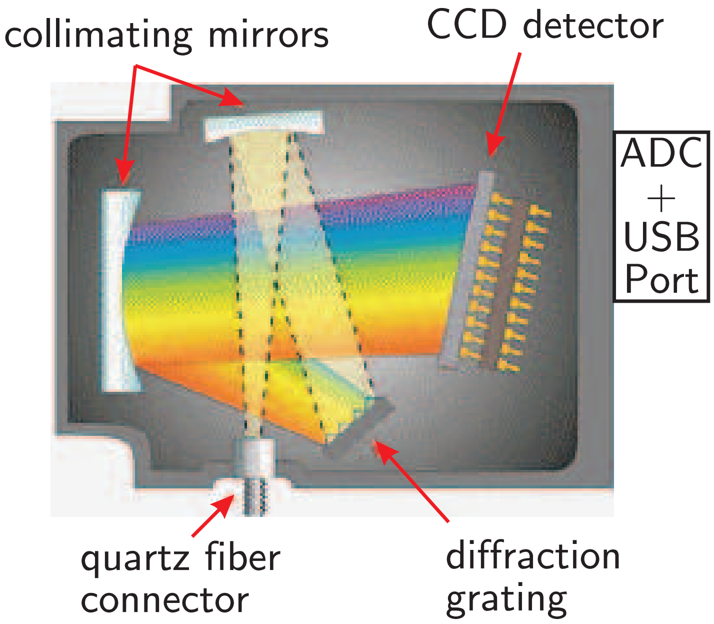

Figure 5.2: *Sketch of the Ocean Optics USB2000 spectrograph-detector unit. Light enters the spectrograph at the quartz fiber connector which includes the entrance slit. It is led via mirrors first to the diffraction grating and then to the CCD detector*

devices. For measurements, it can be mounted on a conventional tripod (see Figure 5.1).

The Mini-MAX-DOAS housing contains a miniature crossed Czerny-Turner spectrograph-detector unit called "USB2000" from Ocean Optics Inc. which is sketched in Figure 5.2. In this work, the Ocean Optics spectrographs were equipped with the diffraction grating #7 with 2400 grooves per mm so that the spectral resolution accounted to about 0.7 nm full width at half maximum (FWHM). It projected a spectral range from about 290 to 420 nm and about 330 to 460 nm, respectively, onto a one-dimensional CCD detector with 2048 pixels. The scattered sunlight is collected and focused by a quartz lens (focal length of 40 mm). A coiled quartz fiber bundle of about 1 m length leads the light into the spectrograph-detector unit. There, a linear arrangement of four quartz fibers (200 μm diameter each) together with an entrance slit of the spectrograph-detector unit (50 μm width) results in a relatively good resolution with maximum light throughput. The spectrograph-detector unit can be cooled by a Peltier cooling to a stable temperature of up to 30° C below ambient temperature in order to minimize changes in optical properties of the spectrograph while, at the same time, reducing detector dark current (see section 5.3.2). To avoid condensation of water vapor, the Mini-MAX-DOAS housing was sealed and a drying agent was included. The housing can be attached to a stepper motor which enables the adjustment of the viewing direction to a desired elevation angle. By means of a spirit-level the Mini-MAX-DOAS device can be aligned to the horizontal so that the stepper motor movements are adjusted to the respective elevation angles. Usually, a stepper motor with Reed end switch has been used which needs 10,000 steps for a movement of 90°. Additionally, the azimuth angle could be adjusted by a second stepper motor which, however, was not used in this work. An electronic board integrated in the housing controls both the Peltier cooling as well as up to two stepper motors. All functions including the readout of the detector can be controlled by PC via USB connection. While the power of the spectrograph-detector unit is provided by the USB port, the cooling and stepper motor movement need a 12 V power supply with 4 A peak current at maximum cooling. In case of absence of mains supply, a conventional lead battery usually can provide this power for a couple of hours. Even if mains supply is available, it can be useful connecting a battery parallel to it in order to smooth out power peaks of the mains supply and to have a fallback power supply in case of a mains supply breakdown. This was done for all Mini-MAX-DOAS setups in this work.

The Mini-MAX-DOAS instruments were operated by the software package DOASIS (DOAS Intelligent System) [Kraus, 2004]. DOASIS allows to execute JScript routines which enable a fully automated measurement procedure. While at night calibration measurements were conducted automatically, at day (in this work at solar zenith angle below 97°) scattered sunlight measurements at predefined elevation angles were performed. Furthermore, all settings could be controlled via JScript, like e.g. the nominal temperature of the spectrograph-detector unit or the solar zenith angle at which it should be switched between night and day measurements. The solar zenith angle was calculated by DOASIS from the geographic position of the measurement and the universal time provided by the computer clock. The JScript routine also adapted the integration time of the measurement scans to the light conditions in order to achieve a constant signal level (i.e. constant signal maximum per exposure), to store the spectra and to control the pointing of the telescopes. In the measurement campaign in the north-east of the USA, the number of scans was set to be fixed to 1000 scans so that the total measurement period was adapted and hence changed according to the light conditions. In contrast, in the measurement campaign in Mexico City, the total measurement period was set to be fixed to 120 seconds. Consequently, the number of scans changed according to the light conditions.

In both campaigns several Mini-MAX-DOAS instruments with a wavelength range of about 290 to 420 nm and one of about 330 to 460 nm were used each. An optical filter UG5 which significantly reduces the light above 400 nm was used for the instruments with the wavelength range from 290 to 420 nm. This provides a better balance of the light intensities at different wavelengths and reduces spectrograph stray light. For the Mini-MAX-DOAS instrument which covered a wavelength range more to the visible, the UG5 filter would have diminished half of the spectrum. Thus,

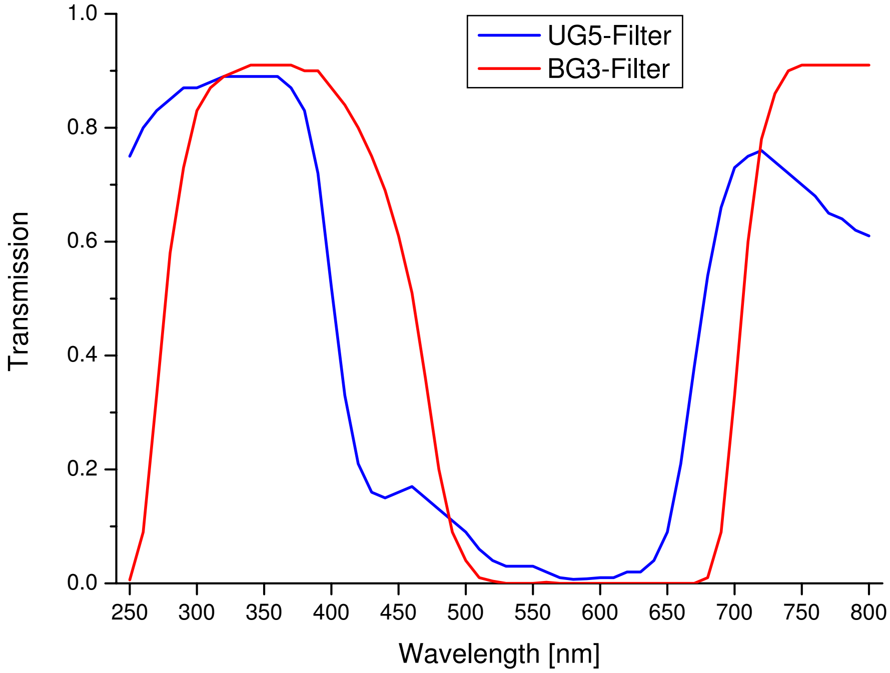

Figure 5.3: *Comparison of the transmission of UG5 and BG3 filter of 1 mm thickness each between 250 and 800 nm.*

in the measurement campaign in the north-east of the USA, no filter and in Mexico City a BG3 filter was applied. The BG3 filter cuts the light more to the visible. A comparison of the transmission of UG5 and BG3 of 1 mm thickness each is shown in Figure 5.3.

5.2 The Polarstern/Schwampel Instrument

The other kind of MAX-DOAS instrument which was used in both campaigns was the Polarstern and Schwampel instrument, respectively. The Polarstern instrument was designed for cruises of the German research vessel FS Polarstern. It features special requirements for the operation onboard a ship and consisted of two spectrograph-telescope systems in the first version. After it was used in the measurement campaign in the north-east of the USA, one of the two spectrograph-telescope systems was separated from the Polarstern instrument and became the Schwampel instrument. The Schwampel instrument was used in the measurement campaign in Mexico City.

During the measurement campaign in the north-east of the USA, the Polarstern instrument was installed on the research vessel RV Ron Brown (see section 7.2). The outdoor part of the instrument consisted of four (grey) telescope units which were arranged in parallel (see Figure 5.4). In each telescope unit, a stepper motor with

Figure 5.4: *Outdoor part of the Polarstern instrument. Setup on the RV Ron Brown during ICARTT 2004 measurement field campaign (see section 7.2). The Cardanic suspension is fixed with wires.*

Reed end switch enabled to adjust it individually to any elevation angle between horizon and zenith. Furthermore, some electronic devices for calibration and protection purposes were integrated: A halogen lamp whose spectrum delivers information on the pixel-to-pixel variability of the detector and a mercury-neon lamp whose line spectrum is used for the determination of the spectrograph's resolution as well as a rough wavelength-to-pixel mapping. A shutter at the entrance of each telescope prevented sunlight from entering the telescope when the shutter was closed. Thus, calibration measurements could not be affected by external light. Furthermore, the shutter closed in case the telescope pointed directly at the sun which was supposed to be detected by a photo diode at the front of the telescope unit. The strong light intensity of direct sunlight possibly would have damaged the detector or the fiber entrances (see below). Finally, a heating foil ensured that the temperature of the telescope unit keeps above the freezing point so that potential ice or hoarfrost could not affect the measurements. However, since the measurement campaigns were conducted in regions and at times at which the ambient temperatures were significantly above the freezing point, the heating of the telescope units actually did not play a role.

To prevent influences on the telescope viewing directions caused by rolling and pitching of the vessel, the telescope units were mounted on a Cardanic suspension which largely compensated for these movements. A weight of 30 kg at the bottom of the moveable suspension stabilized it. Directly underneath the weight, a nail board was attached which passes through a fixed conventional brush at every movement and provided enough friction so that the suspension could not oscillate after movement.

Each telescope unit contained a quartz lens with a focal length of 20 mm which focused the scattered sunlight. The light from one telescope was coupled into a fiber of 800 μm diameter which led it to an Ocean Optics USB2000 spectrograph-detector unit. The Ocean Optics USB2000 covered a wavelength range of 400 to 700 nm. It was placed in a heat insulating Dewar vessel where it was cooled by a two-stage peltier cooling. To prevent condensation of water vapor, the Dewar was evacuated and filled with argon gas with an overpressure of about half of the atmospheric pressure. The heat was removed by a fan on top of the Dewar.

The light from the other three telescopes was focused each on a quartz fiber bundle of seven fibers with 150 μm diameter. Filters reduced spectrograph stray light and balanced light at different wavelengths. While UG5 filters were used in the

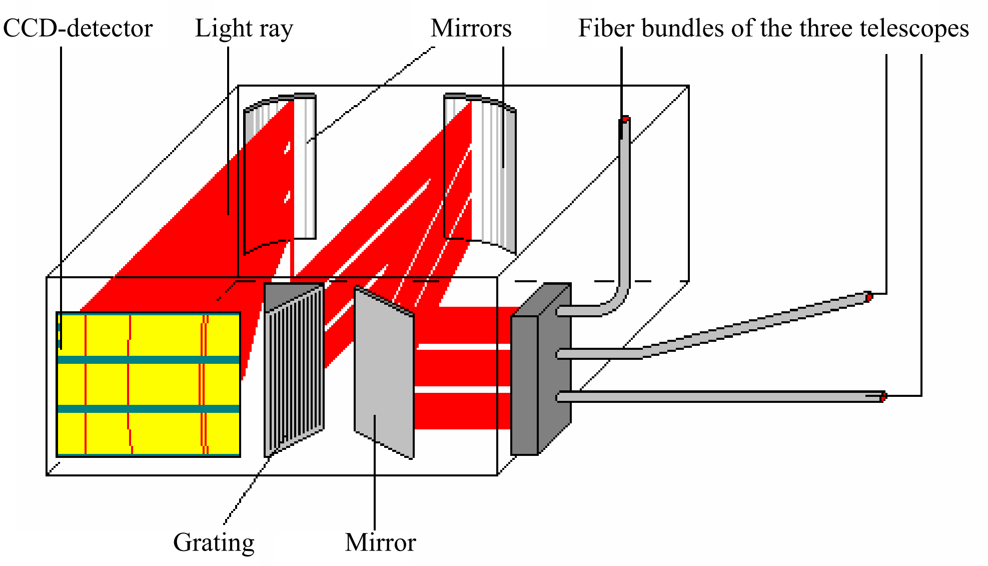

Figure 5.5: *Schematic illustration of the light paths from the fiber bundles of the three telescopes to the two-dimensional CCD detector of the Polarstern instrument.*

measurement campaign in the north-east of the USA, in the campaign in Mexico City BG3 filters were applied (see Figure 5.3). The fibers led the light to the spectrograph where they were all arranged linearly to form the entrance slit. This means that all the fibers of the three different telescopes were aligned one on top of each other. The spectrograph was a commercial instrument with 300 mm focal length (Acton model 300). It covered the wavelength range from approximately 325 to 460 nm and had a resolution of about 0.7 nm FWHM. As illustrated in Figure 5.5, the incoming light from the three telescopes was led to a grating via mirrors where it was dispersed spectrally. A second mirror focused the light onto a two-dimensional imaging CCD detector (Andor model DV420-OE) with 1024 horizontal and 256 vertical pixels. The horizontal pixels mapped the wavelength, while the vertical pixels corresponded to the vertical position in the entrance slit. Thus, the light of the different telescopes was measured simultaneously and the light of the fiber which, for instance, was placed in the middle of the slit was detected also in the vertical middle of the detector. Hence, the signals originating from the three telescopes reached the two-dimensional detector at well defined different areas which allowed them to be clearly separated afterwards. Figure 5.6 shows an example of a measurement. Three areas with measurement signal which are separated from each other by blue background correspond to the light of the three telescopes. Furthermore, each area exhibits lines which are several pixels thick and arise from the seven fibers. For the retrieval of trace gases, the two-dimensional image was converted into three one-dimensional spectra, corresponding to the three areas with measurement signal. Thereby, the

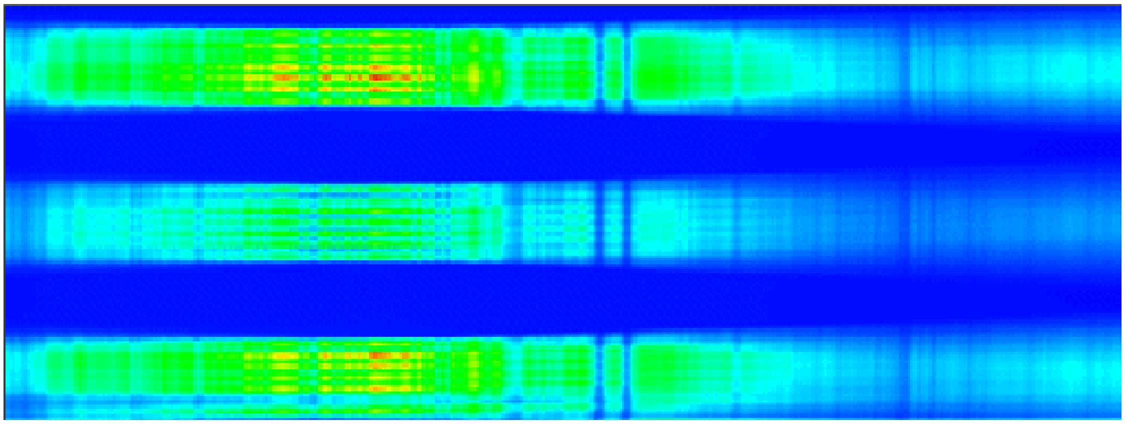

Figure 5.6: *Example of an image of the CCD chip with 256 horizontal lines and 1024 pixel. The light intensity is color coded. Red means high intensity which decreases over yellow and green to blue. The horizontal dimension corresponds to the wavelength (with two Fraunhofer lines in the middle at 393 and 397 nm). Vertically, the three areas with measurement signal can be seen which correspond to the light of the three telescopes. In between, blue background areas are located.*

lines of each area with measurement signal were added and saved in the binary MFC-format which is suitable for retrieval [Gomer et al., 1995].

While the spectrograph was heated to a stable temperature above +30° C in order to minimize changes in its optical properties, the CCD detector was cooled to -30° C in order to reduce detector dark current. The signal of the CCD detector was transferred to a PC via a specialized Andor PCI-board. The stepper motors of the telescopes were operated by Isel controllers which in turn, executed commands given by the PC. Furthermore, a special control unit enabled to individually switch on and off the different lamps of the telescopes as well as to open and close the different shutters. This was also possible via commands from the PC.

The Polarstern instrument was operated by a specialized measurement program [Frieß, 2001] which can deal with both spectrographs simultaneously. It managed the stepper motors in the way that the desired elevation angles of the three telescopes were different for each unit. Thus, each telescope always measured at a different elevation angle which improves the temporal resolution of the measurements. The

Figure 5.7: *Outdoor part of the Schwampel instrument setup in Mexico City during MILAGRO 2006 measurement field campaign (see section 8.2). The three telescopes point to different azimuth directions perpendicular to each other.*

measurement routine was set to acquire measurement spectra for solar zenith angles below 97°. However, between 90° and 97° SZA the elevation angle was fixed for each telescope. Below 90° SZA, the elevation angle sequence was conducted for each telescope. At solar zenith angles above 97°, the shutters closed automatically and spectra of dark current and offset (see section 5.3) as well as mercury-neon and halogen lamp spectra were acquired periodically. The SZA was also calculated by the measurement program using universal time provided by the computer clock and the geographical position. The geographical position was updated manually several times per day during the cruise on the RV Ron Brown. Later during the evaluation of the spectra, the exact geographical position was updated by retrieving the geographical position in log-files of the RV Ron Brown at the acquisition time of each spectrum.

After the measurement campaign in the USA, the Polarstern instrument was split into two instruments. The spectrograph with the two-dimensional CCD detector and the three telescopes were separated from the Polarstern instrument and have been called Schwampel device. Hence, the Polarstern instrument has only contained the Ocean Optics spectrograph with one telescope and the Cardanic suspension.

The three telescopes of the Schwampel instrument were not arranged in parallel. Rather they pointed at azimuth angles perpendicular to each other. Figure 5.7 shows the outdoor setup of the Mexico City measurement campaign. All components and properties have remained identically to the corresponding part of the Polarstern instrument apart from the differences detailed above. Also the same measurement software and routine was used for the Schwampel instrument in the campaign in Mexico City.

5.3 Corrections on the Spectra

The measured raw spectra need to be corrected for background signals prior to the DOAS analysis. This includes electronic offset, dark current and spectrograph stray light.

5.3.1 Electronic Offset

The electronic offset is an artificial electronic signal which is added to the measurement signal to avoid negative signals caused by electronic noise at low intensity level which cannot be handled by the analog-digital converter. In Figure 5.8 an example of an electronic offset of the USB2000 is plotted.

Since the offset signal can disturb the retrieval of trace gases it has to be subtracted from each scan. For correction, the offset spectrum can be acquired when the detector is not exposed to light. The integration time has to be chosen as short as

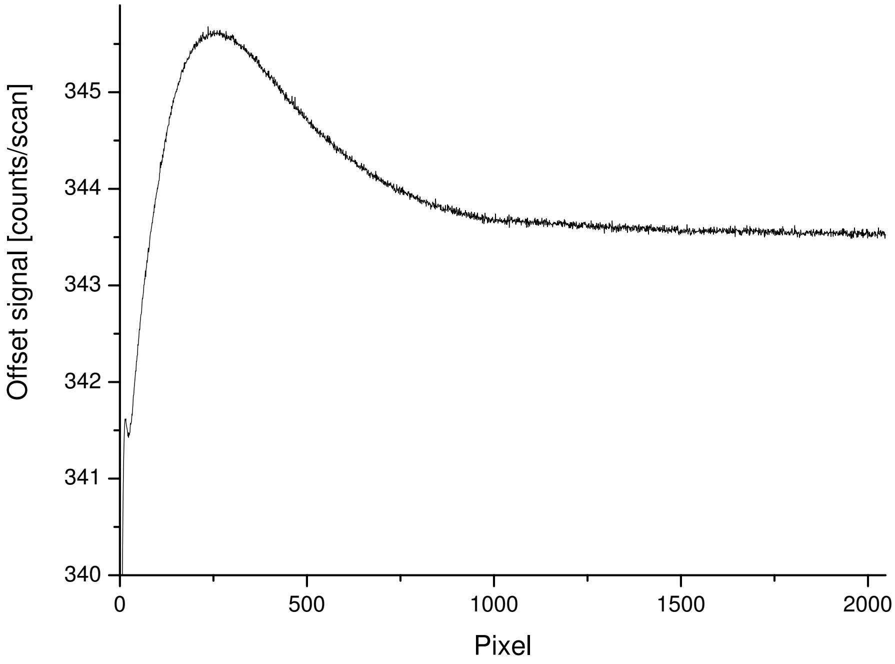

Figure 5.8: *Typical offset spectrum measured from an Ocean Optics USB2000. In this instance, the average counts per scan are 344±1.*

possible to avoid any other signal than the electronic offset. For statistical reasons, the electronic offset is usually measured by adding many scans. It is assumed that, except for detector noise, it does not change by time so that it can be subtracted from each spectrum. Thereby, the ratio of the number of scans of the measurement spectrum and of the offset spectrum have to be multiplied with the offset spectrum in order to match the offset signal in the measurement spectrum. It is noteworthy that the intensity of the electronic offset may change if the temperature varies. This was observed for the Ocean Optics USB2000 spectrometers whose offset signal increases with lower temperature.

5.3.2 Dark Current

Another signal which is overlaid to the measured spectra is the dark current. It arises due to self dischargement of the CCD detector. Thermally excited electrons contribute to the charge of the measurement signal so that the dark current spectrum is superimposed to the measurement signal. The dark current is proportional to the Boltzmann factor $e^{-\Delta E/kT}$. Since it increases exponentially with temperature it can be reduced significantly by cooling the detector. The dark current is acquired also in the absence of light. A single scan with an integration time as long as possible

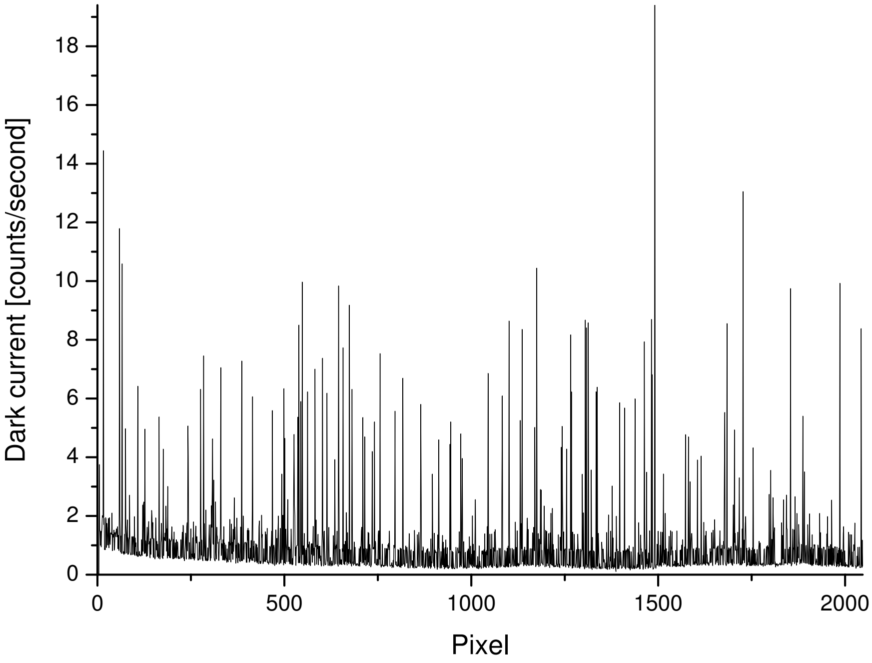

Figure 5.9: *Typical dark current spectrum measured from an Ocean Optics USB2000. In this instance, the spectrum features many peaks (hot pixels) and the average counts per second are 0.99±1.47.*

is taken and corrected for the offset signal. A typical dark current spectrum of the Ocean Optics USB200 at a temperature of 0° C is shown in Figure 5.9. In this example, the dark current spectrum features many peaks which probably occur due to errors in the endowment of the CCD detector array (hot pixels) so that the average counts per second are 0.99±1.47. Generally the average intensity of the dark current is relatively small and is typically less than 0.0001 for almost saturated spectra. Nevertheless, it may play a major role when the measured intensity is low or in case of strong peaks (e.g. the peak closely below pixel 1500 in Figure 5.3.2).

It is assumed that the dark current signal is proportional to the integration time of the measurement. Hence, the dark current signal can easily be corrected by subtracting the dark current spectrum weighted with the ratio of the integration times of the measured spectrum and the dark current spectrum. However, in reality, the proportionality is not fully correct because the dark current is slightly dependent on the saturation level of each CCD pixel [Stutz, 1991]. Nevertheless, the proportional correction accounts for the dark current approximately correct and was applied in this work.

5.3.3 Spectrograph Stray Light

Stray light in the spectrograph is light which has not traversed the destined path through the sprectrograph or is diffracted by the grating in higher order. Nevertheless it may reach the detector and lead to an additional measurement signal which can significantly disturb the original measurement signal. Like the electronic offset and dark current, it has to be accounted for. However, the correction is typically much more difficult because the intensity of stray light depends on the light intensity, also of wavelengths which are actually not measured. Since at any wavelength the intensity of the original spectrum is not known, the derivation of the stray light spectrum can hardly be accomplished. Yet in practice, to some extent, the stray light can be accounted for during the spectral analysis procedure by fitting an additional polynomial (see section 3.4.1). Nevertheless, it is of advantage to identify the stray light before analyzing the measurement spectra.

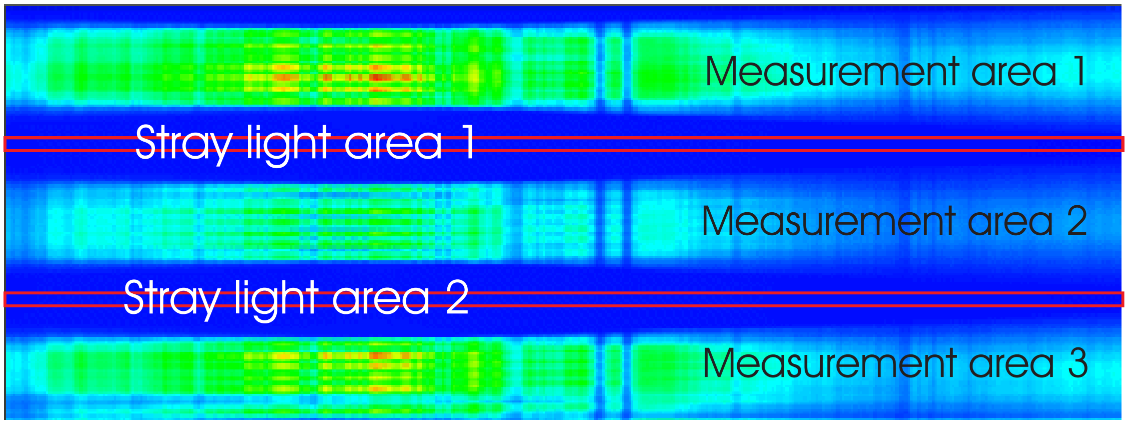

Figure 5.10: *Image of the CCD chip. The minimum areas on the CCD-chip of about ten lines are framed red. These areas feature relativ constant intensity and can be used to determine the spectrograph stray light.*

The Ocean Optics USB2000 miniature spectrographs have already been characterized elsewhere [e.g. Weidner, 2005; Weidner et al., 2005]. There it turned out that spectrograph stray light only plays a minor role and does not require a special correction. However, the two-dimensional CCD-chip of the Polarstern/Schwampel instrument detects the light of three telescopes simultaneously. This holds the risk that light from one line of the CCD-chip reaches another line owing to e.g. reflections in the spectrograph. This is apparent in the measured images, where elevated values occur also in the background areas. To further investigate the stray light, the minimum areas on the CCD-chip between the measurement areas were searched. A minimum base of about ten lines was identified in which the intensity is relatively constant, each in the middle between the measurement areas (see Figure

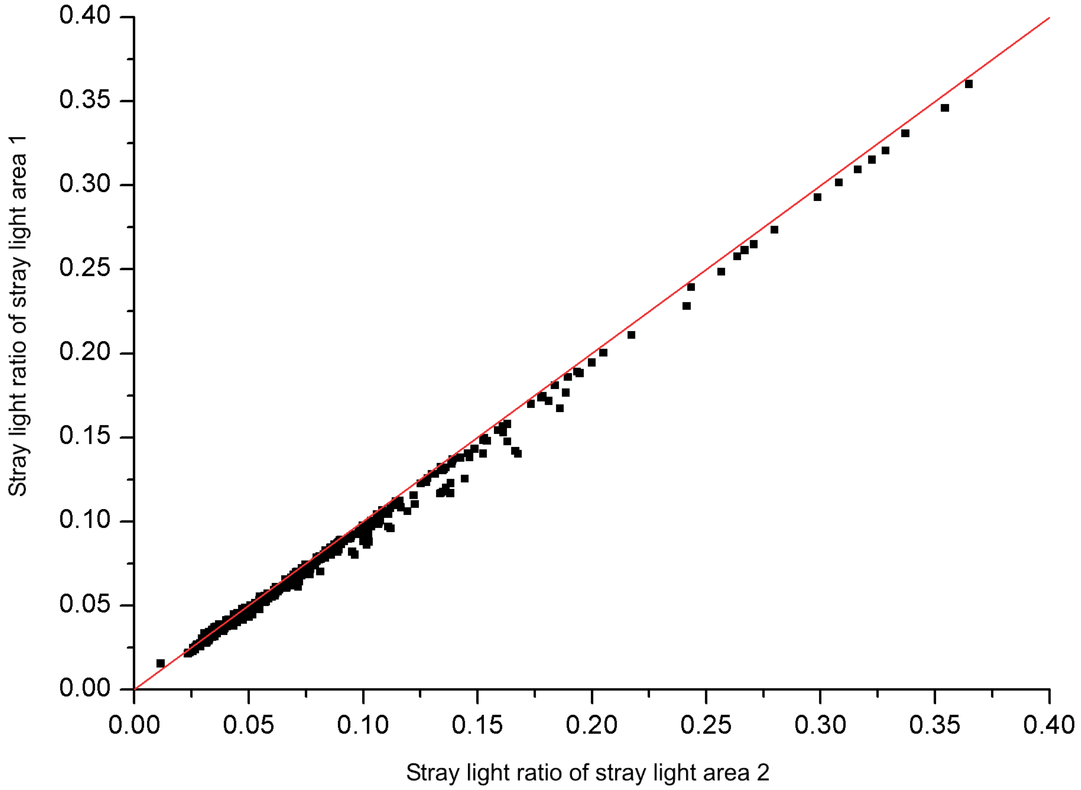

Figure 5.11: *Comparison of the ratios of the two stray light areas to the measurement signal during two days of measurement. In red, the one-to-one line is plotted.*

5.10). Based on that, it was concluded that besides offset and dark current, only spectrograph stray light could be found there. It turned out that stray light could amount to up to 40 % of the measurement signal. Typical values were between 3 and 15 %. Furthermore, the two stray light areas had approximately the same values (see Figure 5.11). Thus, spectrograph stray light can be assumed to be distributed homogeneously over the lines of the CCD detector. This allows to subtract the values of the stray light from the measurement areas, weighted with the number of lines each, which was done in this work.

6 Spectral Retrieval

6.1 General Procedure

The retrieval was supposed to deliver mainly ΔSCDs, hence the differential slant column densities with respect to a zenith spectrum at the same solar zenith angle. This leads not only largely to an elimination of the stratospheric contribution to the ΔSCD. It also cancels mostly influences of instrumental instabilities.

The ΔSCDs were derived from the recorded spectra by an analysis procedure using a combination of the software packages Doas Intelligent System (DOASIS) from Institute of Environmental Physics of the University of Heidelberg [Kraus, 2004] and Windoas [Fayt and van Roozendael, 2001] from IASB (Belgium Institute for Space Aeronomy). The Windoas software fitted several trace gas cross sections as well as the logarithm of a Fraunhofer reference spectrum (FRS), a Ring spectrum and a polynomial based on a non-linear least squares fitting algorithm to the logarithm of the measured spectrum. The Ring spectrum and the polynomial correct for Raman scattering as well as Rayleigh and aerosol scattering, respectively. Also, included in the fitting routine was an intensity offset to account for possible instrumental stray light. The measurement spectrum was allowed to shift and squeeze against the FRS, the Ring spectrum and the cross sections.

The retrieval was performed by starting JScript commands in DOASIS which also called the Windoas evaluation procedure for each measurement spectrum. The combination of DOASIS and Windoas was applied for several reasons:

- To retrieve ΔSCDs the Fraunhofer reference spectrum had to be changed from measurement sequence to measurement sequence. This option is not included in the Windoas software package. Thus, DOASIS updated the FRS if applicable before the next measurement analysis was conducted. Finally, the zenith spectrum from the previous measurement sequence was generally chosen. The Ring spectrum was calculated from the respective FRS for each sequence and thus changed from sequence to sequence, too. However, also retrievals with fixed FRS were possible which yielded dSCD.

- Since the wavelength-to-pixel mapping can change with time due to instrumental instabilities the calibration had to be performed newly for each FRS. Thus, the following procedure was applied using the DOASIS software: First, the wavelength calibration was performed for an arbitrary reference spectrum by fitting the Fraunhofer reference spectra to a high resolution Fraunhofer spectrum [Kurucz et al., 1984] convolved with a instrument's slit function. The slit functions were derived by emission lines of mercury. Then, the other zenith spectra were shifted to the calibrated spectrum. Thus, they all were on the same wavelength-to-pixel grid before the respective Ring spectra were calculated and the analyses of the measurement spectra were performed.

- DOASIS allowed to largely separate out oversaturated zenith spectra so that they were not used as FRS. The criterion for separation was the level of the maximum intensity per measurement scan which was chosen to allow not more than 93 %. This also considers that only some scans could be oversaturated which can not not be recognized in the spectrum with added scans.

The following absorption cross sections were used in the spectral retrievals:

- For NO_2 Vandaele et al. [1998] at 294 K.
- For ozone Bogumil et al. [2003] at 223 K and 243 K since the ozone cross section is very temperature dependent in the UV wavelength range.
- For HCHO Meller and Moortgat [2000].
- For SO_2 Vandaele et al. [1994].
- For CHOCHO CHOCHO Volkamer et al. [2005].
- For HONO Stutz et al. [2000].
- For O_4 Hermans et al. [1999], if not stated Greenblatt et al. [1990] (with manual adjustments of the wavelength axis [Andreas Richter, pers. comm.]) in the detailed descriptions. The O_4 cross section is given by the O_2-O_2 collision pair cross section and has the unit molec^2/cm^5 [Greenblatt et al., 1990].
- For BrO Wilmouth et al. [1999] at 228 K.

These cross sections were convolved with the instrumental slit function to match the spectral resolution of the instruments (except for the O_4 spectrum which was interpolated). The specific retrieval settings of the trace gases are described in the following sections.

6.2 Spectral Retrieval of NO_2

NO_2 was analyzed in the wavelength range from 368 to 390 nm including the cross sections NO_2, O_3 and O_4. These cross sections were convolved with the instrumental slit function determined by measuring the emission line of a mercury lamp at 405

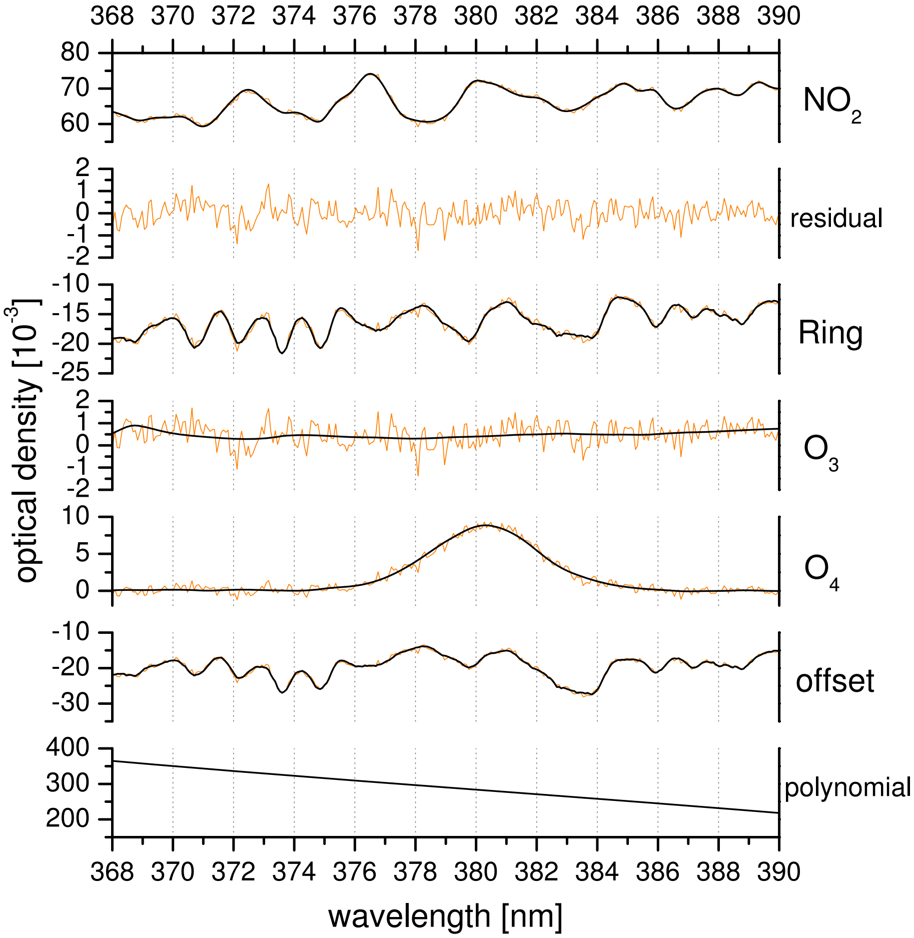

Figure 6.1: *NO$_2$ example retrieval of a spectrum taken at MIT on 26 July 2004, 11:14AM (local time) at 3° elevation angle. The optical densities (black) and the added residuals (orange) as a function of wavelength are plotted for the different scaled cross sections, the Ring spectrum, the intensity offset and the polynomial. In the second row, the residual is plotted.*

nm. Furthermore, the Ring spectrum, a polynomial of degree 3 and an intensity offset of degree 2 were fitted. An example retrieval is shown in Figure 6.1. The optical densities of the fitted components as a function of wavelength are shown in black, whereas the orange lines show the sum of the scaled cross sections and the residual. The measurement spectrum was taken at 3° elevation angle on 26 July 2004 11:14AM (local time) at MIT and delivered a NO$_2$ ΔSCD of 1.12×10^{17} molec/cm^2. The root mean square amounted to 5.29×10^{-4} which is two orders of magnitude smaller than the retrieved optical density of NO$_2$.

In context with CHOCHO (calculation of CHOCHO-to-NO_2 ratio), exceptionally NO_2 was retrieved from the analysis of CHOCHO which is also suitable for a NO_2 retrieval (see section 6.3).

6.3 Spectral Retrieval of CHOCHO

This spectral retrieval was the first time CHOCHO was detected by MAX-DOAS [Sinreich et al., 2007]. CHOCHO was analyzed in the spectral range from 420 to 460 nm (458 nm on the RV Ron Brown due to the restricted spectral range of the instrument), encompassing three main CHOCHO absorption bands. Besides the Ring spectrum, an intensity offset (polynomial of degree 1) and an polynomial of degree 5, the following cross sections were included in the retrieval: CHOCHO, NO_2, ozone at 223 K and O_4 ([Greenblatt et al., 1990] with manual adjustments of the wavelength axis [Andreas Richter, pers. comm.]). These cross sections were convolved with the instrumental slit function determined by measuring the emission line of a mercury lamp at 436 nm. In addition, a water vapor reference spectrum derived from own atmospheric measurements was used. This was done because the literature water vapor cross sections are still of poor quality, especially in the wavelength range used in the retrievals. The measured water vapor reference spectrum was derived from the ratio of two spectra [Solomon et al., 1989; Heintz, 1996; Wagner et al., 2000], one with high (at 3° elevation angle) and one with low water vapor absorption (at zenith direction). In order to minimize the potential interference with CHOCHO absorption we restricted our measured water vapor reference spectra to the wavelength range of the actual water vapor absorption (from 438.5 to 454 nm). For the MIT instrument, the morning of 17 July 2004, when the humidity was high, was selected. The same was done for the RV Ron Brown by using observations performed on 6 July 2004, also a day with water vapor amounts above average. The water vapor measurements were taken at about 7 am and 6 am, respectively, when the least amount of CHOCHO is expected to be present in the atmosphere. Since the water vapor reference spectra were derived by the instruments themselves, their specific optical properties are inherently leading to a better spectral retrieval with less systematic structures.

Typically, NO_2 is the dominant absorber in the retrieval and its absorption cross section shows characteristic structures. Thus, even small potential errors in the analysis of the NO_2 absorption (e.g. due to the temperature dependence of the cross section or due to an inaccurate wavelength calibration) might substantially affect the retrieved CHOCHO results. In this case, the CHOCHO-to-NO_2 ratio should provide an indication of a potential interference with NO_2. Since the CHOCHO-to-NO2 ratio showed a variable behavior for each elevation angle and for both sites (for 3° elevation angle see Figure 7.24) such an interference could be clearly excluded.

Several sensitivity studies were performed in order to quantify any systematic error

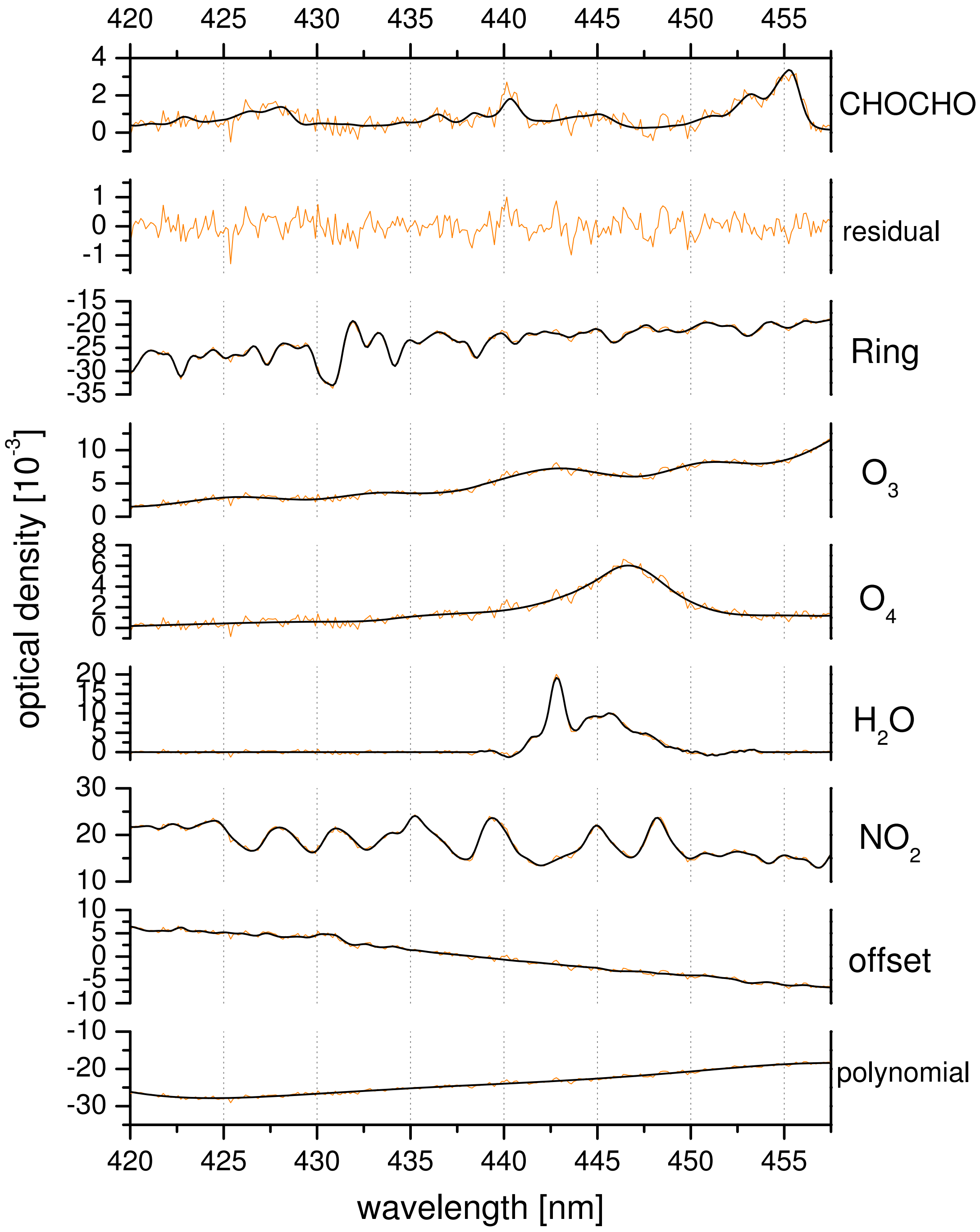

Figure 6.2: *CHOCHO example retrieval of a spectrum taken onboard the RV Ron Brown on 10 July 2004, 5:15PM (local time) at 3° elevation angle. The optical densities (black) and the added residuals (orange) as a function of wavelength are plotted for the different scaled cross sections, the Ring spectrum, the intensity offset and the polynomial. In the second row, the residual is plotted.*

in the CHOCHO retrieval. The wavelength range and the degree of the polynomial as well as of the intensity offset were varied. Furthermore, a water vapor cross section from literature [Rothman et al., 1998] instead of our measured water vapor reference spectrum was used. While the residual structures were significantly larger, the results for CHOCHO were almost the same as for the original settings. This indicates that the retrieved water vapor reference indeed does not contain significant absorption structures of CHOCHO. Finally, for the measurements at MIT we also a measured NO_2 reference spectrum was used instead of the cross section taken from literature (for the RV Ron Brown no measured NO_2 spectrum was available). It was measured in the early afternoon of 12 July 2004, a slightly hazy, but sunny day with constant lighting conditions, from two zenith spectra one with and one without a NO_2 cell in the field of view. For the described sensitivity studies the results for CHOCHO were robust within 15 %.

An example for the retrieval of CHOCHO from the instrument onboard the RV Ron Brown is shown in Figure 6.2. The spectrum was taken under sunny conditions on 10 July 2004, at about 5:15PM (local time) at an elevation angle of 3°. At this time, the vessel was cruising along the coast of Massachusetts (42.09 N, 70.59 W) with wind from westward directions. The optical densities of the fitted components as a function of wavelength are shown in black, whereas the orange lines show the sum of the scaled cross sections and the residual. The root mean square variation of the residual in this evaluation is 0.34×10^{-3} which is less than one tenth of the retrieved optical density of CHOCHO (approx. 3.5×10^{-3}) and therefore is clearly low enough to allow an unambiguous detection of CHOCHO [Stutz and Platt, 1996]. The corresponding ΔSCD amounts to 6.74×10^{15} molec/cm^2 at a 1 σ error of 3.00×10^{14}. The ΔSCDs of NO_2, water vapor, O_4 and O_3 are also clearly identified.

6.4 Spectral Retrieval of HCHO

HCHO was analyzed in the wavelength range from 337 to 357.5 nm including the cross sections HCHO, NO_2, O_3 for 223 K as well as 243 K, BrO and O_4. These cross sections were convolved with the instrumental slit function determined by measuring the emission line of a mercury lamp at 405 nm. Furthermore, the Ring spectrum, a polynomial of degree 3 and an intensity offset of degree 1 were fitted. An example retrieval is shown in Figure 6.3. The optical densities of the fitted components as a function of wavelength are shown in black, whereas the orange lines show the sum of the scaled cross sections and the residual. The two cross sections of ozone were added in the figure. The measurement spectrum was taken at 3° elevation angle on 3 August 2004 12:35PM (local time) at Pinnacle State Park and delivered a HCHO ΔSCD of 4.47×10^{16} molec/cm^2. The root mean square amounted to 3.52×10^{-4} which is significantly smaller than the retrieved optical density of HCHO.

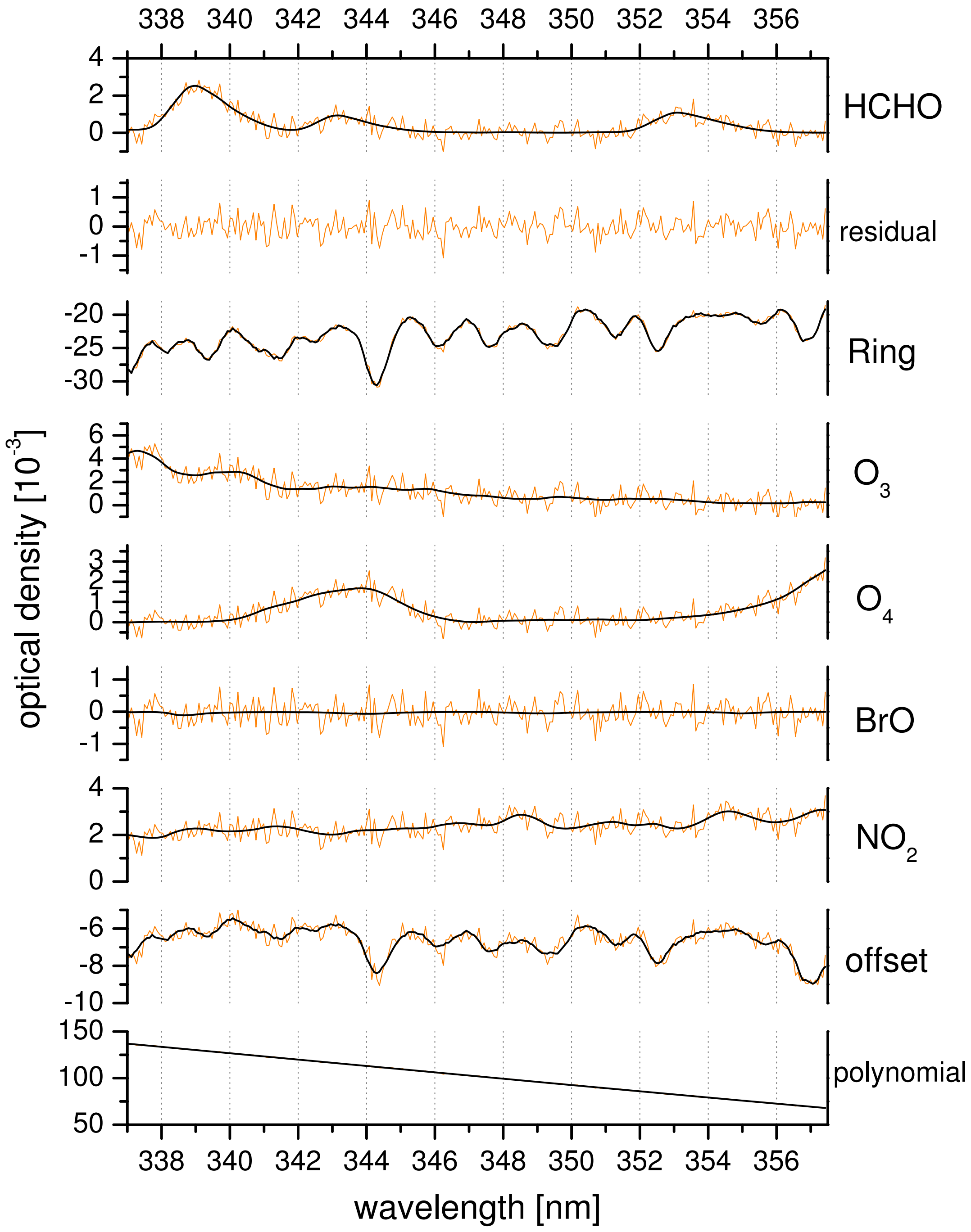

Figure 6.3: *HCHO example retrieval of a spectrum taken at Pinnacle State Park on 3 August 2004, 12:35PM (local time) at 3° elevation angle. The optical densities (black) and the added residuals (orange) as a function of wavelength are plotted for the different scaled cross sections, the Ring spectrum, the intensity offset and the polynomial. In the second row, the residual is plotted.*

6.5 Spectral Retrieval of HONO

Also the first MAX-DOAS measurements of HONO are described in this thesis. In the analysis the cross sections of HONO, NO_2, ozone at 223 K as well as 243 K, O_4, BrO and HCHO were included. They were convolved with the instrumental slit function determined by measuring the emission line of a mercury lamp at 405 nm. Furthermore, the Ring spectrum, a polynomial of degree 5 an intensity offset (polynomial of degree 2) were fitted. The spectral range from 340 to 390 nm was chosen encompassing four strong HONO absorption bands, which minimizes any interference with the HCHO absorption structure.

Since HONO is formed by NO_2 and H_2O heterogeneously, NO_2 cross sections might generally be suspected to be contaminated with HONO absorption structures. This would lead to a significant underestimation of the retrieved HONO values. Therefore, the used NO_2 cross section Vandaele et al. [1998] was examined in terms of a HONO content by fitting it to an assumed HONO free NO_2 cross section and the HONO cross section [Stutz et al., 2000] in the spectral range from 340 to 390 nm. This procedure has already been performed concerning HONO and is described in detail in Veitel et al. [2002]. Voigt et al. [2002] and Schneider et al. [1987] were used as (HONO free) reference NO_2 cross sections. Voigt et al. [2002] was checked in Veitel et al. [2002] and was concluded to be free of HONO. In Kleffmann et al. [2006], the HONO retrievals by DOAS and by long path absorption photometer (LOPAP) were compared and showed good agreement (less than 1.5 % difference). Since Schneider et al. [1987] was used in this DOAS retrieval it can therefore also be regarded as free of HONO. The fitting resulted in 0.4 % less HONO content in Vandaele et al. [1998] each than in the reference NO_2 cross sections. While the fit of Voigt et al. [2002] was significant enough the fit of Schneider et al. [1987] was too noisy to derive an unambiguous value of the HONO content. Anyhow it can be concluded, that Vandaele et al. [1998] does not show absorption structures of HONO and that therefore it does not adulterate the HONO retrieval.

An example fit of HONO is shown in Figure 6.4. The according spectrum was taken on 31 March 2006 at about 7:06AM (local time) at an elevation angle of 1° in Mexico City (T0) pointing into southern direction. The optical density of HONO as a function of wavelength is shown in black, whereas the orange line shows the sum of the scaled cross-section and the residual. The two cross sections of ozone were added in the figure. The root mean square variation of the residual in this evaluation is 0.93×10^{-3} which is less than one tenth of the retrieved optical density of HONO (approximately 1×10^{-2}) and therefore is clearly low enough to allow an unequivocal detection of HONO [Stutz and Platt, 1996]. The corresponding ΔSCD amounts to 2.42×10^{16} molec/cm^2 at a 1 σ error of 6.65×10^{14} While the root mean square of the HONO retrieval can reach values of 3×10^{-3} in the very morning and evening for the lowest elevation angle, it is typically below 8×10^{-4} from 9AM in the morning and ranges between 2×10^{-4} and 5×10^{-4} around midday. Since

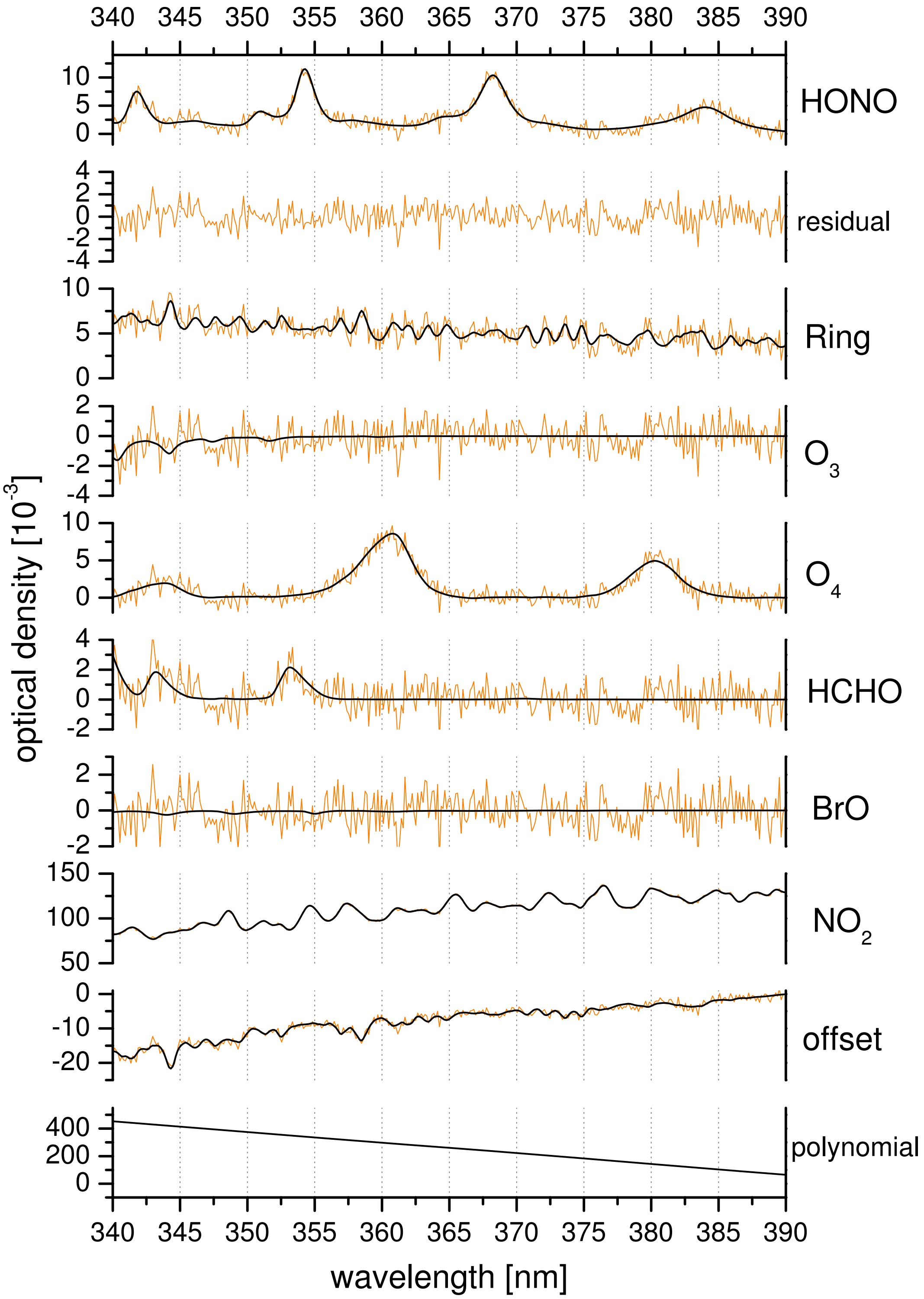

Figure 6.4: *HONO example retrieval of a spectrum taken in Mexico City (T0) pointing into southern direction on 31 March 2006, 7:06AM (local time) at 1° elevation angle. The optical densities (black) and the added residuals (orange) as a function of wavelength are plotted for the different scaled cross sections, the Ring spectrum, the intensity offset and the polynomial. In the second row, the residual is plotted.*

the usual HONO optical density in the afternoon, when the lowest concentration is expected, has values around 1 × 10^{-3} it can be concluded that HONO could be measured unambiguously all over the day.

6.6 Spectral Retrieval of SO_2

SO_2 was analyzed in the wavelength range from 303.5 to 317 nm including the cross sections SO_2, NO_2, O_3 for 223 K as well as 243 K, HCHO and BrO. These cross sections were convolved with the instrumental slit function determined by measuring the emission line of a mercury lamp at 334 nm. Furthermore, the Ring spectrum, a polynomial of degree 3 and an intensity offset of degree 1 were fitted. An example retrieval is shown in Figure 6.5. The optical densities of the fitted components as a function of wavelength are shown in black, whereas the orange lines show the sum of the scaled cross sections and the residual. The two cross sections of ozone were added in the figure. The measurement spectrum was taken at 3° elevation angle on 26 July 2004 12:08PM (local time) at Thompson Farm and delivered a SO_2 ΔSCD of 2.15×10^{17} molec/cm^2. The root mean square amounted to 2.00×10^{-3} which is two orders of magnitude smaller than the retrieved optical density of SO_2. However, the influence of ozone absorption is very strong in this wavelength range and might have adulterated slightly the SO_2 values. Variations in the wavelength range resulted in deviations of up to 20 %. Also, the low light intensity affected the retrieval. Quite often the fit did not converge, especially in the morning and evening.

6.7 Spectral Retrieval of O_4

O_4 was analyzed in the wavelength range from 338.5 to 367 nm including the cross sections O_4, NO_2, O_3 for 223 K as well as 243 K, HCHO and BrO. These cross sections were convolved with the instrumental slit function determined by measuring the emission line of a mercury lamp at 405 nm. Furthermore, the Ring spectrum, a polynomial of degree 3 and an intensity offset of degree 2 were fitted. An example retrieval is shown in Figure 6.6. The optical densities of the fitted components as a function of wavelength are shown in black, whereas the orange lines show the sum of the scaled cross sections and the residual. The two cross sections of ozone were added in the figure. The measurement spectrum was taken at 3° elevation angle on 11 July 2004 12:25PM (local time) at Narragansett and delivered a O_4 ΔSCD of 2.46×10^{43} $molec^2/cm^5$. The root mean square amounted to 3.87×10^{-4} which is more than one order of magnitude smaller than the retrieved optical density of O_4.

The O_4 cross section of Hermans et al. [1999] was used except for spectra acquired at MIT and on RV Ron Brown where the O_4 cross section from Greenblatt et al. [1990] (with manual adjustments of the wavelength axis [Andreas Richter,

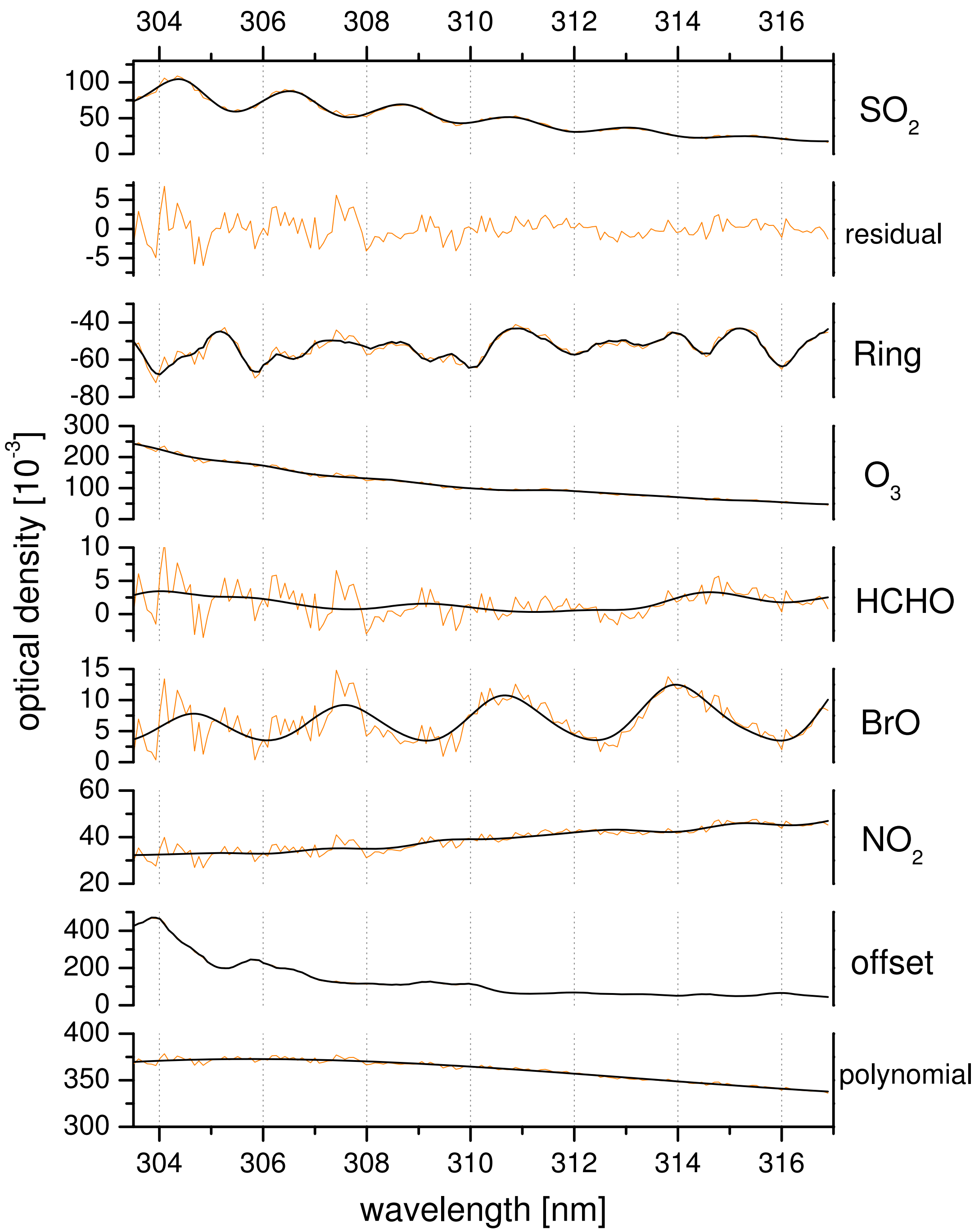

Figure 6.5: *SO_2 example retrieval of a spectrum taken at Thompson Farm on 26 July 2004, 12:07PM (local time) at 3° elevation angle. The optical densities (black) and the added residuals (orange) as a function of wavelength are plotted for the different scaled cross sections, the Ring spectrum, the intensity offset and the polynomial. In the second row, the residual is plotted.*

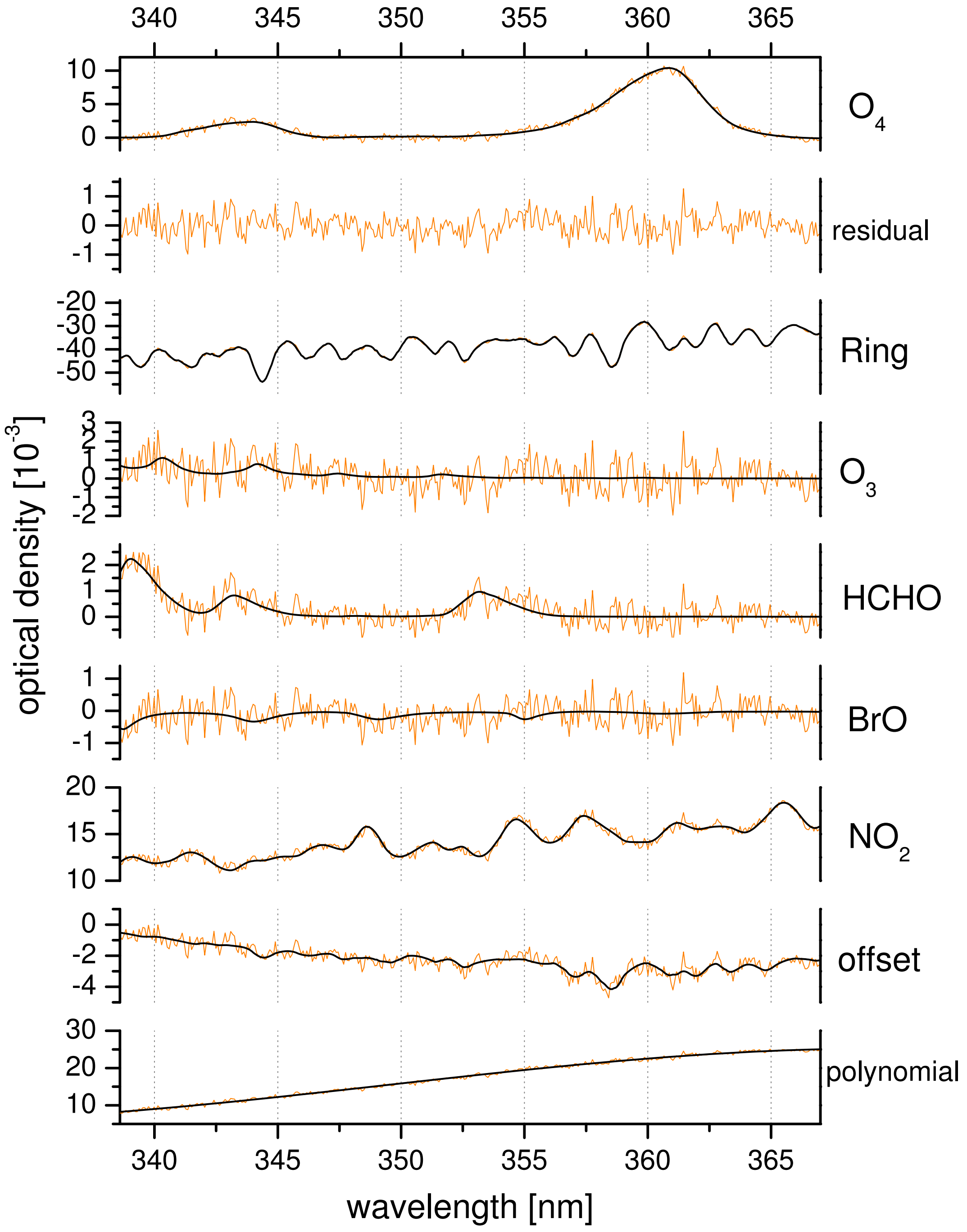

Figure 6.6: *O_4 example retrieval of a spectrum taken at Narragansett on 11 July 2004, 12:25PM (local time) at 3° elevation angle. The optical densities (black) and the added residuals (orange) as a function of wavelength are plotted for the different scaled cross sections, the Ring spectrum, the intensity offset and the polynomial. In the second row, the residual is plotted.*

pers. comm.]) was fitted. However, sensitivity studies did not show any significant difference between these two cross sections.

6.8 Error Estimation

Different error sources contribute to the total measurement error. They can be divided in the statistical error which determines the detection limit of the spectral retrieval and potential systematic error sources.

The statistical error is composed by photon and instrumental noise. The photon noise is Poisson distributed and proportional to the square root of the detected photons. Thus, the signal-to-noise ratio decreases with more light intensity. The instrumental noise is given by the detector and is determined by noise of the dark current and electronic offset. At measurements during daylight, the photon noise typically dominates the statistical error. The 1 σ error is calculated by Windoas for each fit and reflects its quality. The 2 σ error gives the detection limit of the retrieval [Stutz and Platt, 1996].

The retrieval errors stated in this thesis refer to the statistical errors. Additionally, several sources of systematic errors can be determined:

- In case not all absorbers being relevant in the fit wavelength range were considered the absorption signal of this absorber can be attributed to other absorbers in this wavelength range or to the residual as systematic structures. Both increases the uncertainty of the retrieval.

- The absolute values of the trace gas cross sections are often not correctly determined. This uncertainty is reproduced in the retrieval of the slant column densities. The respective error is typically in the order of 5 %, but also can reach higher percentages.

- The trace gas cross sections are temperature dependent. Thus, they are determined for a specific temperature. However, trace gases in the atmosphere not only occur at this ambient temperature but are often present over a wide temperature range. This error depends on the strength of the temperature dependency of the trace gas.

- If the wavelength-to-pixel mapping of the measurement spectrum is not consistent with the calibrations of the cross sections and the reference spectrum an additional systematic error can occur.

- Correlations between trace gases, such as SO_2 and ozone in the UV wavelength range, could lead to over- or underestimated values. The dimension of this error depends on the strength of the correlation.

- Instrumental shortcomings, such as spectrograph stray light and non-linearity of the detector signal, are also potential sources for systematic errors.

The overall error of the retrievals is estimated to be in the order of 10-15 % owing to findings from sensitivity studies. For the retrieval of SO_2 and HCHO, the error is assumed to be up to 20 % due to the correlation of SO_2 with ozone and the uncertainty in the absolute calibration of the HCHO cross section (see Volkamer et al. [2005]).

7 Results from ICARTT 2004 Field Measurements

7.1 Objectives of the ICARTT 2004 Campaign

The International Consortium for Atmospheric Research on Transport and Transformation (ICARTT) was formed to study the sources, sinks, chemical transformations and transport of ozone, aerosols and their precursors to and over the North Atlantic Ocean. The ICARTT 2004 field campaign builds upon previous studies, such as the 2002 New England Air Quality Study (NEAQS 2002) and includes several projects: New England Air Quality Study - Intercontinental Transport and Chemical Transformation (NEAQS-ITCT) 2004, Intercontinental Chemical Transport Experiment - North America (INTEX-NA), CO_2 Budget and Rectification Airborne study (COBRA), Meteorological Service of Canada (MSC), Intercontinental Transport of Pollution (ITOP), University of New Hampshire - AIRMAP, Harvard Forest, Harvard University University of Massachusetts Robotic Aerostat Research Lab (RARL), Atmospheric Sciences Research Center (ASRC), U.S. Department of Energy (DoE) Atmospheric Chemistry Program, and California Institute of Technology (Caltech). Furthermore, about 100 institutions from North America and Europe took part in the ICARTT 2004 field campaign.

ICARTT connected regional surface air quality with the important features of transport and chemistry that occur higher up in the atmosphere. During the ICARTT 2004 field study, a comprehensive network of ground-based sites and the NOAA research vessel Ronald H. Brown (RV Ron Brown) were operated in the region. Ground-based sites provided a continuous record of regional surface air quality over the continent and the vessel snapshots of polluted air leaving North America. For instance, Figure 7.1 shows the total NO_x emissions over North America from 1999, provided by the National Environmental Satellite, Data, and Information Service (NESDIS), which typically are leaving the continent towards East.

A major activity during ICARTT 2004 was a coordinated measurement effort of the polluted air mass as it moves from America to Europe. Aircrafts were operated over both continents to collect horizontal extension and vertical information about the meteorology and composition of the atmosphere. Furthermore, satellite data was integrated into the study both for aircraft flight planning purposes and for post-campaign validation. This information was supposed to be used in evaluating and improving air-quality models and model forecasts.

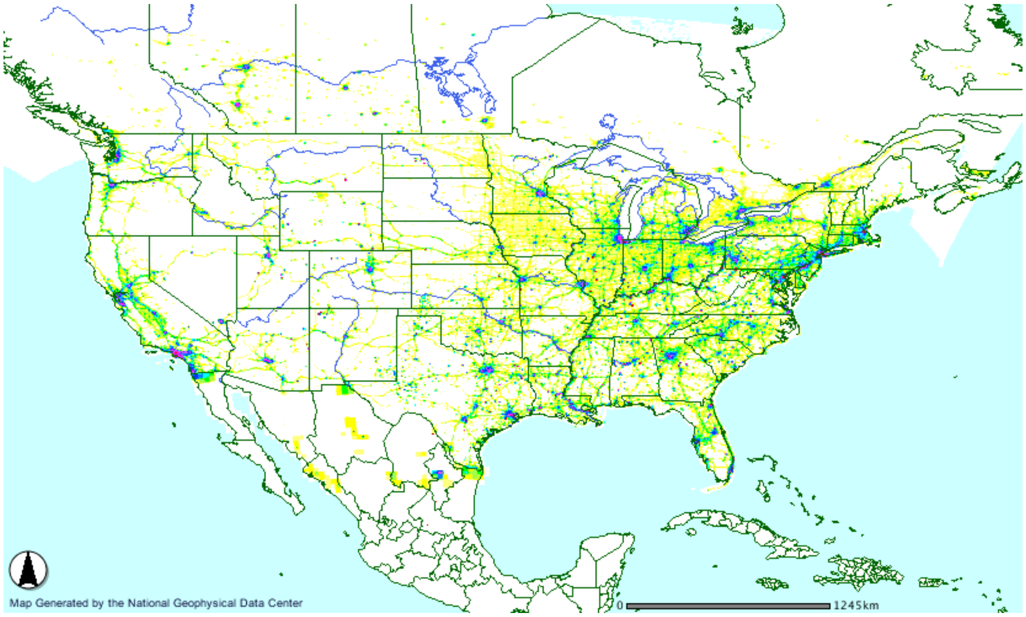

Figure 7.1: *Total NO_x emissions over North America from 1999, provided by the National Environmental Satellite, Data, and Information Service (NESDIS). The emissions are color-coded signifying higher values from yellow over green and blue to purple. The most emissions can be seen in the north-east of the USA.*

The aim of the ICARTT 2004 field campaign was to understand the impact of anthropogenic and natural emissions on regional and global climate, air quality, and human health. Over 100 international institutions took part on ICARTT 2004 which took place from 1 July through 15 August 2004. More detailed information on the ICARTT activities can be found at http://www.esrl.noaa.gov/csd/ICARTT/index.shtml.

To complement the various measurement activities during ICARTT, the University of Heidelberg provided several MAX-DOAS instruments at different locations. From MAX-DOAS measurements, information on the total column density of several trace gases can be derived. Such information is especially important for the quantification of total fluxes and budgets of pollutants. The MAX-DOAS instruments were installed at locations inside and outside regions of major emission sources. MAX-DOAS observations also provide (limited) information on the vertical profile of trace gas concentrations and aerosol properties.

7.2 Measurement Sites

In the framework of NEAQS-ITCT and AIRMAP (the air quality and climate program of the University of New Hampshire), seven MAX-DOAS devices were set up by the University of Heidelberg during ICARTT 2004. The different sites are illus-

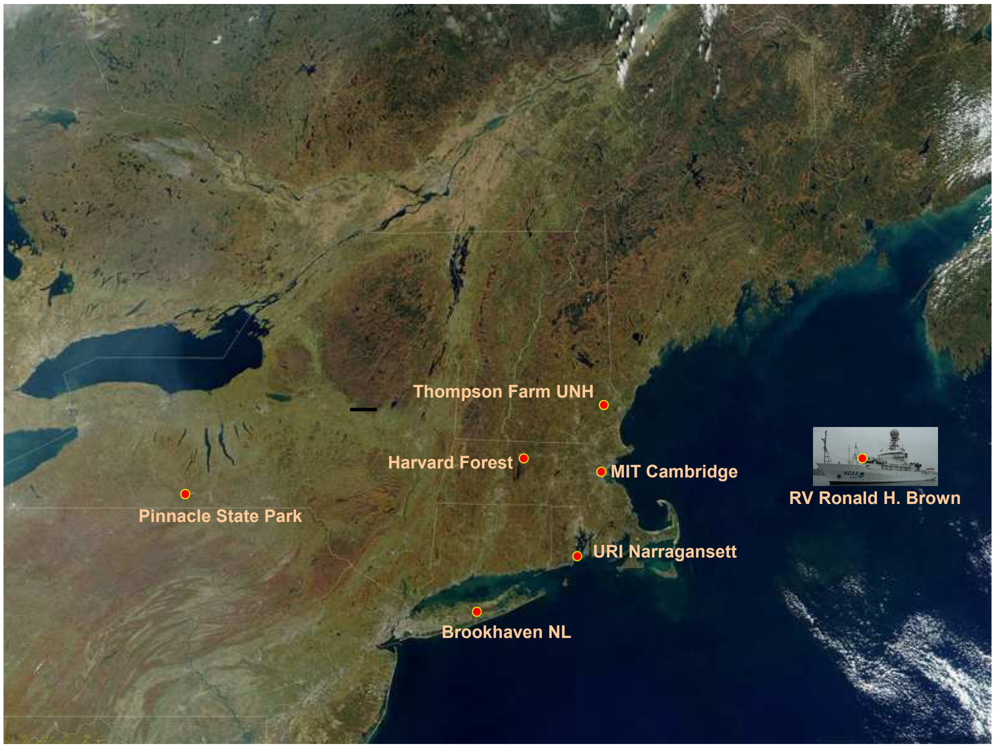

Figure 7.2: *MAX-DOAS sites set up by the University of Heidelberg during ICARTT 2004 marked on a satellite picture of the north-east of the USA. MAX-DOAS instruments were installed on the mainland at the Brookhaven National Laboratory, at the University of Rhode Island in Narragansett, at the Massachusetts Institute of Technology in Cambridge, at Thompson Farm of the University of New Hampshire near Durham (NH), at Harvard Forest near Athol (MA), and at Pinnacle State Park near Addison (NY), and on the research vessel Ron H. Brown cruising in the Gulf of Maine.*

trated in Figure 7.2. For all instruments, elevation angles of 3°, 6°, 10°, 18°, and 90° were chosen.

The Polarstern instrument was installed on the RV Ron Brown which is a 83.5 m long research vessel operated by the National Oceanic and Atmospheric Administration (NOAA). The RV Ron Brown has a cruising speed of 12 kts with maximum speed of 15 kts. It accomodates 25 persons staff of the vessel and up to 34 persons scientific staff. The outdoor part of the Polarstern instrument including the Cardanic suspension was fixed with wires on a trailer pointing starboard (see Figure 5.4). The chimney of the vessel was located behind the instrument with respect to the cruising direction. Thus, influences from exhaust emissions of the vessel itself on the measurements were avoided as good as possible. The indoor part of the instrument was set up in the trailer screwed to the bottom so that rolling and pitching of

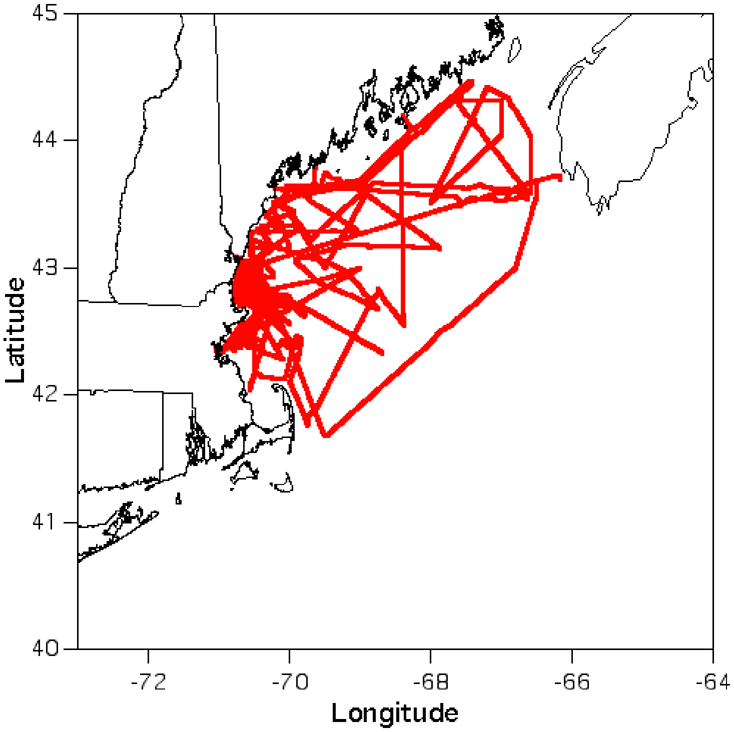

Figure 7.3: *Cruise track of the RV Ron Brown during ICARTT 2004. The cruise took place from 5 July through 12 August 2004 [National Oceanic and Atmospheric Administration (NOAA), adopted from http://www.esrl.noaa.gov/csd/tropchem/2004NEAQSITCT/RHB/index.html.*

the vessel could not move it.

The RV Ron Brown cruised in the Gulf of Maine often near the coast investigating the outflow of pollution from North America. The cruise track, which is plotted in Figure 7.3, took place from 5 July through 12 August 2004 though the MAX-DOAS measurements already started on 2 July 2004 in the harbor of Portsmouth (NH) for the first days. The cruise is divided in two legs (5 through 23 July and 26 July through 12 August) with start and end point at Portsmouth (NH). Unfortunately, on about one third of the cruise drizzle, fog or thick and deep clouds occurred (on 8, 9, 13, 14, 15 morning, 18, 19, 20, 22 morning and 27 July as well as on 3 and 4 August) so that MAX-DOAS measurements on these days are difficult to interpret.

The other MAX-DOAS devices are Mini-MAX-DOAS instruments which all were installed on the mainland (see Figure 7.2). They were spread over the New England states in order to investigate the pollution inventories, which were emitted at the corresponding measurement sites or transported there. It should be noted that the main wind direction is from west to east. Thus, part of the MAX-DOAS instruments were expected to observe rather clean air masses (in the west) while others (in the east) were assumed to measure more polluted air. It is noteworthy to mention that individual sources, such as cities and power plants, of course, affect the amount of pollution.

The Mini-MAX-DOAS instruments were set up at the Brookhaven National Laboratory on Long Island (NY), the University of Rhode Island in Narragansett (RI), the Massachusetts Institute of Technology in Cambridge (MA), Thompson Farm of the University of New Hampshire near Durham (NH), at Harvard Forest (near Athol, MA) provided by the Harvard University in Cambridge (MA), and at Pinnacle State Park (near Addison, NY) provided by the University at Albany (NY). In the following, a brief overview on the specific properties of the instruments at the different sites is given.

The measurement site at the Brookhaven National Laboratory (Brookhaven NL) was located on Long Island at 40.87° N and 72.88° W. The Mini-MAX-DOAS device was mounted on a tripod which was stabilized with stones on the roof of a former institute for nuclear physics, building 703 (see Figure 5.1). It had a free view towards north. This site was chosen to measure the near-field outflow of the New York City plume when the wind was coming from the west. Unfortunately, during the evaluation of the spectra it turned out that only relatively noisy results could be retrieved. After the measurement campaign, the spectrograph-detector unit was heated and this noise disappeared. Thus, it is assumed that humididty penetrated into the spectrograph and negatively affected the light throughput. In a measurement campaign directly before the setup at Brookhaven, this problem was not recognized and the instrument ran well. Since the instrument was affected from the beginning, the humidity probably could have been intruded into the instrument during the transportation or the clearing. Possibly, the transport security agency or the customs opened the device.

At the University of Rhode Island in Narragansett (URI Narragansett), at 41.49° N, 71.42° W, the Mini-MAX-DOAS was also placed on a tripod. It was located on the roof of the building of the Graduate School of Oceanography (GSO). The tripod was screwed on the roof (see Figure 7.4) and the Mini-MAX-DOAS instrument was pointing at approximately eastern direction (about 100° from north), viewing over the sea. This more rural site was supposed to provide information on the far-field outflow of the New York City plume.

The measurement site in Cambridge is further north than URI Narragansett and is affected by metropolitan pollution. The Mini-MAX-DOAS instrument was fixed on a handrail on one of the buildings (Building 54, the so-called Green Building) of the Massachusetts Institute of Technology (MIT) at 42.36° N and 71.09° W. The instrument was pointing to the north.

Thompson Farm (43.11° N and 70.95° W) is a field observation station north of Boston surrounded by some forest and operated by the University of New Hampshire. At this site, a Mini-MAX-DOAS instrument was fixed on the top of a metal scaffolding tower of about 10 m (see Figure 7.4) pointing to southeast (about 145°

Figure 7.4: *Setups of the Mini-MAX-DOAS instruments at Narragansett (left) where the tripod was screwed on a roof and at Thompson Farm (right) fixed on the top of a metal scaffolding tower.*

from north) with free view over trees. This site was chosen to measure the outflow from Boston.

The measurement site in Harvard Forest was located near Athol (MA) in the middle of a large forestal area and was situated further away from the coast at 42.54° N and 72.17° W. It was supposed to deliver information on the inflow to Boston. The site was also equipped with a metal scaffolding tower. Since the tower reached a height of about 30 m, the top enabled a free view over the tops of the trees at a height of about 287 m above sea level. The Mini-MAX-DOAS was mounted on a small tripod which was strapped thoroughly at a staff of the tower. The viewing direction of the Mini-MAX-DOAS device was aligned to the east (about 100° from north). Unfortunately, heavy rain at the beginning of the campaign and a leaky housing led to the intrusion of water into the instrument. This caused a momentous short circuit in the electronic board which had to be replaced afterwards. Since the board had to be shipped from Germany the replacement required almost two weeks. Afterwards, the Mini-MAX-DOAS instrument acquired spectra for more than two weeks. However, the evaluation of the spectra yielded only very noisy results without any significance. Since after the campaign, the heating of the spectrograph-detector unit let disappear this strong noise it is assumed that humidity also intruded into the spectrograph as at the Brookhaven site.

The sixth site on the mainland was located farthest in the west, at Pinnacle State Park (near Addison, NY), at 42.09° N, 77.21° W in the west of the state New York. It was chosen to measure the inflow into the New England states. The Mini-MAX-DOAS instrument again was fixed on a tripod which was located on the roof of a measurement trailer of the University at Albany. The tripod was strapped on a railing of the trailer. The measurements took place in south-east direction at about 120° from north.

The measurement periods of the Mini-MAX-DOAS instruments and the days at which the measurement broke down for different reasons are listed in Table 7.1.

Table 7.1: *Measurement periods of the Mini-MAX-Doas instruments during ICARTT 2004.*

Measurement site	Measurement period	Days of breakdown
Brookhaven NL	9.7.-17.8.2004	23.7.-25.7.
URI Narragansett	10.7.-17.8.2004	23.7., 24.7., 4.8.
MIT Cambridge	8.7.-18.8.2004	29.7.
Thompson Farm	14.7.-16.8.2004	17.7., 21.7., 23.7.
Harvard Forest	(26.7.-10.8.2004)	5.8.
Pinnacle State Park	16.7.-12.8.2004	20.7.-23.7., 30.7.-2.8.

All Mini-MAX-DOAS instruments covered a wavelength range from about 290 to 420 nm except for the Mini-MAX-DOAS instrument set up at MIT which had a wavelength range from 330 to 460 nm (like the Polarstern instrument). Thus, NO_2, HCHO and SO_2 could be measured. At MIT, the spectrometer contained the spectral range of CHOCHO absorption structures instead of SO_2. The highlights of these measurements are discussed in the following sections whereby the whole data set is attached in Appendix A.1. One focus is on the comparison of the measured trace gas amounts at the different sites. A second focus is on the identification of various emission sources using trajectory analyses. Thus, backward trajectory analyses using the HYSPLIT model (HYbrid Single-Particle Lagrangian Integrated Trajectory Model, access via NOAA ARL READY Website (http://www.arl.noaa.gov/ready/hysplit4.html, see Draxler and Hess [1998]) were performed.

7.3 NO_2 Measurements

7.3.1 Overview on the Results of the Different Sites

At all sites (except for Harvard Forest), enhanced NO_2 could be detected (see Figures 7.5 and 7.6). An overview on all time series of the NO_2 ΔSCD for 3° elevation angle for the sites on the mainland. Considerable variation in space and time is apparent. In general, the lowest values are found at Pinnacle State Park which is located most west and relatively far away from major emission sources. Highest ΔSCDs were typically retrieved at MIT with values of up to 3×10^{17} molec/cm^2. Also, at Brookhaven rather high values were found, but due to the instrumental problems with quite high uncertainty. At Narragansett and Thompson Farm, NO_2 ΔSCDs are typically between the values of MIT and Pinnacle State Park. Overall these data can be understood taken into account the average wind direction from west to east and the location of the major emission sources at the north-east of the USA. As discussed in more detail below, a clear weekly cycle can be found for MIT. For the other sites, the weekly cycle is not dominating the temporal variation.

7.3.2 Attribution of Enhanced NO_2 ΔSCDs to Individual Emission Sources

Inspecting the individual time series (Figures 7.5 and 7.6) several events of enhanced NO_2 ΔSCDs can be identified. By trajectory calculations, these enhanced values were attributed to possible emission sources (Figure 7.7). In most of the cases a clear attribution was possible as outlined below.

At Brookhaven, the NO_2 ΔSCDs were frequently in the range of 5×10^{16} molec/cm^2 for the 3° elevation angle. Exceptions could be found when the wind came from the west. In these cases, air masses from New York City were transported into the field of view of the MAX-DOAS instrument and the NO_2 ΔSCDs values increased to up to 2.5×10^{17} molec/cm^2 for the 3° elevation angle. Higher values with air masses coming from New York City could be observed on 15, 16, slightly 19, 20, slightly 31 July as well as 3, slightly 10, and 14 August. On 14 August, values of up to 1.7×10^{17} molec/cm^2 were measured. However, the backward trajectories at that day showed that air masses were coming from south along the coast where no source could be identified. Particularly low values (2×10^{16} molec/cm^2) were found on 18 July when the wind came from south-east and carried a clean air mass.

At Narragansett, NO_2 ΔSCDs were typically lower than at Brookhaven. They amounted to 2×10^{16} molec/cm^2 or less. Significantly higher values were retrieved when the wind was coming from New York City (on 16 July and slightly on 10 August) or significant other sources (see NO_2 point sources of north-east of the USA in Figure 7.7). Such a point source was a close power plant ("Usgen") in the north-east of the measurement site. When the wind blew from that direction, its

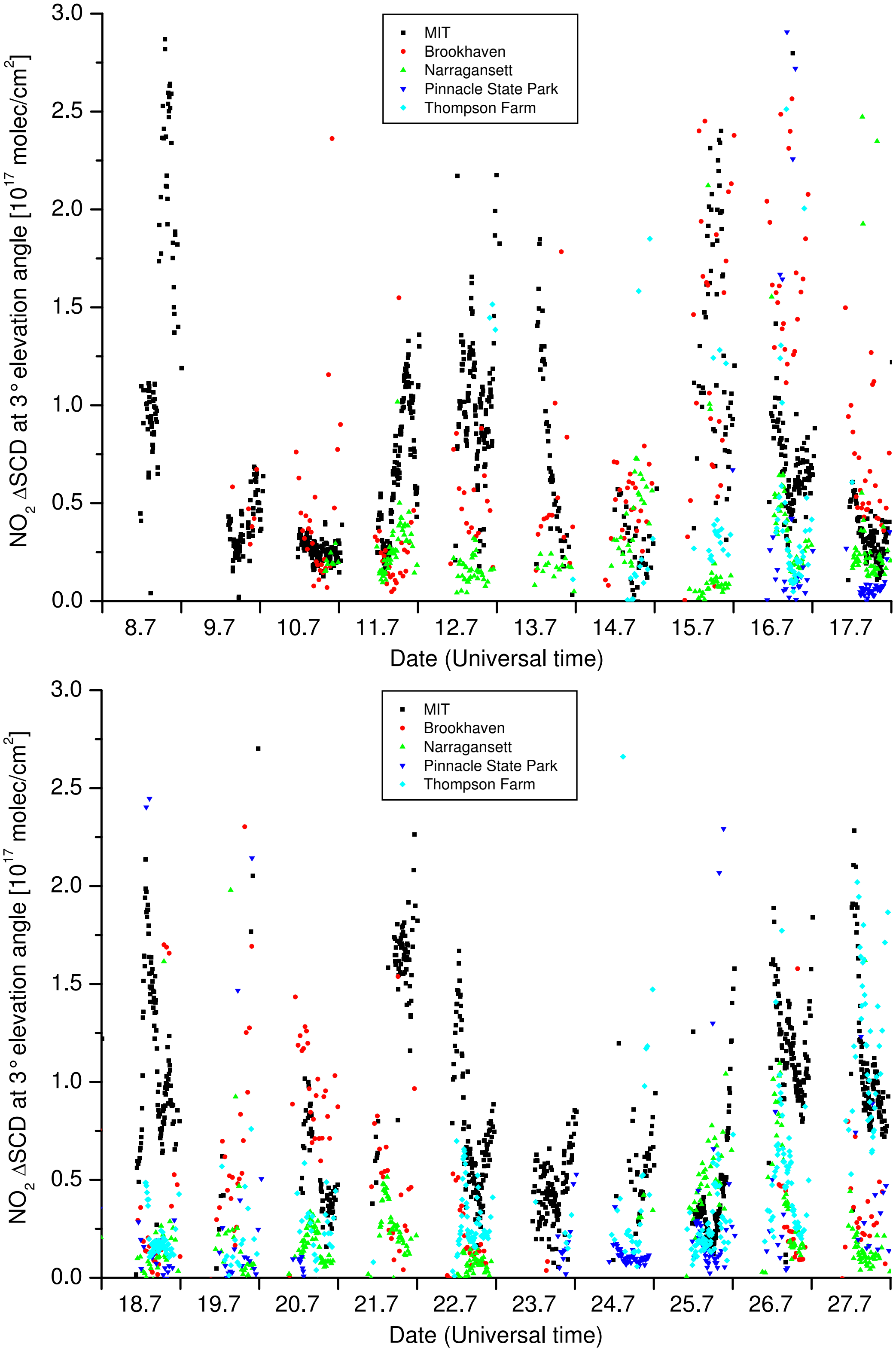

Figure 7.5: *NO_2 ΔSCDs at 3° elevation angle.*

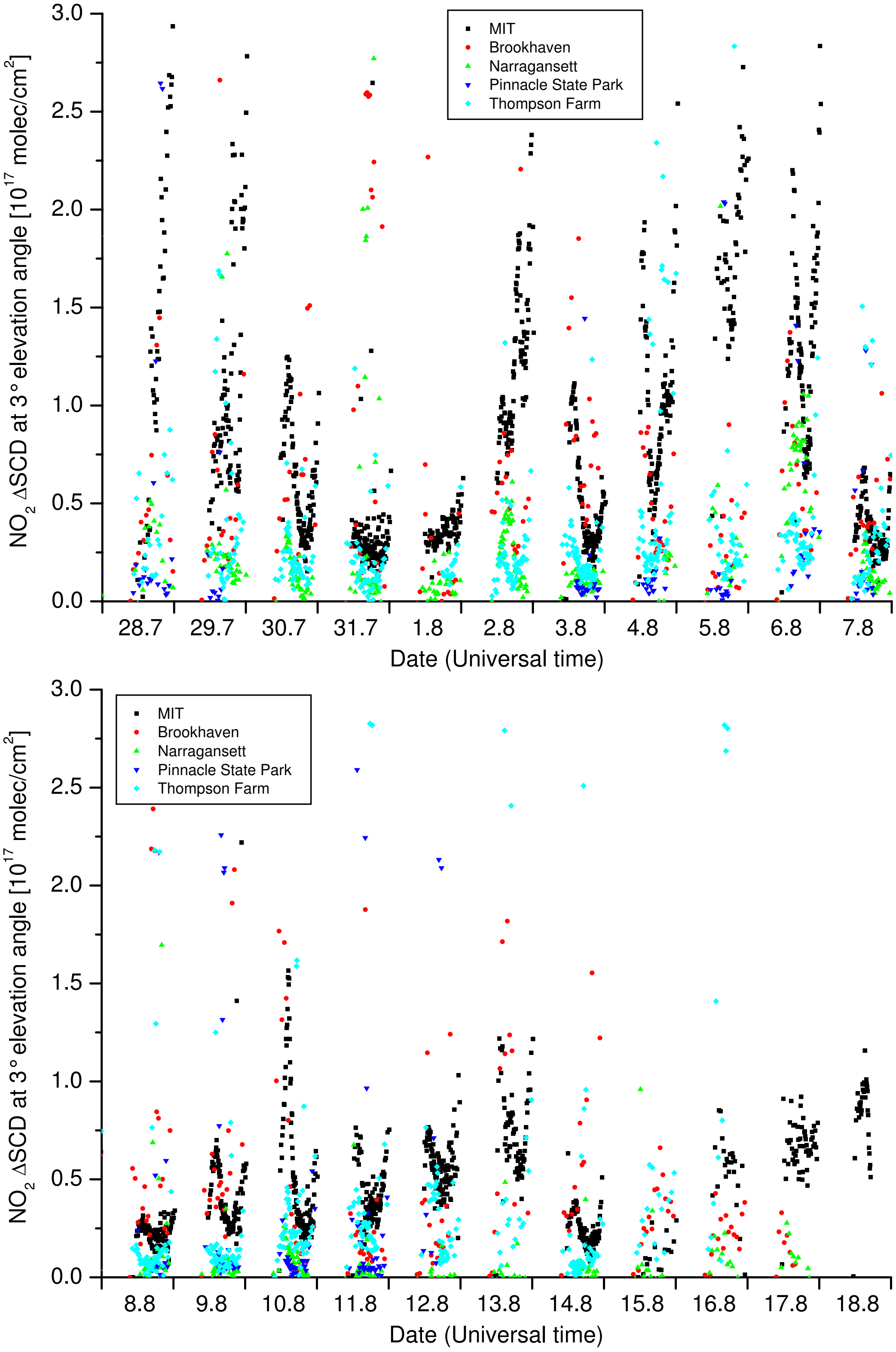

Figure 7.6: *NO$_2$ ΔSCDs at 3° elevation angle.*

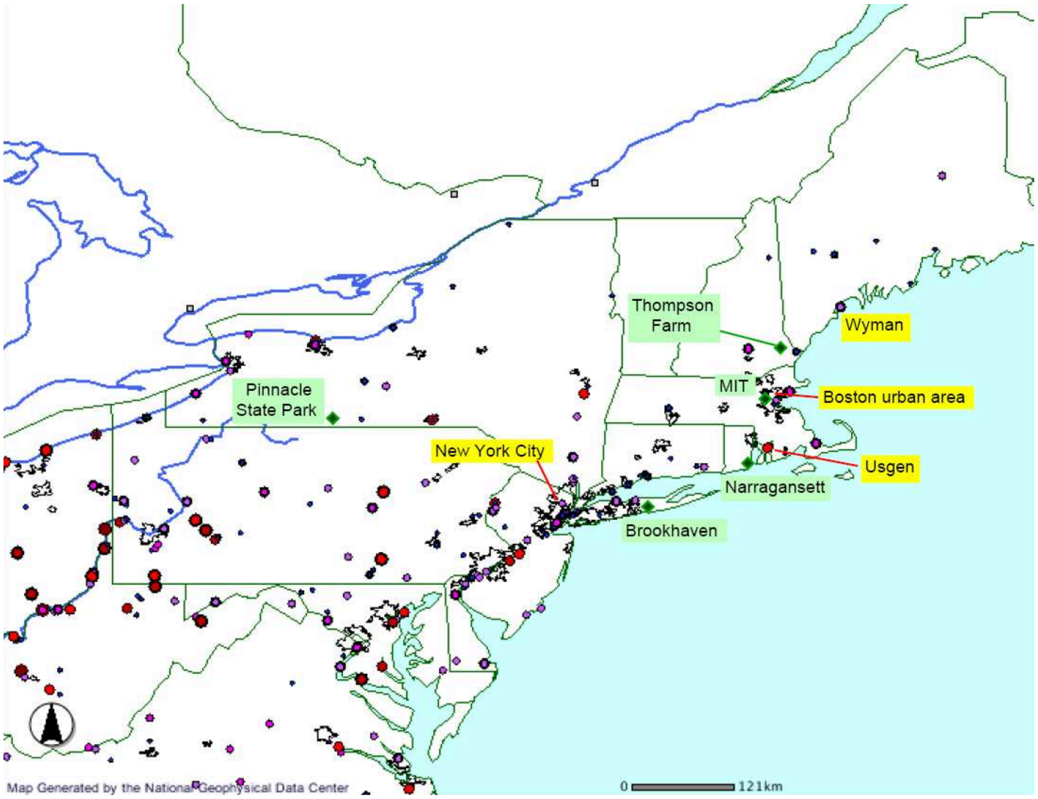

Figure 7.7: *NO_2 point sources in the north-east of the USA from 1999, provided by the National Environmental Satellite, Data, and Information Service (NESDIS). The sources are marked by dots in dark red (higher emissions) over red to purple (lower emissions). Some sources which affected the measurements are labeled in yellow. The measurement sites are marked by green diamonds and labeled in green.*

emissions could be measured (on 11, 14, 25 and 26 July). NO_2 ΔSCDs of up to 8×10^{16} molec/cm^2 where retrieved during these periods, which were highest in the measurement period at Narragansett. On 21 July, possibly emissions from the capital of New York, Albany, could be measured, on 30 July from point sources south-west of New York City and on 6 August from Boston urban area. On 2 August also higher NO_2 ΔSCDs were retrieved, with wind coming from north-west. However, the sources could not be determined because the backward trajectory did not pass a known source. Nevertheless, also higher values of SO_2 could be found at that day (see section 7.6).

The NO_2 ΔSCDs at MIT in Cambridge were mostly determined by local emissions from the Boston urban area. A daily cycle with morning and evening peak values could often be observed indicating emissions from traffic rush hours. Furthermore, a weekly cycle with low NO_2 ΔSCDs on Saturdays and Sundays showed

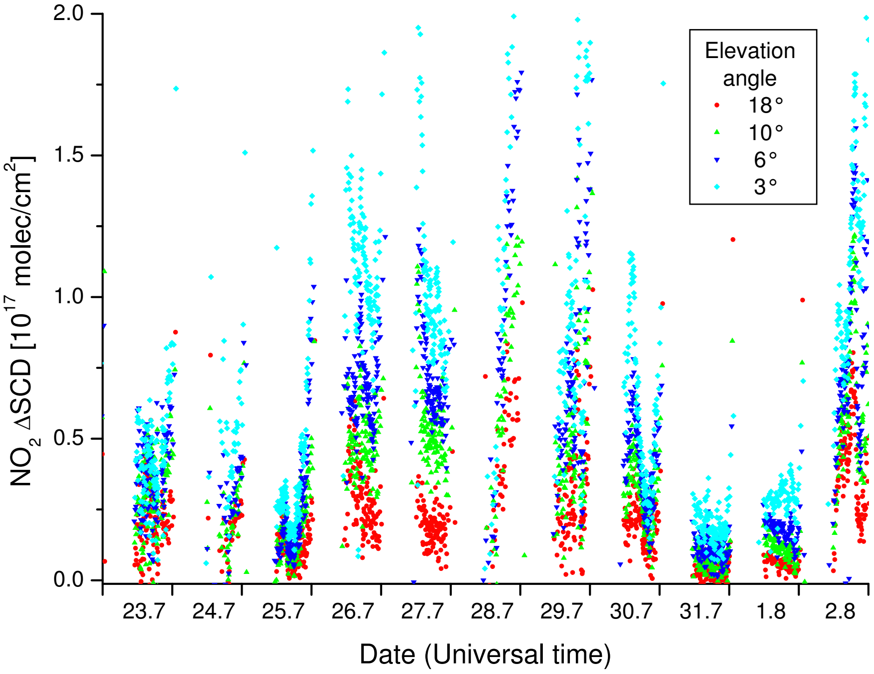

Figure 7.8: *NO_2 ΔSCDs at MIT in Cambridge from 23 July through 2 August. At weekends (24 and 25 July as well as 31 July and 1 August) lower values can be observed due to less anthropogenic activities.*

a strong influence of the traffic on the measurements. An example is plotted in Figure 7.8. Maximum NO_2 ΔSCDs of up to 3×10^{17} molec/cm^2 were retrieved on the most polluted days whereby typical maximum values were in the range of 1×10^{17} molec/cm^2. A correlation with the wind direction was not apparent though the MAX-DOAS instrument was located in the northern part of the Boston urban area pointing to the north. Thus, higher values might have been expected when the wind came from southern directions.

At Pinnacle State Park no significantly enhanced NO_2 ΔSCDs were retrieved. The values were mostly below 1×10^{15} molec/cm^2 indicating the absence of nearby NO_2 sources. This is in agreement with the remote and rural character of the measurement site. Some outliers with up to 3×10^{17} molec/cm^2 were measured, especially on 16 July when the wind came partly from Buffalo in the north-west.

The strongest NO_2 event at Thompson Farm was on 27 July with ΔSCDs of up to 2×10^{17} molec/cm^2. The wind blew from north-west to west at the surface veering to the south to south-east at 1500 m altitude. Since the elevation angles were clearly separated it can be concluded that the NO_2 was transported in layers close to the ground and the source was located north-west to west of Thompson Farm. On 15 and 16 August wind from Portsmouth, which is situated to the west, was also measured, but NO_2 ΔSCDs of at most 5×10^{16} molec/cm^2 were retrieved. Thus, an additional source in the north of Portsmouth is assumed. This is possibly the power plant "Wyman" from where air masses could also be measured on 25 July. At that day however, NO_2 ΔSCDs of only up to 8×10^{16} molec/cm^2 were measured. On 12 and 13 August wind from Boston urban area led to NO_2 ΔSCDs of over 1×10^{17} molec/cm^2. The other days the wind came from westerly directions and the peak values remained typically below 5×10^{16} molec/cm^2. At Thompson Farm also in-situ measurements of NO_2 were performed in the MAX-DOAS measurement period from 25 July through 16 August 2004 [Griffin et al., 2007]. The features described above could also be recognized in the in-situ data set. The highest value of the mixing ratio was found on 27 July with almost 12 ppb.

The attribution of point source emissions to enhanced measured values yielded a very good agreement for most of the events. In cases of mismatch, maybe emissions from unknown point sources were detected, like on 2 August at Narragansett. The measurement of enhanced values for two different trace gases indicate that it might not be an artefact. Generally, the MAX-DOAS technique can be concluded as very suitable for this kind of monitoring because it detects the whole column and not only the surface-near air mass.

Also for the RV Ron Brown, events of enhanced NO_2 ΔSCDs were observed. However, because trajectory calculations are especially complicated for moving instruments in the following only a rough source attribution was performed. The NO_2 measurements during the cruise on the RV Ron Brown yield the highest NO_2 ΔSCDs when air masses were measured coming from the Boston urban area. This happened on 11, 12, 16, 29 and 30 July as well as on 8 and 9 August with NO_2 ΔSCDs of up to 1.5×10^{17} molec/cm^2 at 3° elevation angle. However, the increase in NO_2 on 12 July was possibly caused by measurements of the vessel's exhaust emissions because the wind came from the direction of the chimney at that time. Further high values occurred when the RV Ron Brown was located in the harbor of Portsmouth on 2 through 5 July as well as 23 through 26 July. In these cases, the NO_2 ΔSCDs increased to up to 1×10^{17} molec/cm^2. Air masses from other parts of the mainland also contained significant NO_2. Yet, the NO_2 ΔSCDs were typically below 5×10^{16} molec/cm^2.

7.3.3 Determination of the Aerosol Extinction

In order to compare the MAX-DOAS data set quantatively with other measurements The NO_2 ΔSCDs can be converted to vertical column densities or average mixing ratios. Usually the tropospheric VCD can be determined from measurements of high elevation angles using a geometrical approximation of the light paths. In case of high aerosol load present in the atmosphere, the geometrical approximation might not hold even at the highest off-axis elevation angle of 18°. This effect is investigated in detail in the following. First the aerosol extinction has to be determined. For this,

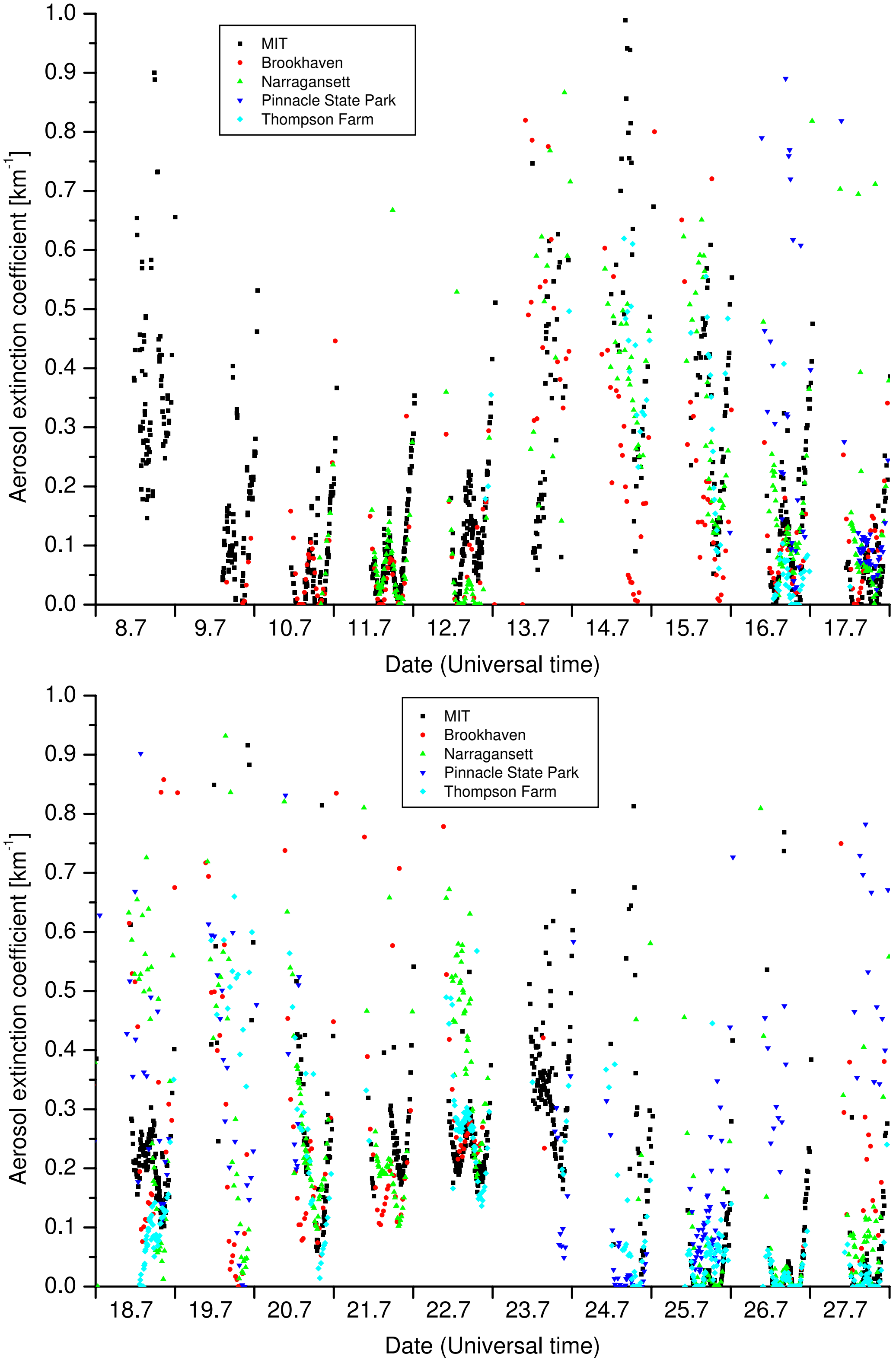

Figure 7.9: *Fitted aerosol extinction coefficients derived from MAX-DOAS measurements.*

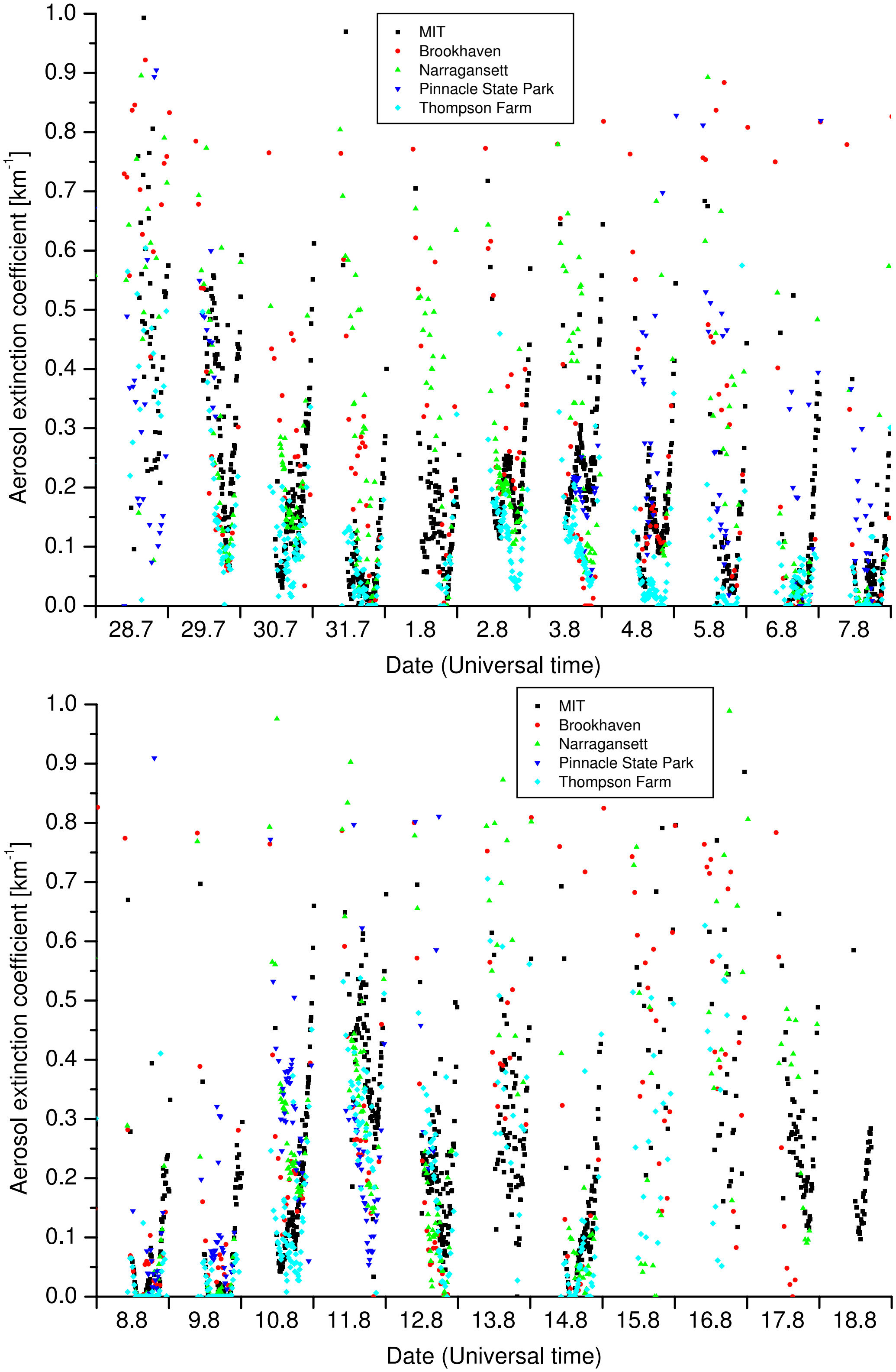

Figure 7.10: *Fitted aerosol extinction coefficients derived from MAX-DOAS measurements.*

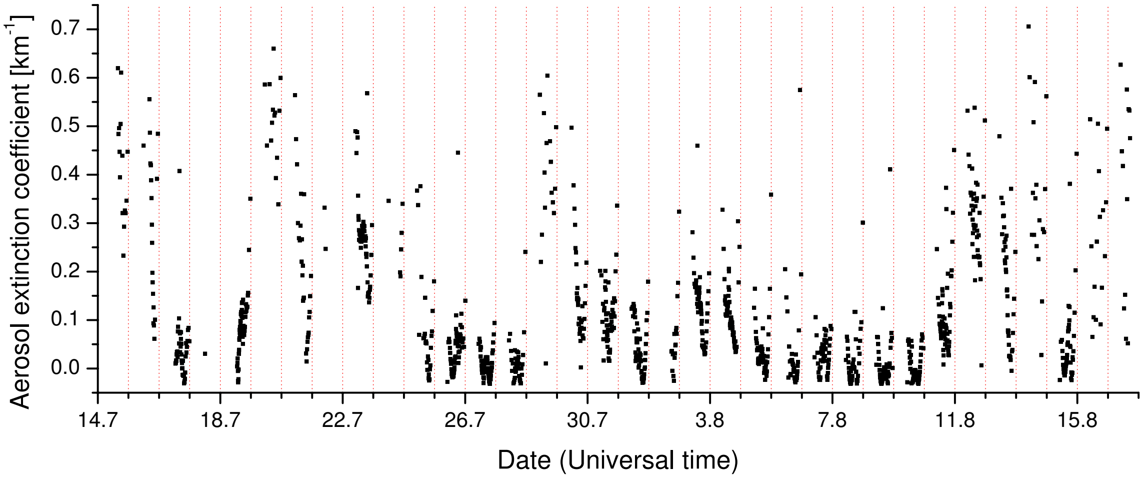

Figure 7.11: *Fitted aerosol extinction coefficients derived from MAX-DOAS measurements at Thompson Farm from 14 July through 16 August 2004.*

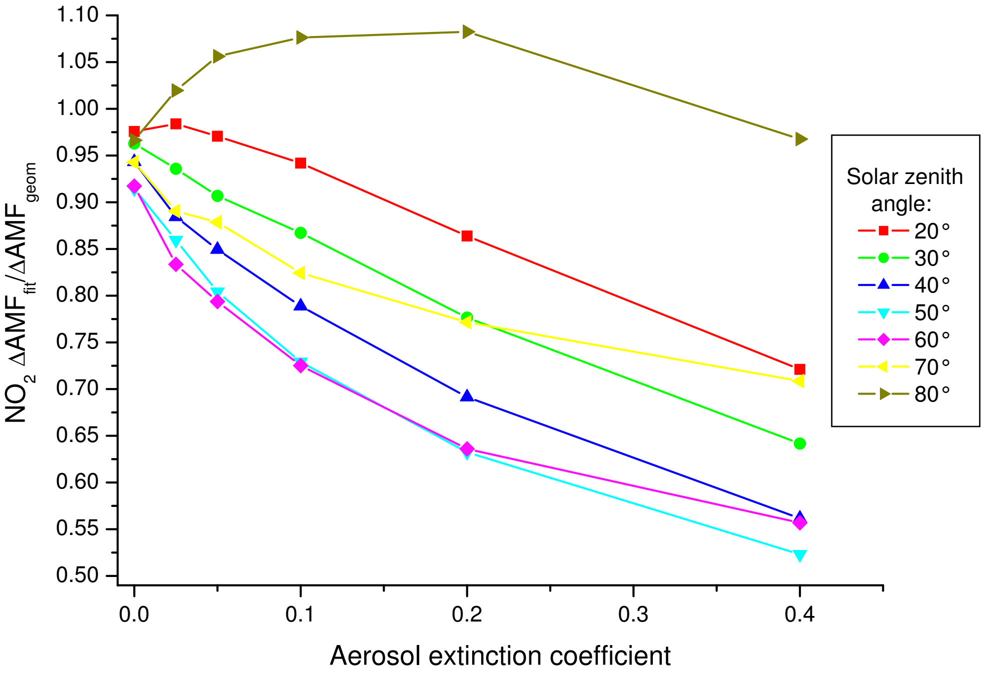

Figure 7.12: *Ratio of modeled air mass factors (ΔAMF_{mod}) and geometrical NO_2 $\Delta AMFs$ (ΔAMF_{geom}) versus the aerosol extinction coefficient. They differ up to a factor of two for specific cases.*

radiative transfer modeling was performed using Tracy-II. O_4 ΔAMFs at different solar zenith angles and for different aerosol loads were calculated. The O_4 ΔAMFs were yielded by subtracting the AMF for 90° elevation angle from the corresponding value for 3° elevation angle which is the most sensitive elevation angle of the measurement for the light path close to the ground. The aerosol extinction height profile was assumed to be constant in the first kilometer and zero above. This aerosol layer is high enough so that the average scattering distance is usually smaller than the direct light path through the layer at 3° elevation angle. The wavelength of the calculation was 360 nm where a strong O_4 absorption band is situated, which has been used for the retrieval of O_4 in the MAX-DOAS analysis. Henyey-Greenstein type phase function with an asymmetry parameter of 0.68 and a single scattering albedo of 0.9 was chosen. For the estimation of the aerosol extinction, a two-dimensional polynomial of second degree z=f(x,y) was fitted, with z being the aerosol extinction coefficient, x the solar zenith angle and y the O_4 ΔAMF. The following function represents the aerosol extinction as a function of SZA and O_4 ΔAMF:

$$\begin{aligned} z = 1.17 - 0.574y + 0.0831y^2 - 0.0223x + 0.00157xy + 0.000751xy^2 + \\ 0.000192x^2 + 0.0000395x^2y - 0.0000202x^2y^2 \end{aligned} \tag{7.1}$$

with a standard deviation of 0.043 km^{-1}. The fit was applied to the measured O_4 ΔAMFs and the corresponding solar zenith angles of the measurements. The O_4 ΔAMFs were derived from the measured O_4 ΔSCDs by dividing by a typical O_4 VCD of 1.3×10^{43} $molec^2/cm^5$ which is the total column of the squared oxygen concentration. The fitted aerosol extinction coefficients are plotted in Figures 7.9 and 7.10 for the sites on the mainland. They exhibit a strong variability reaching values up to 1 km^{-1}. On some days, a remarkable similarity in the course is apparent, such as on 22 July. Similar to the NO_2 ΔSCDs, the highest aerosol extinctions were found for MIT, and the lowest for Pinnacle State Park. In Figure 7.11 the aerosol extinction coefficients are plotted separately for the measurements at Thompson Farm from 14 July through 16 August 2004. At some days, the values are quite scattered probably due to clouds, but often the values show a continuous course. They vary from 0.7 km^{-1} to slightly below zero. The negative values are most probably caused by the oversimplification due to the fitting procedure, varying cloud cover or by the assumptions of the radiative transfer calculations, such as a fixed azimuth angle. Thus, they were considered as zero for the further calculations.

7.3.4 Determination of the Tropospheric NO_2 VCD

Using the aerosol coefficients it is now possible to calculate NO_2 VCDs. For this, NO_2 ΔAMFs at different solar zenith angles and for different aerosol extinction coefficients were calculated. The modeling was performed at 380 nm in the center of the NO_2 retrieval wavelength range and at 18° elevation angle. The NO_2 concentration and aerosol extinction were assumed to be constant from 0 to 1.5 km. The elevation angle of 18° is chosen as a compromise between two properties: On one hand, NO_2

absorption is still strong enough to ensure good signal to noise, on other hand the AMFs are least influenced by aerosols. A comparison of the modeled air mass factors (ΔAMF$_{mod}$) with the geometrical NO_2 ΔAMFs (ΔAMF$_{geom}$) is shown in Figure 7.12 where their ratios are displayed versus the aerosol extinction coefficient. The geometrical NO_2 ΔAMFs were calculated by the approximation $\frac{1}{\sin(18°)} - 1$, yielding about 2.24. It can be seen that in this example a difference of up to a factor of two can occur between geometrical and modeled air mass factor.

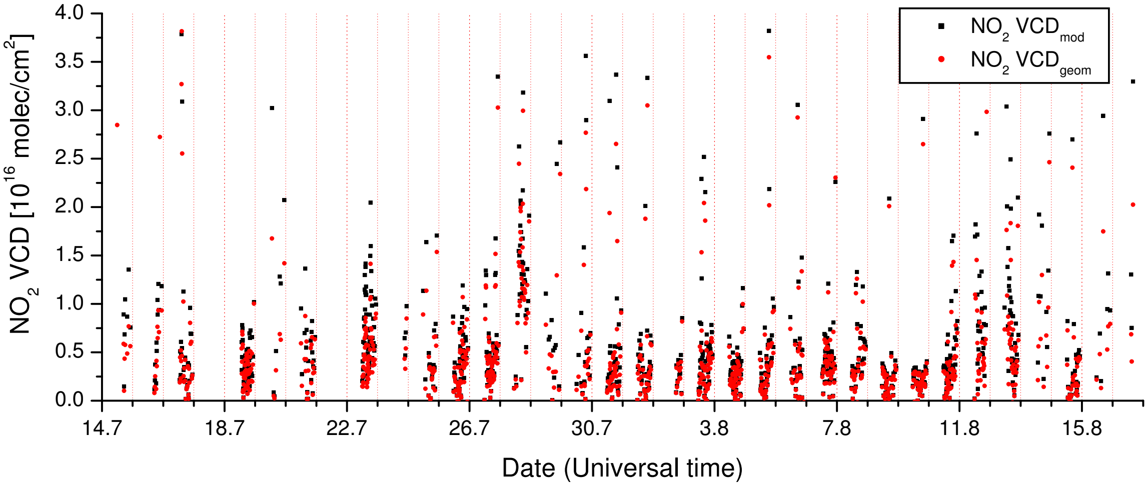

Figure 7.13: *Tropospheric NO_2 vertical column densities of the MAX-DOAS measurements at Thompson Farm from 14 July through 16 August 2004 calculated by both the modeled (VCD$_{mod}$, black) and the geometrical (VCD$_{geom}$, red) ΔAMF. Only solar zenith angles below 80° were considered. Since the ΔAMF$_{mod}$ are typically lower than the ΔAMF$_{geom}$, the VCD$_{mod}$ are larger than the VCD$_{geom}$.*

Again, a two-dimensional polynomial of second degree z=f(x,y) was fitted, with, this time, z being the NO_2 ΔAMF, x the solar zenith angle and y the aerosol extinction coefficient. The following function was fitted:

$$z = 2.59 + 7.92y - 18.5y^2 - 0.0218x - 0.529xy + 1.01xy^2 + 0.000209x^2 + 0.00564x^2y - 0.0105x^2y^2 \tag{7.2}$$

The standard deviation of this fit is 0.069. Using this approximation, NO_2 ΔAMFs were calculated using the aerosol extinction coefficients derived as described above. Then, the measured NO_2 ΔSCDs of the measurement at 18° elevation angle were divided by the modeled NO_2 ΔAMFs yielding tropospheric NO_2 VCD values. In Figure 7.13, the tropospheric NO_2 vertical column densities of the MAX-DOAS measurements at Thompson Farm from 14 July through 16 August 2004 calculated by both the calculated (VCD$_{mod}$, black) and the geometrical (VCD$_{geom}$, red) ΔAMF

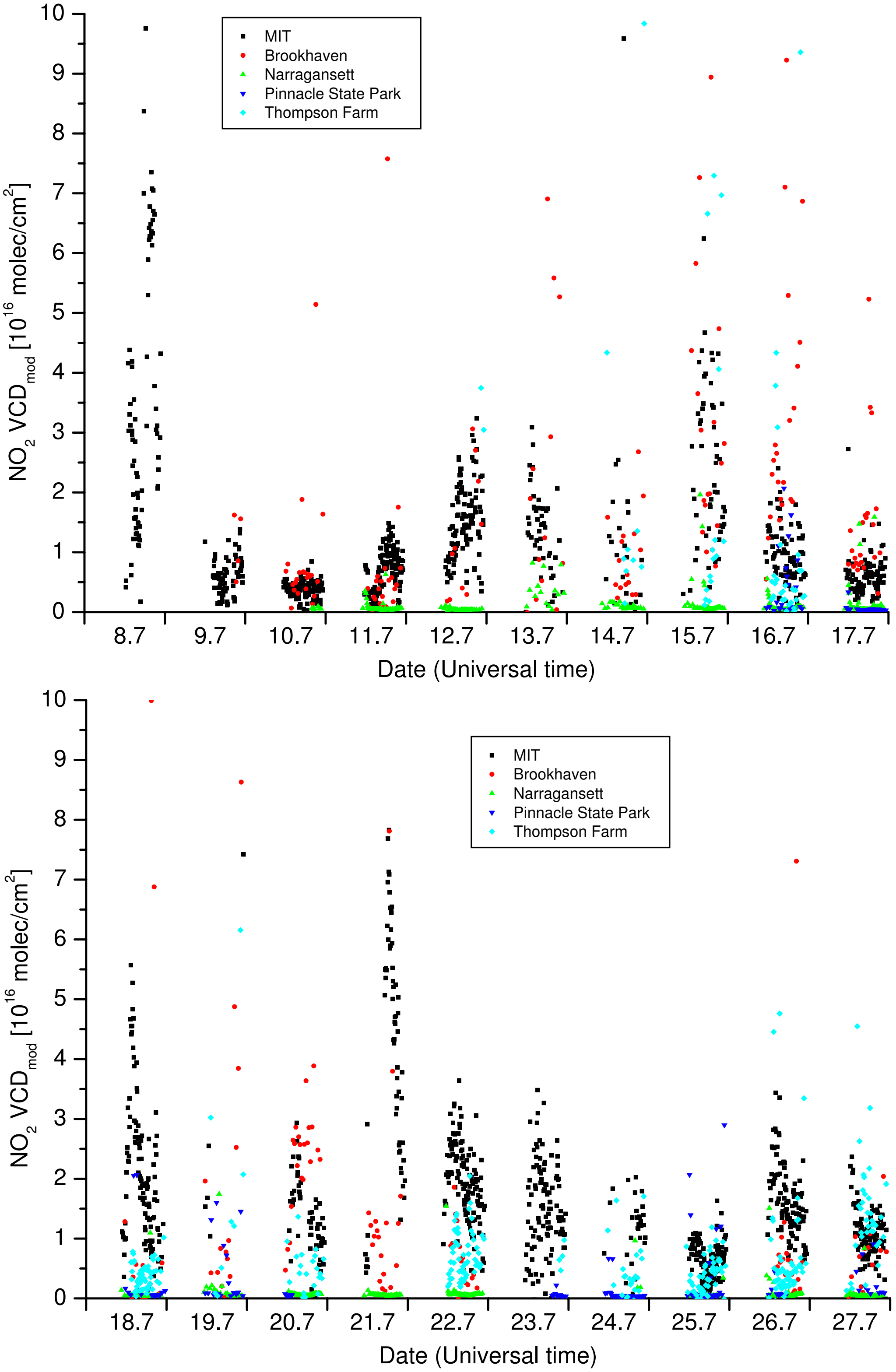

Figure 7.14: *Tropospheric NO_2 VCDs.*

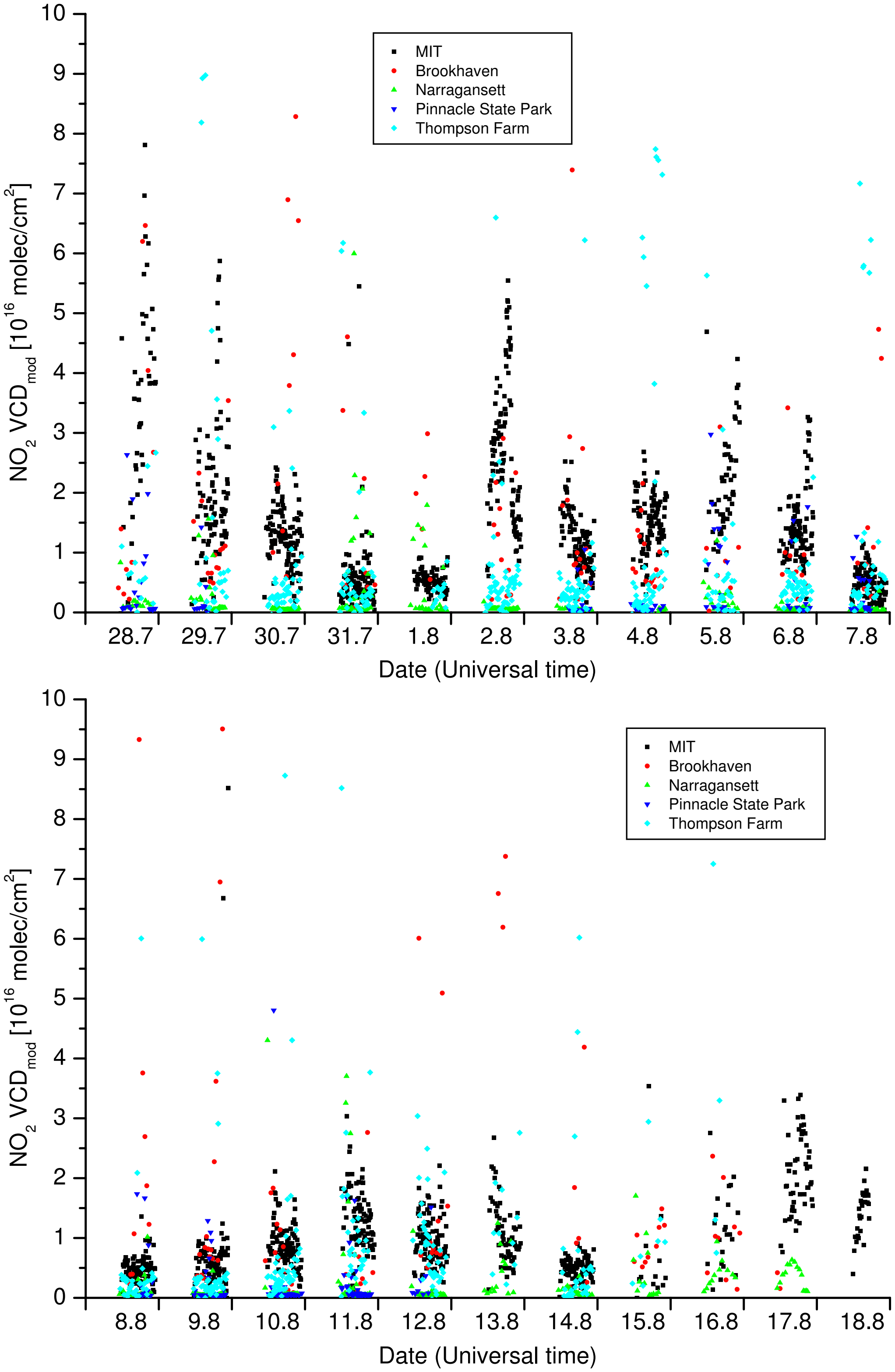

Figure 7.15: *Tropospheric NO_2 VCDs.*

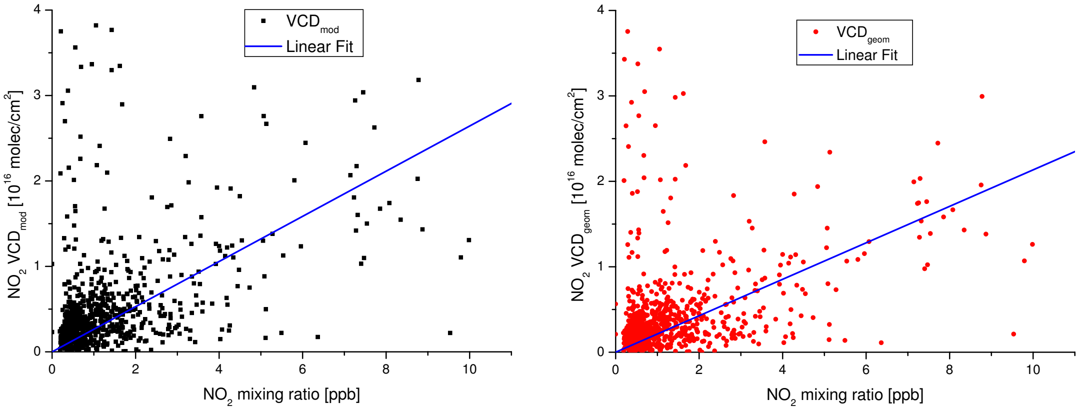

Figure 7.16: *Tropospheric NO_2 VCD_{mod} (left panel) and VCD_{geom} (right panel) versus NO_2 mixing ratios measured in situ. For both a linear fit was applied with correlation coefficients of 0.40 for the modeled values and 0.38 for the geometrical calculation.*

are plotted. Only solar zenith angles below 80° were considered. For most observations, the VCD$_{mod}$ and the VCD$_{geom}$ show very similar values. However, since the ΔAMF$_{mod}$ are typically lower than the ΔAMF$_{geom}$, the VCD$_{mod}$ are larger than the VCD$_{geom}$.

In Figures 7.14 and 7.15, the tropospheric NO$_2$ vertical column densities of the MAX-DOAS measurements on the mainland are compared with highest values mostly at MIT, like at the NO$_2$ ΔSCDs. Also a conversion to mixing ratios can be performed if a fixed layer height with constant NO$_2$ concentration is assumed. For a layer height of 1 km, 1×10^{16} molec/cm^2 corresponds to 4 ppb (assuming 1 ppb as 2.51×10^{10} molec/cm^3 at 293 K and 1013 mbar). The calculated tropospheric NO$_2$ VCDs at Thompson Farm are compared with the in-situ measurements from 25 July through 16 August in Figure 7.16. The VCD$_{mod}$ (left panel) and the VCD$_{geom}$ (right panel) are plotted versus the mixing ratios. A linear fit was applied for both. Although the values are quite scattered a small linear dependency could be recognized for both with correlation coefficients of 0.40 for the modeled values and 0.38 for the geometrical calculation. Probably, the measurement of different air masses between MAX-DOAS and in-situ measurement result in this small correlation. Thereby, the NO$_2$ layer height could have varied, its altitude profile could have been not constant and horizontal NO$_2$ gradient could have occurred. The determined slopes yield information on the averaged NO$_2$ layer heights. The values at low mixing ratio and high VCD are probably due to clouds in the air mass where NO$_2$ was present. For the modeled ΔAMFs, a height of 1.1 ± 0.1 km and for the geometrical approach 0.9 ± 0.1 km were derived. These values are lower than the 1.5 km roughly assumed in the modeling as an average over 23 days with different conditions, also over the day. Considering this, the result and the assumption fit surprisingly well.

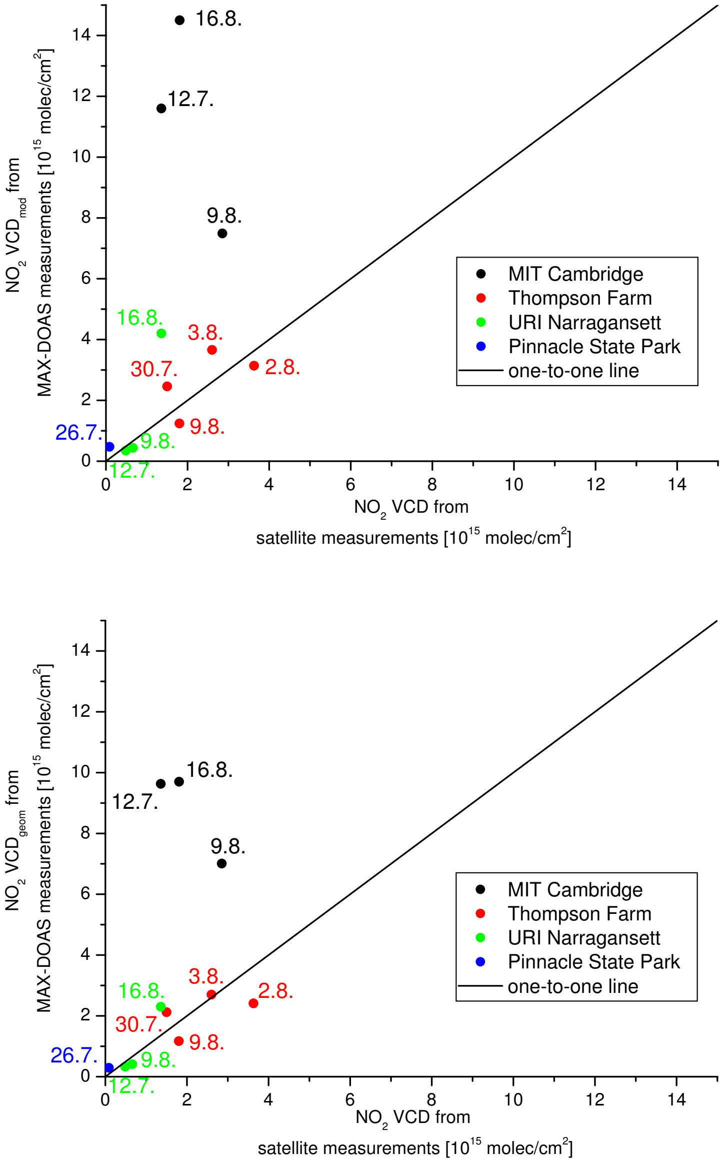

Figure 7.17: *Tropospheric NO$_2$ VCDs from MAX-DOAS measurements versus tropospheric NO$_2$ VCDs from satellite measurements (without cloud correction) for MIT (black), Thompson Farm (red), Narragansett (green) and Pinnacle State Park (blue). The upper panel compares the VCDs from the modeling and the lower panel from the geometrical calculation. Additionally a one-to-one line is drawn and the values are labeled with the date of acquisition.*

The NO$_2$ VCD retrieval using modeled ΔAMFs was also applied to measurements at other sites. The retrieved VCDs as well as VCDs calculated by the geometrical approximation were compared with VCDs measured from the DOAS satellite instrument SCIAMACHY. Local overpass time of SCIAMACHY is about 10:30AM. The instrument averages over a pixel of about 30 × 60 km^2. It covers the same location every six days at the equator so that daily measurements were not available. Also, many values were missing during the measurement period of ICARTT 2004. Nevertheless, the available satellite VCDs could be used for comparison whereby the cloud fractions was not accounted for [Steffen Beirle, pers. comm.].

In Fig 7.17, the tropospheric NO_2 VCDs from the MAX-DOAS measurements are plotted versus the tropospheric NO_2 VCDs of SCIAMACHY for MIT, Thompson Farm, Narragansett and Pinnacle State Park. They are labeled with date of acquisition. Additionally a one-to-one line was drawn. The upper panel compares the VCDs from the retrieval using modeled ΔAMFs and the lower panel from the geometrical calculation. Both show fair agreement except for the MIT site which is assumably due to spatial averaging of the satellite measurement over the environment of the Boston urban area. This is likely the reason why the values of the MAX-DOAS measurements which were taken in the Boston urban area are higher. Furthermore, the geometrical approach seems to fit better which probably is the case because the VCDs from satellite used here do not account for aerosol effects on the light path. The geometrical approach which does not account for these effects is based on the same rough assumptions. Additionally, cloud effects were not considered in the VCD retrieval of the satellite. Hence, NO_2 which is located under clouds could at best only partly be detected by the satellite instrument. This could be observed at Narragansett or MIT, both on 16 August, where the cloud fraction amounted to 0.93 and 0.94[1], respectively. Also in the retrieved aerosol extinctions (Figure 7.10), high and scattered values were found on 16 August.

7.4 Glyoxal Measurements

Glyoxal (CHOCHO) could be measured at MIT in Cambridge and onboard RV Ron Brown due to a wavelength range of the spectrometer reaching up to 460 nm. Elevated concentrations of CHOCHO were detected at both sites on more than 10 days during the measurement period. The ΔSCDs are generally significantly lower at MIT than onboard RV Ron Brown which is apparent in Figures 7.18 and 7.19 for measurements at 3° elevation angle. While the CHOCHO ΔSCDs at MIT reach values of up to 4×10^{15} molec/cm^2 on the RV Ron Brown double as high CHOCHO ΔSCDs could be measured.

Examples for measurements at both sites with all elevation angles are shown in Figure 7.20, where tropospheric ΔSCDs of CHOCHO, NO_2 and O_4 as well as the solar zenith angles are plotted, each on a clear day, which can be identified

---

[1] data from Fast Retrieval Scheme for Cloud Observables (FRESCO) provided by the Royal Netherlands Meteorological Institute (KNMI)

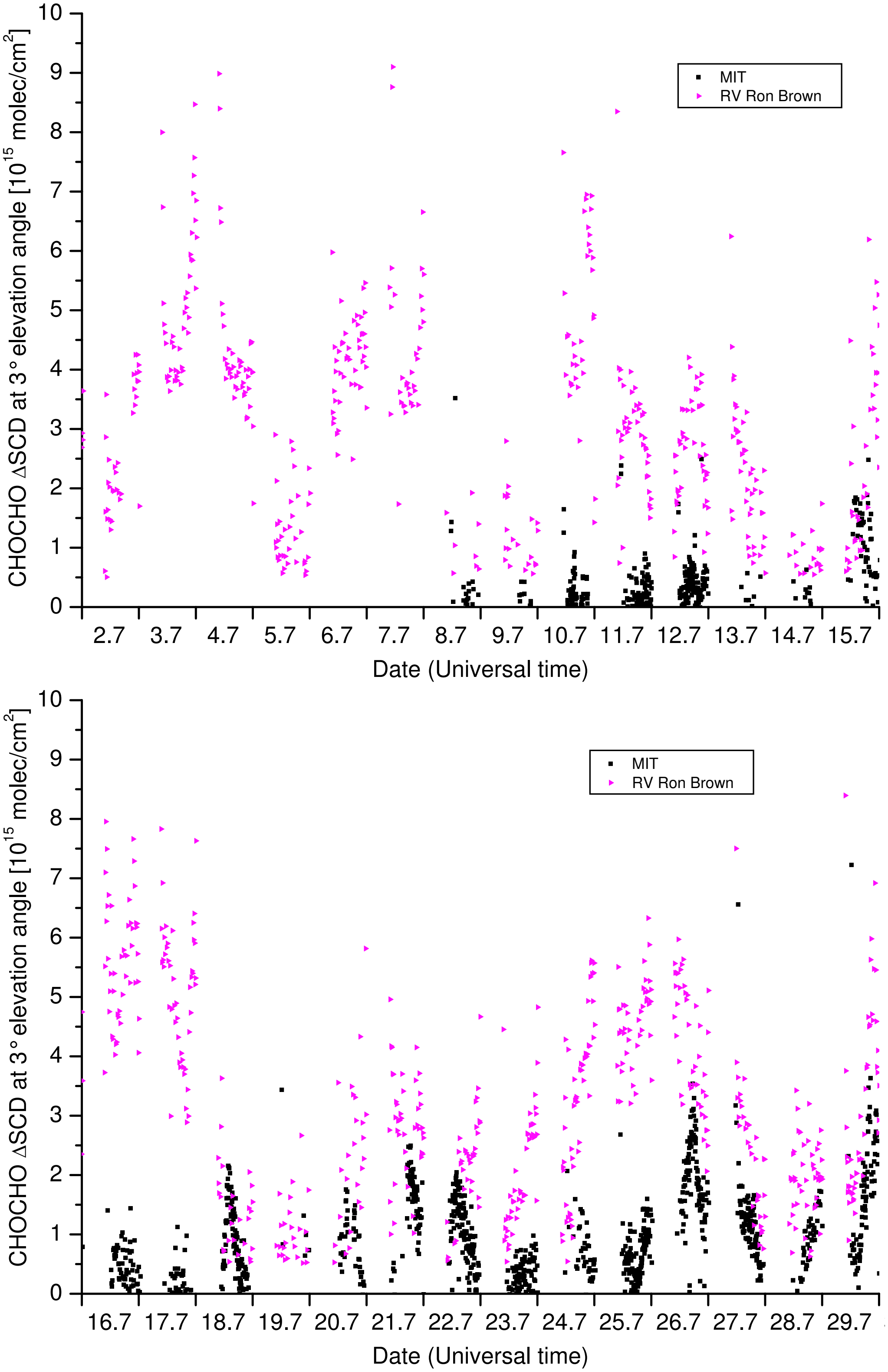

Figure 7.18: *CHOCHO ΔSCDs at 3° elevation angle for MIT and RV Ron Brown.*

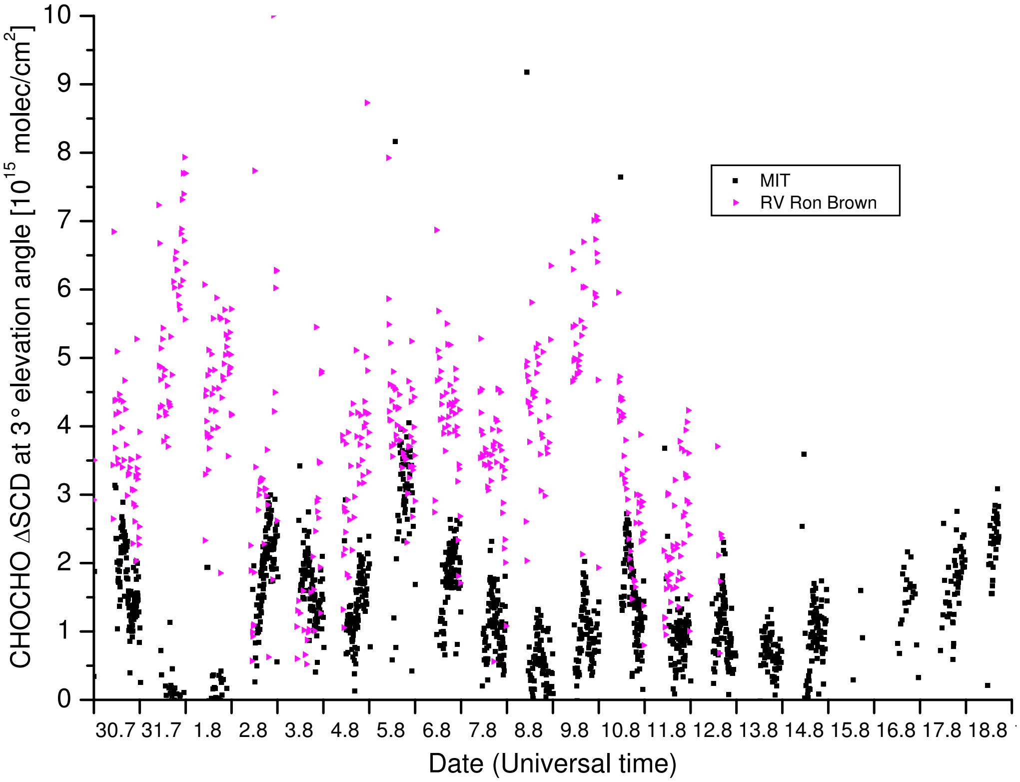

Figure 7.19: *CHOCHO ΔSCDs at 3° elevation angle for MIT and RV Ron Brown.*

by a relatively smooth variation of the O_4 ΔSCDs. For these days, a detailed analysis was applied, which is described in the following (see also [Sinreich et al., 2007]). At MIT, on 26 July, an increase in the CHOCHO ΔSCDs (Figure 7.20a) to up to about 3.5×10^{15} molec/cm^2 occurred in the morning, indicating a high rate of volatile organic compound (VOC) oxidation on that day. In the afternoon, the values decreased again, most probably owing to chemical loss. Especially the MAX-DOAS observations at high elevation angles (e.g. 18°) are sensitive for the total VCD and consequently a mere dilution effect in a rising planetary boundary layer would hardly affect the CHOCHO ΔSCDs (of course this is different at low elevation angles). The behavior of the CHOCHO ΔSCDs is consistent with active DOAS observations in Mexico City [Volkamer et al., 2005]. The NO_2 ΔSCDs do not show such a pronounced diurnal cycle, although a decrease in the afternoon can also be observed. The diurnal variation of NO_2 appears to be dominated by light path changes, as can be seen from the similarity to the variation in the O_4 ΔSCDs. On 17 July, the RV Ron Brown cruised around 69° W and 43° N in the Gulf of Maine mainly in eastward direction, at about the same latitude as Portsmouth, New Hampshire. The wind came from southwest to west and the sky was clear

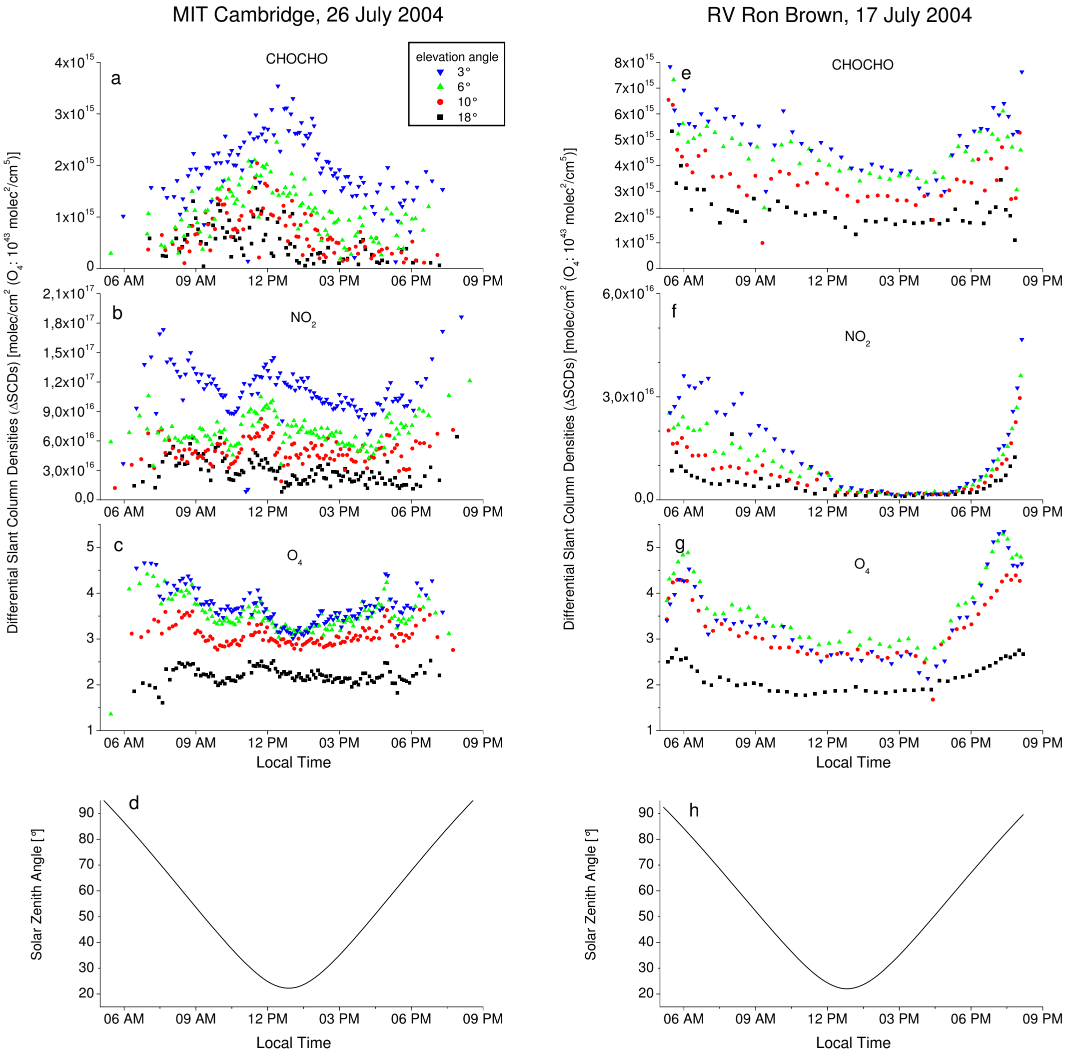

Figure 7.20: *ΔSCDs of CHOCHO, NO_2 and O_4 at MIT in Cambridge on 26 July 2004 (a-c) and RV Ron Brown on 17 July 2004 (e-g). The elevation angles are indicated by the symbol color as denoted in the legend. In (d) and (h) the solar zenith angle at MIT and RV Ron Brown, respectively, is plotted.*

during the day. Here the CHOCHO ΔSCDs (Fig. 7.20e) are stronger influenced by the light path variations whereas the NO_2 ΔSCDs show high tropospheric NO_2 in the morning which disappeares in the afternoon. In the late afternoon, the course of the vessel changed to northwest and a new air mass with slightly less aerosol load seemed to be present.

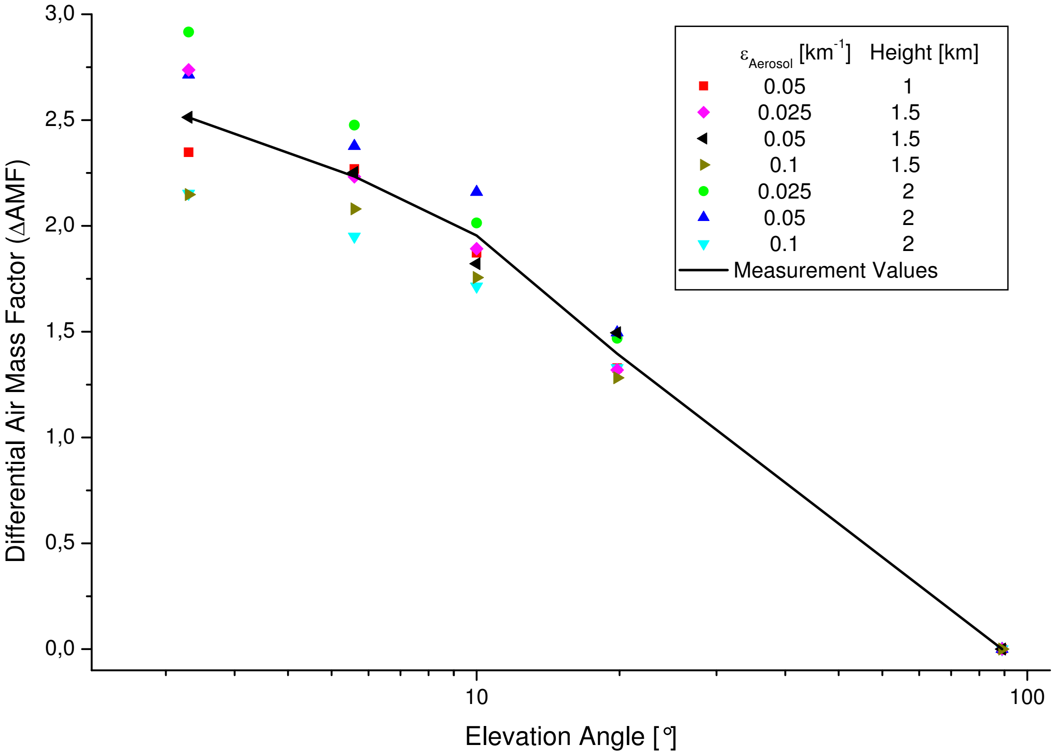

Figure 7.21: *From measurements calculated O_4 ΔAMFs (black line) compared with modeled O_4 ΔAMFs for different homogenously mixed aerosol layers (see legend) as a function of the logarithm of the elevation angle for an SZA of about 40° at MIT.*

For both days, radiative transfer modeling was performed with Tracy to convert ΔSCDs into mixing ratios using the direct comparison approach. For these calculations, an O_4 cross section value of 5×10^{46} $cm^5/molec^2$ (for the 360 nm absorption band) and an asymmetry parameter of 0.68 (Henyey-Greenstein phase function) were used. Figure 7.21 shows an example of the aerosol retrieval at MIT in the morning (about 40° SZA). O_4 ΔAMFs calculated from the measurement (black line) are compared with modeled O_4 ΔAMFs for different homogenously mixed aerosol layers. Owing to clearness the number of scenarios was reduced here. Obviously, the third scenario (black) with an aerosol extinction of 0.05 km^{-1} and a layer height of 1.5 km matches best to the measurement values. In Figure 7.22, the estimated

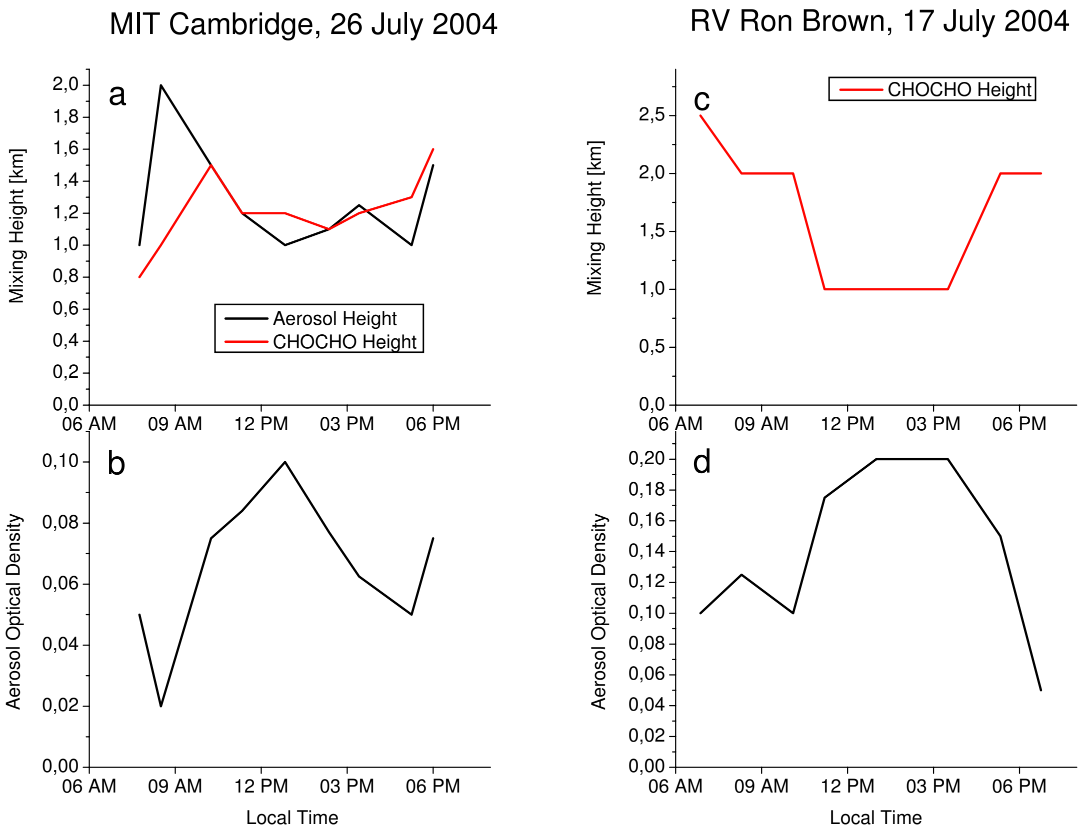

Figure 7.22: *Estimated mixing height for CHOCHO and aerosol (only for MIT) as well as aerosol optical density at MIT in Cambridge on 26 July 2004 (a and b) and RV Ron Brown on 17 July 2004 (c and d) retrieved by radiative transfer modeling.*

profile heights H and aerosol optical densities (AODs) are shown for both sites. The aerosol and CHOCHO profile heights at MIT generally match well, except for some deviations in the morning and evening, when CHOCHO ΔSCDs were lowest. During mid-day, the signal to noise ratio of the ΔSCDs is highest and the radiative transfer modeling is more accurate. At RV Ron Brown, the modeling of the aerosol layer height did not lead to an unequivocal result due to the relatively high aerosol optical density (of course, in reality even much higher AODs can occur. Nevertheless, the sensitivity of the O_4 absorption on the AOD decreases with increasing AOD) and possibly the complexity of the real aerosol scenario. The AOD at MIT peaked around noon, which is consistent with the estimation of the aerosol extinction coefficient presented in section 7.3. It generally increased in the course of the day which indicates an accumulation of aerosol load during that day. At RV Ron Brown, an accumulation can also be observed whereas a sudden decrease in the late afternoon indicates an altered air mass as already concluded from the ΔSCDs. The resulting CHOCHO mixing ratios at MIT (see Figure 7.23a) have their maximum at noon with about 140 ± 35 ppt (1 ppt corresponds to 2.51×10^7 molec/cm^3 at 293 K and 1013 mbar). In contrast, there is no such clear maximum on RV Ron Brown (Fig. 7.23c) and the maximum values are almost three times higher (up to 340 ± 110 ppt). In the MCMA-2003 campaign, values up to 1.82 ppb were measured [Volkamer et al., 2005]. Typical daytime maxima were about five times larger in Mexico City than in Cambridge. In Fig. 7.23b and 7.23d the vertical column densities observed at MIT and RV Ron Brown, respectively, are plotted which have basicly the same diurnal cycle as the mixing ratios.

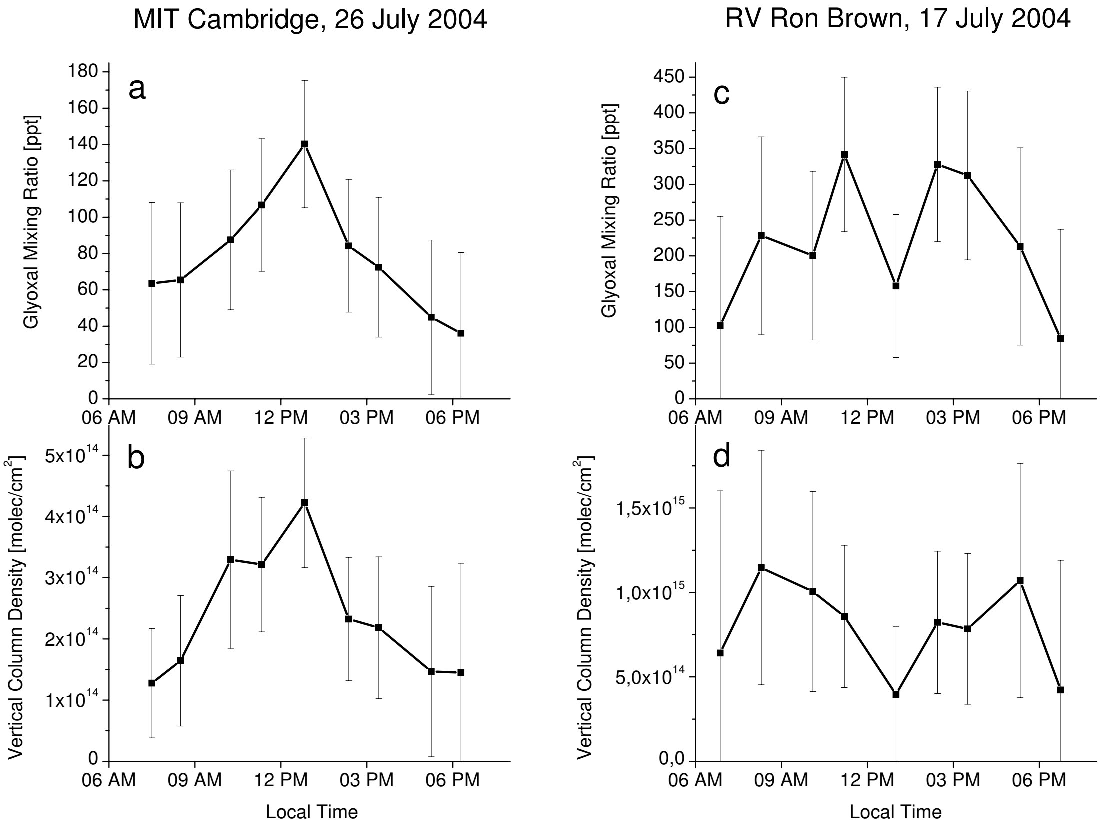

Figure 7.23: *CHOCHO mixing ratios and VCDs at MIT in Cambridge on 26 July 2004 (a and b) and RV Ron Brown on 17 July 2004 (c and d) retrieved by radiative transfer modeling from CHOCHO ΔSCDs.*

In order to investigate a possible dependence of the CHOCHO ΔSCDs on the NO_2 ΔSCDs the CHOCHO-to-NO_2 ΔSCD ratio at 3° elevation anglefor the chosen days for MIT (Figure 7.24a) and RV Ron Brown (Fig. 7.24b) are shown. At MIT, the ratio reached its maximum (0.028 ± 0.008) at 12:30PM, a much smaller value than

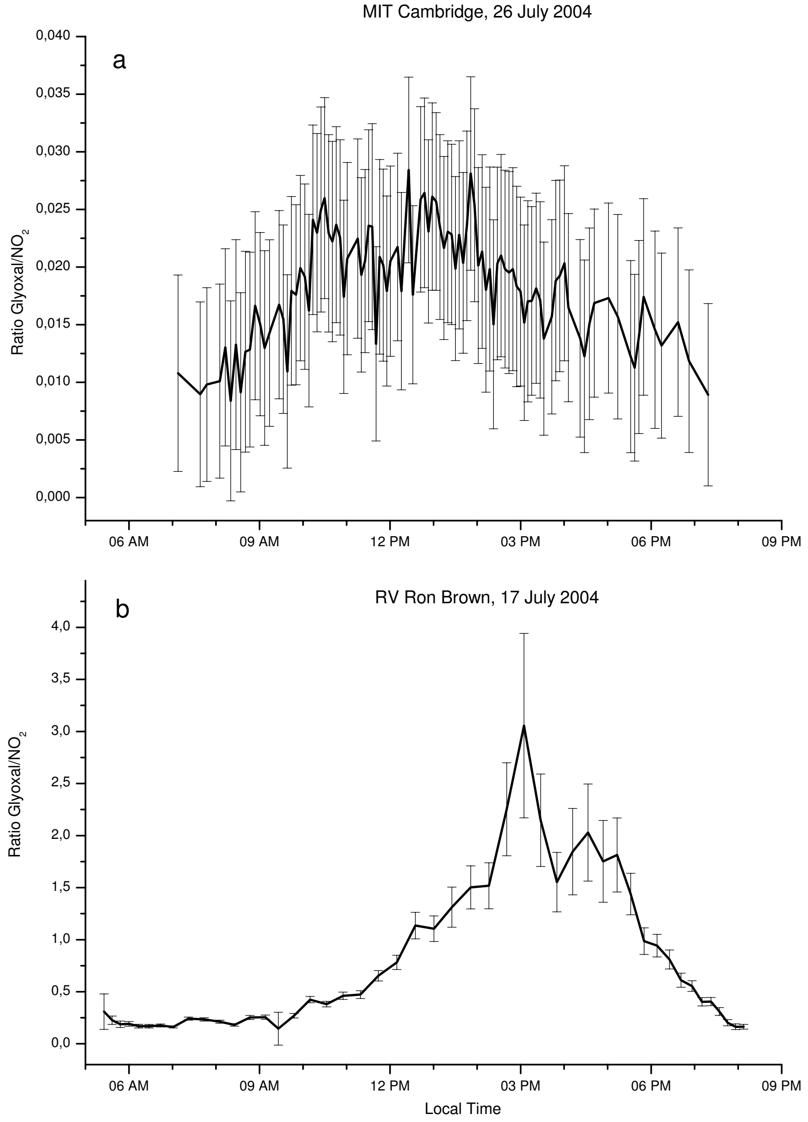

Figure 7.24: *CHOCHO-to-NO$_2$ ΔSCD ratios of the 3° elevation values at MIT in Cambridge on 26 July 2004 (a) and RV Ron Brown on 17 July 2004 (b).*

observed during MCMA-2003 where daily maximum ratios varied between 0.045 and 0.14 [Volkamer et al., 2005]. The MCMA-2003 campaign average ratio (0.081) is two to three times higher than in Cambridge, possibly reflecting differences in the VOC/NO$_x$ ratio between both urban sites. The ratio in Cambridge also peaked relatively late, reflecting more active and earlier PBL dynamics in Mexico City [de Foy et al., 2005] than in Cambridge. In contrast, the ratios onboard RV Ron Brown were much higher and peaked even later in the day. On 17 July 2004, the ratio reached up to 3.1 ± 0.9 at 3PM. This is 110 ± 45 times higher than at MIT. The considerably higher CHOCHO-to-NO_2 ratio over the sea compared to

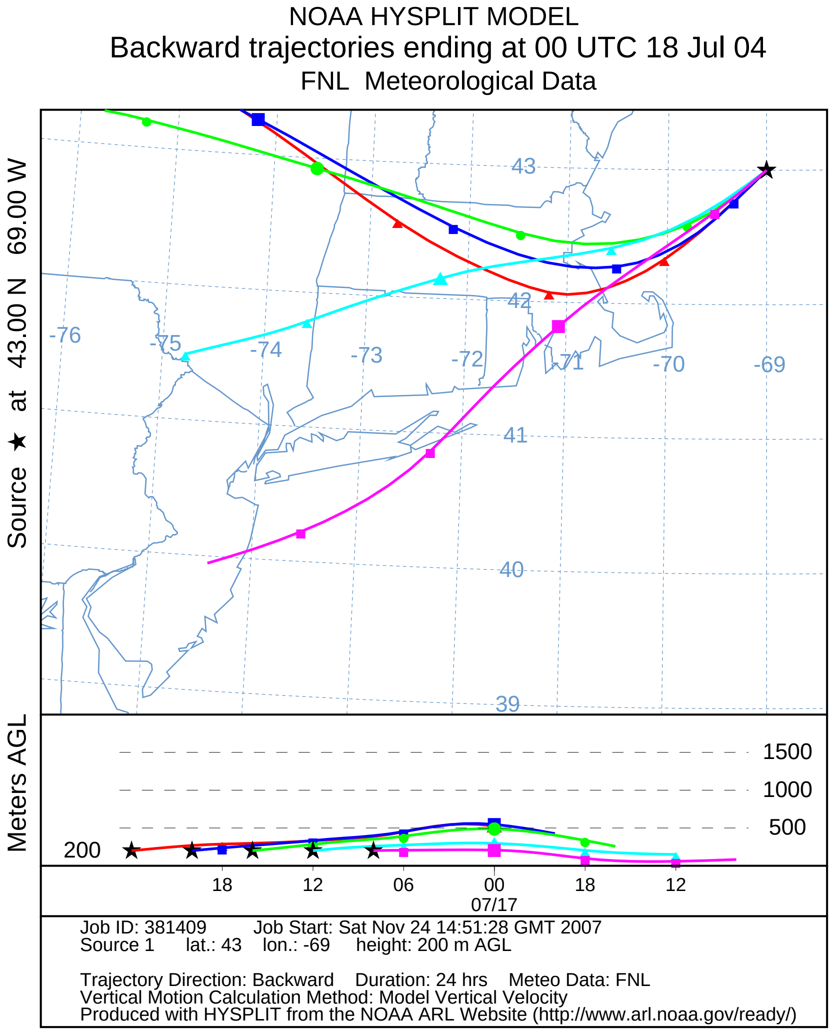

Figure 7.25: *HYSPLIT backward trajectories starting at 69° W and 43° N where the RV Ron Brown was located on 17 July 2004. The trajectories were calculated for 200 m height with a time step of 4 hours starting at 8AM UT on 17 July 2004 (purple), followed by 12PM (turquoise), 4PM (green), 8PM (blue) and 12AM on 18 July (red).*

the MIT values can partly be explained by the fact that CHOCHO is a secondary pollutant, i.e. formed from the airborne VOC oxidation, in contrast to NO_2 from NO_x emissions. Sustained CHOCHO formation from longer lived VOC precursor oxidation in combination with NO_x removal in the photochemical plume will thus lead to higher CHOCHO-to-NO_2 ratios downwind of emission sources. For a rough estimate of the extent of the NO_2 removal effect, we assume that the air mass needed half a day to reach the RV Ron Brown from the last emission source (with a distance of about 200 km and a wind speed of about 5 m/s). This is confirmed by backward trajectories which are shown in Figure 7.25. Furthermore, it is assumed that the air mass contained an OH concentration of about 2.6×10^6 molecules/cm^3. This number is the retrieved 24h average OH concentration during NEAQS-2002 for air masses that had been impacted by major urban areas such as New York City and Boston and by biogenic emissions in New Hampshire and Maine [Warneke et al., 2004]. Under these assumptions, only considering the reaction with OH, the lifetime of NO_2 amounts to 9.7 hours with a rate coefficient of 1.1×10^{-11} cm^3/s (from Sander et al. [2003] for 285 K and 1013 mbar). After 12 hours, only 29 % of the initial NO_2 is present. Together with the measured 2.5 times higher CHOCHO concentrations, the CHOCHO-to-NO_2 ratio would increase by a factor of about 9 which is one magnitude less than the measured ratio of the CHOCHO-to-NO_2 peaks. Thus, it is likely that there are other processes contributing to the high CHOCHO-to-NO_2 ratio than only NO_x removal by OH. Such processes could include additional NO_x sinks, reduced CHOCHO sinks over the Gulf of Maine compared to Cambridge, CHOCHO formed by photochemical oxidation, or an additional CHOCHO source to the atmosphere over the Gulf of Maine.

7.5 HCHO Measurements

Enhanced values of formaldehyde (HCHO) could be detected at all measurement sites. HCHO is produced by photochemical degradation of VOCs. Besides the oxidation of CH_4 (causing a quite constant formaldehyde background), enhanced HCHO values can be attributed to increased VOC degradation, from both natural (e.g. isoprene) and anthropogenic sources. Thus, HCHO can generally be measured in air masses from both rural and industrial areas. This was also apparent in the MAX-DOAS measurements. Yet, at all sites the HCHO values were significant lower when air masses came from the sea, where neither biogenic nor anthroponic sources are expected. On the RV Ron Brown, the highest values occurred when the vessel was close to the coast and air masses came from the mainland. Then ΔSCDs up to 8×10^{16} molec/cm^2 were measured. In contrast, the lowest HCHO ΔSCDs (2×10^{16} molec/cm^2) were retrieved during periods of fog. However, this decrease is partly caused by smaller light path differences between the viewing directions which inherently leads to lower differential slant column densities. Often HCHO values around 4×10^{16} molec/cm^2 could be measured.

The HCHO ΔSCDs of the sites at the mainland at 3° elevation angle are illustrated in Figures 7.26 and 7.27. The courses of the different sites show a relatively similar behavior indicating a large scale source, such as vegetation. At the measurement sites located at coastal mainland (Brookhaven, Narragansett, MIT and Thompson

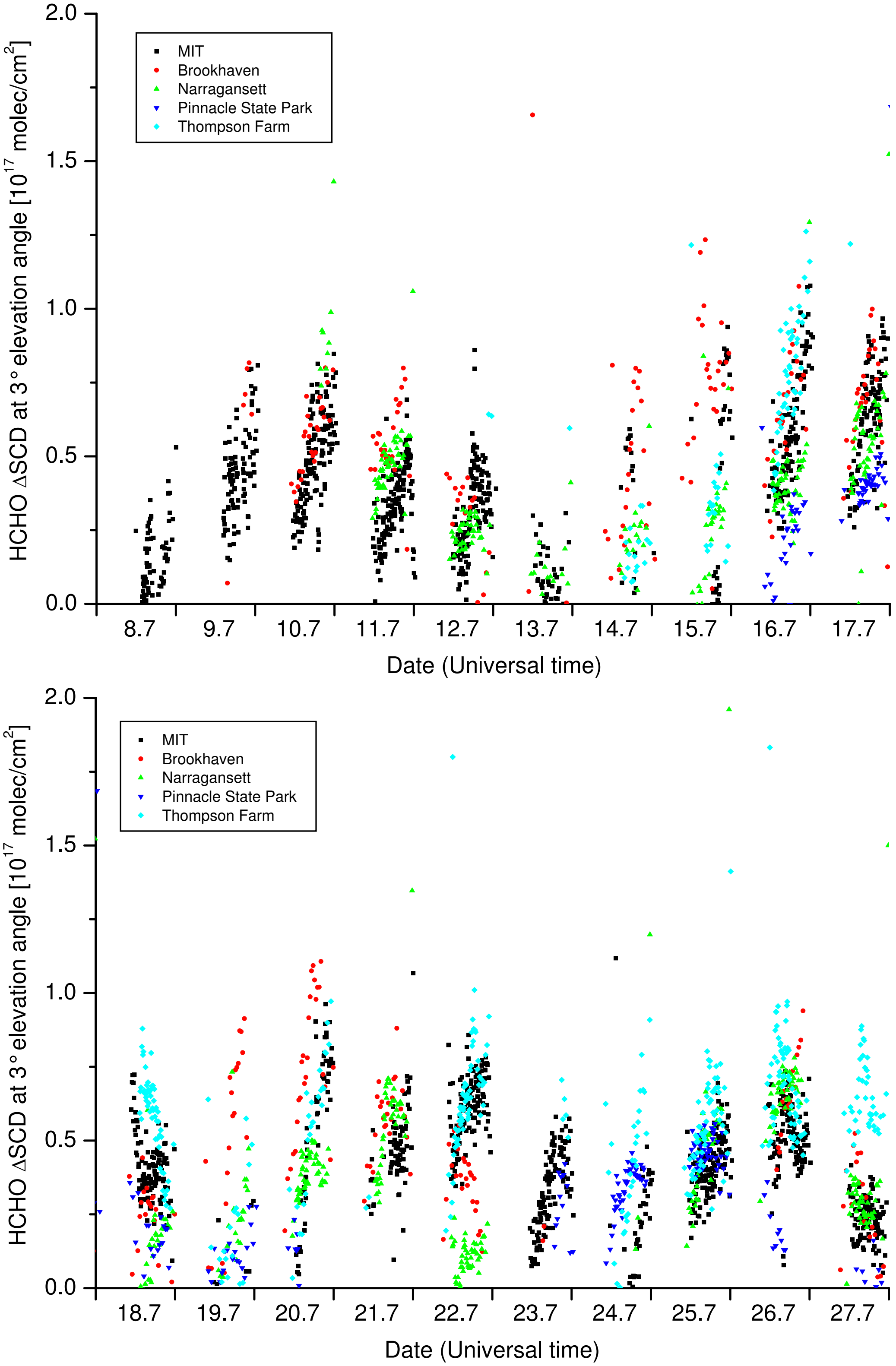

Figure 7.26: *HCHO ΔSCDs at 3° elevation angle for all locations at the mainland.*

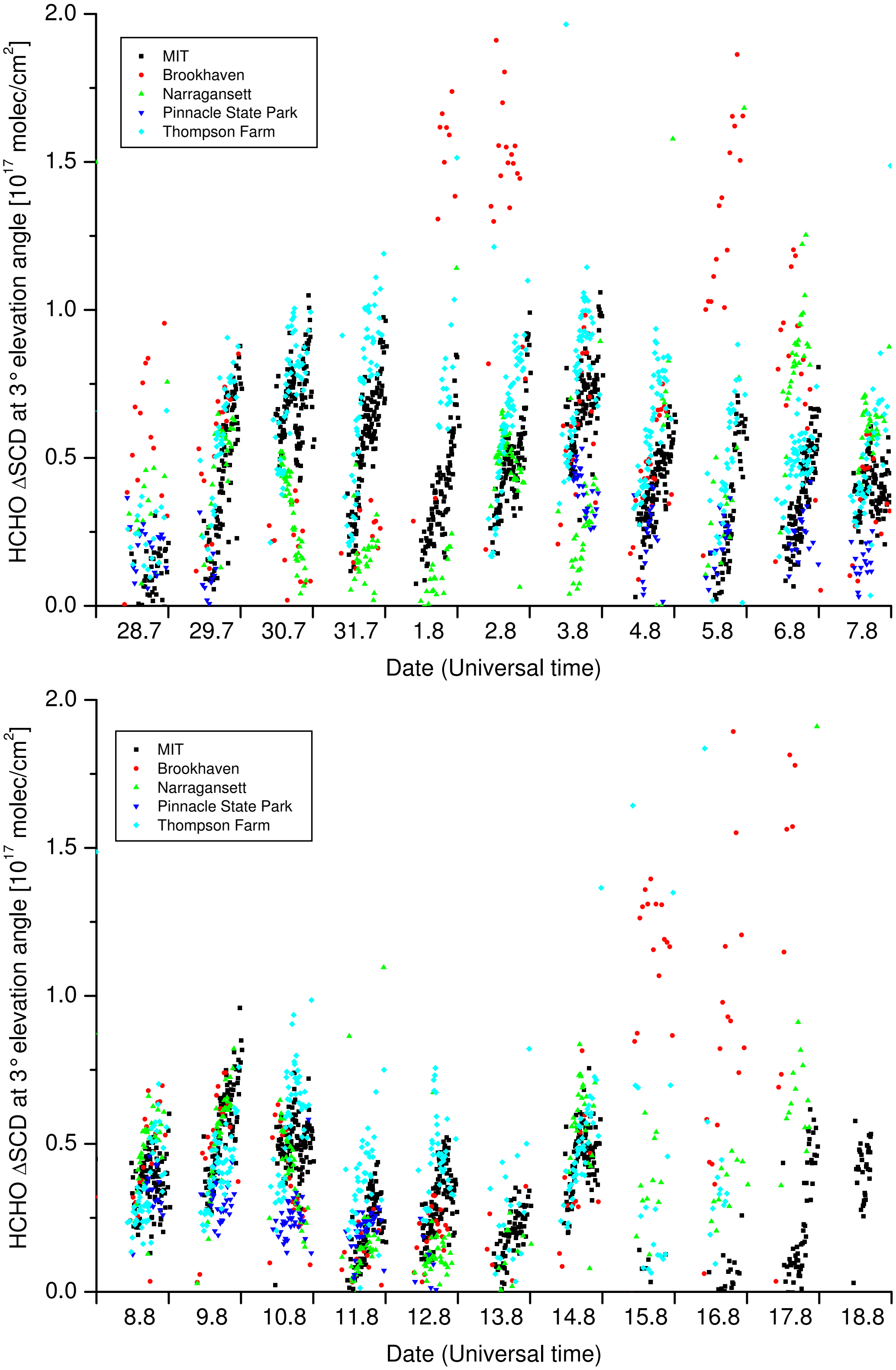

Figure 7.27: *HCHO ΔSCDs at 3° elevation angle for all locations at the mainland.*

Farm), low HCHO ΔSCDs occurred without exception when the measured air mass was transported from the sea. At Brookhaven this happened on 12, 13, 18, 22, 27, 30 and 31 July and on 1 early morning, 10 afternoon and 11 through 13 August with ΔSCDs between 4 and 5 × 10^{16} molec/cm^2. At this site, the highest values reached up to 2 × 10^{17} molec/cm^2 which happened on 2 and 5 August. These were also the highest ΔSCDs of all measurement sites in this campaign. At Narragansett, wind from the sea came on 12 through 15, 18, 19, 27 and 31 July as well as on 1, 11 through 13, 15 and 16 August leading to low ΔSCDs. The highest HCHO ΔSCDs were between 8 × 10^{16} and 1 × 10^{17} molec/cm^2 and were measured on 10 and 17 July as well as on 6 August when the air mass passed the Boston urban area. At MIT, the highest values also amounted to 1 × 10^{17} molec/cm^2, e.g. on 2 August. The lowest values were retrieved on 14, 15 morning, 18 and 27 July as well as on 15 and 16 August. Largely the same result could be found at Thompson Farm: The highest ΔSCDs were between 8 × 10^{16} and 1.2 × 10^{17} molec/cm^2, e.g. on 16 July. Low values occurred on 14, 15 morning, 18 and 27 July as well as on 15 and 16 August due to wind from the sea.

Pinnacle State Park is situated much more in the mainland so that a similar dependency from wind direction could not be observed there. Nevertheless, the lowest values (2 to 3 × 10^{16}) were retrieved when the wind came from south-east, namely on 18, 19, 26 and 27 of July. On the other days, HCHO ΔSCDs up to 6 × 10^{16} were measured. Such high values occurred on 16, 17 and 25 of July.

7.5.1 Comparison of HCHO and CHOCHO

Both HCHO and CHOCHO are produced by photchemical oxidation of hydrocarbons. However, HCHO is partly generated by emissions from vegetation and CHOCHO mainly by aromatics produced anthropgenically. Thus, the ratio of both can provide information on the nature of the sources of the air mass. Examplarily, the CHOCHO-to-HCHO ratio was calculated at MIT for the 26 and 27 July 2004. In Figure 7.28, additionally the ΔSCDs of HCHO and CHOCHO are plotted. These two days show the range of the ratio on days when CHOCHO was measured unequivocally. Days with ratios between 0.04 and 0.06 indicate a rather rural air mass while higher ratios typically arise from human activities (see Wittrock et al. [2006] and references therein). On 26 July, the ratios vary between 0.04 and 0.06 during the day not showing a strong influence of industrial activity. In contrast, on 27 July, the ratio reached values of over 0.1 in the morning going down significantly in the evening. Although the values are quite scattered, the ratio is clearly higher and in the range of anthropogenic influences. The ratios for all days (not shown) has a strong day-to-day variation with values between 0 and 0.12.

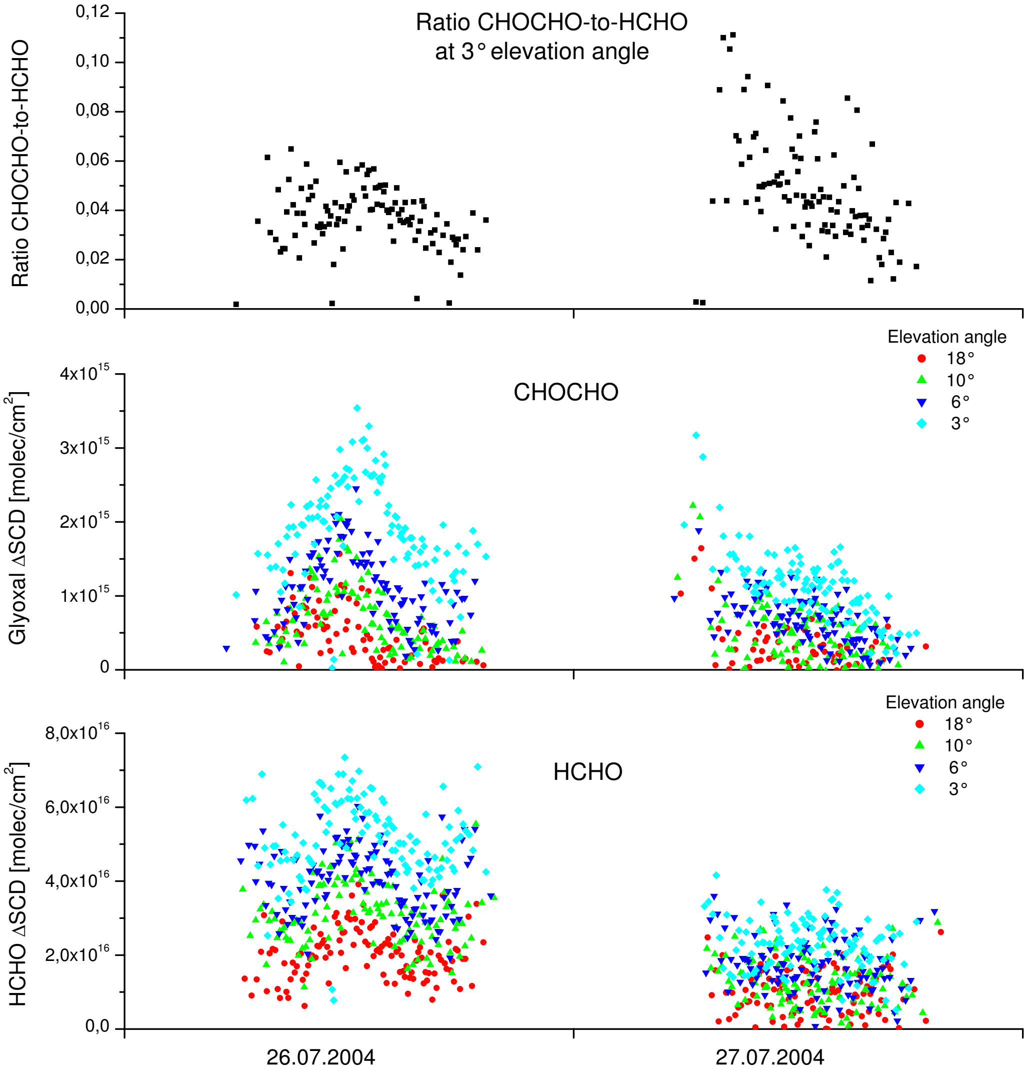

Figure 7.28: *CHOCHO-to-HCHO ratios (upper panel) and ΔSCDs of CHOCHO (middle) and HCHO (lower panel) on 26 and 27 July at MIT. The CHOCHO-to-HCHO ratios varied mainly between 0.04 and 0.1 throughout the campaign.*

7.5.2 Comparison of HCHO MAX-DOAS and In-situ Measurements

In the following, the MAX-DOAS measurements of HCHO will be compared to in-situ measurements of formaldehyde performed during ICARTT 2004. At Pinnacle State Park in-situ measurements of HCHO were performed with a commercial gas phase formaldehyde analyzer [Schwab et al., 2004]. Two identical diffusion scrubber/liquid fluorescence analyzers (DS/LFA) were operated side-by-side to evaluate instrument precision, simultaneously with a tunable diode laser system (TDLAS). From the side-by-side evaluation, a precision of the analyzers of about 25 % was concluded.

MAX-DOAS measurements on four relatively clear days were compared with these in-situ HCHO measurements. Thereby, the direct comparison approach was applied using the radiative transfer model Tracy to calculate mixing ratios averaged in height. For a better accuracy and also simplification, the MAX-DOAS data was averaged to about one value for every 10° interval of the solar zenith angle. For the estimation of the aerosol extinction, the simulation was performed at 360 nm where an absorption band of O_4 is located. For the retrieval of the HCHO mixing ratios the modeling was conducted for 339 nm featuring the strongest HCHO absorption band in the DOAS analysis (see section 6.4). In Figures 7.29 - 7.32, the retrieved HCHO mixing ratios from the MAX-DOAS measurements (red line) are compared with the data of the diffusion scrubber/liquid fluorescence analyzers (DS/LFA, blue line). On 24 July, also data of the tunable diode laser system (TDLAS) was available. The additional dashed black line shows the mixing ratios derived from MAX-DOAS measurements, however divided by a factor of 1.136. This was done due to the results from cross-calibration of ultraviolet and infrared spectral parameters of HCHO [Volkamer et al., 2005]. It was found that the HCHO cross-section of Meller and Moortgat [2000], which is used in the DOAS analysis of this work, is too small.

The measurements yielded mixing ratios of 0.5 to 5.0 ppb for the 4 chosen days, which is in the typical range for a rural site. They match best on 3 August where the highest mixing ratios are measured. Also, the course during the day mostly complies with each other. While on 3 August the corrected MAX-DOAS values are even closer to the in-situ measurements, they match worse on 24 July when also measurements with TDLAS were performed. However, the two in-situ measurements also show significant discrepancies between each other. On 9 August, a compliance can be recognized at least in the course. On 11 August, the DS/LFA measurements started at 5PM (Local Time) due to calibration measurements and yielded significant higher mixing ratios than the MAX-DOAS retrieval.

Generally, a good agreement in the diurnal course can be observed while the absolute values partly differ considerably. On the one hand, the simplified assumptions of the mixing ratio estimation could be the reason for the discrepancies. However, the matching diurnal courses lead to the assumption that that they rather play a subordinate role. On the other hand, the in-situ and the MAX-DOAS measurements monitor different air masses. While the in-situ measurements only detect HCHO in the ambient air, MAX-DOAS measurements, as a remote sensing method, measures through the whole atmosphere. Thus, a vertical gradient inherently leads to differences in the absolute values.

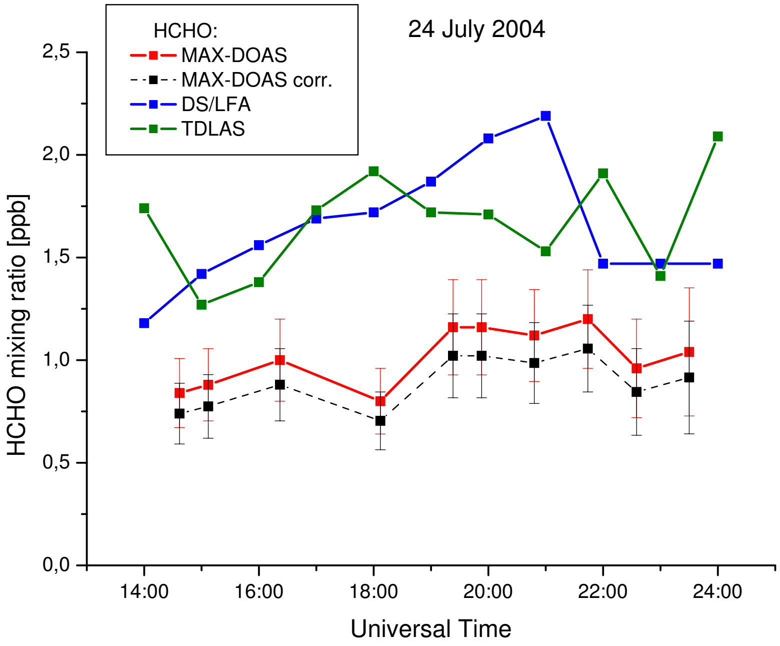

Figure 7.29: *Comparison of HCHO mixing ratios retrieved from MAX-DOAS measurements with and without a correction factor (dashed black and red line, respectively) with data of diffusion scrubber/liquid fluorescence analyzers (DS/LFA, blue line) and a tunable diode laser system (TDLAS) on 24 July 2004.*

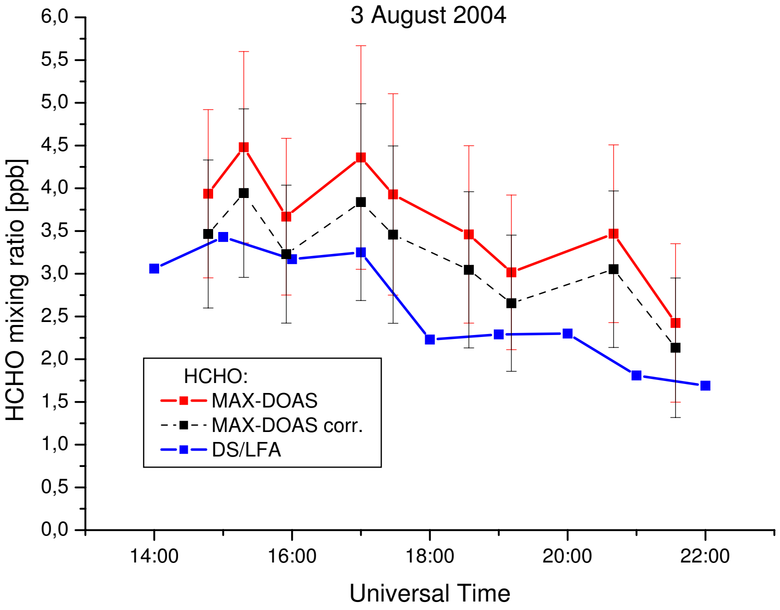

Figure 7.30: *Same as Figure 7.29, but on 3 August 2004.*

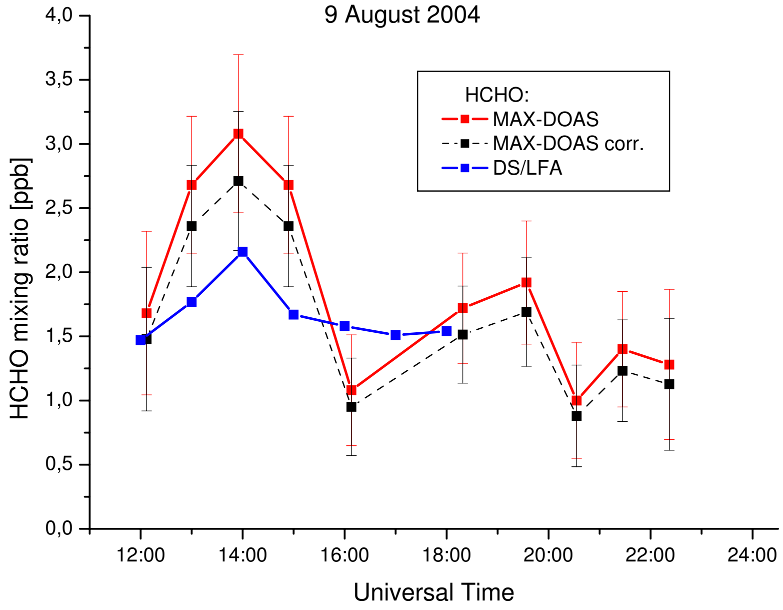

Figure 7.31: *Same as Figure 7.29, but on 9 August 2004.*

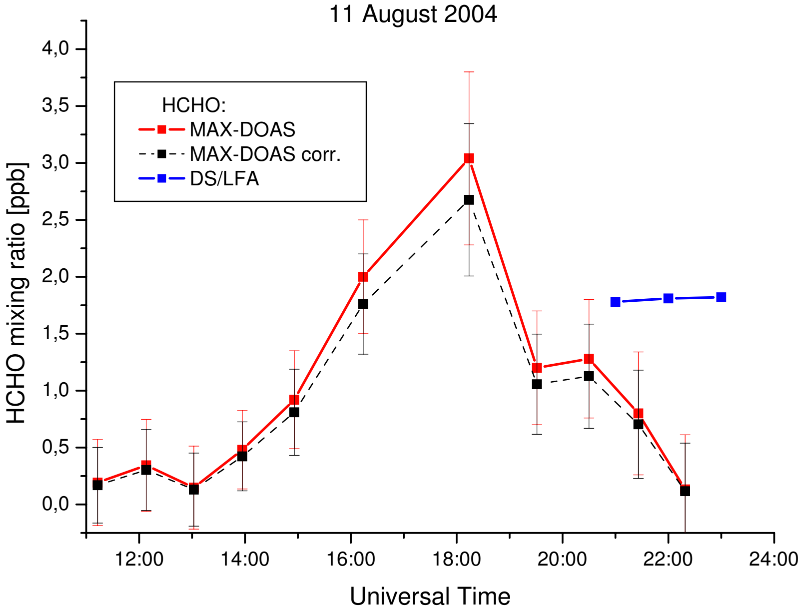

Figure 7.32: *Same as Figure 7.29, but on 11 August 2004. The DS/LFA measurements started very late on this day.*

7.6 SO_2 Measurements

SO_2 could be measured at Brookhaven, Narragansett, Thomson Farm and Pinnacle State Park. At MIT and RV Ron Brown, the wavelength range of the spectrographs did not cover the absorption bands of SO_2. However, due to the low intensity of sunlight in the wavelength range where SO_2 absorbs and interference with absorption of ozone, only strong SO_2 events could be detected. In Figures 7.33 and 7.34, the SO_2 ΔSCDs at 3° elevation angle are plotted for the whole campaign. At Brookhaven, elevated SO_2 ΔSCDs could be observed when the wind was coming from western direction. In these cases, emissions from New York City and north of New York City could be measured (see SO_2 point sources in the north-east of the USA shown in Figure 7.35). Values up to 1×10^{17} molec/cm^2 were retrieved on the same days when elevated NO_2 ΔSCDs occurred, namely on 15, 16, 19, 20 and slightly 31 July as well as 3, slightly 10 and, 14 August. Furthermore, emissions from a power plant on Long Island in the north-west of Brookhaven (especially "Northport") could be detected on 17, 19 and 29 July and 8, 9 and 14 August. On the other days when the wind direction was different no significant SO_2 values could be found.

At Narragansett, like for the NO_2 ΔSCDs, elevated values for the SO_2 ΔSCDs could be attributed to different sources: Wind from New York City brought SO_2 on 16 July and 10 August. On 15 July the trajectory was slightly south of New York City passing some SO_2 point sources. However, on that day the NO_2 ΔSCDs were particularly low which is not yet understood. Emissions from the power plant in the north-east ("Usgen") were measured on 11, 25 and 26 of July with maximum SO_2 ΔSCDs of 1×10^{17} molec/cm^2. However, on 14 July no elevated values could be retrieved for SO_2 though the trajectories passed the power plant site. On 20 July and 14 August, probably air masses from Orange were transported to the measurement site, and on 30 July from point sources south-west of New York City. Like for NO_2, higher SO_2 ΔSCDs were retrieved also on 2 and 6 August. While on 6 August the wind came from Boston urban area the source on 2 August could not be determined.

At Pinnacle State Park, SO_2 could be retrieved from plenty point sources around the site with maximum values around 1.2×10^{17} molec/cm^2. The highest values were found on 3, 10 and 11 August for air masses from west and south-west direction. On 19 July a small peak could be observed when the wind came from east. Probably, SO_2 emissions from the power plant "Goudey" were measured. Also when the wind came from north passing "Rochester" slightly elevated values could be observed as on 5, 6 and 7 August.

At Thompson Farm typical SO_2 ΔSCDs of around 5×10^{16} molec/cm^2 could be found. However, the spectral analysis of the July data frequently did not converge so that on some days no SO_2 ΔSCDs could be retrieved. Nevertheless, some peak events could be observed. On 12 and 13 August the wind came from the south and transported air masses from Boston urban area. On 25 July emissions from the power plant "Wyman" was measured and led to higher SO_2 values. On 26

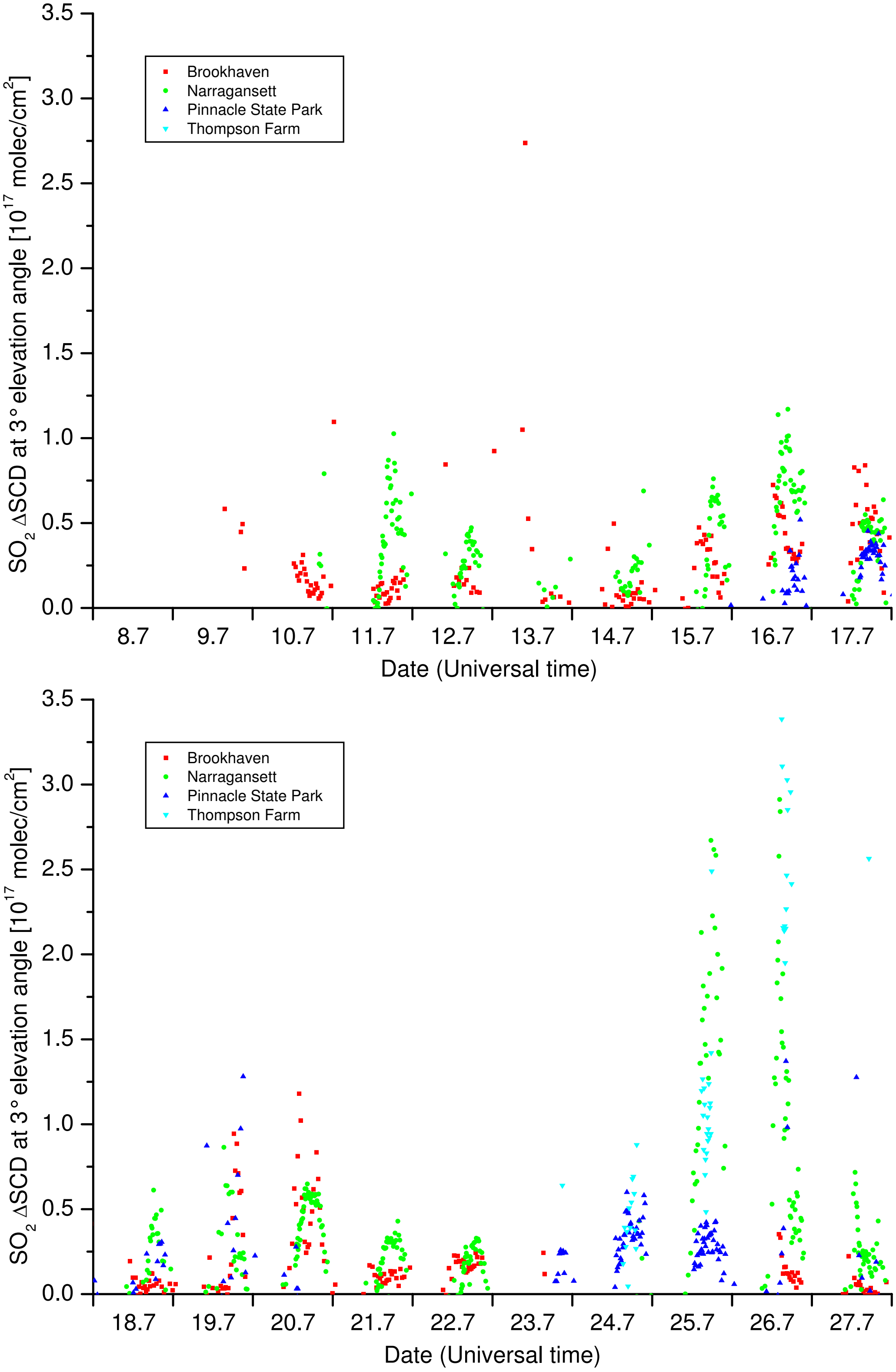

Figure 7.33: *SO_2 ΔSCDs at 3° elevation angle for all sites at the mainland except for MIT.*

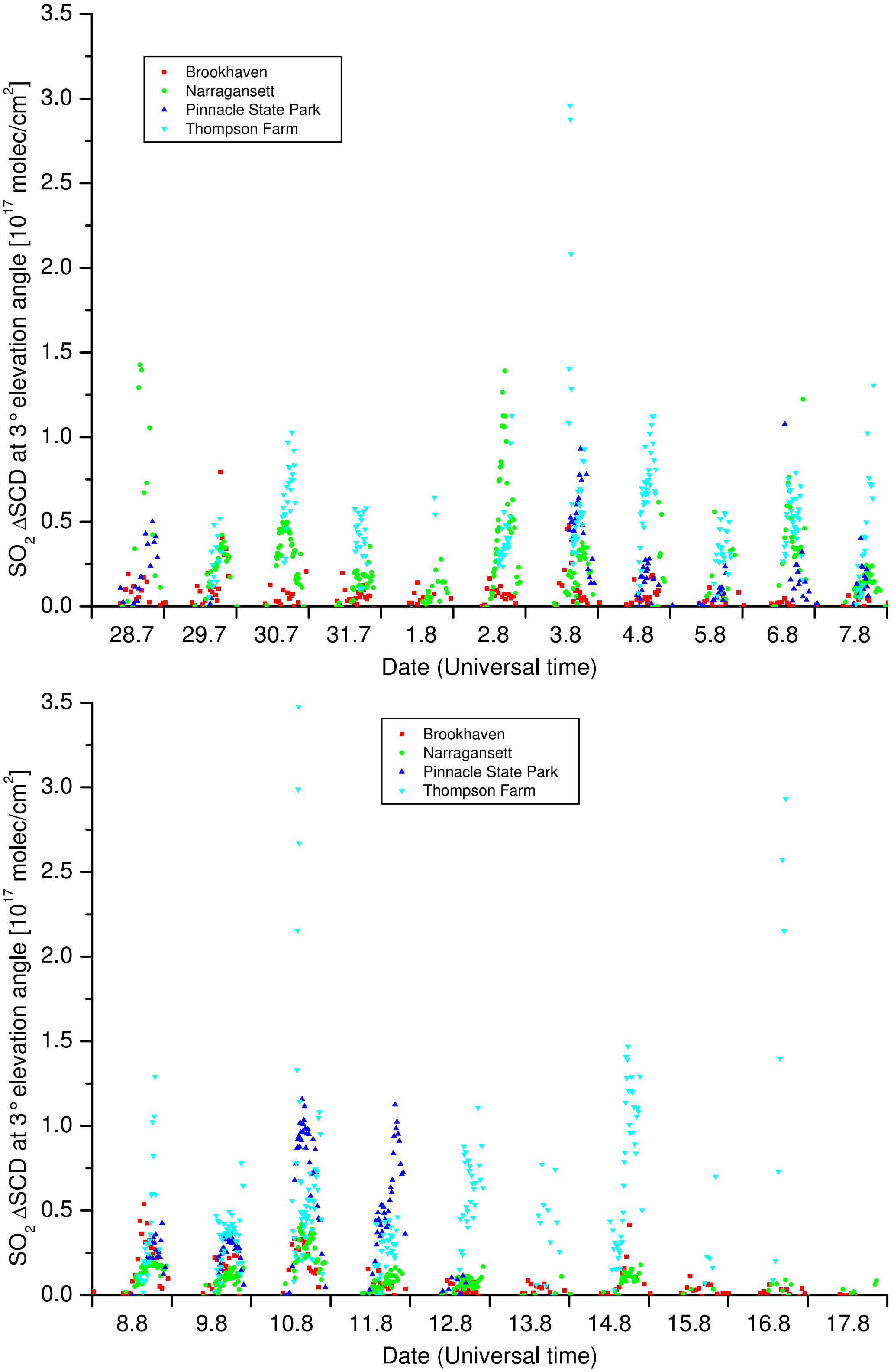

Figure 7.34: *SO_2 ΔSCDs at 3° elevation angle for all sites at the mainland except for MIT.*

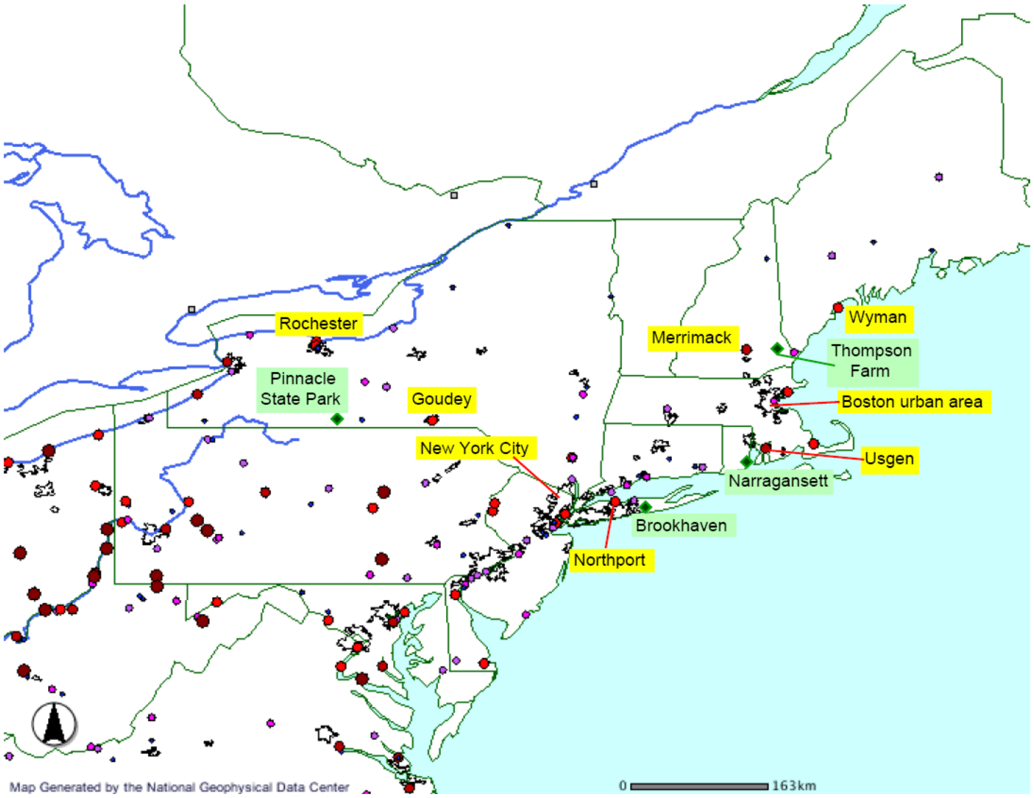

Figure 7.35: *SO_2 point sources in the north-east of the USA from 1999, provided by the National Environmental Satellite, Data, and Information Service (NESDIS). The emissions are signified by dots in dark red (higher emissions) over red to purple (lower emissions). Some sources which affected the measurements are labeled in yellow. The measurement sites are marked by green diamonds and labeled in green.*

July, SO_2 ΔSCDs of over 4×10^{17} molec/cm^2 were detected with air masses coming from the north. However, no potential source could be identified for this strong event which led to higher values also in the NO_2 ΔSCDs (see Figure 7.5). Maybe, a new emission source arised after the construction of the inventory of NESDIS in 1999 (see Figure 7.35). Yet, when wind came from the west the emissions of the power plant "Merrimack", which is closely located to the west, led to SO_2 ΔSCDs of up to 3.5×10^{17} molec/cm^2. This happened on 3, 10, and 14 August. An example is shown in Figure 7.36 with a SO_2 peak value of 3×10^{17} molec/cm^2 for 3° elevation angle at around 2:45PM UT. After 3:30PM UT only background SO_2 was present. Backward trajectories indicate that the wind came from south-west and turned to west for a short time. Then, the SO_2 plume from the power plant could be measured by the MAX-DOAS instrument before the wind slowly changed back to south-west. This continuously happened in the layer from 0 to 1.6 km which

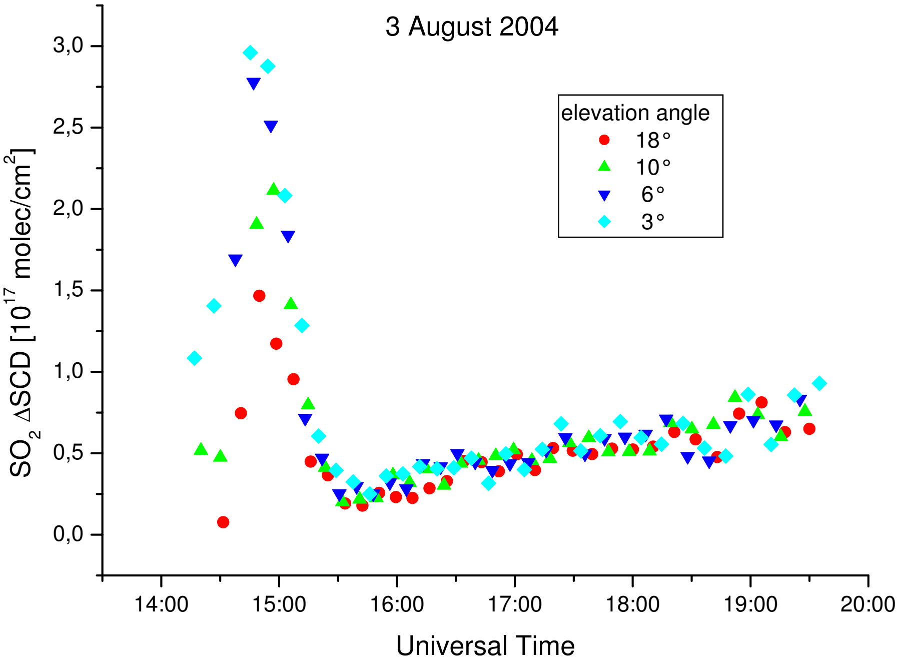

Figure 7.36: *MAX-DOAS measurements of a SO_2 plume on 3 August at Thompson Farm. The SO_2 ΔSCD peaked at around 2:45PM UT with values of 3×10^{17} molec/cm^2 at 3° elevation angle.*

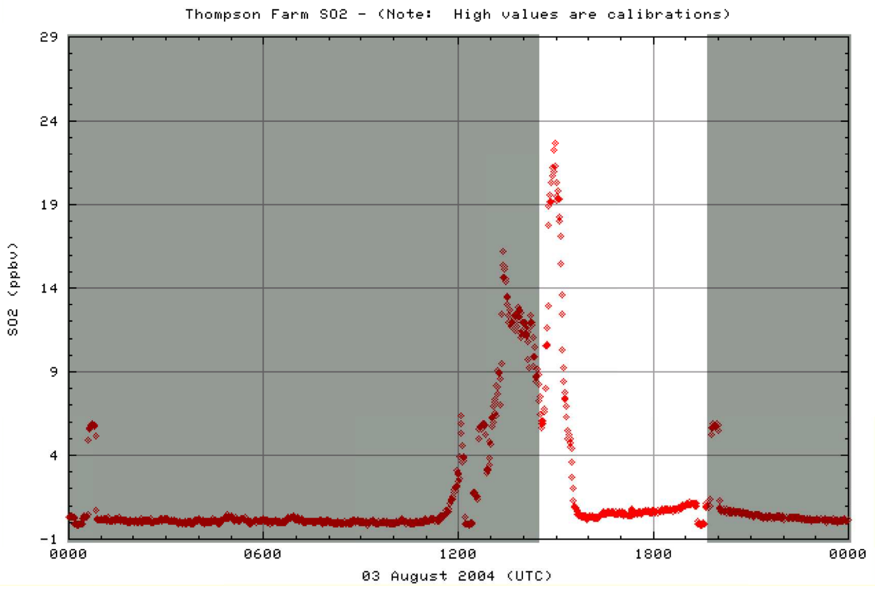

Figure 7.37: *In-situ SO_2 measurements at the AIRMAP observing station Thompson Farm (data available at http://airmap.unh.edu/data/) with a peak value of 23 ppb. The bright area indicates the time frame of the MAX-DOAS measurements.*

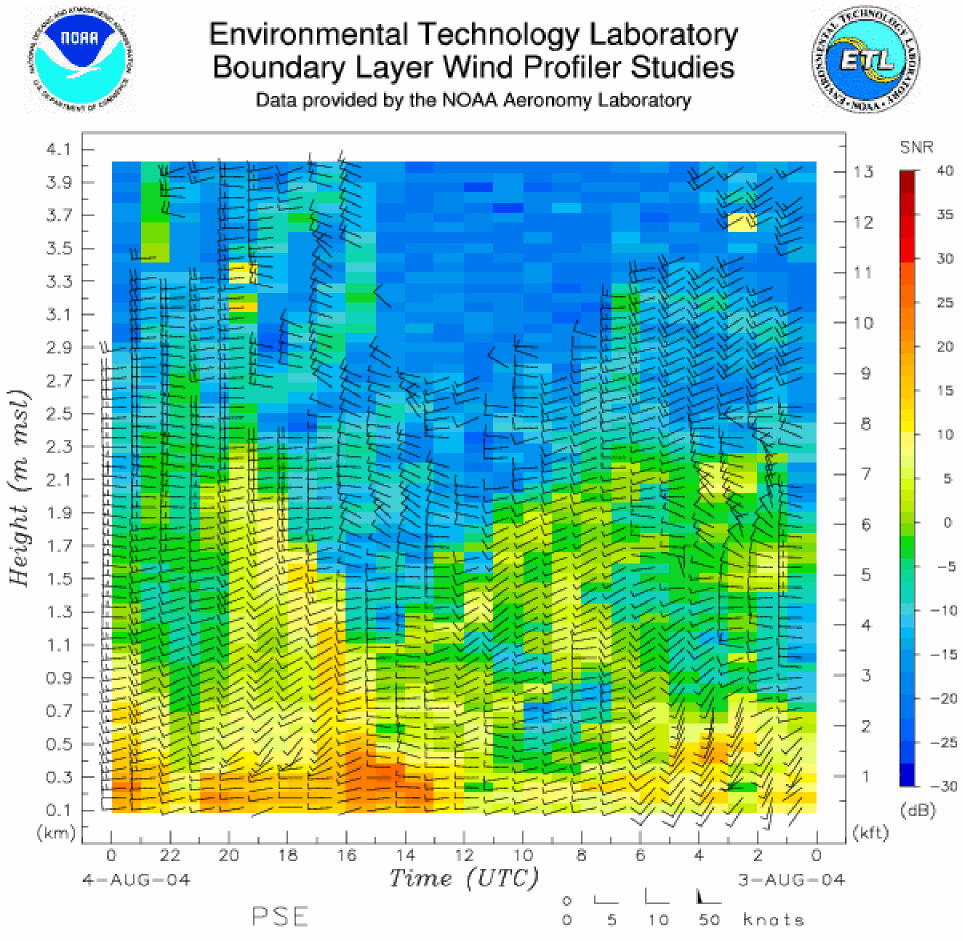

Figure 7.38: *Boundary layer wind profiler measurements from 3 August 2004 provided by the NOAA Aeronomy Laboratory. The arrows indicate the wind direction and strength. The course of time is from right to left.*

could be derived by boundary layer wind profiler studies provided by the NOAA[2] Aeronomy Laboratory (see Figure 7.38). The SO_2 peak could be confirmed by in-situ SO_2 measurements of the AIRMAP observing station Thompson Farm[3]. The bright area of the in-situ measurement in Figure 7.37 corresponds to the time when MAX-DOAS measurements were performed and shows the peak with a maximum mixing ratio of 23 ppb. Comparing the MAX-DOAS and the in-situ measurements the mixing height of the SO_2 plume could be estimated. Thereby, only the values of the 18° elevation angle were considered because the averaged scattering distance in the wavelength range of the SO_2 retrieval (303.5-317 nm) is relatively short.

---

[2] National Oceanic and Atmospheric Administration

[3] data available at http://airmap.unh.edu/data/

The averaged scattering distance depends on the aerosol load present in the air mass. The modeled estimation of the aerosol extinction in section 7.3.3 yielded an extinction coefficient of 0.2 km^{-1}. This value was used to model the averaged scattering distance for 310 nm by the radiative transfer model McArtim. For 3° elevation a distance of only 3.3 km, and for 18° elevation angle of 5.9 km was calculated. Yet, the comparison for the 18° elevation angle values resulted in a path through the layer of 3.8 km, which corresponds to 22.4 km at 3° elevation angle. Thus, it can be assumed that at lower elevation angles the light path through the SO_2 plume is considerably shortened due to scattering and the corresponding ΔSCDs cannot be taken for the retrieval of the layer height (even in case of no aerosols present in the atmosphere the averaged scattering distance amounts to 8.2 km). The comparison of the in-situ measurements and the MAX-DOAS measurements at 18° elevation angle yielded a layer height of 1.2 km (considering 1 ppb as 2.51×10^{10} molec/cm^3 at 293 K and 1013 mbar).

7.7 Ozone Titration Event

A special event was detected at URI Narragansett on 28 July 2004 which lasted until the morning of 29 July. The MAX-DOAS measurements of O_4 and NO_2 shown in Figure 7.39 exhibited atypical behaviors. Exceptionally, a fixed reference was used for a better illustration and accordingly dSCDs are shown. On 27 and the afternoon of 29 July, the typical U-shape can be observed in NO_2 dSCDs and especially in O_4 dSCDs. The U-shape arises due to a longer light path through the upper part of the atmosphere at larger solar zenith angles. Furthermore, the values of the different elevation angles are separated, in particular for O_4.

However on 28 July and the morning of 29 July, the dSCDs of both O_4 and NO_2 showed a special behavior. The O_4 dSCDs of the different elevation angles were not separated like on the day before. Hence, the visibility was very low for every looking direction due to scattering on aerosols. Furthermore, the O_4 dSCDs were relatively high. This matches with increased probability for multiple scattering present near the surface, as if e.g. low altitude clouds are present. Also the NO_2 dSCDs were enhanced compared to other days. Like usually, the NO_2 dSCDs show a strong dependency on the elevation angle. The dSCDs of lower elevation angles are higher than the dSCDs of higher elevation angles. This is especially remarkable since this separation at different elevation angles could not be observed for the O_4 dSCDs which are an indicator for the light path distribution. Thus, the presence of a shallow layer with high NO_2 concentrations close to the surface is likely. Additionally, low radiances could be observed which is expressed by the length the integration time that was adapted automatically to the light intensity in the spectra. On 28 July the integration times were particularly long. In Figure 7.39 can be observed that the number of measurement points are significantly lower on 28 July than on the days

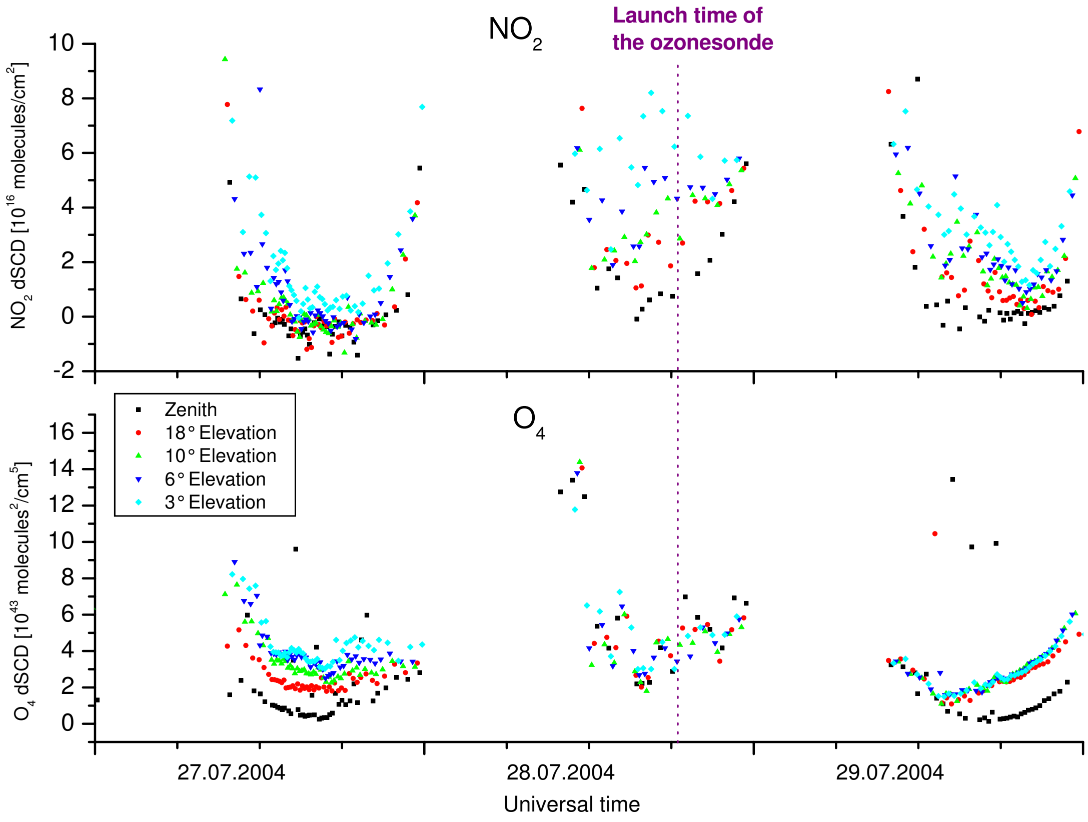

Figure 7.39: *MAX-DOAS measurements of NO_2 and O_4 from 27 to 29 July at Narragansett. Exceptionally, a fixed reference was used for a better illustration so that on 27 and 29 July the dSCDs exhibit a typical U-shape due to absorption in the upper part of the atmosphere. On 28 July, a high aerosol load as well as high NO_2 dSCDs can be observed. The launch time of an ozonesonde is shown in purple.*

before and afterwards.

At URI Narragansett also ozone profiles were measured daily around 6PM UT using an Electro-Chemical Cell ozonesonde (En-Sci Inc., model 2Z) with a Vaisala RS-80, GPS-equipped radiosonde. 1% unbuffered KI was used in the cathode cell, and saturated KI in the anode cell. The sonde was prepared several days earlier using procedures developed by the NOAA CMDL group. Figure 7.40 shows the O_3 mixing ratio up to 2 km on July 28 at 6:30PM UT. The surface air temperature was 18.7° C in persistent fog, and the profile was at or near saturation to above 13 km. The measured ozone was <1 ppb up to 200 m above sea level, near the base of a 500 meter thick, 2.5° C temperature inversion (see Figure 7.41). In this layer the ozone mixing ratio increased to 46 ppbv. The winds were weak, generally less than 4 m/s from the north-north-west below the inversion, veering to south and south-west

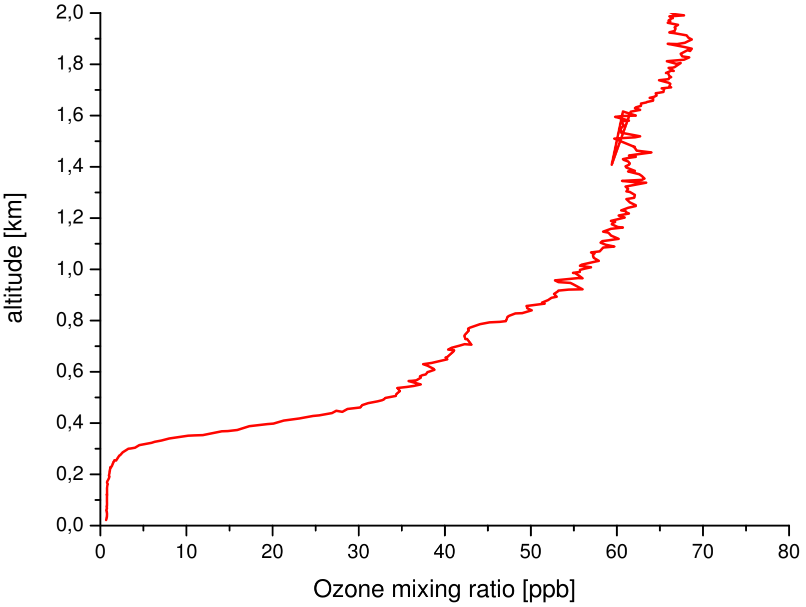

Figure 7.40: *Ozonesonde measurement from 28 July 6:30PM UT at Narragansett. The plot of the first 2 km shows very low ozone values up to about 200m. The day before about 35 ppt where measured in the first 200 m.*

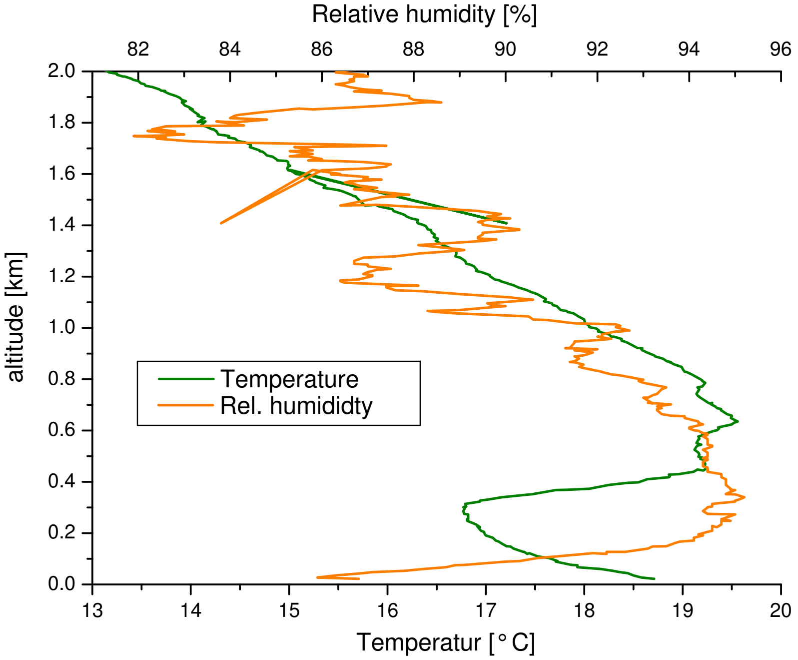

Figure 7.41: *Temperature and relative humidity from the Ozonesonde measurement from 28 July 6:30PM UT at Narragansett for the first 2 km.*

above this layer. Ozone mixing ratios varied from 50-90 ppb from 1 km to 13.5 km, near the tropopause. Furthermore on July 28 reduced light intensity in the presence of surface fog and deep clouds were observed [John Merrill, pers. comm.].

To further investigate this event, HYSPLIT backward trajectory calculations were performed. The trajectories for 28 July at ground level as well as 100 m above ground level showed air masses coming from south to south-west the whole day. This corresponds to the wind direction measurements of the ozonesonde above the inversion layer, but not to wind direction in the shallow air mass below the inversion. Thus, assumably the HYSPLIT model could not resolve this layer and the air mass below the inversion is assumed to come from north to north-west. However, the trajectories showed significant changes in the wind directions in the night to 28 July and during the morning of 29 July. This matches with start and end time of this special event derived from the MAX-DOAS measurements.

Eventually, all observations indicate an ozone titration event where ozone is degraded and not produced sufficiently to reach significant concentrations. In this event, probably ozone was destroyed by NO producing large amounts of NO_2. Precondition of an ozone titration event is a strong inversion so that the air masses cannot mix and balance out the loss of ozone. Furthermore, photochemical activity has to be reduced because otherwise the photolysis of NO_2 would produce enough ozone. Moreover, the exposure of air masses to vegetation accelerates the degradation of ozone due to adhesion of ozone on plants and its adsorption via stomata, hence dry deposition. Since in the the north or north-west of Narragansett much vegetation is present all assumptions are given to conclude that an ozone titration event has occurred.

Ozone titration events are not rarely observed in cities in the early morning where large amounts of ozone reducing NO are available and the sunlight is too weak to produce ozone photochemically. However, in more rural areas, such as at Narragansett this is a remarkable and special event. Also, the duration of more than one day is an atypical phenomenon. Unfortunately, it is not clear where exactly such large amounts of NO came from. However, the NO flux was steady enough to last at least 30 hours.

8 Results from MILAGRO 2006 Field Measurements

8.1 Objectives of the MILAGRO 2006 Campaign

The Megacity Initiative: Local and Global Research Observations (MILAGRO) 2006 field campaign had the goal to observe and quantify the fate of anthropogenic pollutants emitted from Mexico City, the world's second largest city with more than 20 million inhabitants. Since the number of urban areas and Megacities (cities with at least 10 million inhabitants) increases continuously the pollution caused by such dense anthropogenic activity is getting more and more important. The MILAGRO 2006 campaign was supposed to investigate this pollution in order to manage better its negative impacts on air quality. Furthermore, Megacities become more and more important since they are also major sources of aerosols and greenhouse gases that are impacting regional and global scale climate. Mexico City is especially suited to investigate the transformation of pollutants because its location at 2200 m and at only about 20° northern latitude favors photochemical transformations due to higher solar radiation. Furthermore, the topography with high mountains to the west and east of Mexico City favor rapid accumulation of the pollutants.

The MILAGRO 2006 campaign is a continuation of Mexico City Metropolitan Area (MCMA) 2003 and is split in four coordinated components:

MCMA-2006 (Mexico City Metropolitan Area - 2006) was led by the Molina Center on Energy and the Environment, to examine emissions and boundary layer concentrations within the Mexico City Basin by gathering measurements on aerosols, VOCs and other gases, meteorological and solar radiation parameters. The MAX-DOAS measurements were part of MCMA-2006.

MAX-Mex (Megacity Aerosol Experiment in Mexico City) examined the evolution of aerosols and gas-aerosols interactions in the immediate urban outflow including measurements from a G-1 aircraft and a ground station.

MIRAGE-Mex (Megacity Impacts on Regional and Global Environments) investigated the evolution of the Mexico City plume on larger regional scales from ground stations, aircraft, and satellites.

INTEX-B (Intercontinental Chemical Transport Experiment - Phase B), studied the evolution and transport of pollution on global scales.

In the MILAGRO campaign more than 60 institutions mainly from the USA and Mexico took part. The field campaign was scheduled for 1 through 30 March 2006.

8.2 Measurement sites

In the framework of MCMA-2006 several MAX-DOAS measurement sites were set up by the University of Heidelberg in and around Mexico City. Thereby, the Schwampel and 5 Mini-MAX-DOAS instruments were used. However, effectively only three Mini-MAX-DOAS instruments were operated due to instrument breakdowns (see below). Figure 8.1 shows the Mexico City metropolitan area from satellite perspective.To the east and west of Mexico City, in dark green high mountains of over 3000 m height can be seen. The MAX-DOAS sites are marked with yellow dots. Additionally, the viewing directions are indicated by colored lines starting at these points. The measurement names (white) and periods (colored) of each site are labeled next to the points.

The Schwampel instrument (blue color in Figure 8.1) was located on the rooftop of a building in the "Instituto Mexicano de Petroleo" (IMP) at 19.48° northern latitude and 99.13° westerly longitude in the northern part of Mexico City. It is denoted with T0 and was one of three so-called supersites. The three telescopes which measured simultaneously pointed approximately to the north, south and west and were mounted on a wooden box to guarantee a free view also at lower elevation angles (see Figure 5.7). The Schwampel instrument was installed from 2 March through 11 April 2006.

All the other MAX-DOAS instruments were Mini-MAX-DOAS instruments. They are labeled red and yellow in Figure 8.1, whereby the yellow color indicates the Mini-MAX-DOAS instrument which had a wavelength range from about 330 to 460 nm instead of about 290 to 420 nm, like the others. Thus, the yellow labeled Mini-MAX-DOAS instrument covered the absorption structures of CHOCHO.

Unfortunately, short circuits in the electronic boards let break four of the five Mini-MAX-DOAS instruments down. The reason for the short circuits is still unclear. Two of the devices were broken sustainably for the whole measurement campaign. The other two could be repaired by soldering whereby one of them still had problems to stabilize the cooling temperatur of the spectrograph-detector unit throughout the campaign which was recognized afterwards. The latter was the device which covered the wavelength range of CHOCHO (labeled yellow in Figure 8.1). So, only one of the repaired instruments could be used for the measurements. In total, only two of the originally planned 5 Mini-MAX-DOAS instruments could be used. They were set up at the supersites T1 and T2 during MILAGRO 2006. Later they were installed in the north and south-east of Mexico City for a couple of days, which however was not in the focus of MILAGRO 2006.

The supersite T1 was situated in the north of Mexico City on the area of the

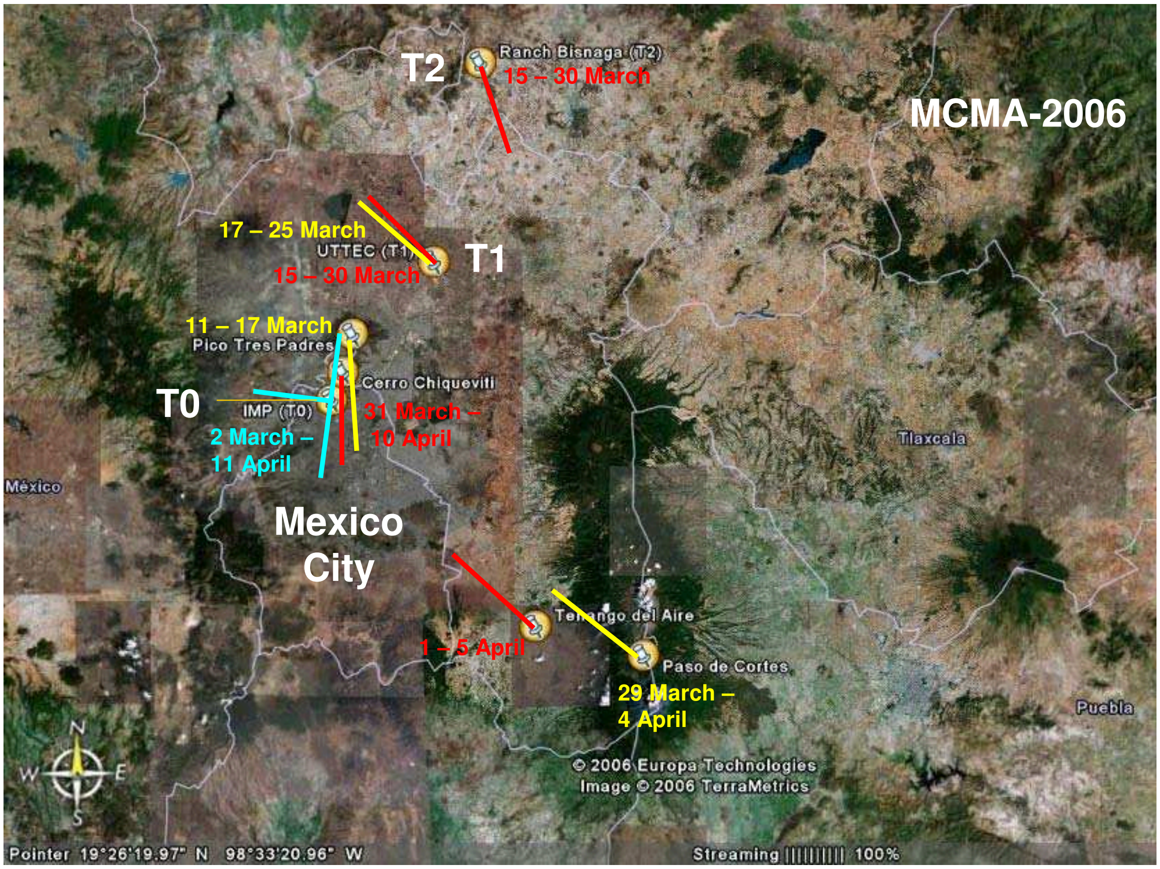

Figure 8.1: *MAX-DOAS sites set up by the University of Heidelberg in the framework of the MILAGRO 2006 campaign marked on a satellite picture. The MAX-DOAS sites are marked with yellow dots and the viewing directions are indicated by colored lines starting at these points. The measurement names (white) and periods (colored) of each site are labeled next to the points.*

Universidad Tecnológica de Tecámac. It was located about 30 km north-east of T0 at around 19.70° N and 98.98° W. The Mini-MAX-DOAS instrument was fixed on the roof of a trailer and pointed to north-west (about 310° from north). The measurements were performed from 15 through 30 March 2006 with a failure between 19 through 25 March.

On the ranch "Bisnaga" further north at 20.01° N and 98.91° W (about 63 km north-east from T0) the third supersite T2 was set up. The Mini-MAX-DOAS instrument was screwed on a wodden board which was stabilized by stones (see Figure 8.2). It pointed approximately to south (about 170° from north) into a wide valley. It measured from 15 through 30 March with 16 and 17 March as failure days.

The measurements were performed at elevation angles of 1°, 3°, 6°, 10°, 20°, 45° and towards the zenith. At T2 additionally an elevation angle of -1.5° was chosen in

Figure 8.2: *Mini-MAX-DOAS setup at T2. The instrument was screwed on a wodden board which was stabilized by stones. It pointed approximately to south (about 170° from north) into a wide valley.*

order to measure the air masses near to the ground of the valley. The complete time series of ΔSCDs of NO_2, HONO, HCHO, CHOCHO and O_4 of all sites are attached in Appendix A.2. The following sections highlight the most important results of these measurements. In particular, they demonstrate the transformation of the polluted air masses while being transported across the different sites. Furthermore, horizontal gradients and the photochemical processing will be investigated.

8.3 NO_2 Measurements

Enhanced NO_2 ΔSCDs could be measured at T0, T1 and T2. At T0 (southern direction) the NO_2 ΔSCDs are largest with values of up to 5×10^{17} molec/cm^2 in the beginning of April. These values are about double as high as the peak values in the ICARTT 2004 campaign. Typically the maximum ΔSCDs varied between 2 and 4 $\times 10^{17}$ molec/cm^2. At all elevation angles, a diurnal cycle with a significant morning peak and increasing values in the evening could be observed (as instance see Figure 8.10) which is probably caused by traffic emissions. Figure 8.3 shows the ΔSCDs at 3° elevation angle for the period of 15 through 30 March when measurements for all three sites T0, T1 and T2 were available. The diurnal cycle can also be found

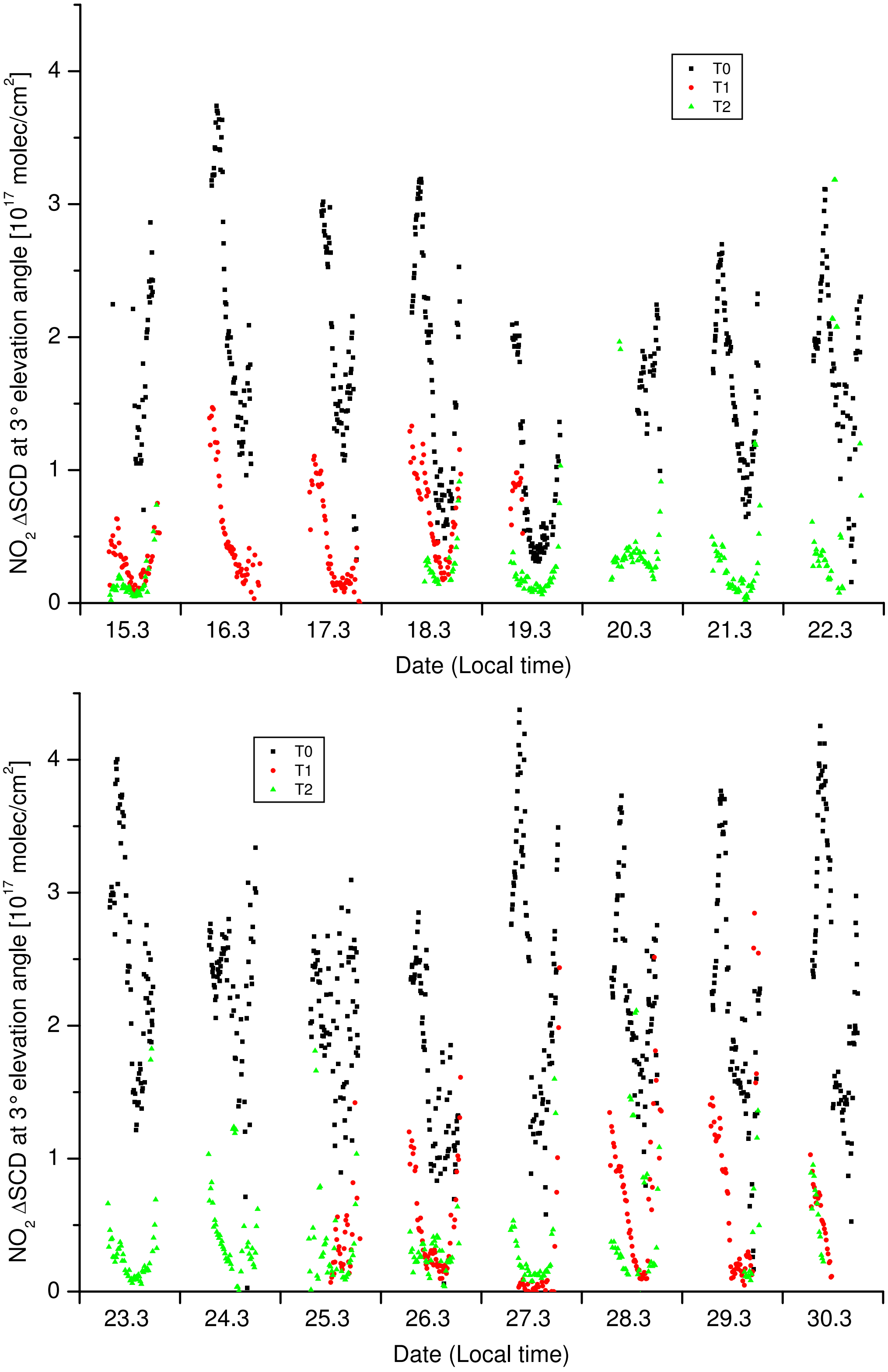

Figure 8.3: *NO_2 $\Delta SCDs$ at 3° elevation angle from 15 through 30 March for the instruments at T0, T1 and T2.*

in the observations at T1 and T2 whereby the peak values are 2 to 4 times smaller than at T0 which can be explained by the distance to Mexico City. NO_2 emitted in Mexico City is chemically degraded and diluted before it can be measured at T1 and T2, respectively.

Surprisingly at T0, the NO_2 ΔSCDs do not follow a weekly cycle with lower values on weekends or at least on Sundays. 19 and 26 March 2006 were Sundays, with lower values at least on 19 March (see Figure 8.3). However, the 19 March was affected by relatively strong wind [Fast et al., 2007] which probably has led to the reduction rather than less emissions. Also for other Sundays (not plotted in the figure), no significant NO_2 ΔSCD reduction was observed, except on 9 April which assumably is an outlier. At T1 and T2, the measurement period was too short and too often interrupted to derive a conclusion concerning a weekly cycle.

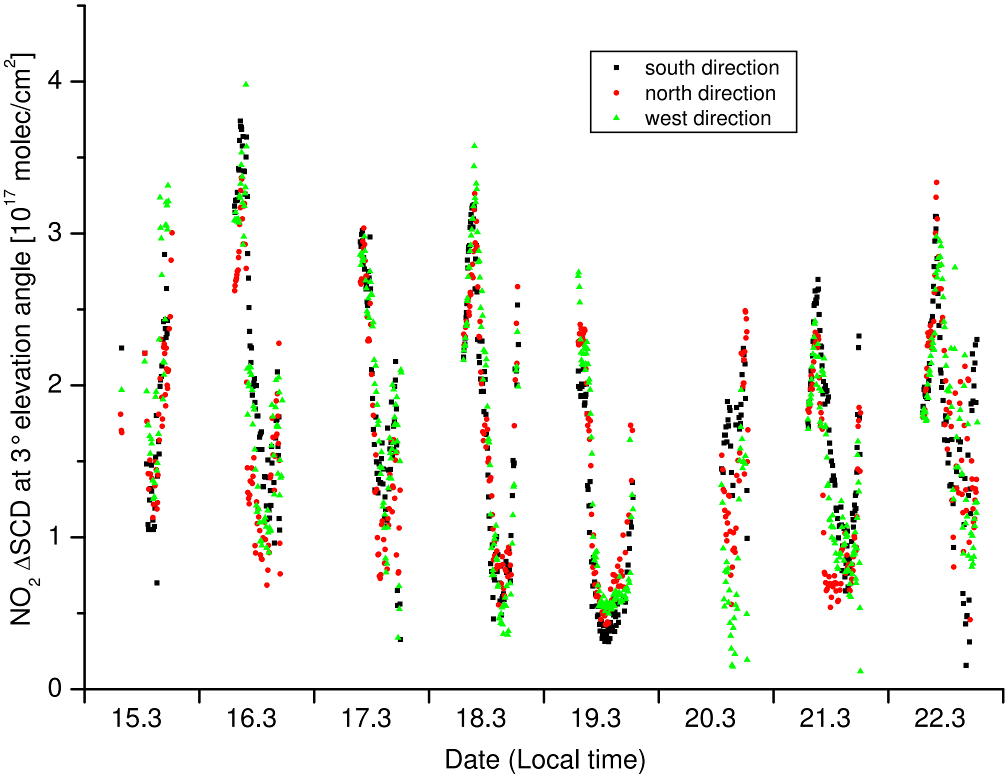

Figure 8.4: *NO_2 ΔSCDs at 3° elevation angle from measurements pointing to the south, north and west.*

At T0, ΔSCDs at three azimuth angles (south, north and west) were measured which can provide information on the horizontal distribution of NO_2. Especially, differences between the south and the north direction might have benn expected because the measurement site was located almost at the northern border of Mexico City. In Figure 8.4, the NO_2 ΔSCDs at 3° elevation angle of the different azimuth directions are compared for one week exemplarily. Generally, they show a similar course, however none of them exhibits systemic higher or lower values than the others. Thus, the NO_2 content in the air did not show a systematic horizontal gradient in the scope of the MAX-DOAS instrument.

In order to quantify the NO_2 values, the MAX-DOAS NO_2 ΔSCD were converted in tropospheric VCDs by applying the geometrical differential air mass factor to the measurements of 20° elevation angle. The selection of this rather high elevation angle is considered as a compromise between good signal to noise values and least influence of aerosols. Thereby, is is assumed that light is not scattered within the NO_2 layer. The geometrical NO_2 ΔAMFs were calculated by the approximation $\frac{1}{\sin(20°)} - 1$, yielding about 1.92. The tropospheric NO_2 VCDs for T0, T1 and T2 from 15 March through 30 March are illustrated in Figure 8.5. At T0, like already observed in the NO_2 ΔSCDs for 3° elevation angle, the tropospheric VCD values exhibit strong morning and smaller evening peaks. Thereby, the maximum values vary mostly between 8×10^{16} molec/cm^2 and 1.2×10^{17} molec/cm^2. During ICARTT 2004, smaller peak tropospheric NO_2 VCDs of 8×10^{16} molec/cm^2 were found at MIT indicating less NO_2 pollution in the Boston urban area than in Mexico City. At T1 and T2, the tropospheric VCDs are much smaller except for some outliers and typically amount to not more than 3×10^{16} molec/cm^2. The values at T2 seem to be slightly smaller than at T1 which would be expected because of the larger distance from Mexico City of T2.

Similar to the ICARTT campaign, the tropospheric NO_2 VCDs were compared to DOAS satellite measurements from SCIAMACHY. Figure 8.6 shows the tropospheric NO_2 VCDs of the three azimuth measurement angles of the Schwampel instrument versus the tropospheric VCDs derived from satellite [Steffen Beirle, pers. comm.]. Thereby, the acquisition times of the MAX-DOAS values corresponds to the overpass times of the satellite. Additionally, a one-to-one line is drawn in the figure. As a result of the comparison, the MAX-DOAS measurements mostly have clearly higher values than the VCDs from satellite. This can partly be explained by shielding effects from clouds which occurred e.g. on 30 and 31 March. Clouds might also have caused the difference in the MAX-DOAS VCDs between south and north direction on these days. Furthermore, because of the spatial resolution of the satellite instrument of 30×60 km^2 it averages the NO_2 VCD over a large area including also regions outside the center of Mexico City. This is shown in Figure 8.7 where the three most excentric pixels are drawn (white rectangles), which still include the MAX-DOAS site T0. It can be recoginzed that each rectangle is larger than the extent of Mexico City. Thus, any satellite measurement measuring the Mexico City area also includes some part of the environment. The most excentric pixel in Figure 8.7 even covers hardly Mexico City. Therefore, the relatively good accordance on 5 March (at least in west and south measurement direction) is surprising and can only be explained by a counteracting effect, e.g. aerosol influence.

Also active DOAS measurements were performed at T0 during MILAGRO 2006

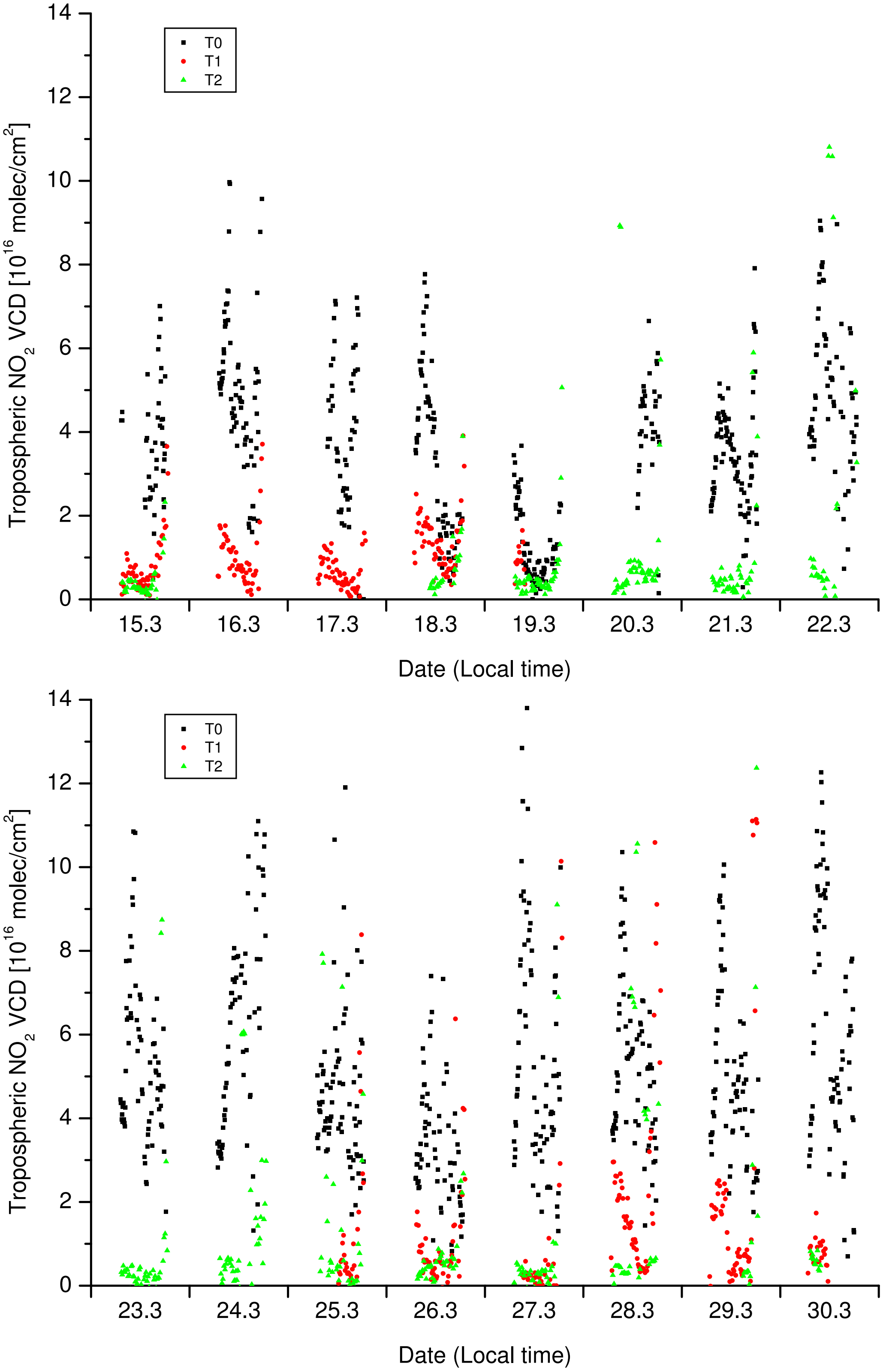

Figure 8.5: *Tropospheric* NO_2 *vertical column densities from 15 through 30 March for the instruments at T0, T1 and T2.*

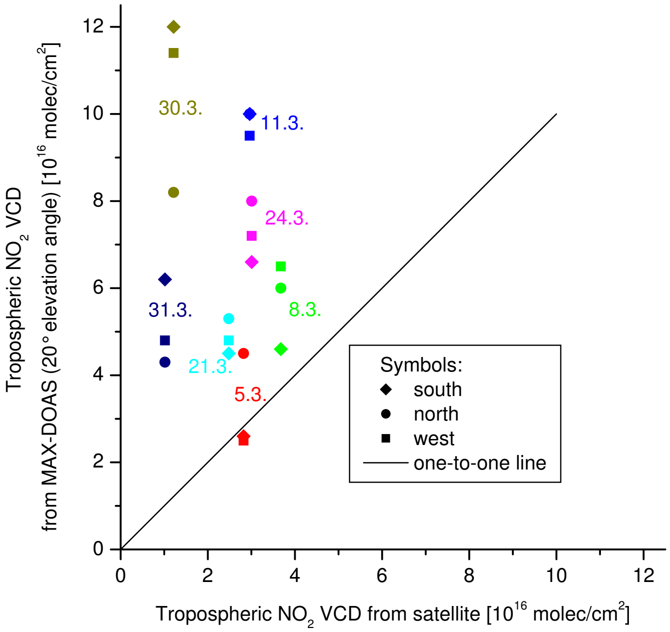

Figure 8.6: *Tropospheric NO_2 VCDs of the three azimuth angles of the Schwampel instrument at T0 derived by geometrical approximation of the 20° elevation angle values versus tropospheric NO_2 VCDs derived from satellite.*

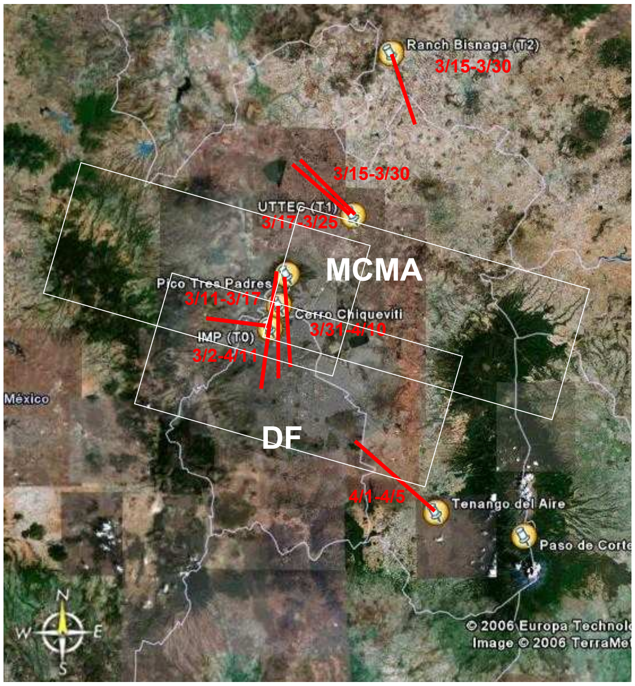

Figure 8.7: *Satellite picture of the MAX-DOAS measurement sites with the field of view of the satellite instrument SCIAMACHY over Mexico City in March 2006. The three most excentric pixels are drawn (white rectangles) which still include the MAX-DOAS site T0.*

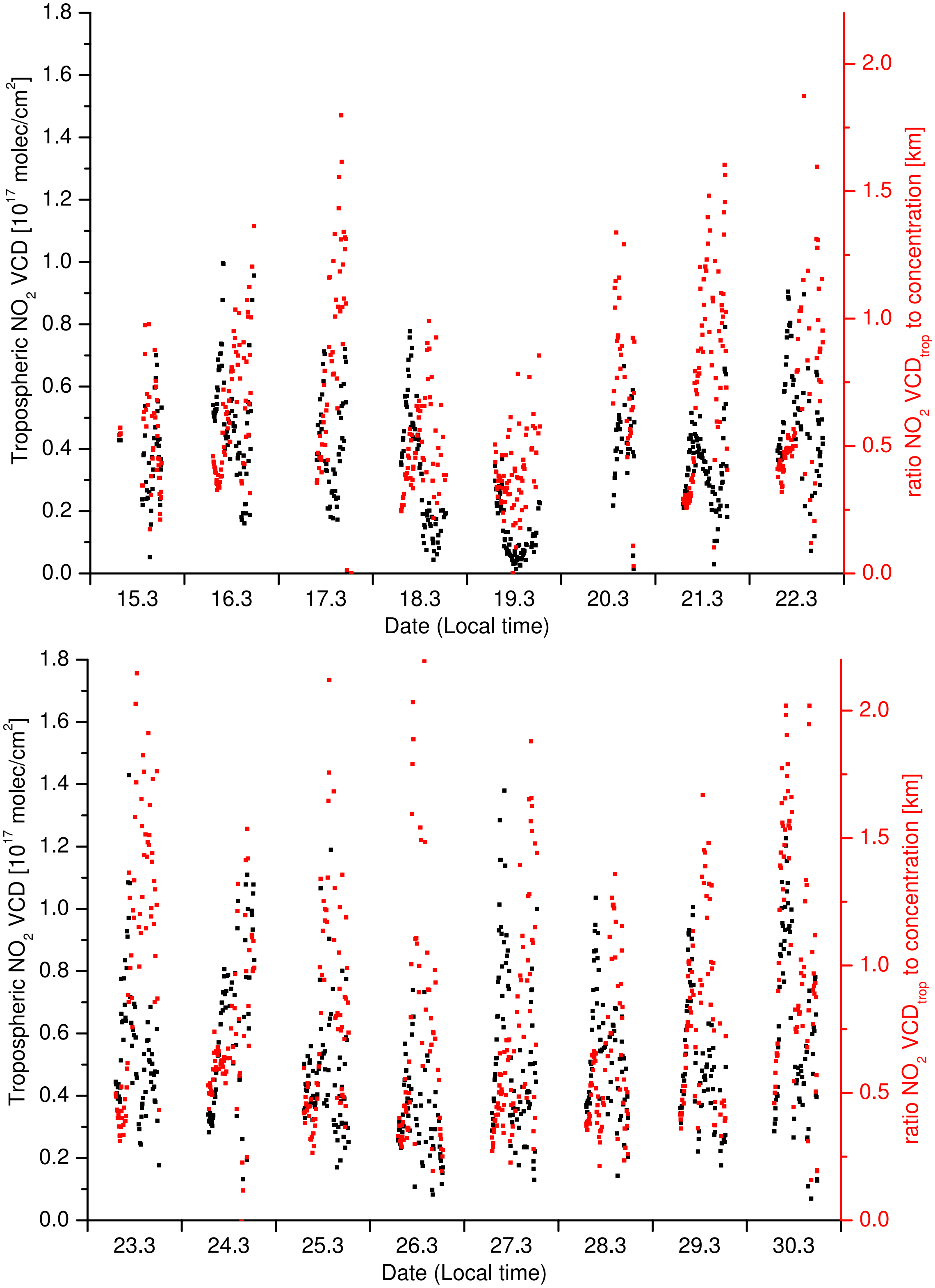

Figure 8.8: *Tropospheric NO_2 VCDs from MAX-DOAS measurements (black) and the ratio of the VCDs to the NO_2 concentrations from active DOAS measurements (red) at T0 from 15 through 30 March.*

by the University of Heidelberg [André Merten, pers. comm.]. For the active DOAS measurements, a light beam from a Xe-arc lamp was emitted from a Newton telescope at T0 in southern direction. The light was reflected in about 2640 m by a retro-reflector array reaching again the Newton telescope where it was detected by a spectrometer. Hence, the active DOAS measurements deliver surface-near concentrations averaged over the light path. The ratio of the tropospheric NO_2 VCDs from MAX-DOAS measurements to the NO_2 concentrations provide information on the layer height of NO_2. In Figure 8.8, these ratios (red) and the tropospheric NO_2 VCDs (black) are plotted (for the southern viewing direction). Assuming a constant vertical NO_2 concentration up to top of the layer the ratio can be regarded as the layer height. Mostly, an increase of the layer height during the day can be observed with a decline in the afternoon and evening, respectively. The maximum heights can be found at around 2 km and are typically between 1 and 2 km. However, the values show a high variability and are rather lower limits of the layer height for two reasons. Although the boundary layer is mostly well mixed so that the NO_2 height profile can be approximated by a box profile, a vertical decline is possible since strong NO_x sources are located mainly at the ground. Furthermore, aerosols and clouds typically reduce the tropospheric light path. Both effects tend to result in an underestimation of the layer height derived by the used ratio.

8.4 HONO Measurement

The presented HONO data in this work constitute the first HONO measurements retrieved by MAX-DOAS. HONO was found at all three sites T0, T1 and T2 which can be seen tn Figure 8.9 where the ΔSCDs at 3° elevation angle are plotted for the period of 15 through 30 March. At T0, values up to 2×10^{16} molec/cm^2 were measured in the morning with a strong decline until noon. At T1 and T2, the values are often smaller than at T0 at the same time and more scattered. However, at some days also higher morning values can be observed.

The elevated ΔSCDs of HONO at T0 were detected throughout the whole measurement campaign and in all three azimuth directions whereby the diurnal cycle was very similar every day. Also for HONO, no systematic difference in the measurements of different azimuth angles could be observed. Thus, the further discussion refers to a single, the southern, viewing direction. Two examples are shown in Figure 8.10 where ΔSCDs of HONO are plotted for two days, 9 and 19 March 2006, together with O_4, NO_2, HCHO and CHOCHO. At sunrise, the typical diurnal cycle begins with high HONO ΔSCDs as expected owing to an accumulation of HONO over night. The differences in the ΔSCDs of the elevation angles bear the assumption that HONO is located in the lower troposphere. During the morning, the HONO ΔSCDs decrease due to photolytic dissociation. After about noon, they remain on a relatively constant level not being zero which indicates a HONO production during

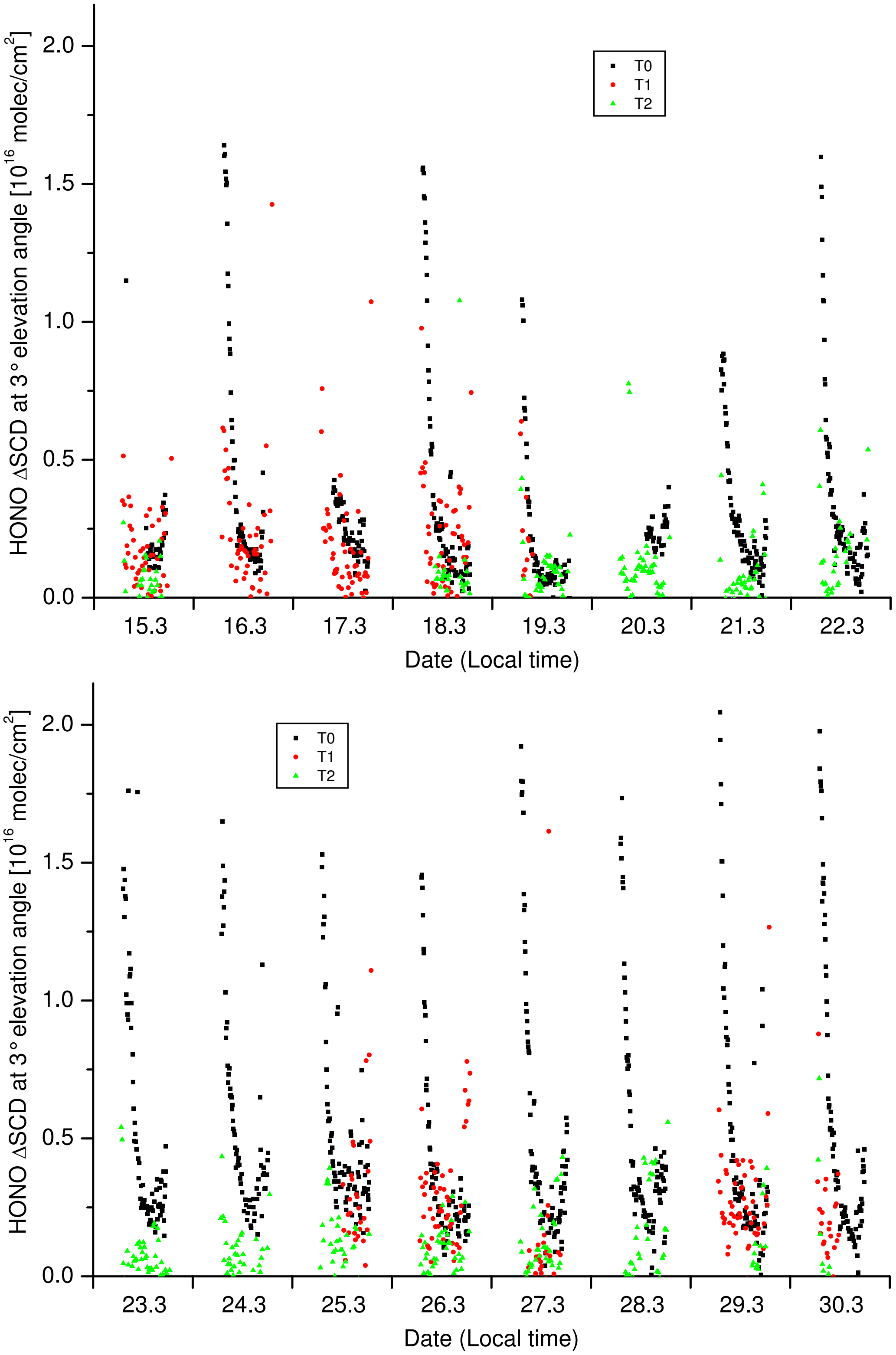

Figure 8.9: *HONO ΔSCDs at 3° elevation angle for the instruments at T0, T1 and T2.*

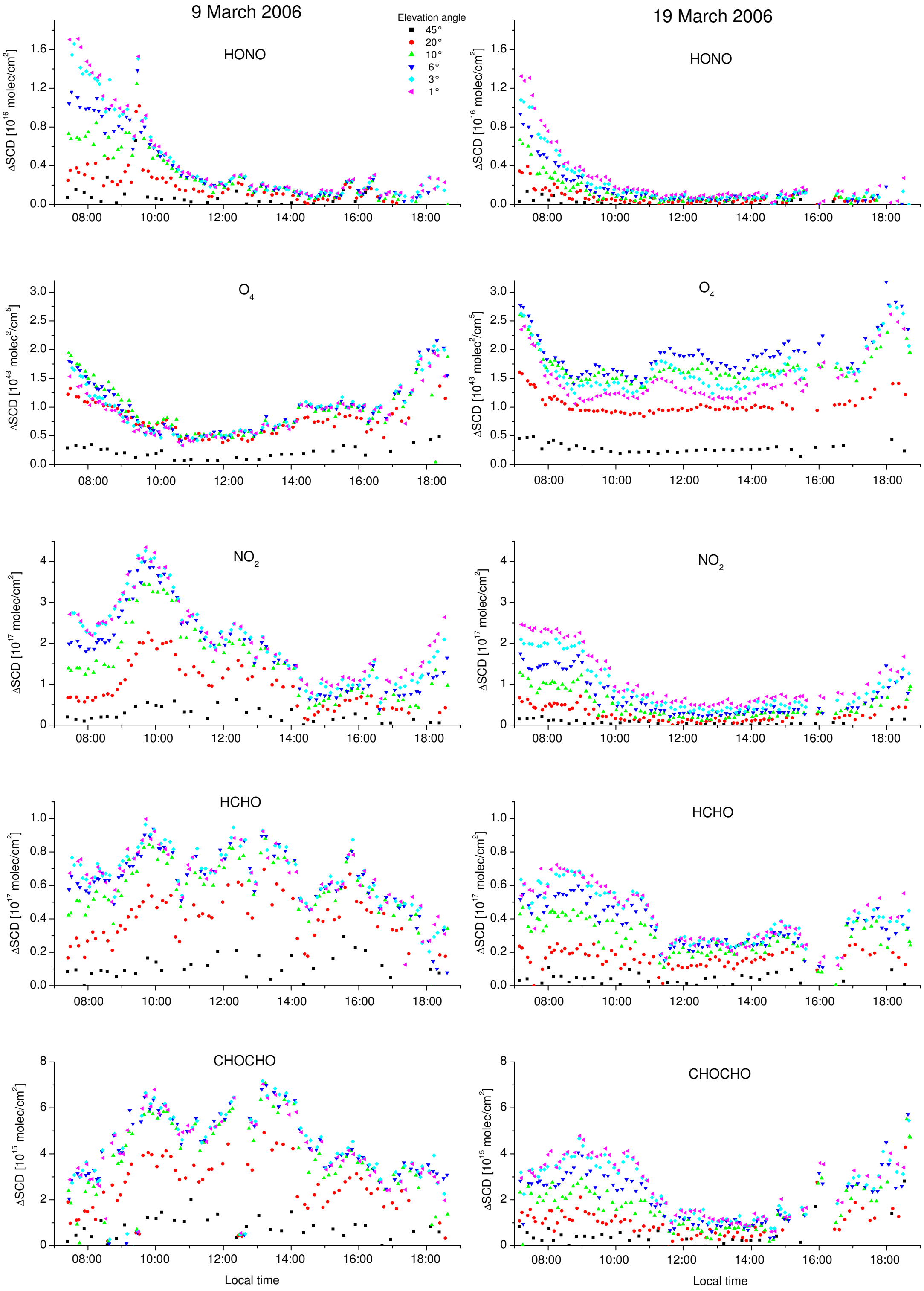

Figure 8.10: *ΔSCDs of HONO, O_4, NO_2, HCHO and CHOCHO on 9 (left panel) and 19 (right panel) March 2006 at T0 (southern direction).*

the whole day. Sometimes a slight accumulation of HONO can be recognized in the late evening.

9 and 19 March differ significantly in the occurrence of aerosols in the atmosphere: While 9 March is a day with high aerosol load compared to other days during the measurement campaign, 19 March was a day with a still significant, but relatively low aerosol load. This is reflected in the ΔSCDs of O_4 (see Figure 8.10). Without aerosols (so that only scattering on molecules took place (pure Rayleigh case)) a clear separation of the values at different elevation angles would be expected whereby the values become higher the more the viewing direction is tilted towards the horizon. In contrast, on March 9, the O_4 ΔSCDs of the different elevation angles between 1° and 10° can hardly be distinguished except for the early morning. Around midday, also the 20° values overlap with the other ΔSCDs at lower elevation angles. On March 19, at least the O_4 ΔSCDs of the different elevation angles can be distinguished, but they are closer together than in the pure Rayleigh case. Furthermore, on both days the order of the elevation angles is changed which is typical throughout the measurement campaign. On March 19, the highest ΔSCDs values come from the 6° elevation angle followed by 10°, 3°, 1°, 20° and 45° mostly in this order. On March 9 in the morning, even the 10° values are on top, while in the afternoon it seems that the 3° values are highest. The changed order of the O_4 ΔSCDs for low elevation angles is caused by the quite strong aerosol extinction. In contrast to other tropospheric trace gases (such as NO_2 or HCHO), the scale height of O_4 is rather high (about 4 km) and substantial O_4 concentrations exist still above the aerosol layer. Thus, the strongest O_4 absorptions are often observed at elevation angles around 10°, for which the aerosol extinction is less than for the smaller elevation angles.

The order in the elevation angles of the HONO ΔSCDs is mainly in the expected order for both days (and also throughout the whole measurement campaign) which indicates a significant HONO concentration close to the ground. Furthermore, the O_4 ΔSCDs are smaller especially at lower elevation angles on 9 March compared to the 19 March which means a shorter light path through the atmosphere caused by a higher aerosol load. In contrast, on 9 March the HONO ΔSCD are higher and in the morning, amounted to about 1.7×10^{16} molec/cm^2, on 19 March to about 1.3×10^{16} molec/cm^2. They also do not decrease as strong and to so low values as on 19 March. Finally, it can be concluded that on 9 March a higher HONO concentration was present in the atmosphere. For the same reason, on 9 March, higher concentrations also of NO_2, HCHO and CHOCHO can be concluded.

Less aerosols and trace gases on 19 March could be explained by a relatively strong wind on this day. Wind speed measurements by rawinsondes as well as forecasting analyses yielded maximum values for the campaign of around to 8 m/s at 1000 m above ground level blowing from south to south-west direction [Fast et al., 2007]. Therefore, a transportation of relatively clean air masses is suspected which diluted the typically more polluted air mass above Mexico City.

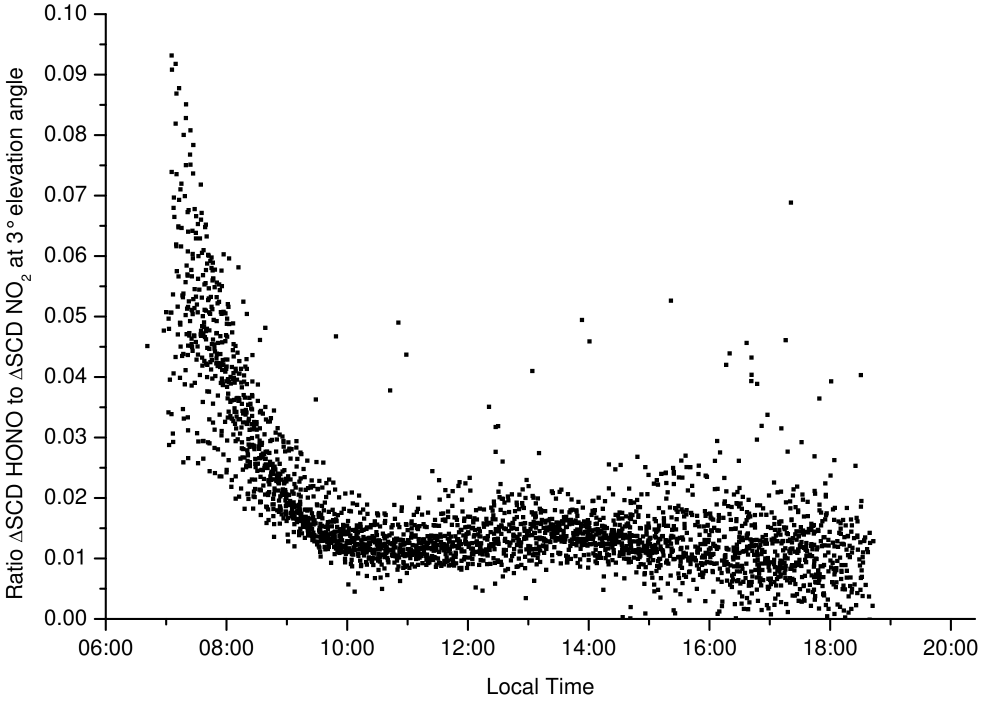

Figure 8.11: *HONO-to-NO_2 ratios at 3° elevation angle for the whole campaign at T0.*

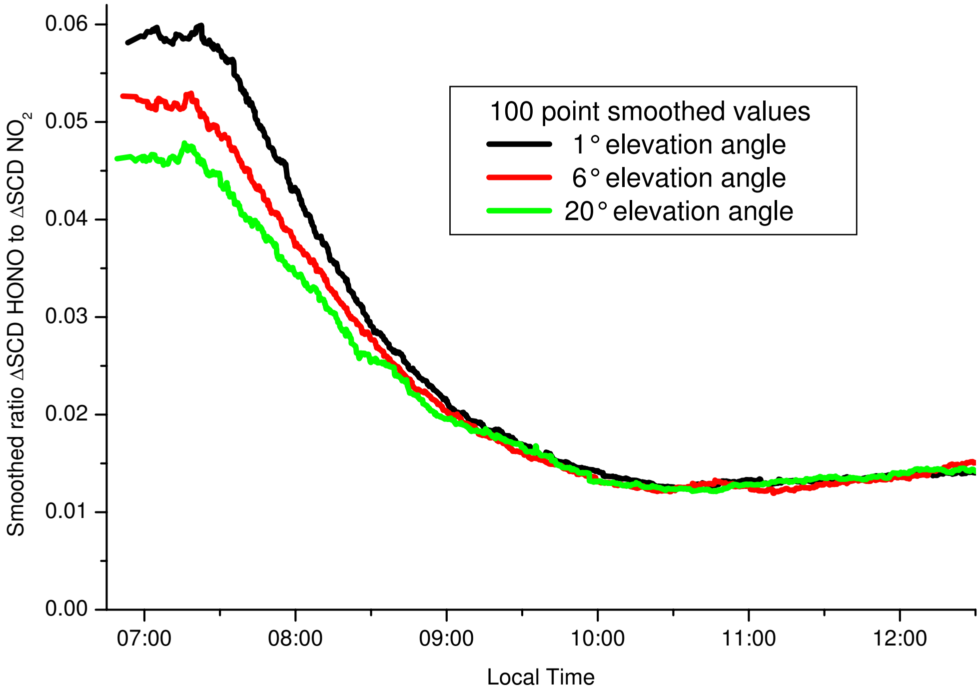

Figure 8.12: *100 points smoothed HONO-to-NO_2 ratios for the whole campaign at T0.*

To investigate the formation of HONO (it is still under discussion if HONO is produced on surfaces rather at the ground than on aerosols) the HONO-to-NO_2 ratio was calculated. Since HONO is generated from NO_x the ratios provide information on the steady state HONO production. The steady state is given when the conversion from NO_2 to HONO has the same strength as the HONO loss [Stutz et al., 2004]. In Figure 8.11 the HONO-to-NO_2 ratio for the 3° elevation angle is plotted for the whole campaign at T0. A very clear behavior can be observed with high morning values of almost 10 %. Then a strong decline can be observed until around 10 AM. From then, HONO and NO_2 are in steady state with ratios mainly between 1 and 1.5 %. In the evening, slightly higher scatter occurred. This general course is observable at each elevation angle. Yet, in the early morning a significant difference in the absolute values of the ratio was found which is shown in Figure 8.12. For a better illustration, the HONO-to-NO_2 ratios are smoothed (100 points smoothing) and only the 1°, 6° and 20° elevation angle are plotted. The lower the elevation angle the smaller is the ratio in the morning. This means that the HONO proportion decreases with height. Thus, a HONO source at the ground can be concluded. This does not exclude that part of the observed HONO is also produced on aerosols. In fact, the quite small decrease of the HONO-to-NO_2 ratio with elevation angle indicates that an additional source apart from the surface exists. This os confirmed by the following consideration on lifetime and vertical mixing: Additional measurements of a spectral radiometer at T0 provided photolysis rates of HONO [Rainer Volkamer, pers. comm.]. The corresponding life times of HONO amounted to about 10^4 s at 7 AM and 400 s at noon. Thus, transportation of HONO within its life time to e.g. 1000 m height at noon would imply a vertical wind speed of 2.5 m/s which is rather high. Therefore, even assuming a well mixed boundary layer a considerable fraction of HONO had to be formed also in the air most probably due to reaction on aerosols.

8.5 HCHO and CHOCHO Measurements

At all three sites enhanced ΔSCDs of HCHO were detected. The HCHO ΔSCDs at 3° elevation angle (southern direction) are displayed in Figure 8.13. At T0, the highest ΔSCDs were found to be up to 1.2×10^{17} molec/cm^2. At T1 and T2, the values are around half of the values of T0 whereby the ΔSCDs of T2 are slightly higher than of T1 despite the larger distance to Mexico City. Possibly emissions from vegetation enhanced the values at T2. Mostly, the peaks of HCHO can be observed in the middle of the day when the photochemical oxidation of VOCs is highest. While this can be recognized on 9 March (see Figure 8.10) on 19 March the HCHO ΔSCDs are decreased around noon due to the strong wind on that day.

CHOCHO which like HCHO is formed by oxidation of VOCs was only measured at T0 because at the other sites the instruments did not cover the spectral range of the

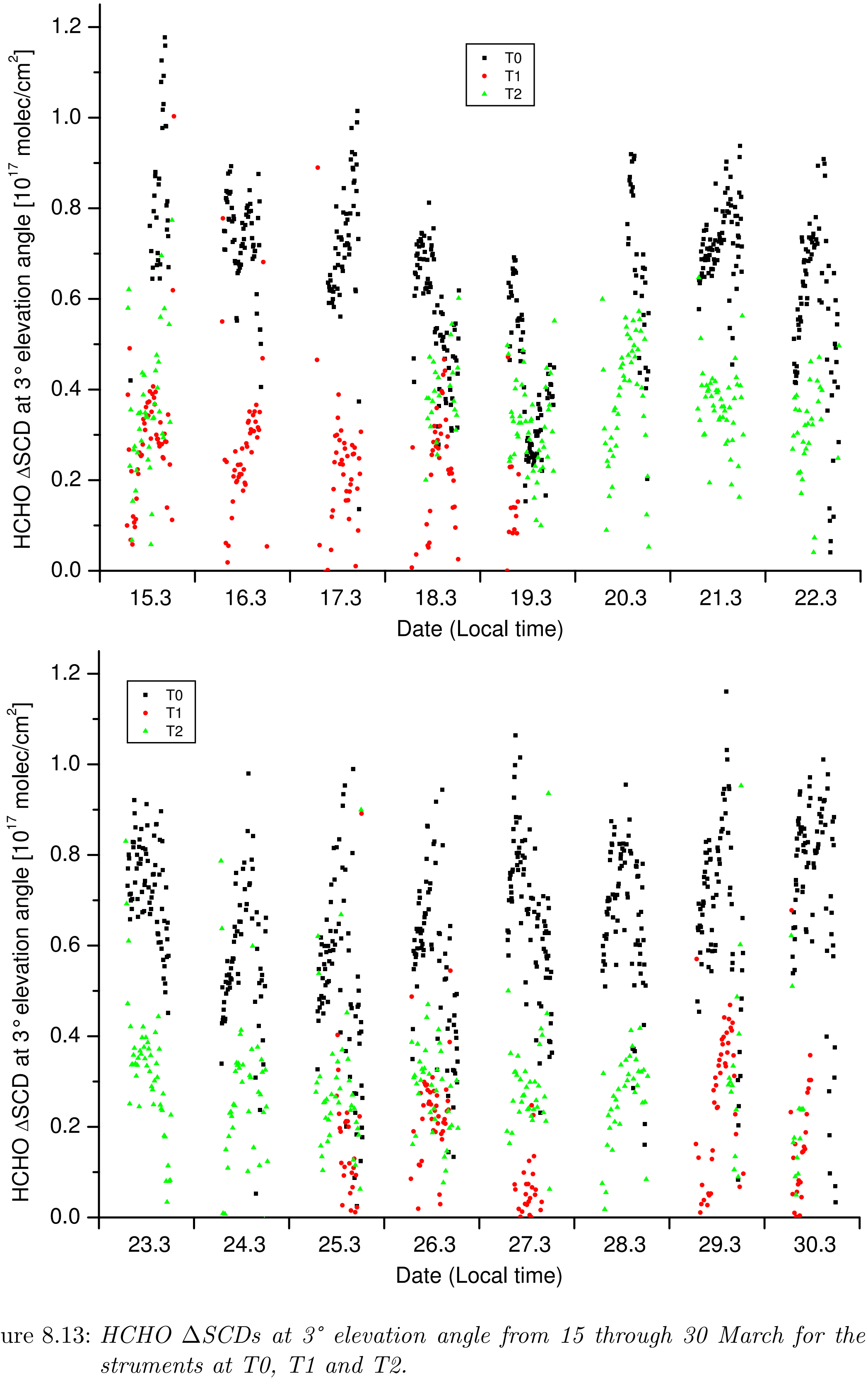

Figure 8.13: *HCHO ΔSCDs at 3° elevation angle from 15 through 30 March for the instruments at T0, T1 and T2.*

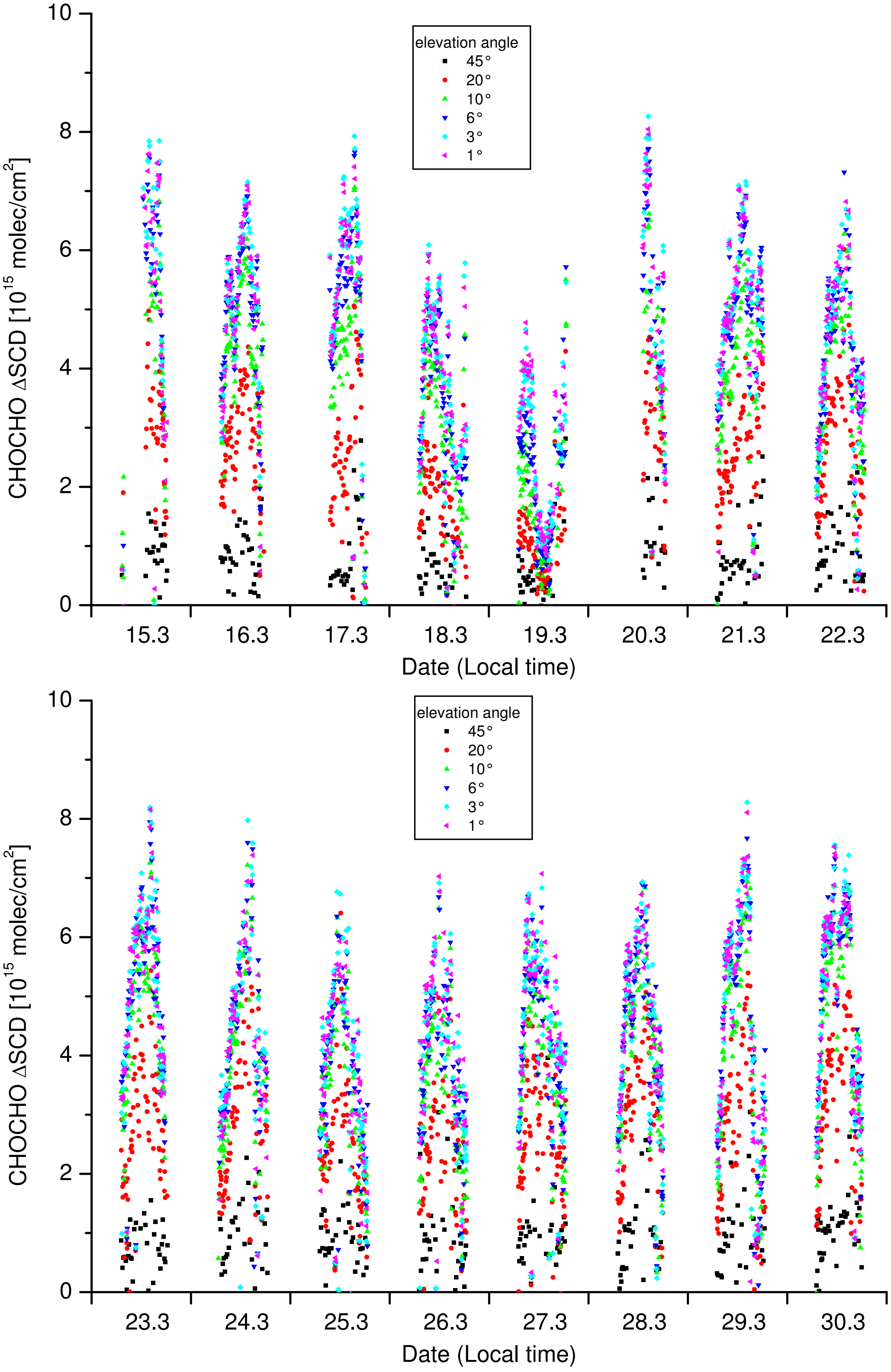

Figure 8.14: *CHOCHO ΔSCDs from 15 through 30 March at T0.*

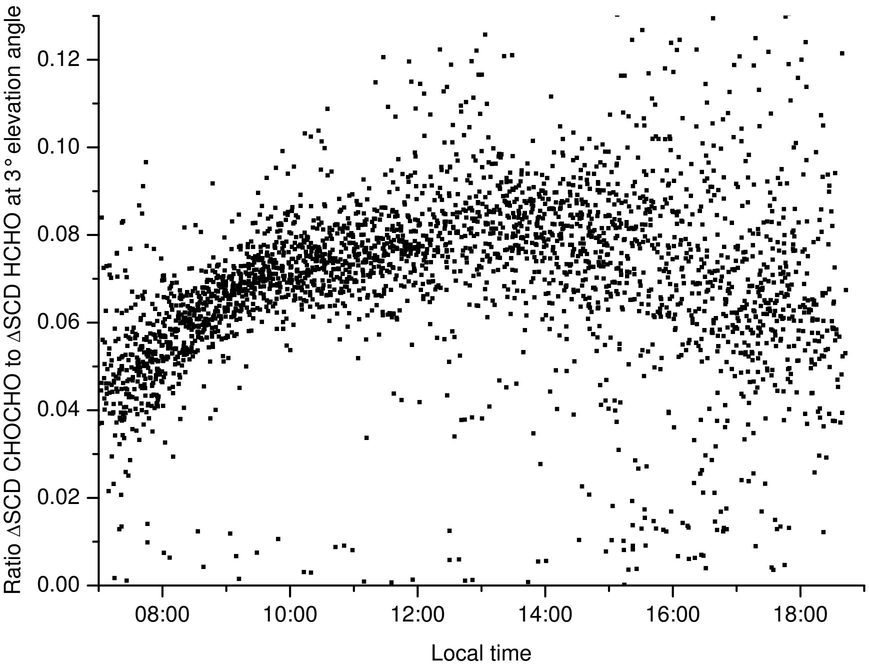

Figure 8.15: *CHOCHO-to-HCHO ratios at 3° elevation angle for the whole campaign at T0.*

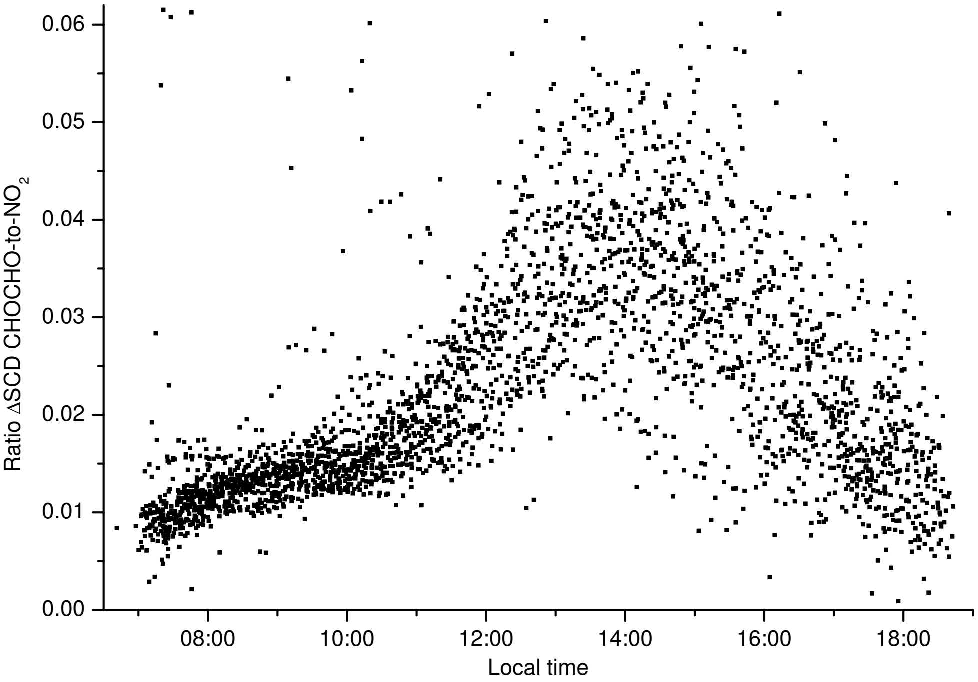

Figure 8.16: *CHOCHO-to-NO_2 ratios at 3° elevation angle for the whole campaign at T0.*

CHOCHO absorptions. Thus, all elevation angles (southern direction) are shown in Figure 8.14 from 15 through 30 March. The peaks in the middle of the days are pronounced. The course on 19 March is an obvious exception. The maximum ΔSCDs for the 3° elevation angle are at around 9×10^{15} molec/cm^2 and typically between 6 and 8×10^{15} molec/cm^2.

The similar diurnal courses of HCHO and CHOCHO in Figure 8.10 indicate similar formation processes of HCHO and CHOCHO. Since CHOCHO is generated mainly by (anthropogenic) aromatics, in contrast to HCHO, the CHOCHO-to-HCHO ratio shows the fraction of anthropogenic and natural sources of the measured air mass. In Figure 8.15 the ratio of CHOCHO to HCHO for 3° elevation angle throughout the measurement campaign is shown. The ratios increase soon in the morning over 0.06 and are around 0.08 in the middle of the day at about 1PM. In the afternoon, they are much more scattered, nevertheless largely a decrease can be observed. This course is in agreement with the presence of strong human activity in Mexico City because values larger than 0.06 are typical for industrialized areas (see [Wittrock et al., 2006] and references therein).

Finally, the CHOCHO-to-NO_2 ratio for 3° elevation angle was calculated for the whole campaign (see Figure 8.16). Also this ratio increases in the morning, but reaches its maximum later at around 2PM. The peak values are mainly between 0.03 and 0.05 which is almost double as high as at MIT in the ICARTT 2004 measurement campaign. The reason can be found in higher photochemical activity in Mexico City than in the Boston urban area.

8.6 O_4 Measurements

The concentration O_4, the oxygen dimer, is almost constant in time. Thus, the measurement of the O_4 absorption provides information on the light path distribution and hence on the presence of aerosols. Increasing aerosol extinction reduces the absorption path at low elevation angles and, thus, also the respective O_4 absorptions. The O_4 absorption was measured at T0, T1 and T2. Figure 8.17 shows the O_4 ΔSCDs at 3° elevation angle for T0, T1 and T2. The O_4 ΔSCDs of all three sites are relatively low indicating significant aerosol loads. The lowest values are mostly at T0 where the highest amounts of aerosols are expected.

At T0 and T1, a diurnal course is apparent. In the morning higher values were found which decrease due to accumulation of aerosols. During the day, the boundary layer increases and a dilution of the aerosols occurs which leads to an increase of the O_4 ΔSCDs. In the evening, the rush hour with more particle exhaust leads again to a decline of the O_4 values. This is in agreement with the NO_2 measurements which often increase in the evening, for instance on 9 March (see Figure 8.10). At T2, not always this diurnal course can be observed due to the larger distance from Mexico City.

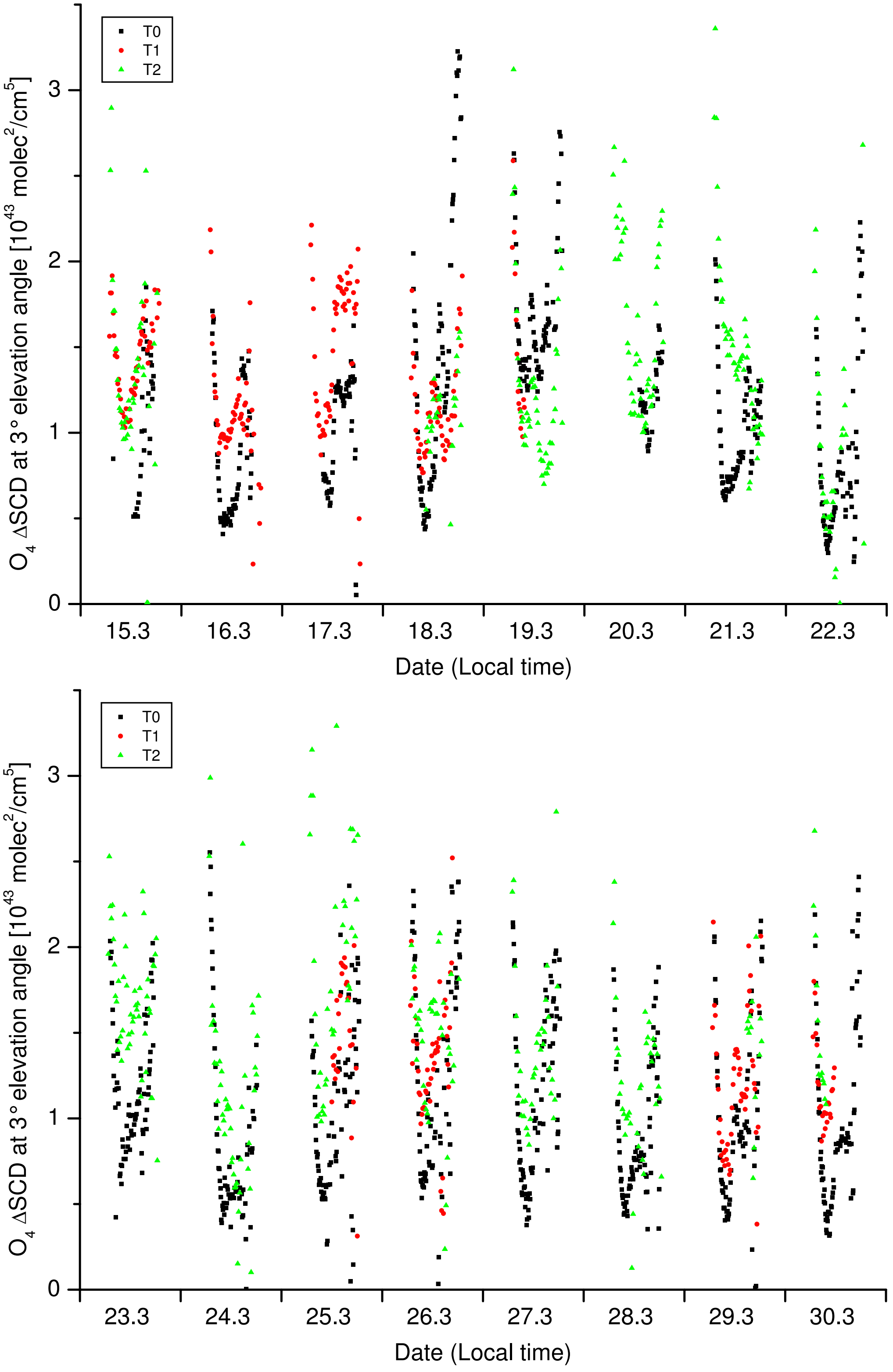

Figure 8.17: *O_4 ΔSCDs at 3° elevation angle from 15 through 30 March for the instruments at T0, T1 and T2.*

8.7 Aerosol Profile Retrieval by Optimal Estimation

The aerosol load in Mexico City was further investigated by calculating an aerosol profile of one day by optimal estimation [Udo Frieß, pers. comm.] according to the method described in section 4.6.3 and by Frieß et al. [2006]. On most of the days, the O_4 ΔSCDs of the different elevation angles overlap so that they can hardly be separated, like on 9 March (see Figure 8.10 left panel). This reduces the information content of the measurement significantly. Therefore, the clearest day of the measurement period, the 19 March, was chosen. On this day, the O_4 ΔSCDs of the elevation angles can be distinguised and provide more sensitivity on aerosol properties (see Figure 8.10 right panel). According to satellite images the sky was cloud free over the measurement site during the whole day (see Figure 8.18).

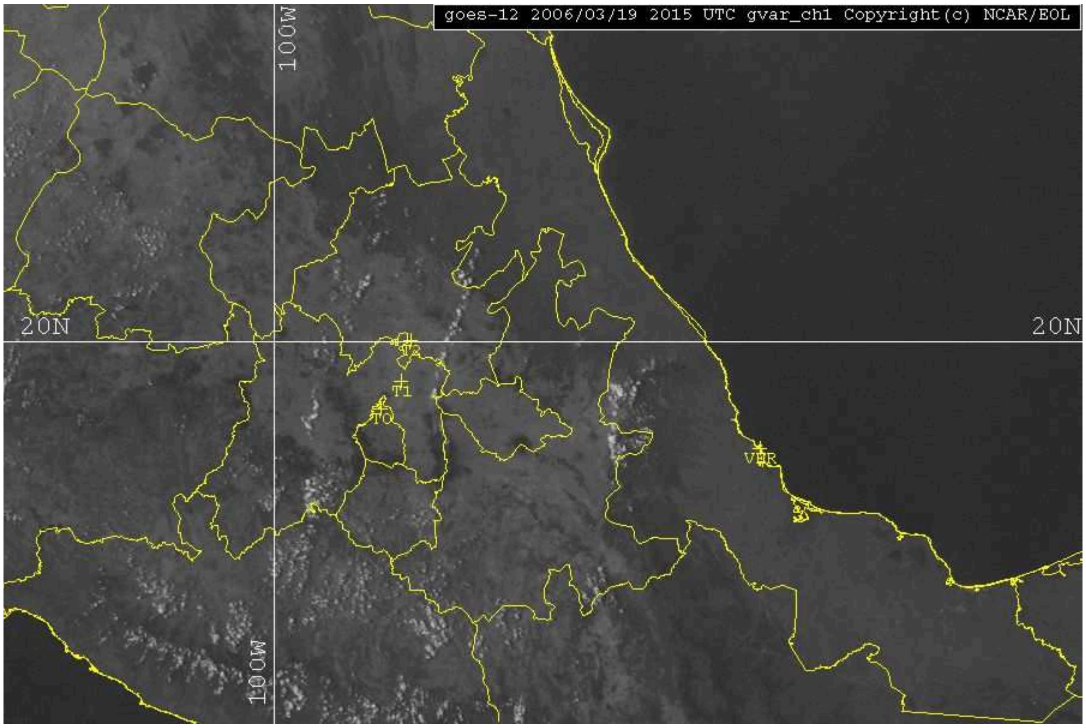

Figure 8.18: *GOES Visible Satellite image of Mexico on 19 March 2006 at 2:15PM local time (http://data.eol.ucar.edu/cgi-bin/codiac/nph-browse). According to the complete time series of satellite images the sky was cloud-free during the whole day.*

Although the sky was cloud-free on the selected day the diurnal variation of the measured intensities as well as the retrieved O_4 ΔSCDs show considerable variation during the day (see Figures 8.10 and 8.19). It is noteworthy that the variations are strongest for the lowest elevation indicating strong variations of the surface-near

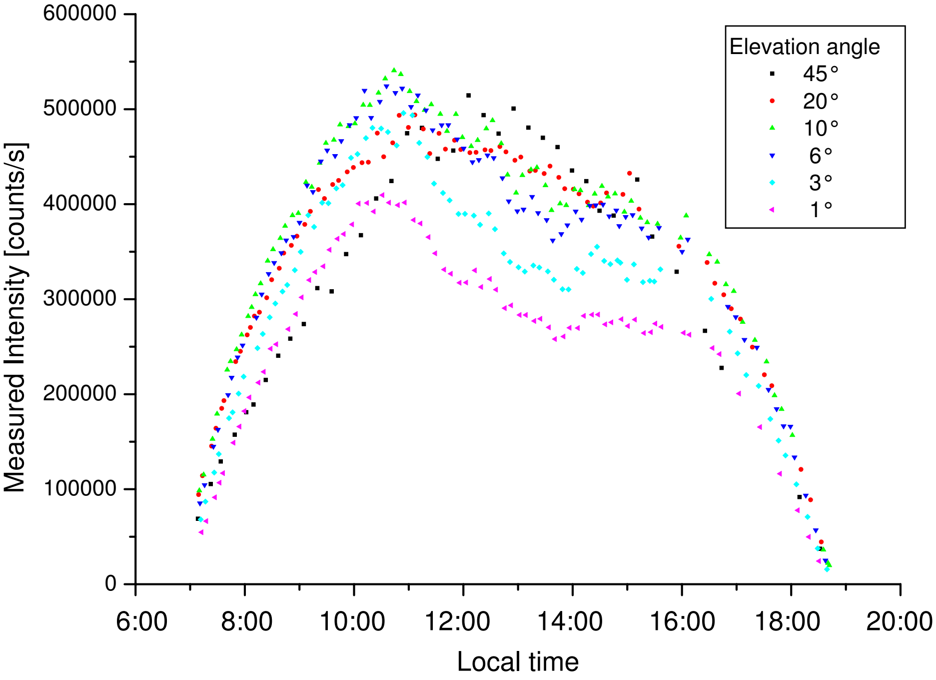

Figure 8.19: *Measured intensities by the MAX-DOAS instrument on 19 March 2006.*

aerosol properties.

The retrieval was performed using the measured differential optical densities of O_4 at the absorption band centered around 360 nm and considering the azimuth dependency of the O_4 air mass factor. For each measurement sequence a profile was retrieved. The a priori aerosol profile was assumed to feature an exponential decrease starting with an aerosol extinction coefficient of 0.2 km^{-1} with a priori errors of ten times of the assumed value. The assumed aerosols consist of 69 % soot and 31 % sulphate.

The retrieved aerosol extinction profiles are shown in two contour plots, for which the retrieved aerosol profiles were interpolated on a 15 minutes time resolution. Figure 8.20 shows the aerosol profiles up to 5 km altitude. High loads of aerosols with coefficients of up to 45 km^{-1} are found between 2 and 5 km in the afternoon. For better illustration, the values are color coded only up to 10 km^{-1}. In Figure 8.21, the first kilometer is zoomed out. Higher aerosol loads with coefficients around 0.25 km^{-1} are situated mostly within the first 300 m. In Figure 8.22, the results for the modeled O_4 differential optical densities are compared to the measured values. The degree of agreement between both data sets indicates the quality of the profile inversion. Accordingly, the highest accuracy of the profile inversion can be expected between 8AM and 9AM.

Figure 8.23 shows four selected retrieved profiles together with the a priori pro-

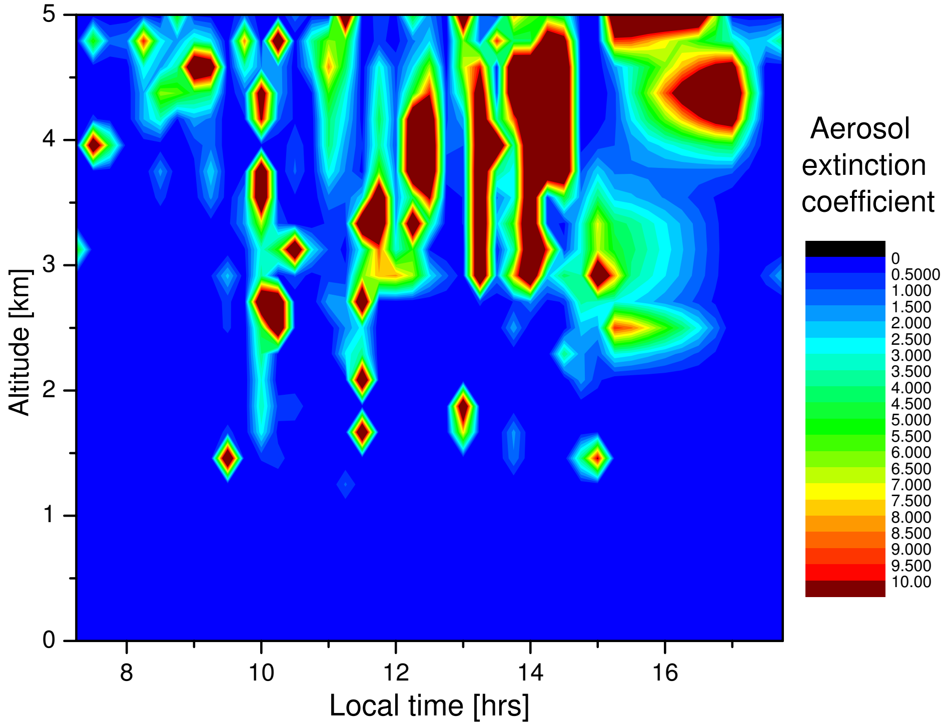

Figure 8.20: *Retrieved aerosol profiles up to 5 km altitude on 19 March. For better illustration, the values are color coded only up to 10 km−1 though up to 45 km^{-1} where found in the afternoon.*

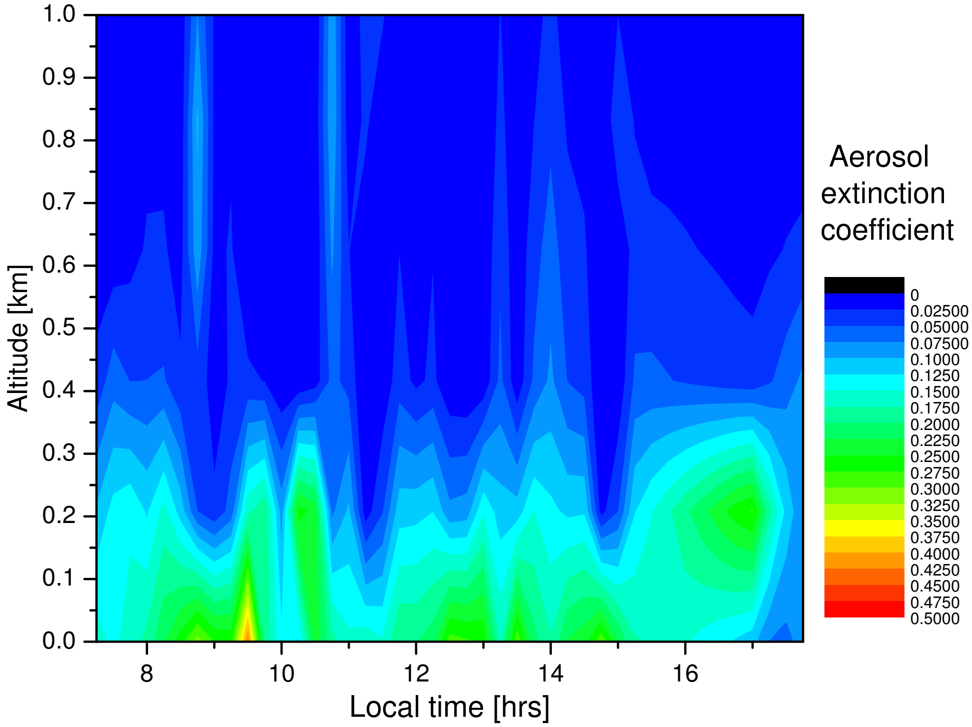

Figure 8.21: *Retrieved aerosol profiles up to 1 km altitude on 19 March with retrieved aerosol extinction coefficients around 0.25 km^{-1}.*

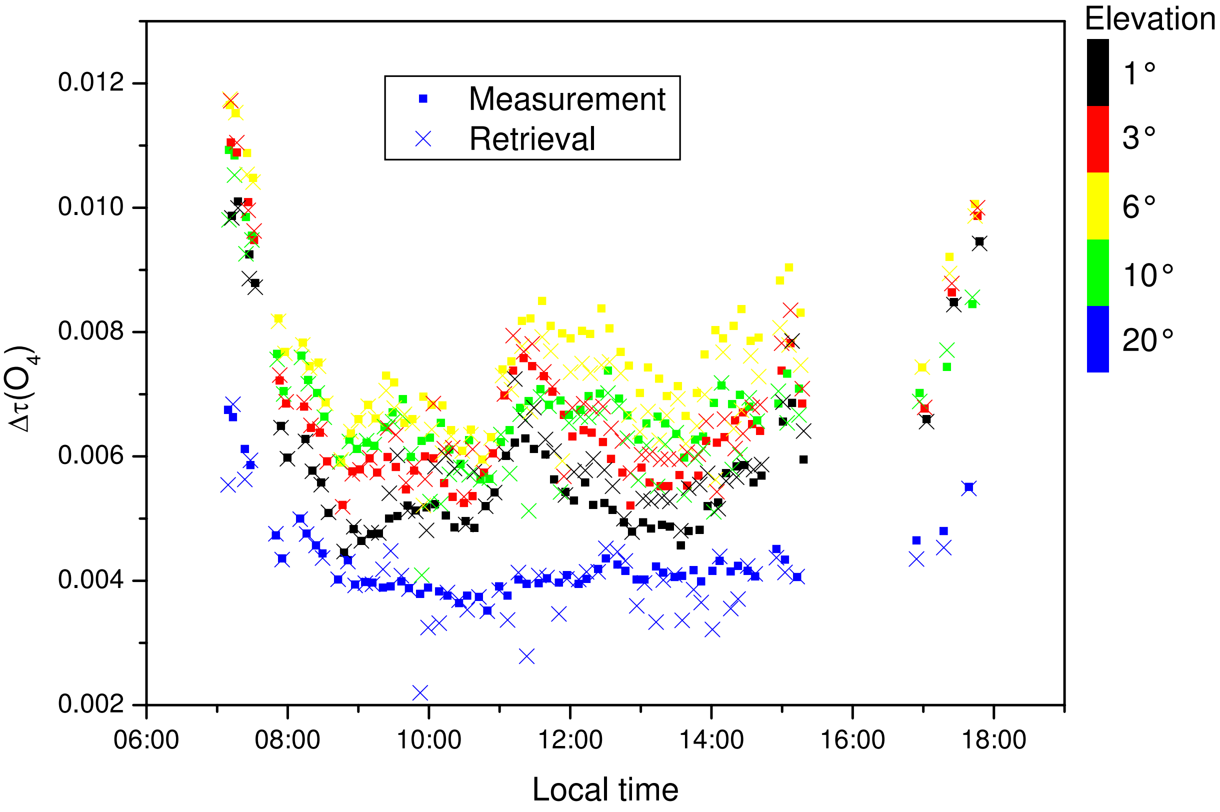

Figure 8.22: *Measured (squares) and modeled (crosses)* O_4 *differential optical densities on 19 March. Different colors indicate different elevation angles as indicated in the legend.*

files. The profile in Figure 8.23a was retrived from the measurement at around 8AM. A relatively low aerosol load can be recognized. Both the retrieved and the a priori errors are relatively high whereby the retrieved errors decrease significantly at altitudes where the retrieved aerosol extinction is high. This a feature that is caused by the non-linear response of the O_4 absorption to the aerosol extinction [Frieß et al., 2006]. Figure 8.23b shows the retrieval at 12PM and is similar to the previous profile except for a strong peak in the aerosol extinction of 7 km^{-1} at about 3 km altitude. In Figure 8.23c, the profile which was acquired at 2:20PM is even more extreme. Additionally to the peak which even increased, much higher aerosol extinction coefficients of almost 45 km^{-1} are retrieved in layers above 3.5 km. The errors in this range are relatively low indicating an unequivocal retrieval. The small aerosol values up to 300 m have disappeared. The profile in Figure 8.23d from 5PM exhibits only significantly elevated aerosol extinctions above 3.5 km reaching still a coefficient of 20 km^{-1}.

The averaging kernels of the two extreme profiles a and c are shown in Figure 8.24.

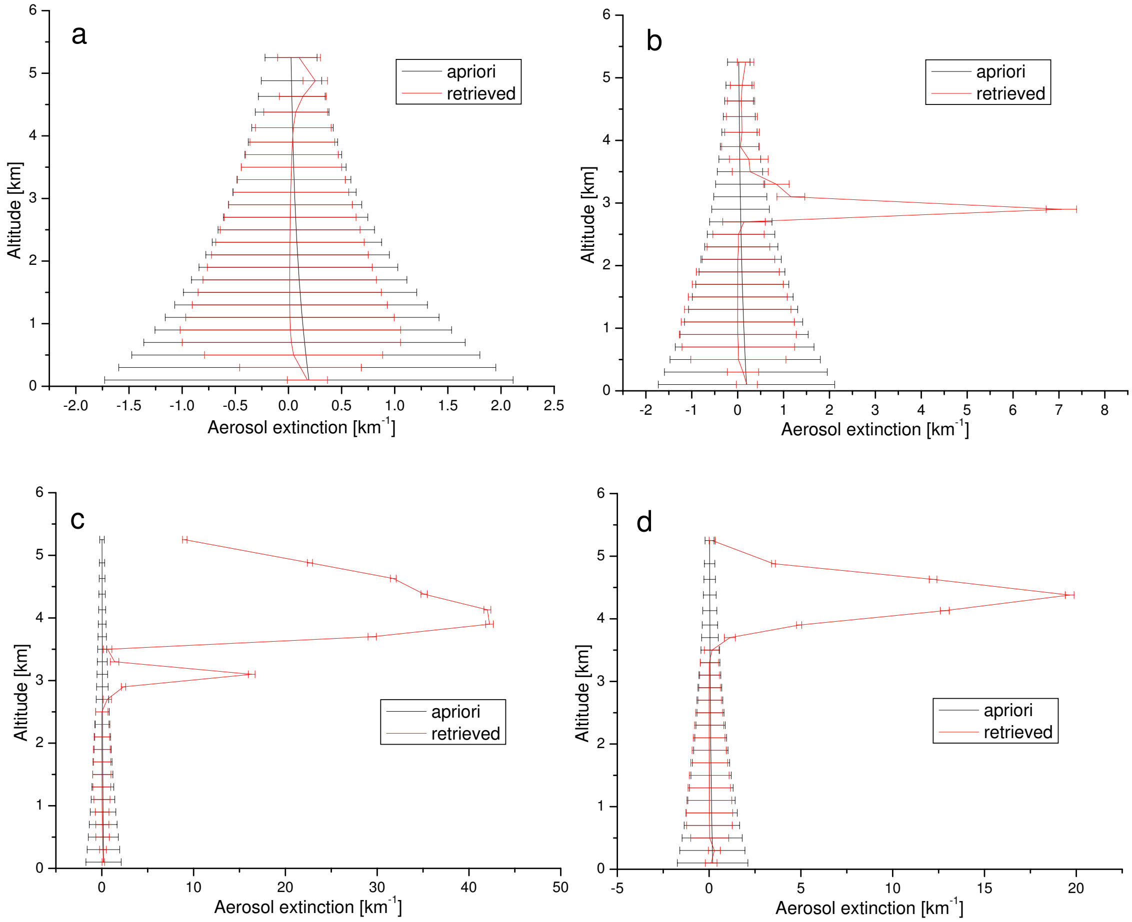

Figure 8.23: *Four selected retrieved profiles and their a priori profiles. The profiles are based on measurements at 8AM (a), 12PM (b), 2:20PM (c) and 5PM (d).*

Both averiging kernel plots show peaks in the surface-near layers at their nominal altitudes indicating a high sensitivity to true profile. However at higher altitudes, they become different. Above 700 m, the averaging kernels from the morning profile exhibit very similar courses for the different nominal values with a maximum around 1 km indicating a small sensitivity of the retrieved profile to the true profile at the nominal altitude. Above 4.6 km, the averaging kernels peak again at their nominal value and have maximum values around one, indicating again that the retrieval is very sensitive to altitudes where enhanced scattering occurs. The averaging kernels from 2:20PM show a relatively good sensitivity to their nominal heights up to 1.3 km. Then, the course of the averaging kernels is quite the same as in the morning values. Beginning with 2.7 km nominal height, a pronounced sensitivity is apparant in layers where a strongly enhanced extinction is retrieved before it decreases significantly at 3.3 km and above.

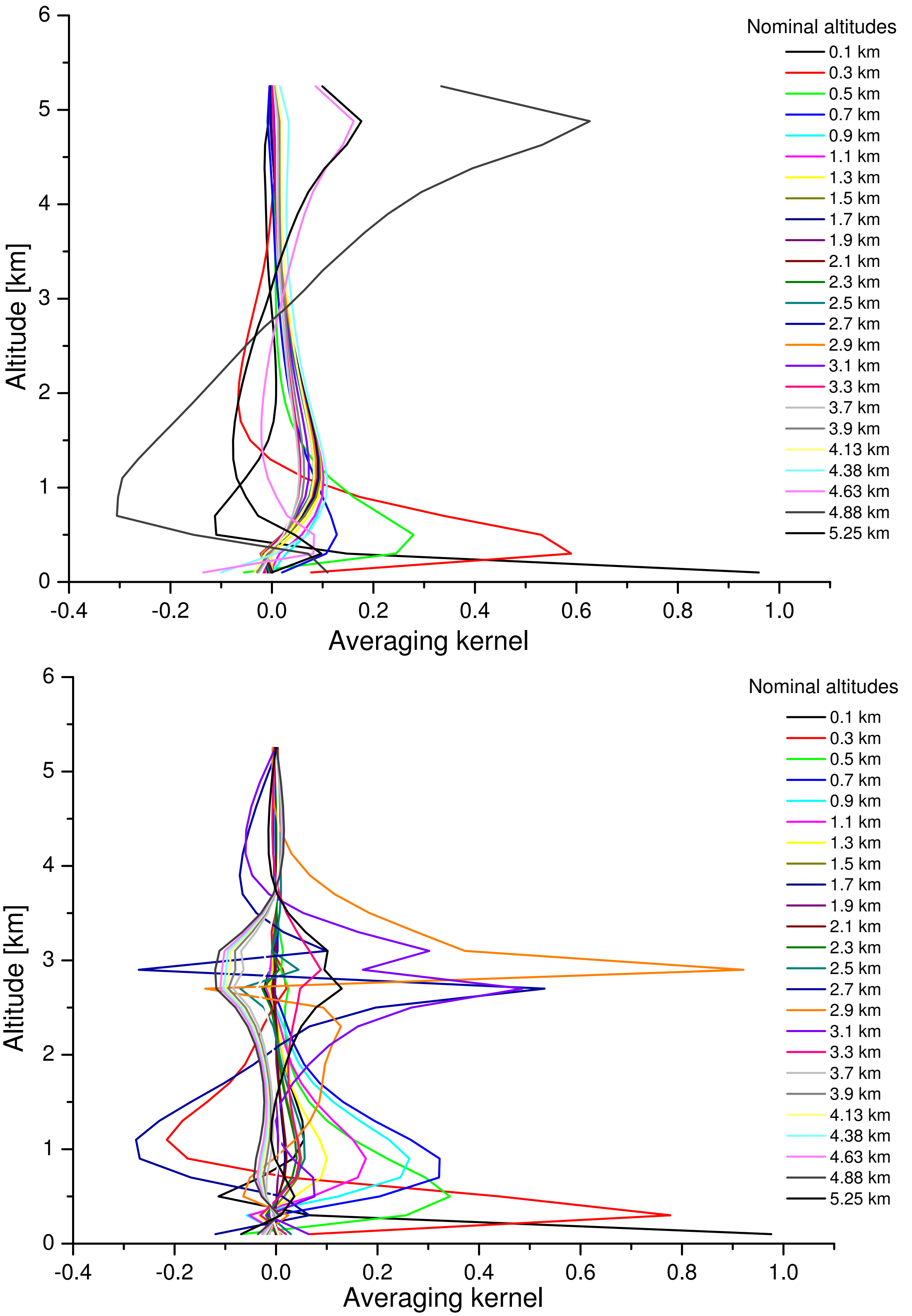

Figure 8.24: *Averaging kernels for the profile at 8AM (upper panel) and 2:20PM (lower panel) (description see text).*

Generally, the retrieval has lower errors at altitudes where high extinction coefficients were found. This is caused by the non-linear nature of this inverse problem, leading to an increase in sensitivity with extinction coefficient. However, the high aerosol extinctions above two kilometers of up to 45 km^{-1} seem unlikely. Furthermore, the averaging kernels do not show a pronounced sensitivity for these layers when these high values were found. The high values of the extinction coefficients at high altitudes might indicate a cloud layer. However, this can be excluded according to satellite images (see Figure 8.18). Possible reasons for these errors are probably wrong assumptions for aerosol properties, namely horizontal inhomogeneities and chemical composition. Furthermore, systematic deviations in the O_4 cross section (for example due to temperature dependence) might add to these errors. It is interesting to note that the most reasonable aerosols profiles are retrieved in the morning when differences between measured and modeled differential optical densities are smallest.

9 Conclusions and Outlook

Within this thesis, networks of MAX-DOAS instruments were operated in two extensive measurement campaigns, one in the north-east of the USA in summer 2004 (ICARTT) and another in Mexico City in spring 2006 (MILAGRO). The aim of both campaigns was the characterization on quantification of emission sources, chemical transformation and transport of pollutants. The selected measurement locations are amongst the most polluted regions on Earth. The MAX-DOAS observations were part of a large amount of other measuring and modeling activities carried out by a large consortium of international scientists. The coordinated operation of a large number of MAX-DOAS instruments constitutes a so far unique effort. MAX-DOAS instruments are very well suited for the quantification and characterization of pollution because of several advantages:

- They are very sensitive especially for several short-lived species, e.g. HONO.
- They integrate over altitude and yield total column densities of tropospheric species. Thus, they do not miss pollutants at higher altitudes.
- From the O_4 absorption, information on the aerosol properties can be derived.
- For the tropospheric trace gases (limited) profile information can be derived.
- MAX-DOAS measurements can be operated automatically, even at remote locations.

During both campaigns several MAX-DOAS instruments were operated during several weeks. In spite of some instrumental problems overall the instruments have been proven to be well suited for continuous pollution monitoring. From the experiences gained during both campaigns it can be recommended to establish a global network of standardized MAX-DOAS instruments performing routine measurements. the results of this thesis give an overview of the large potential of such measurements.

In the following, the specific results during both campaigns are summarized:

ICARTT 2004 campaign: At the various locations, almost continuous time series of NO_2, SO_2, HCHO, CHOCHO and O_4 as well as aerosol extinction were analyzed. The spatial and temporal variation of these observations was investigated with respect to the average transportation path ways and the location of the major emission sources. As expected, the highest values were usually found close to emission sources and in many cases, a clear attribution of individual emission sources was possible. In some cases, enhanced pollution levels were observed, but could not be assigned to dedicated sources. This might be an indication of deficiences in the emission inventories. Several aspects of the retrieved data sets were investigated in more detail. An important discovery was the first detection of glyoxal by MAX-DOAS observations. It turned out that MAX-DOAS observations well-suited for monitoring tropospheric glyoxal concentrations, and from the ratio of glyoxal to formaldehyde, it was possible to characterize the nature of the polluted air masses. Another important development during this thesis deals with the quantitative conversion of the measured ΔSCDs into total tropospheric vertical column densities. These are the prerequisite for a meaningful satellite validation. Also, average mixing ratios can be derived from the vertical column density. From the comparison of the tropospheric VCDs derived from the MAX-DOAS measurements with in-situ observations, it was possible to derive an average height of the mixing layer. Typical values of about 1 km were found in good agreement with the expectations. For some cases, also a full profile retrieval was performed; the resulting surface-near mixing ratios showed good agreement with simultaneous in-situ data. In this thesis, a simple method for the determination of the aerosol extinction from MAX-DOAS O_4 measurements was developed and applied to the observations at the various locations. the resulting extinction coefficients ranged between 0 and 1 km^{-1}; the temporal variation was similar to those of the measured trace gases. The large data sets showed many cases with interesting chemical and meteorolgical conditions. One example was a so called ozone titration event at the rural site Narragansett on 28 July 2004. During this event, exceptionally high NO_2 concentrations and quite low visibilty were observed by the MAX-DOAS instruments. Both observations are in agreement with simultaneously observed complete ozone destruction the lowermost 200 m of the atmosphere. While such an ozone titration event is not unusual in urban environments its occurence in rural environment is rather unexpected.

MILAGRO 2006 campaign: At the three different locations, time series of NO_2, HCHO, HONO, CHOCHO and O_4 were analyzed. The spatial and temporal variation of these observations was investigated dependent on the distance from the city. As expected, the highest values were usually found close to the city center with gradually decreasing values with increasing distance. This decrease can be most probably explained by chemical degradation and dilution. Several aspects of the retrieved data sets were investigated in more detail. An important discovery was the first detection of nitrous acid by MAX-DOAS observations. Enhanced values of HONO were always found in the morning followed by a rapid decrease to small but not zero values during the rest of the day. Especially the magnitude of the retrieved ΔSCDs was rather high; the relative decrease of the HONO concentration with altitude was found to be stronger compared to that of NO_2 indicating that a substantial production of HONO takes place at the ground. Like during the ICARTT campaign, again the ratio of glyoxal and formaldehyde was calculated. The high ratios found indicate a high fraction of VOC emission by anthropogenic emissions. Finally, a complete O_4 absorption sequence including all elevation angles was used for a profile inversion of aerosol extinction by means of optimal estimation. The results prooved to be successful for only a small part of the processed data set; the most probable error sources are probably wrong assumptions on the horizontal homogeneity and the chemical composition of the aerosols. Future improvments should consider also O_4 absorptions at additional wavelengths and the measured intensities.

The results of both campaigns confirmed several assumptions on the chemical transformation and transportation of pollutants, like the systematic decrease of the trace gase slant column densities with increasing distance from the sources. In some cases, also a weekly cycle was discovered in the time series indicating a clear relationship between the temporal pattern of emissions and observed concentrations. In most cases, also a clear attribution to specific emission sources was possible. Another interesting example was that the time series of the aerosol extinction in general agrees well with those of the trace gases. Finally, the expected sources for HONO could be confirmed by the measurements in Mexico City. Nevertheless, several unexpected results were obtained. First, the magnitude of the observed HONO ΔSCDs in Mexico City was unexpectedly high. It would be interesing if model calculations could reproduce these high values. Also, the glyoxal ΔSCDs over the Gulf of Maine were higher than expected and about a factor of ten than those observed in the Boston urban area. Interestingly, the CHOCHO ΔSCDs at Mexico City were typically much higher compared to those observed at the Boston urban area while those of HCHO were rather similar. Both findings indicate that further research on glyoxal chemistry is needed.

The results of this thesis demonstrate that MAX-DOAS observations have contributed for the study to the characterization and quantification emission and transformation of pollution in two strongly polluted regions. the comprehensive data set of the MAX-DOAS observations is available for a detailed comparison to model results. These modeling studies should in particular address open questions with respect to the chemistry of HONO and glyoxal. The data set can also be used for detailed satellite validation studies. The inversion of the MAX-DOAS can also be further improved especially with respect to profile inversion of trace gas concentrations and aerosol properties. Based on the experience during both campaigns the foundation of a global network of automated MAX-DOAS instruments is recommended.

Appendix

A.1 $\triangle$SCDs ICARTT 2004

The following figures show the ΔSCD time series of the different measurement sites of ICARTT 2004: Brookhaven, Narragansett, MIT, Thompson Farm, Pinnacle State Park and RV Ron Brown.

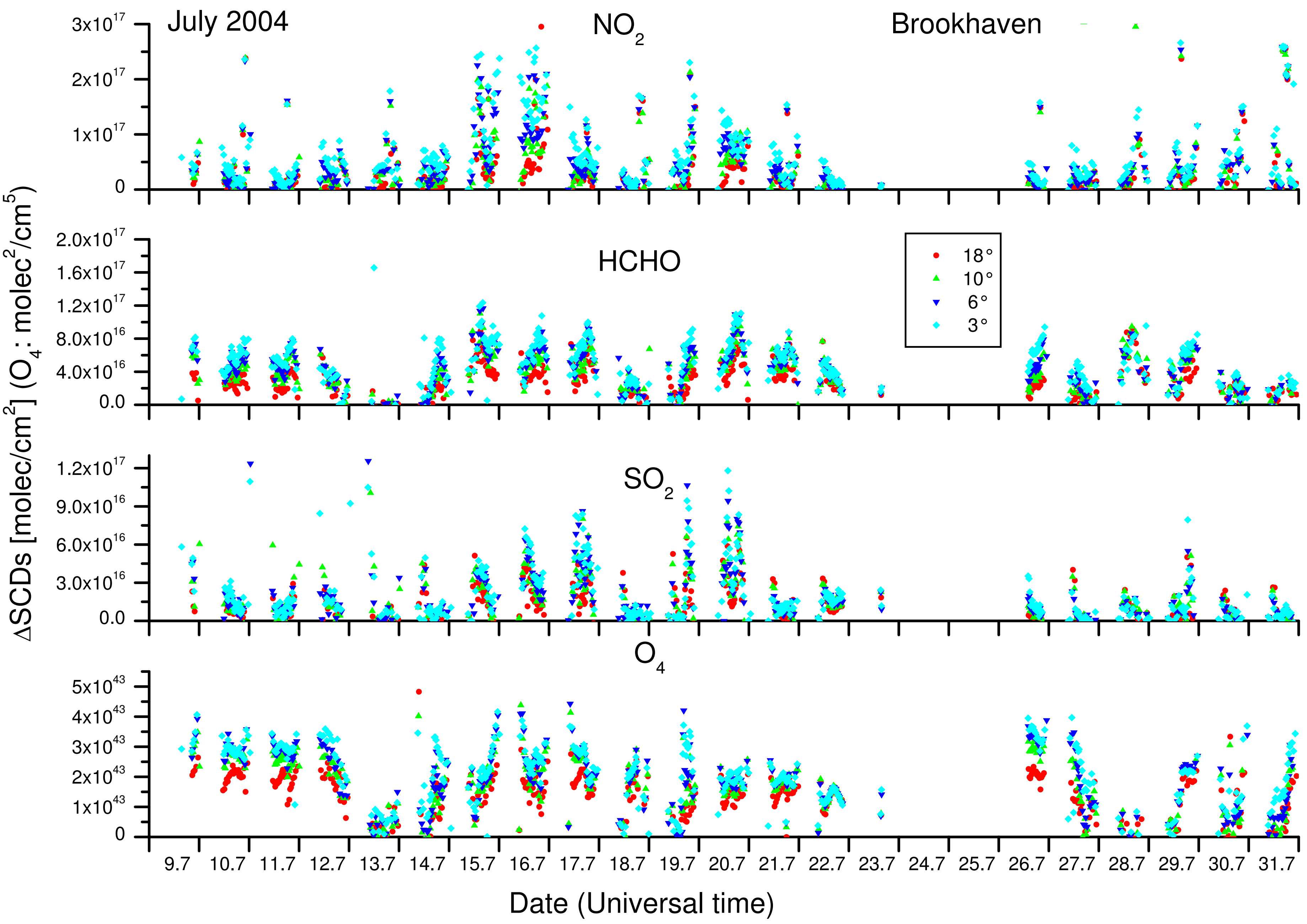
July 2004
NO$_2$
Brookhaven
HCHO
SO$_2$
O$_4$
18°
10°
6°
3°
ΔSCDs [molec/cm^2] (O$_4$: molec^2/cm^5)
3x10^{17}
2x10^{17}
1x10^{17}
0
2.0x10^{17}
1.6x10^{17}
1.2x10^{17}
8.0x10^{16}
4.0x10^{16}
0.0
1.2x10^{17}
9.0x10^{16}
6.0x10^{16}
3.0x10^{16}
0.0
5x10^{43}
4x10^{43}
3x10^{43}
2x10^{43}
1x10^{43}
0
9.7
10.7
11.7
12.7
13.7
14.7
15.7
16.7
17.7
18.7
19.7
20.7
21.7
22.7
23.7
24.7
25.7
26.7
27.7
28.7
29.7
30.7
31.7
Date (Universal time)

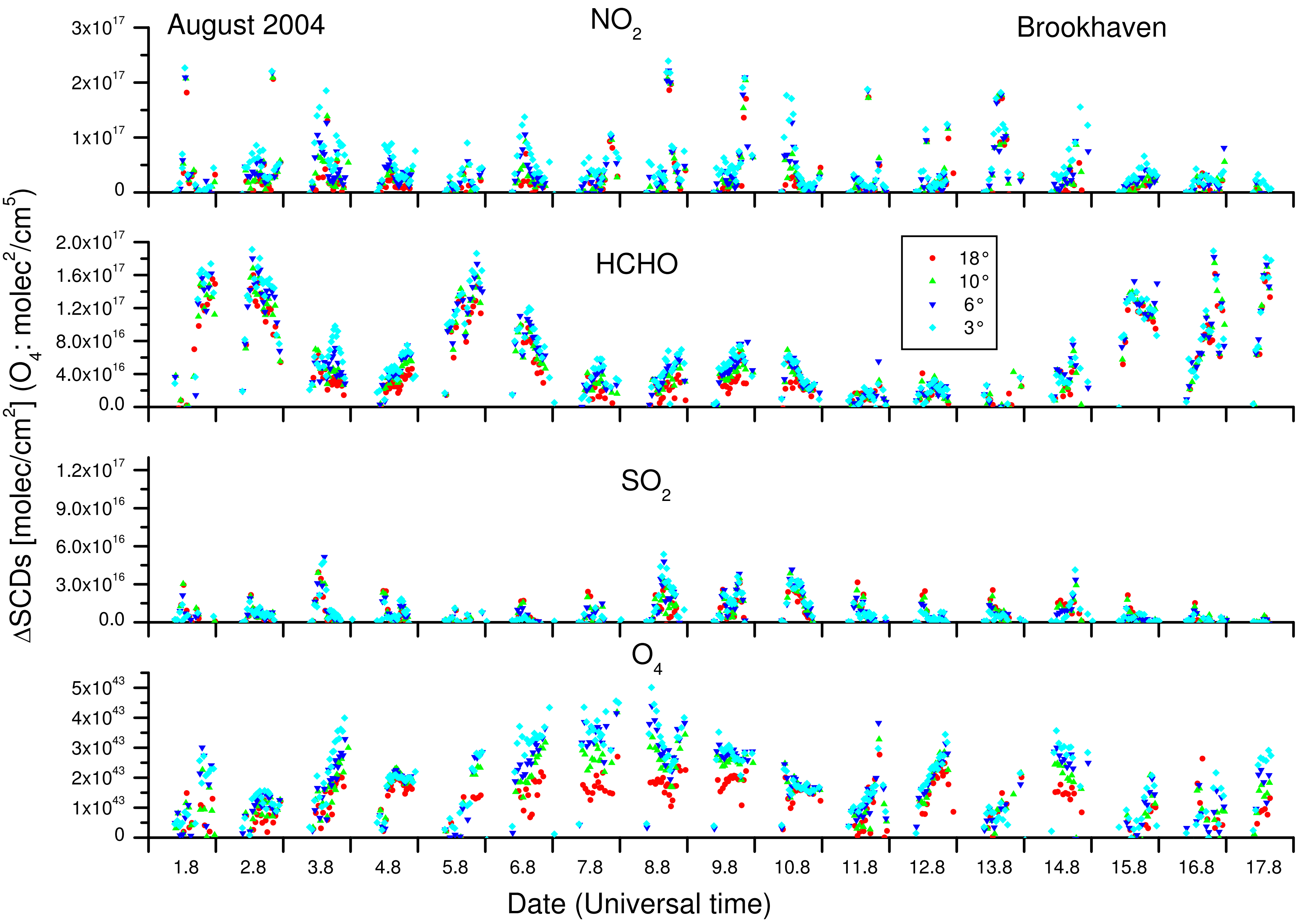
August 2004
NO$_2$
Brookhaven
3x10^{17}
2x10^{17}
1x10^{17}
0
HCHO
2.0x10^{17}
1.6x10^{17}
1.2x10^{17}
8.0x10^{16}
4.0x10^{16}
0.0
18°
10°
6°
3°
SO$_2$
1.2x10^{17}
9.0x10^{16}
6.0x10^{16}
3.0x10^{16}
0.0
O$_4$
5x10^{43}
4x10^{43}
3x10^{43}
2x10^{43}
1x10^{43}
0
ΔSCDs [molec/cm^2] (O$_4$: molec^2/cm^5)
1.8
2.8
3.8
4.8
5.8
6.8
7.8
8.8
9.8
10.8
11.8
12.8
13.8
14.8
15.8
16.8
17.8
Date (Universal time)

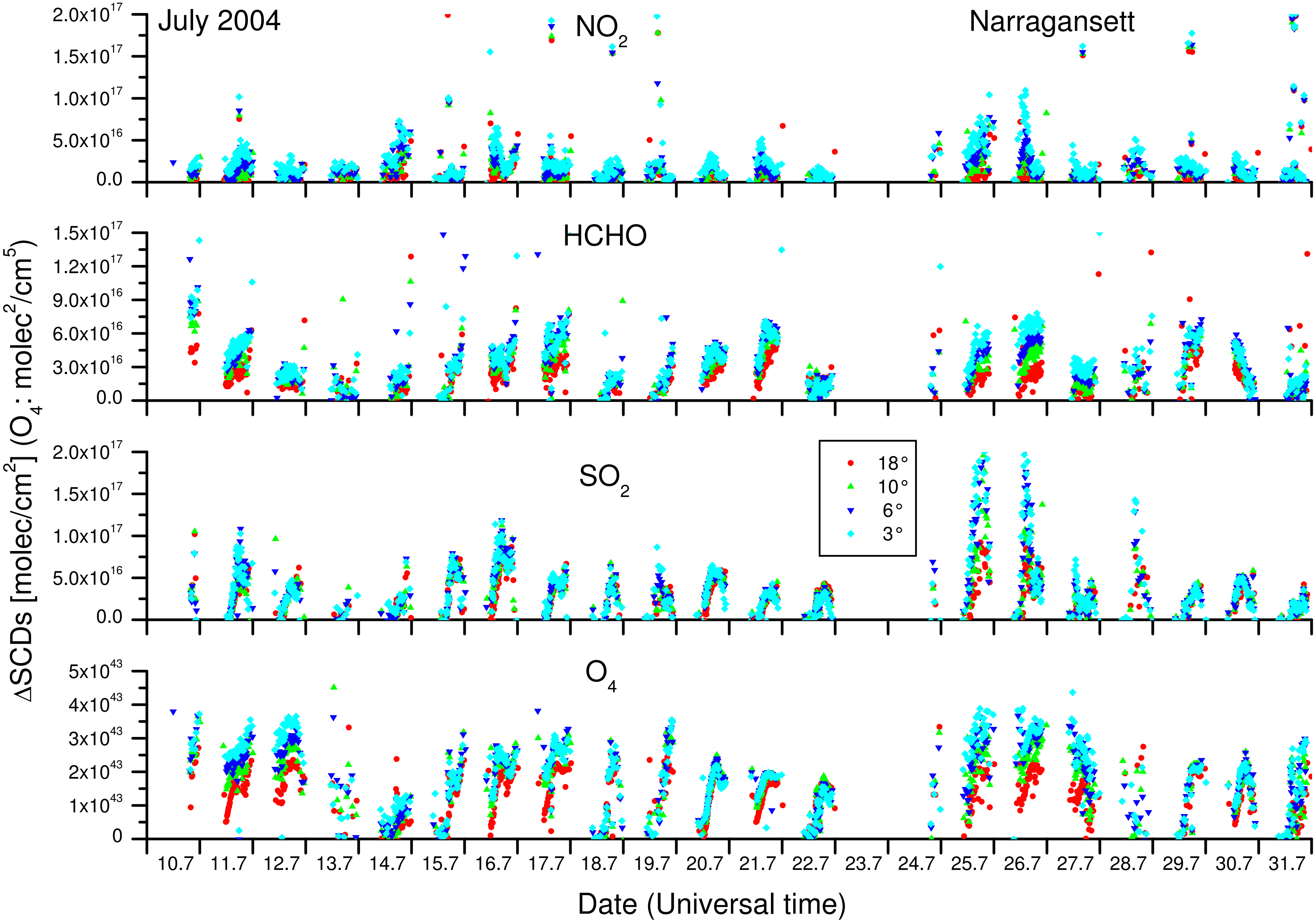
July 2004
NO$_2$
Narragansett
2.0x10^{17}
1.5x10^{17}
1.0x10^{17}
5.0x10^{16}
0.0
HCHO
1.5x10^{17}
1.2x10^{17}
9.0x10^{16}
6.0x10^{16}
3.0x10^{16}
0.0
SO$_2$
2.0x10^{17}
1.5x10^{17}
1.0x10^{17}
5.0x10^{16}
0.0
18°
10°
6°
3°
O$_4$
5x10^{43}
4x10^{43}
3x10^{43}
2x10^{43}
1x10^{43}
0
ΔSCDs [molec/cm^2] (O$_4$: molec^2/cm^5)
10.7
11.7
12.7
13.7
14.7
15.7
16.7
17.7
18.7
19.7
20.7
21.7
22.7
23.7
24.7
25.7
26.7
27.7
28.7
29.7
30.7
31.7
Date (Universal time)

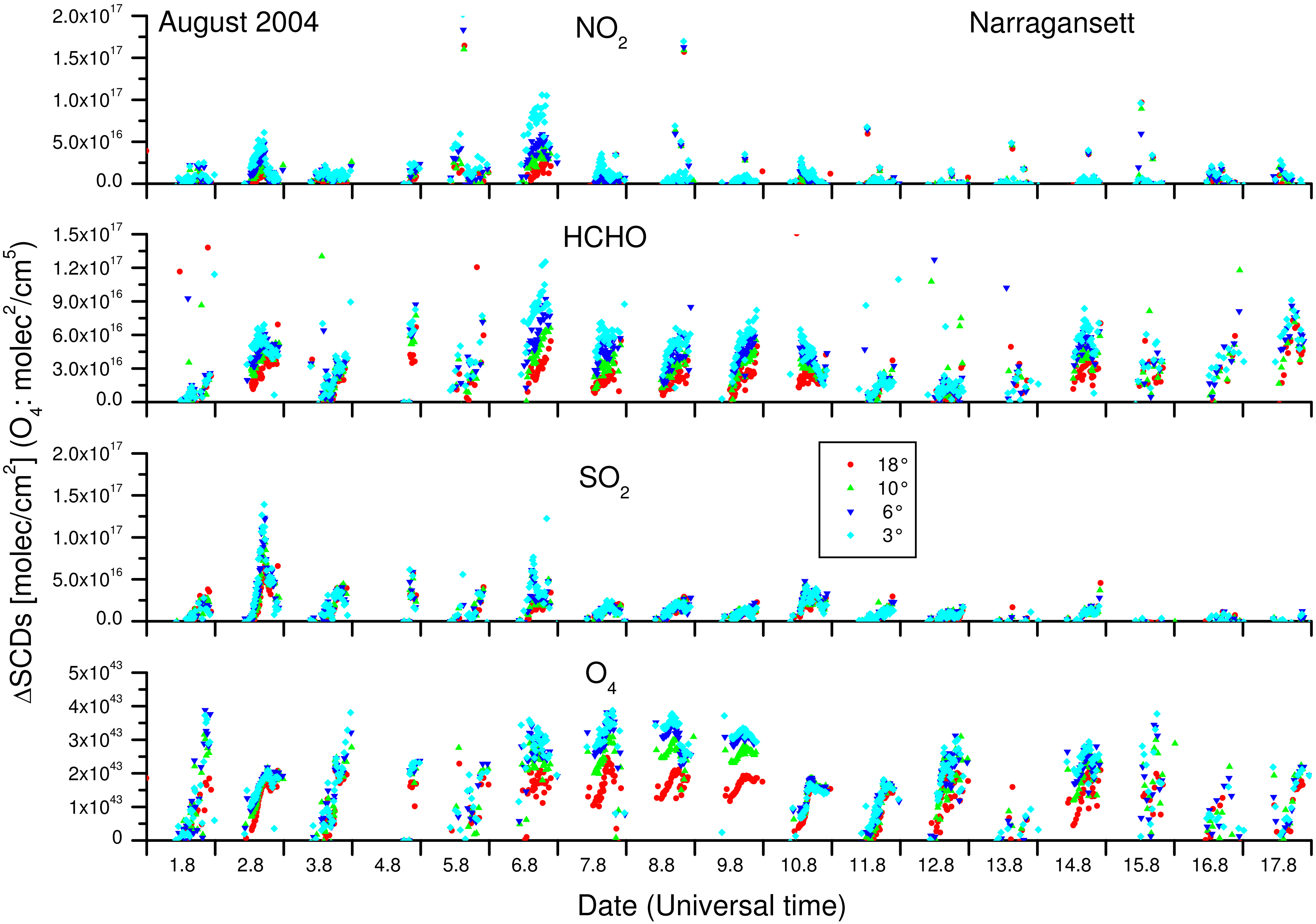
August 2004
Narragansett
NO$_2$
HCHO
SO$_2$
O$_4$
18°
10°
6°
3°
ΔSCDs [molec/cm^2] (O$_4$: molec^2/cm^5)
2.0x10^{17}
1.5x10^{17}
1.0x10^{17}
5.0x10^{16}
0.0
1.5x10^{17}
1.2x10^{17}
9.0x10^{16}
6.0x10^{16}
3.0x10^{16}
0.0
2.0x10^{17}
1.5x10^{17}
1.0x10^{17}
5.0x10^{16}
0.0
5x10^{43}
4x10^{43}
3x10^{43}
2x10^{43}
1x10^{43}
0
1.8
2.8
3.8
4.8
5.8
6.8
7.8
8.8
9.8
10.8
11.8
12.8
13.8
14.8
15.8
16.8
17.8
Date (Universal time)

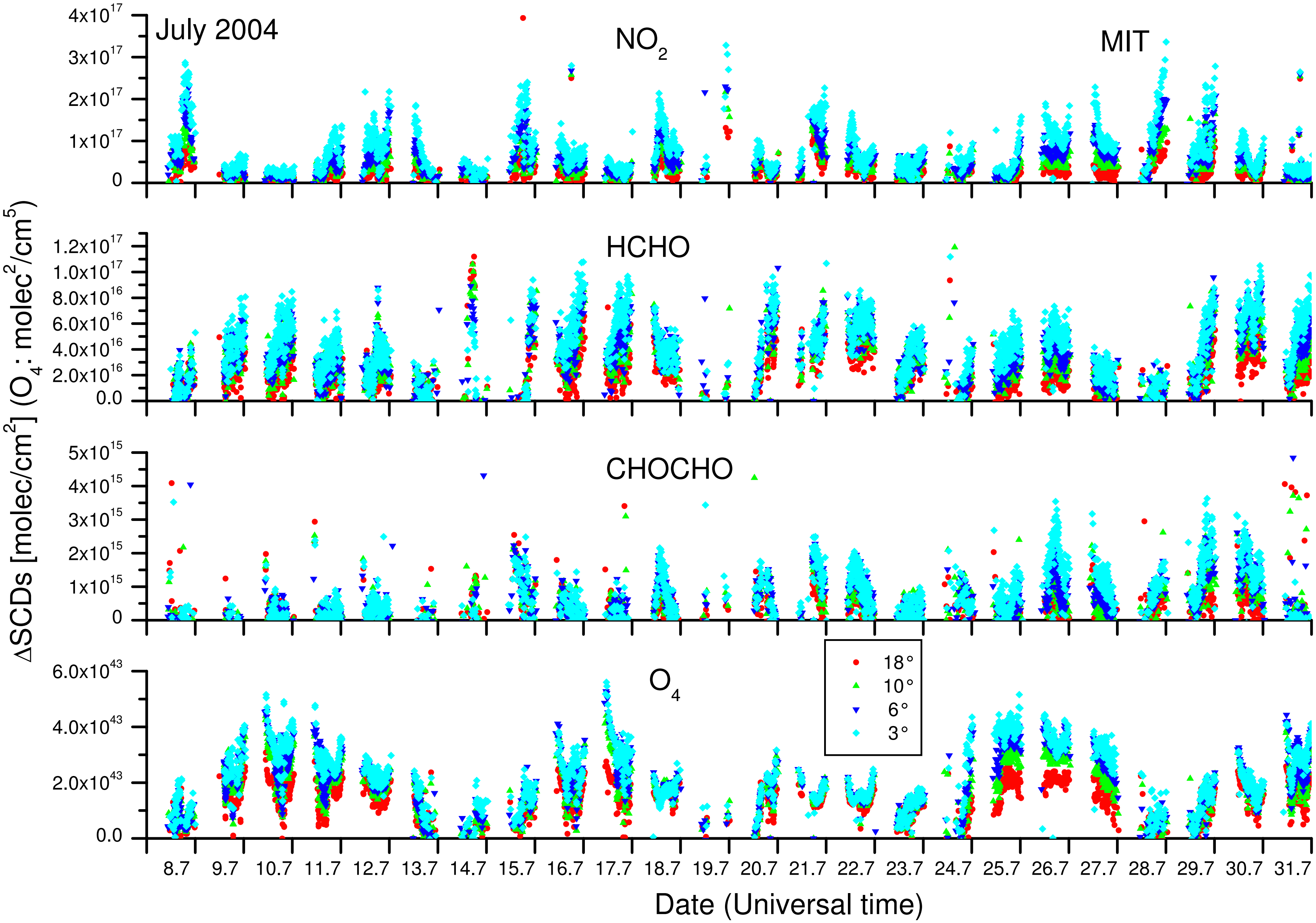
July 2004
NO$_2$
MIT
HCHO
CHOCHO
O$_4$
18°
10°
6°
3°
ΔSCDs [molec/cm^2] (O$_4$: molec^2/cm^5)
4x10^{17}
3x10^{17}
2x10^{17}
1x10^{17}
0
1.2x10^{17}
1.0x10^{17}
8.0x10^{16}
6.0x10^{16}
4.0x10^{16}
2.0x10^{16}
0.0
5x10^{15}
4x10^{15}
3x10^{15}
2x10^{15}
1x10^{15}
0
6.0x10^{43}
4.0x10^{43}
2.0x10^{43}
0.0
8.7
9.7
10.7
11.7
12.7
13.7
14.7
15.7
16.7
17.7
18.7
19.7
20.7
21.7
22.7
23.7
24.7
25.7
26.7
27.7
28.7
29.7
30.7
31.7
Date (Universal time)

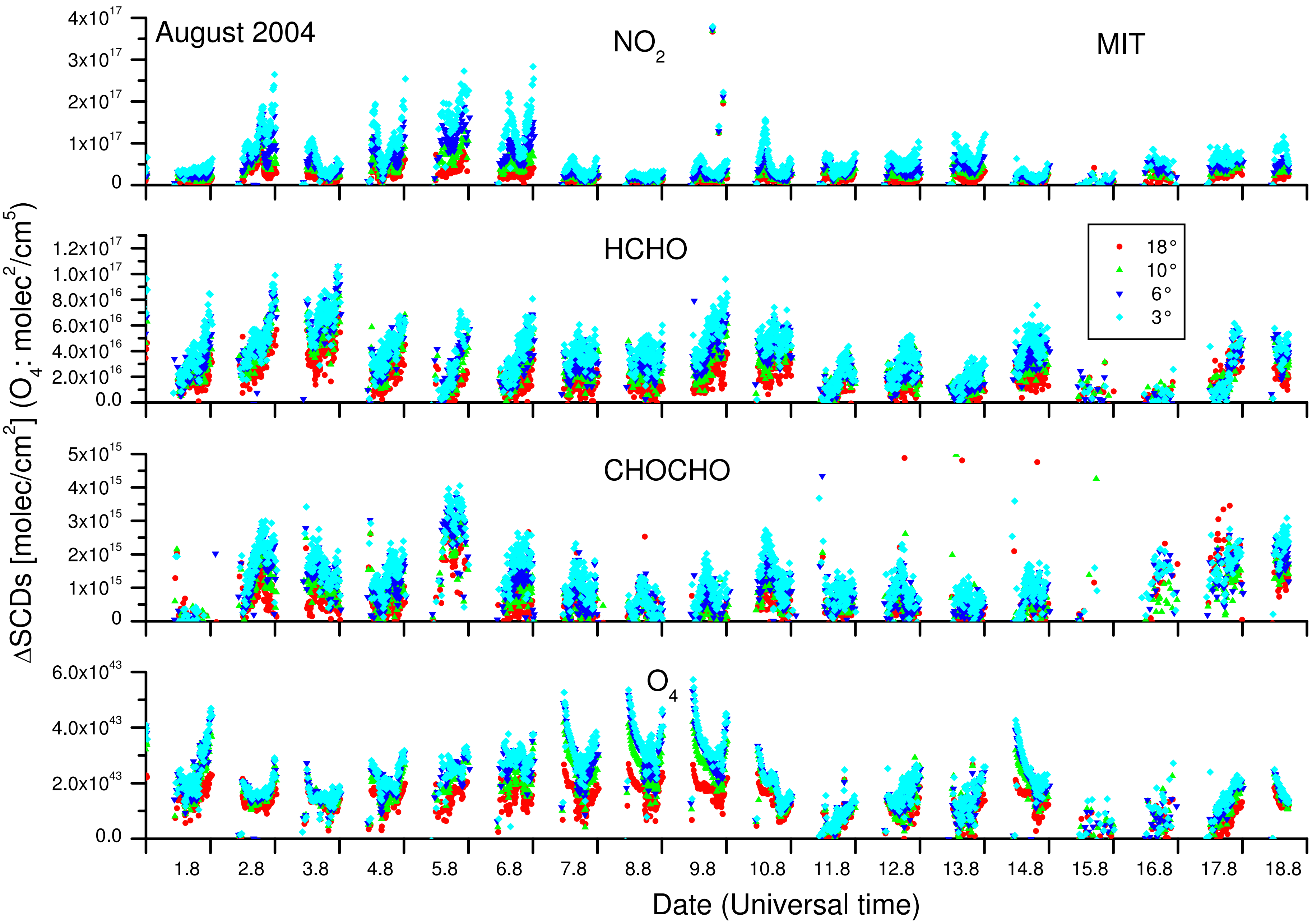
August 2004
NO2
MIT
HCHO
CHOCHO
O4
● 18°
▲ 10°
▼ 6°
◆ 3°
4x10^17
3x10^17
2x10^17
1x10^17
0
1.2x10^17
1.0x10^17
8.0x10^16
6.0x10^16
4.0x10^16
2.0x10^16
0.0
5x10^15
4x10^15
3x10^15
2x10^15
1x10^15
0
6.0x10^43
4.0x10^43
2.0x10^43
0.0
ΔSCDs [molec/cm2] (O4: molec2/cm5)
1.8
2.8
3.8
4.8
5.8
6.8
7.8
8.8
9.8
10.8
11.8
12.8
13.8
14.8
15.8
16.8
17.8
18.8
Date (Universal time)

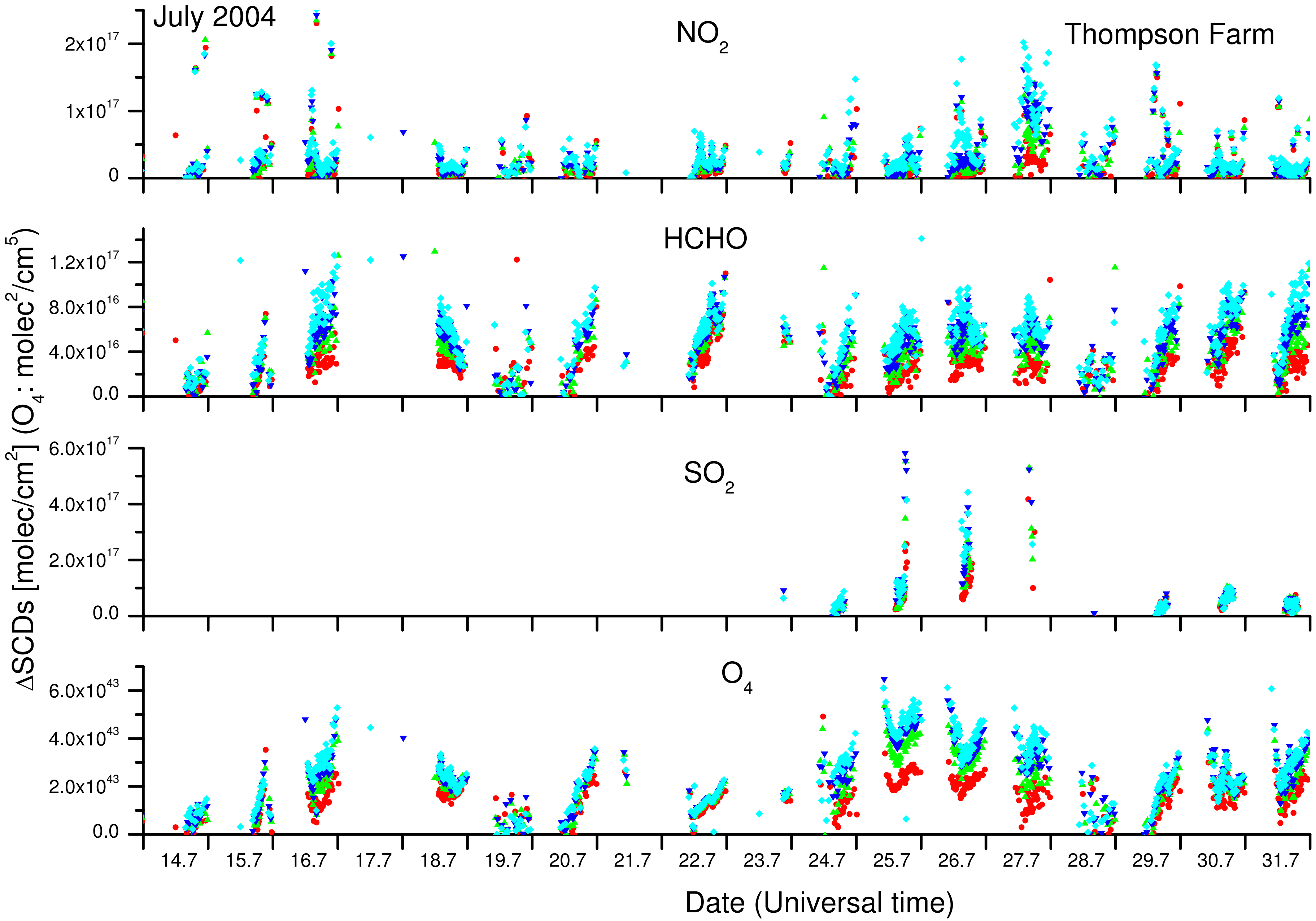
July 2004
Thompson Farm
NO$_2$
HCHO
SO$_2$
O$_4$
ΔSCDs [molec/cm^2] (O$_4$: molec^2/cm^5)
2x10^{17}
1x10^{17}
0
1.2x10^{17}
8.0x10^{16}
4.0x10^{16}
0.0
6.0x10^{17}
4.0x10^{17}
2.0x10^{17}
0.0
6.0x10^{43}
4.0x10^{43}
2.0x10^{43}
0.0
14.7
15.7
16.7
17.7
18.7
19.7
20.7
21.7
22.7
23.7
24.7
25.7
26.7
27.7
28.7
29.7
30.7
31.7
Date (Universal time)

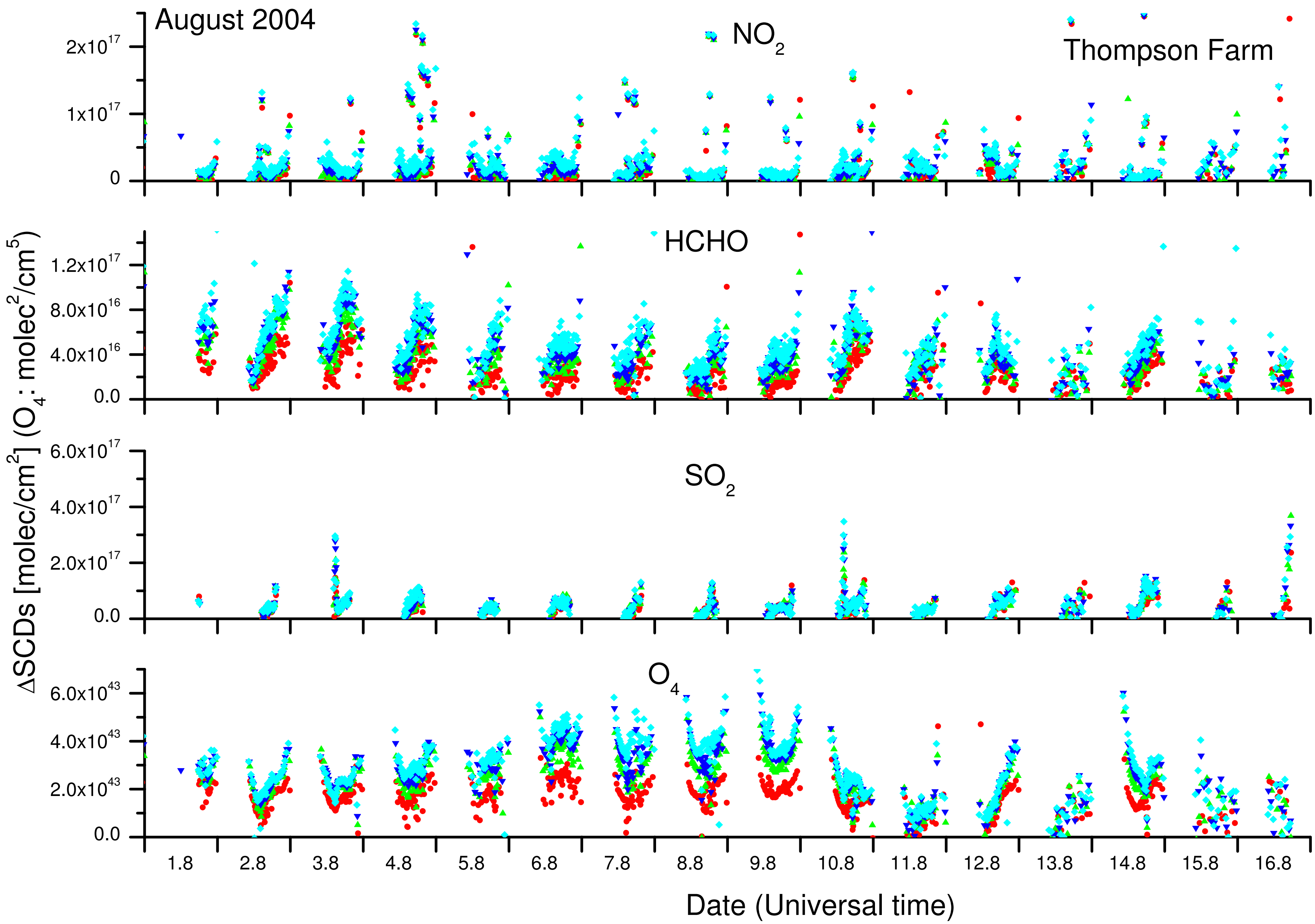
August 2004
NO$_2$
Thompson Farm
HCHO
SO$_2$
O$_4$
2x10^{17}
1x10^{17}
0
1.2x10^{17}
8.0x10^{16}
4.0x10^{16}
0.0
6.0x10^{17}
4.0x10^{17}
2.0x10^{17}
0.0
6.0x10^{43}
4.0x10^{43}
2.0x10^{43}
0.0
ΔSCDs [molec/cm^2] (O$_4$: molec^2/cm^5)
1.8
2.8
3.8
4.8
5.8
6.8
7.8
8.8
9.8
10.8
11.8
12.8
13.8
14.8
15.8
16.8
Date (Universal time)

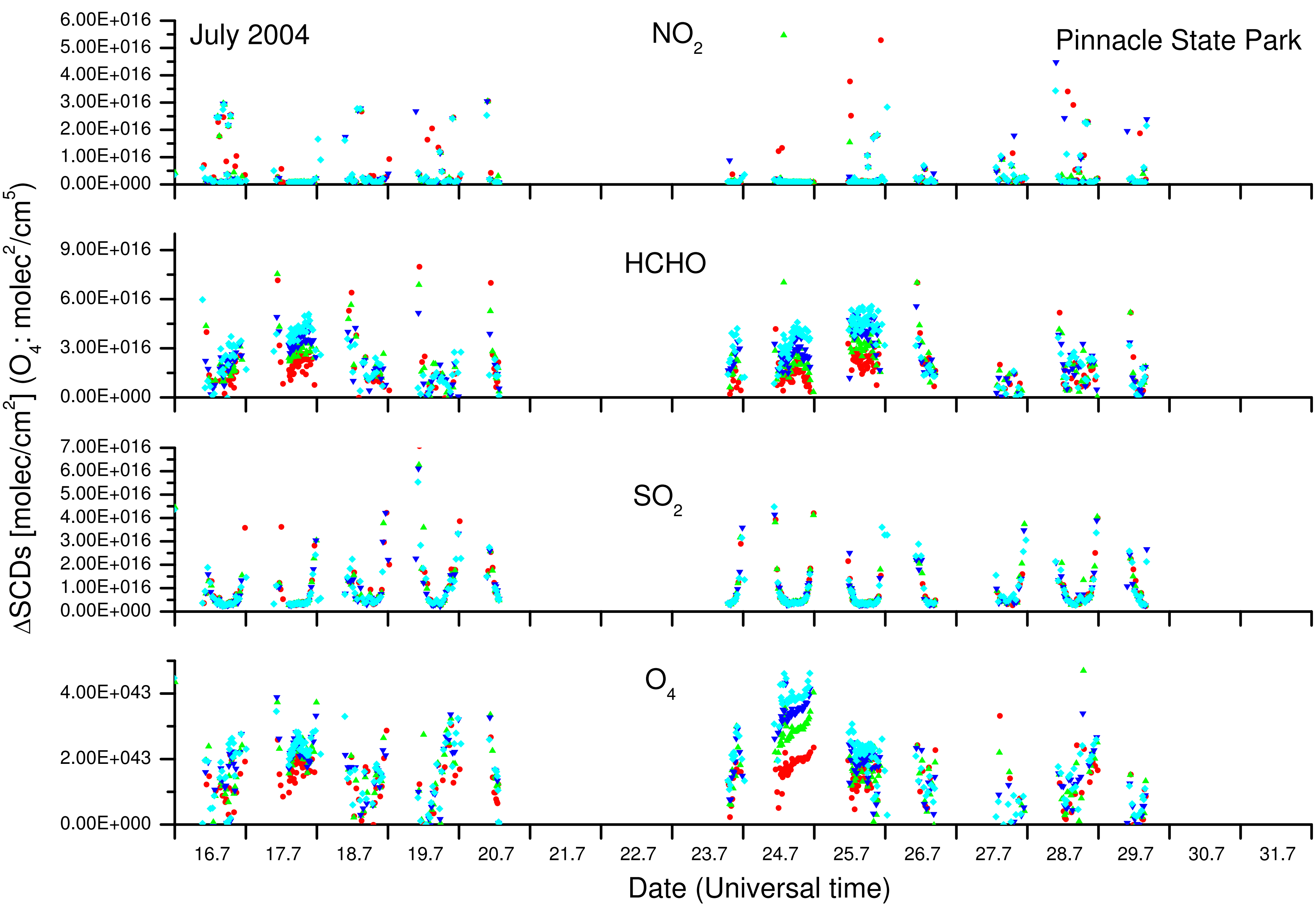
July 2004
NO$_2$
Pinnacle State Park
HCHO
SO$_2$
O$_4$
ΔSCDs [molec/cm^2] (O$_4$: molec^2/cm^5)
6.00E+016
5.00E+016
4.00E+016
3.00E+016
2.00E+016
1.00E+016
0.00E+000
9.00E+016
6.00E+016
3.00E+016
0.00E+000
7.00E+016
6.00E+016
5.00E+016
4.00E+016
3.00E+016
2.00E+016
1.00E+016
0.00E+000
4.00E+043
2.00E+043
0.00E+000
16.7
17.7
18.7
19.7
20.7
21.7
22.7
23.7
24.7
25.7
26.7
27.7
28.7
29.7
30.7
31.7
Date (Universal time)

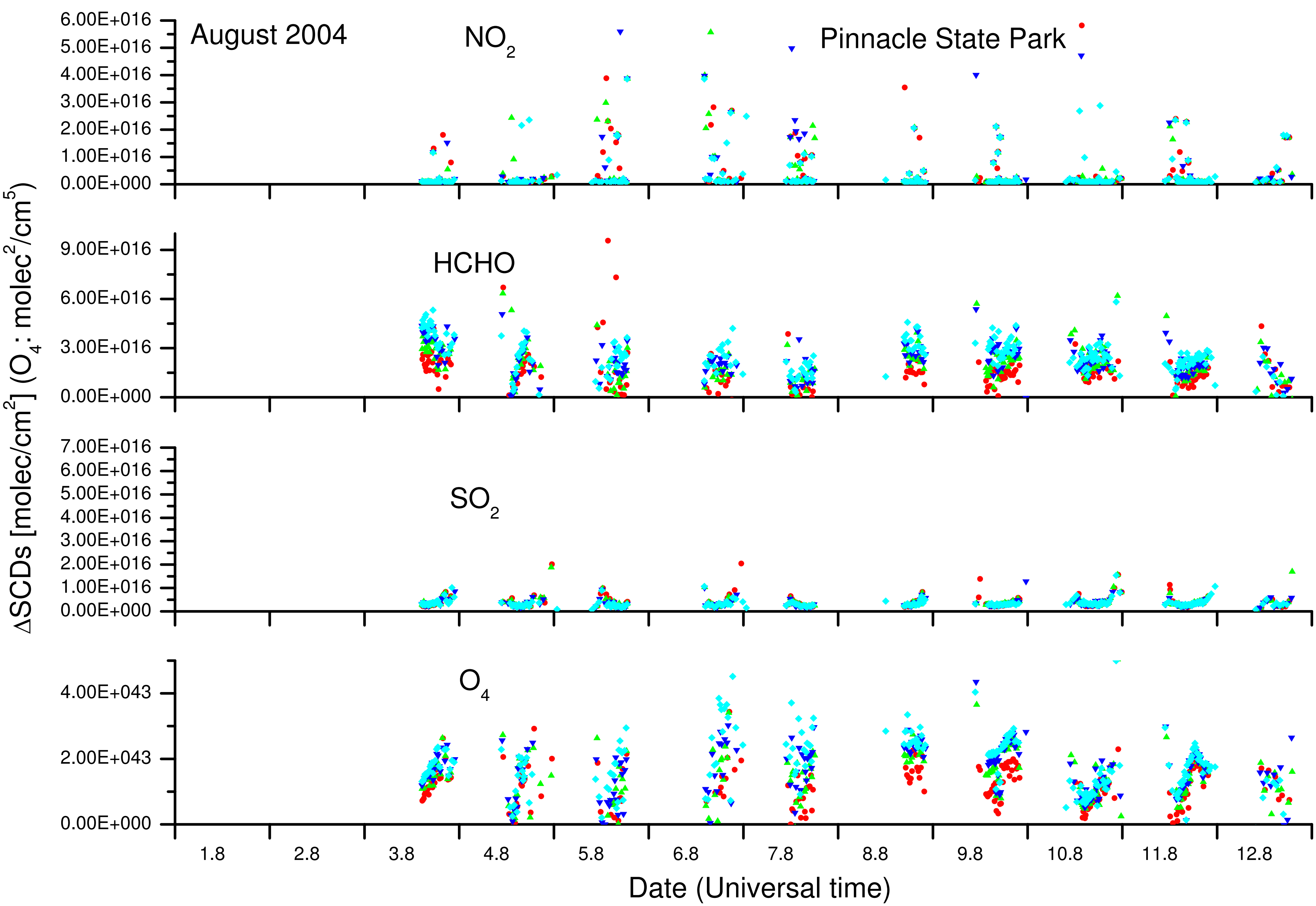
August 2004
Pinnacle State Park
NO2
HCHO
SO2
O4
ΔSCDs [molec/cm2] (O4: molec2/cm5)
Date (Universal time)
6.00E+016
5.00E+016
4.00E+016
3.00E+016
2.00E+016
1.00E+016
0.00E+000
9.00E+016
6.00E+016
3.00E+016
0.00E+000
7.00E+016
6.00E+016
5.00E+016
4.00E+016
3.00E+016
2.00E+016
1.00E+016
0.00E+000
4.00E+043
2.00E+043
0.00E+000
1.8
2.8
3.8
4.8
5.8
6.8
7.8
8.8
9.8
10.8
11.8
12.8

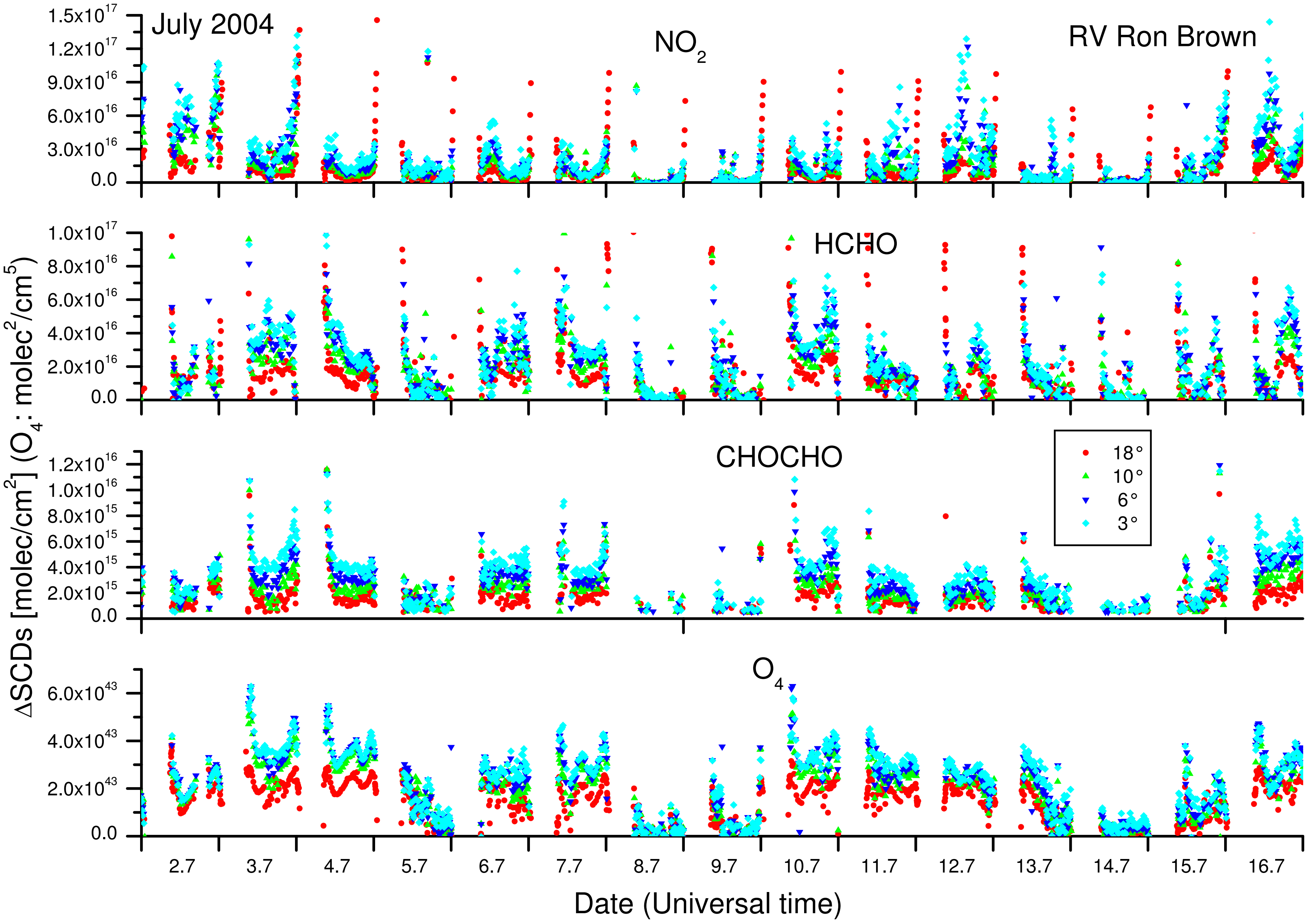
July 2004
NO$_2$
RV Ron Brown
1.5x10^{17}
1.2x10^{17}
9.0x10^{16}
6.0x10^{16}
3.0x10^{16}
0.0
HCHO
1.0x10^{17}
8.0x10^{16}
6.0x10^{16}
4.0x10^{16}
2.0x10^{16}
0.0
CHOCHO
1.2x10^{16}
1.0x10^{16}
8.0x10^{15}
6.0x10^{15}
4.0x10^{15}
2.0x10^{15}
0.0
18°
10°
6°
3°
O$_4$
6.0x10^{43}
4.0x10^{43}
2.0x10^{43}
0.0
ΔSCDs [molec/cm^2] (O$_4$: molec^2/cm^5)
2.7
3.7
4.7
5.7
6.7
7.7
8.7
9.7
10.7
11.7
12.7
13.7
14.7
15.7
16.7
Date (Universal time)

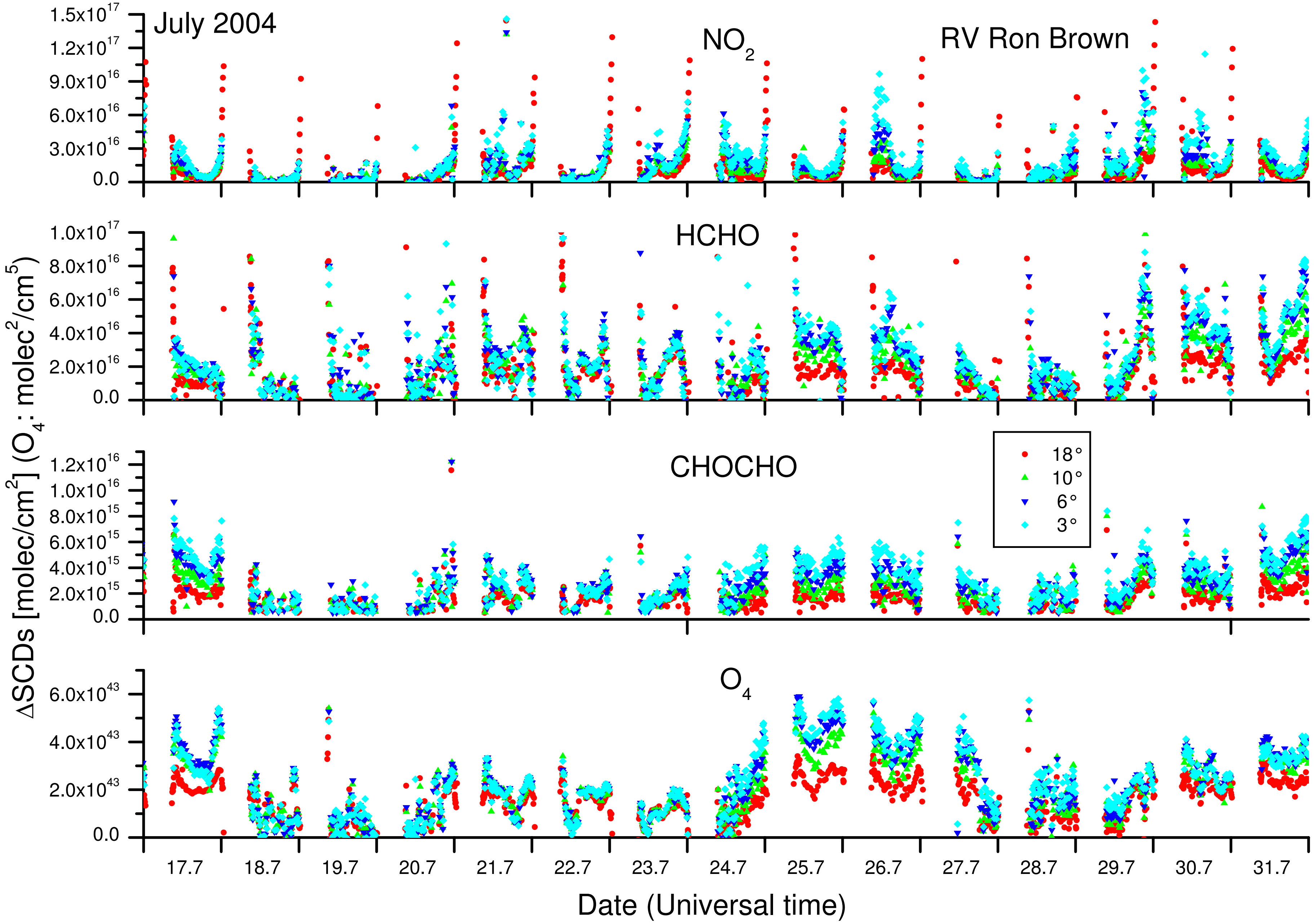
July 2004
NO2
RV Ron Brown
1.5x10^17
1.2x10^17
9.0x10^16
6.0x10^16
3.0x10^16
0.0
HCHO
1.0x10^17
8.0x10^16
6.0x10^16
4.0x10^16
2.0x10^16
0.0
CHOCHO
1.2x10^16
1.0x10^16
8.0x10^15
6.0x10^15
4.0x10^15
2.0x10^15
0.0
18°
10°
6°
3°
O4
6.0x10^43
4.0x10^43
2.0x10^43
0.0
ΔSCDs [molec/cm²] (O4: molec²/cm⁵)
17.7
18.7
19.7
20.7
21.7
22.7
23.7
24.7
25.7
26.7
27.7
28.7
29.7
30.7
31.7
Date (Universal time)

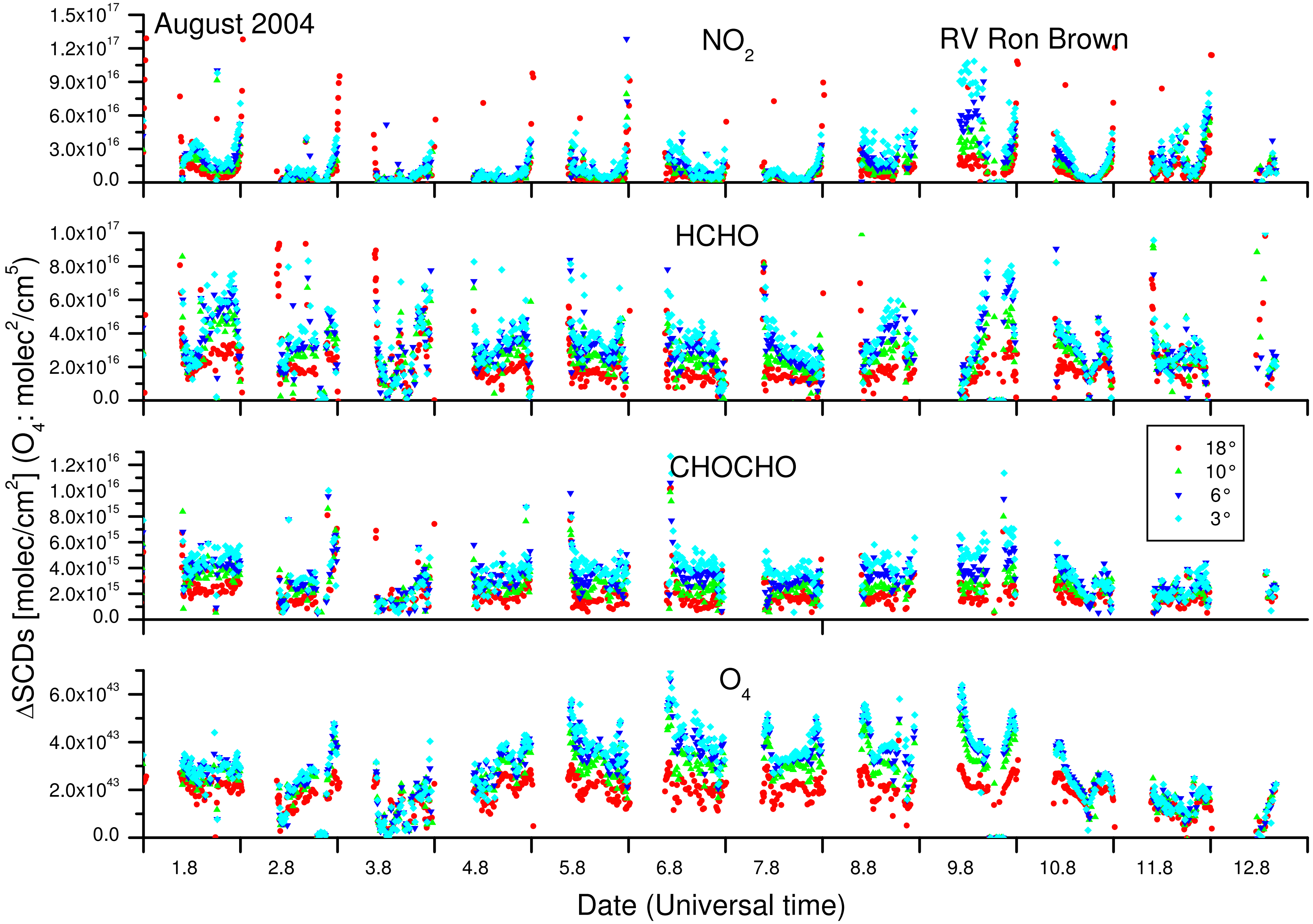
August 2004
NO$_2$
RV Ron Brown
HCHO
CHOCHO
O$_4$
ΔSCDs [molec/cm^2] (O$_4$: molec^2/cm^5)
Date (Universal time)
1.5x10^{17}
1.2x10^{17}
9.0x10^{16}
6.0x10^{16}
3.0x10^{16}
0.0
1.0x10^{17}
8.0x10^{16}
6.0x10^{16}
4.0x10^{16}
2.0x10^{16}
0.0
1.2x10^{16}
1.0x10^{16}
8.0x10^{15}
6.0x10^{15}
4.0x10^{15}
2.0x10^{15}
0.0
6.0x10^{43}
4.0x10^{43}
2.0x10^{43}
0.0
1.8
2.8
3.8
4.8
5.8
6.8
7.8
8.8
9.8
10.8
11.8
12.8
● 18°
▲ 10°
▼ 6°
◆ 3°

A.2 △SCDs MILAGRO 2006

The following figures show the ΔSCD time series of the different measurement sites of MILAGRO 2006: T0 (south, north and west), T1 and T2.

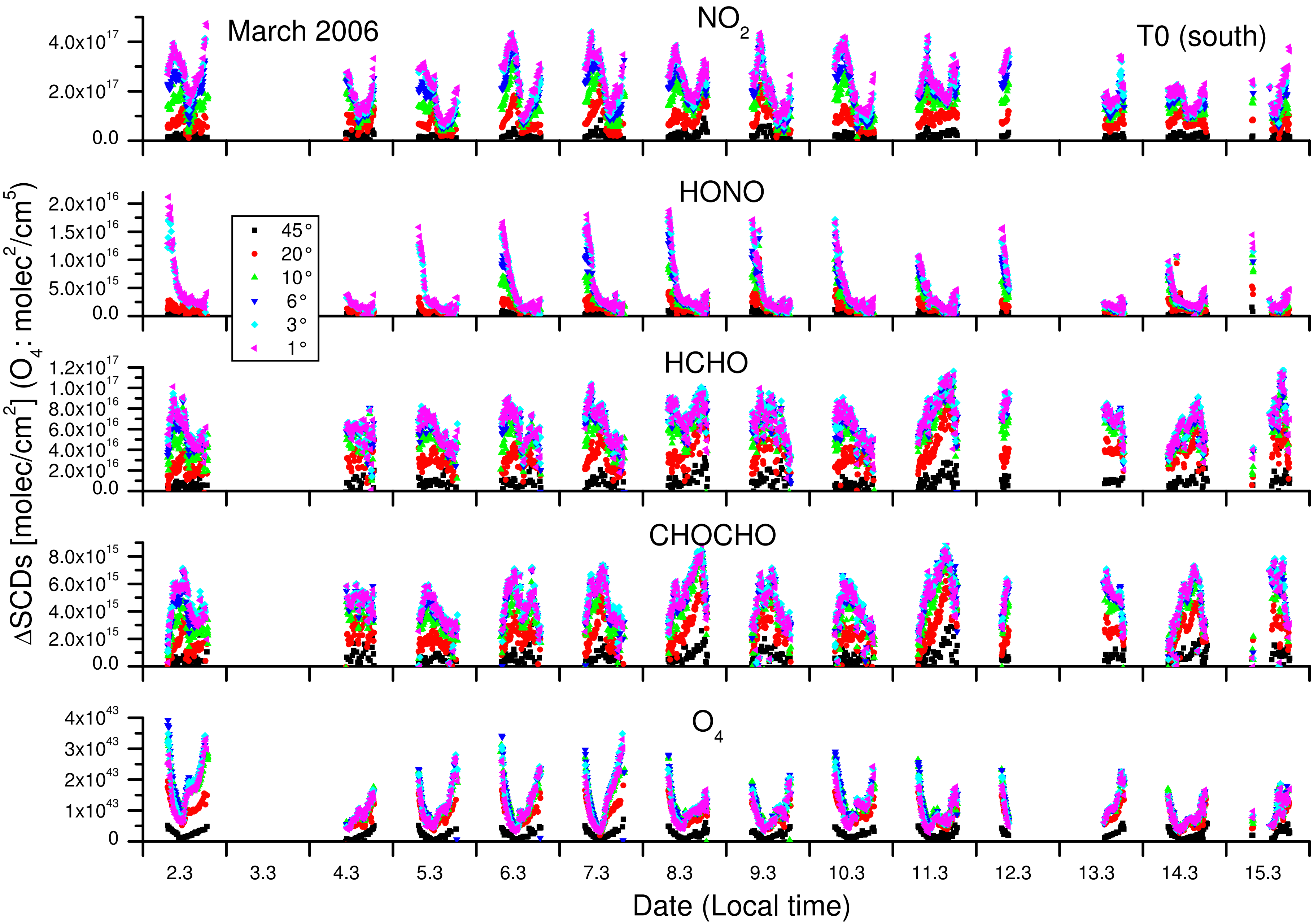
March 2006
T0 (south)
NO$_2$
HONO
HCHO
CHOCHO
O$_4$
45°
20°
10°
6°
3°
1°
ΔSCDs [molec/cm^2] (O$_4$: molec^2/cm^5)
4.0x10^{17}
2.0x10^{17}
0.0
2.0x10^{16}
1.5x10^{16}
1.0x10^{16}
5.0x10^{15}
0.0
1.2x10^{17}
1.0x10^{17}
8.0x10^{16}
6.0x10^{16}
4.0x10^{16}
2.0x10^{16}
0.0
8.0x10^{15}
6.0x10^{15}
4.0x10^{15}
2.0x10^{15}
0.0
4x10^{43}
3x10^{43}
2x10^{43}
1x10^{43}
0
2.3
3.3
4.3
5.3
6.3
7.3
8.3
9.3
10.3
11.3
12.3
13.3
14.3
15.3
Date (Local time)

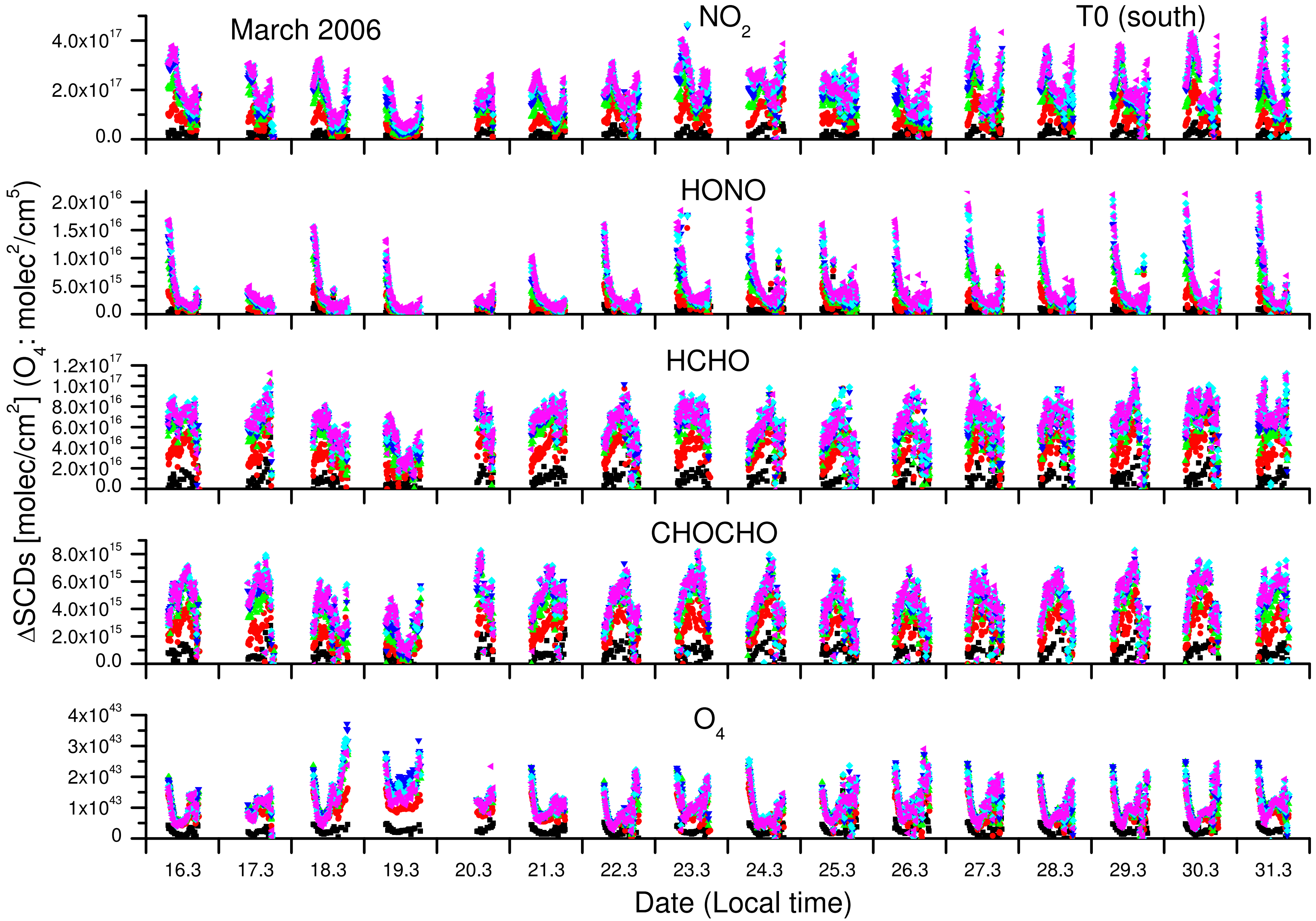
March 2006
NO2
T0 (south)
HONO
HCHO
CHOCHO
O4
ΔSCDs [molec/cm2] (O4 : molec2/cm5)
4.0x10^17
2.0x10^17
0.0
2.0x10^16
1.5x10^16
1.0x10^16
5.0x10^15
0.0
1.2x10^17
1.0x10^17
8.0x10^16
6.0x10^16
4.0x10^16
2.0x10^16
0.0
8.0x10^15
6.0x10^15
4.0x10^15
2.0x10^15
0.0
4x10^43
3x10^43
2x10^43
1x10^43
0
16.3
17.3
18.3
19.3
20.3
21.3
22.3
23.3
24.3
25.3
26.3
27.3
28.3
29.3
30.3
31.3
Date (Local time)

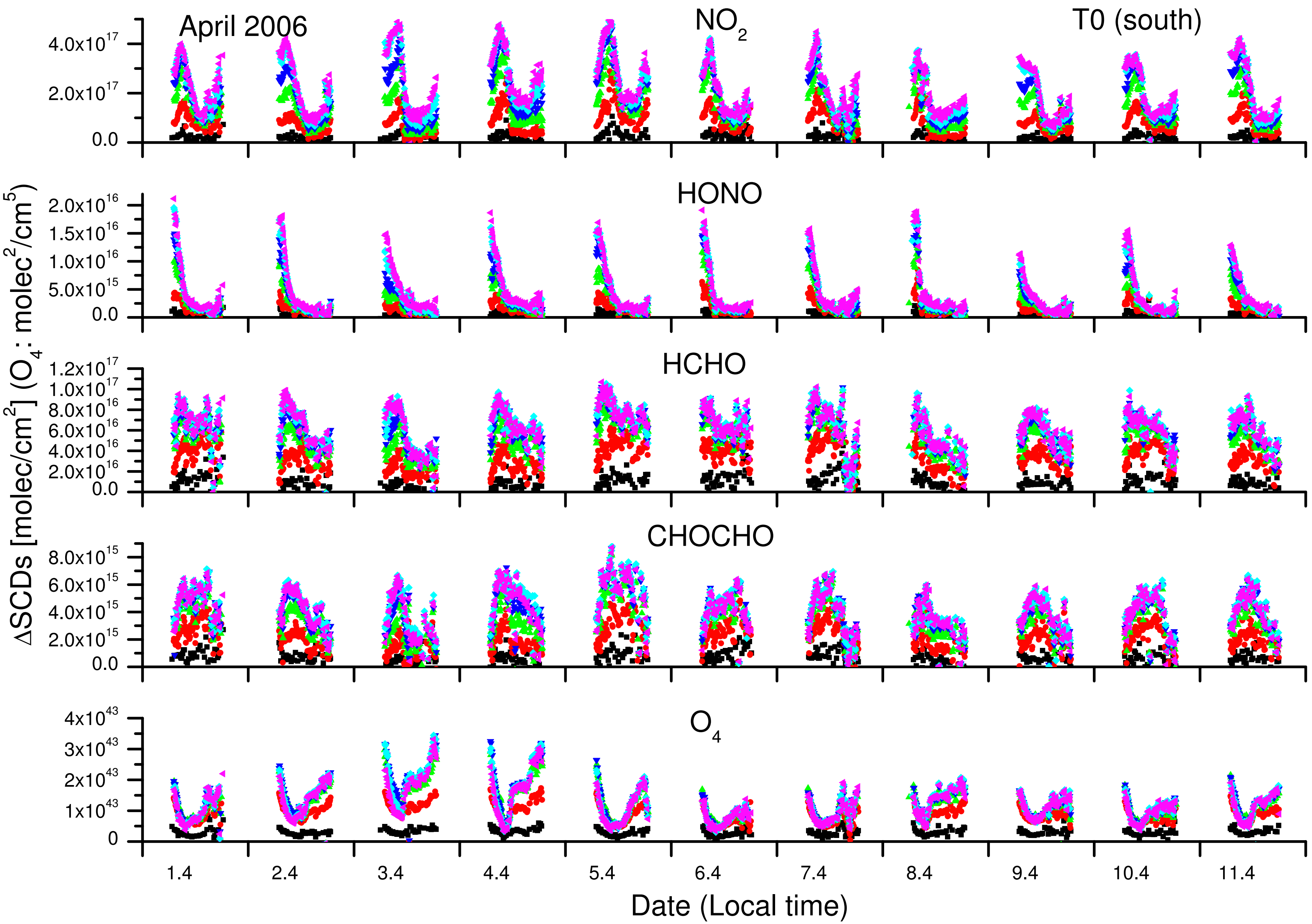
April 2006
NO$_2$
T0 (south)
4.0x10^{17}
2.0x10^{17}
0.0
HONO
2.0x10^{16}
1.5x10^{16}
1.0x10^{16}
5.0x10^{15}
0.0
HCHO
1.2x10^{17}
1.0x10^{17}
8.0x10^{16}
6.0x10^{16}
4.0x10^{16}
2.0x10^{16}
0.0
CHOCHO
8.0x10^{15}
6.0x10^{15}
4.0x10^{15}
2.0x10^{15}
0.0
O$_4$
4x10^{43}
3x10^{43}
2x10^{43}
1x10^{43}
0
ΔSCDs [molec/cm^2] (O$_4$: molec^2/cm^5)
1.4
2.4
3.4
4.4
5.4
6.4
7.4
8.4
9.4
10.4
11.4
Date (Local time)

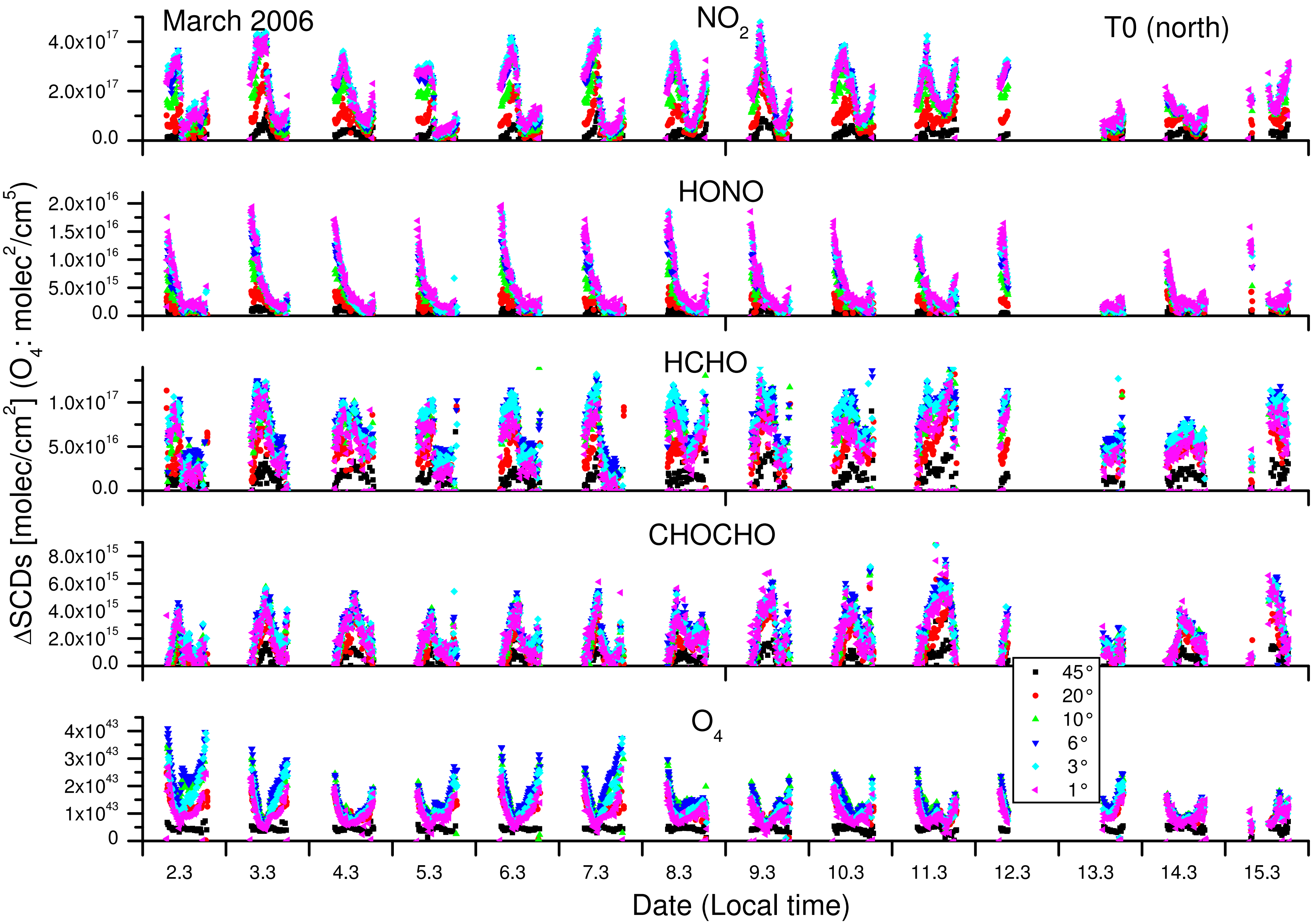
March 2006
NO2
T0 (north)
HONO
HCHO
CHOCHO
O4
ΔSCDs [molec/cm²] (O4: molec²/cm⁵)
4.0x10^17
2.0x10^17
0.0
2.0x10^16
1.5x10^16
1.0x10^16
5.0x10^15
0.0
1.0x10^17
5.0x10^16
0.0
8.0x10^15
6.0x10^15
4.0x10^15
2.0x10^15
0.0
4x10^43
3x10^43
2x10^43
1x10^43
0
45°
20°
10°
6°
3°
1°
2.3
3.3
4.3
5.3
6.3
7.3
8.3
9.3
10.3
11.3
12.3
13.3
14.3
15.3
Date (Local time)

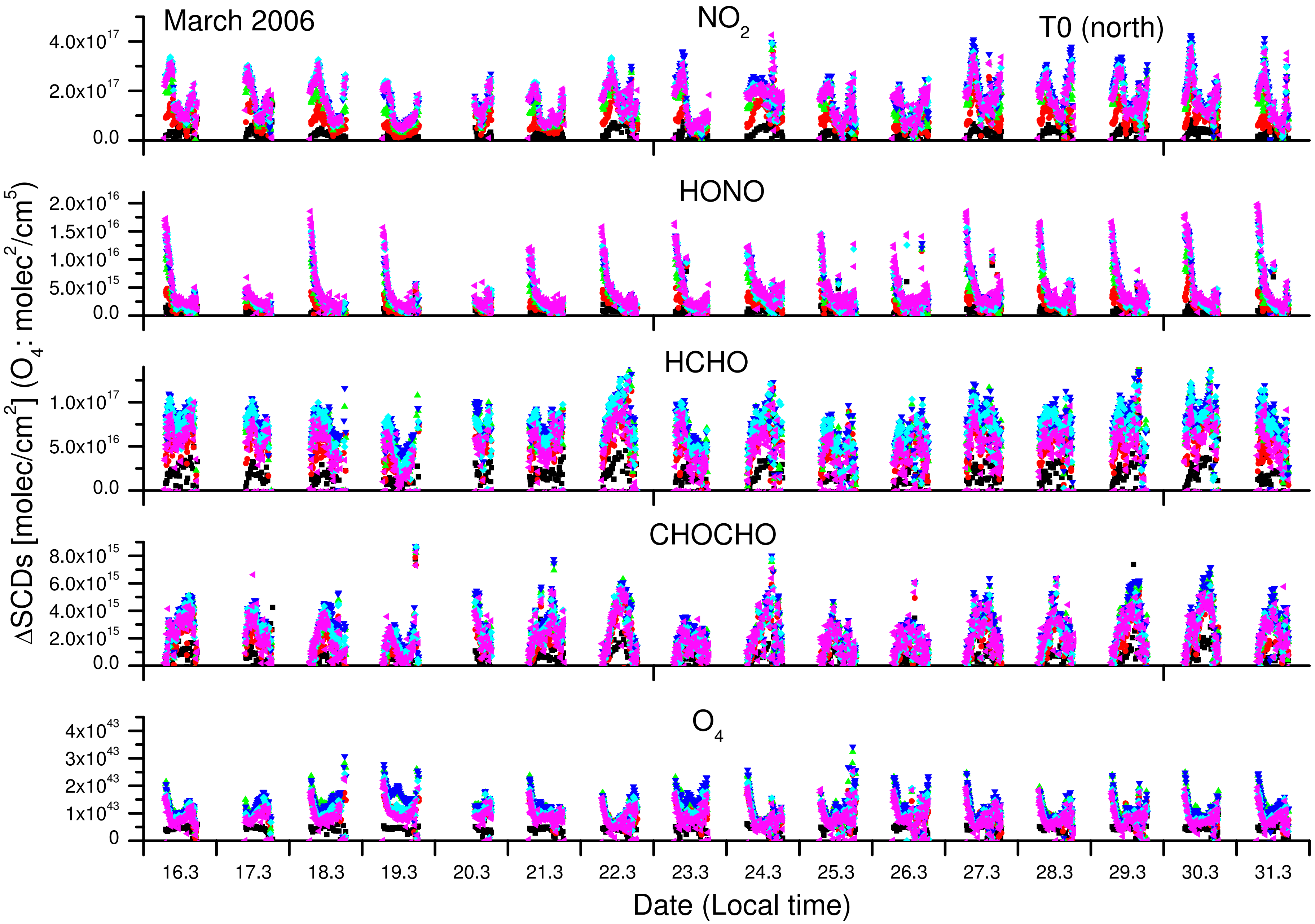
March 2006
T0 (north)
NO$_2$
HONO
HCHO
CHOCHO
O$_4$
ΔSCDs [molec/cm^2] (O$_4$: molec^2/cm^5)
4.0x10^{17}
2.0x10^{17}
0.0
2.0x10^{16}
1.5x10^{16}
1.0x10^{16}
5.0x10^{15}
0.0
1.0x10^{17}
5.0x10^{16}
0.0
8.0x10^{15}
6.0x10^{15}
4.0x10^{15}
2.0x10^{15}
0.0
4x10^{43}
3x10^{43}
2x10^{43}
1x10^{43}
0
16.3
17.3
18.3
19.3
20.3
21.3
22.3
23.3
24.3
25.3
26.3
27.3
28.3
29.3
30.3
31.3
Date (Local time)

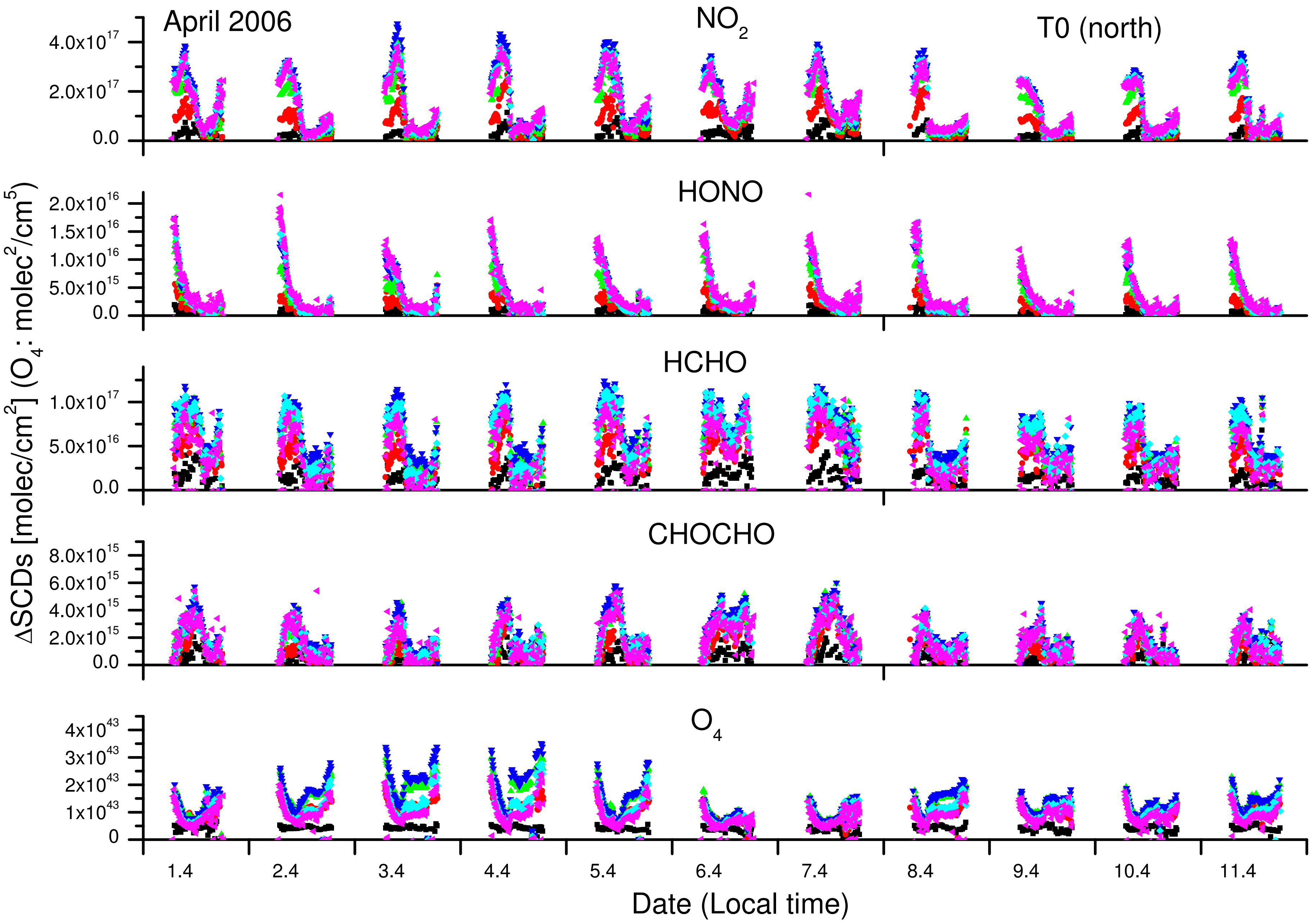
April 2006
NO2
T0 (north)
HONO
HCHO
CHOCHO
O4
ΔSCDs [molec/cm²] (O4: molec²/cm⁵)
4.0x10^17
2.0x10^17
0.0
2.0x10^16
1.5x10^16
1.0x10^16
5.0x10^15
0.0
1.0x10^17
5.0x10^16
0.0
8.0x10^15
6.0x10^15
4.0x10^15
2.0x10^15
0.0
4x10^43
3x10^43
2x10^43
1x10^43
0
1.4
2.4
3.4
4.4
5.4
6.4
7.4
8.4
9.4
10.4
11.4
Date (Local time)

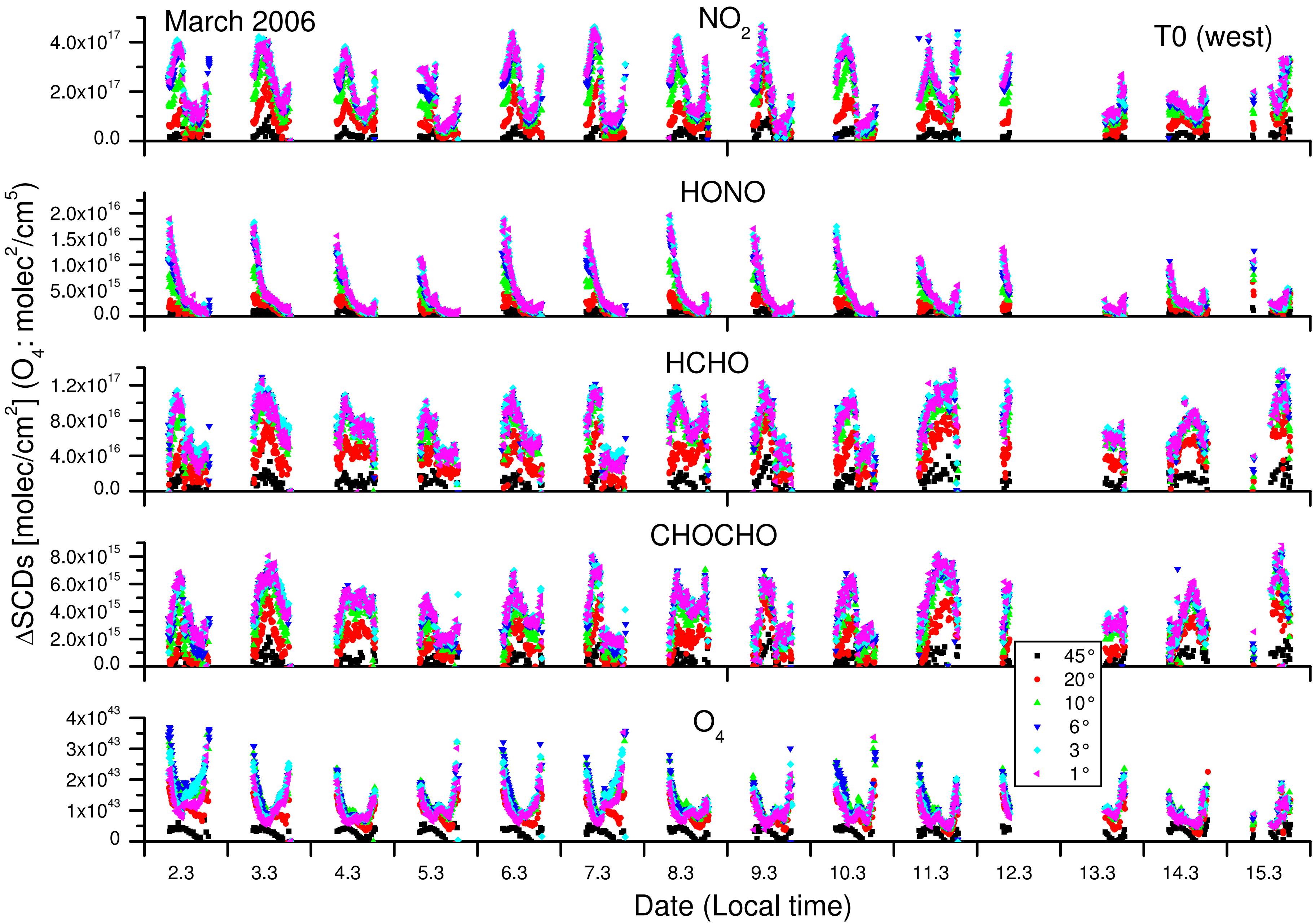
March 2006
NO$_2$
T0 (west)
4.0x10^{17}
2.0x10^{17}
0.0
HONO
2.0x10^{16}
1.5x10^{16}
1.0x10^{16}
5.0x10^{15}
0.0
HCHO
1.2x10^{17}
8.0x10^{16}
4.0x10^{16}
0.0
CHOCHO
8.0x10^{15}
6.0x10^{15}
4.0x10^{15}
2.0x10^{15}
0.0
O$_4$
4x10^{43}
3x10^{43}
2x10^{43}
1x10^{43}
0
ΔSCDs [molec/cm^2] (O$_4$: molec^2/cm^5)
45°
20°
10°
6°
3°
1°
2.3
3.3
4.3
5.3
6.3
7.3
8.3
9.3
10.3
11.3
12.3
13.3
14.3
15.3
Date (Local time)

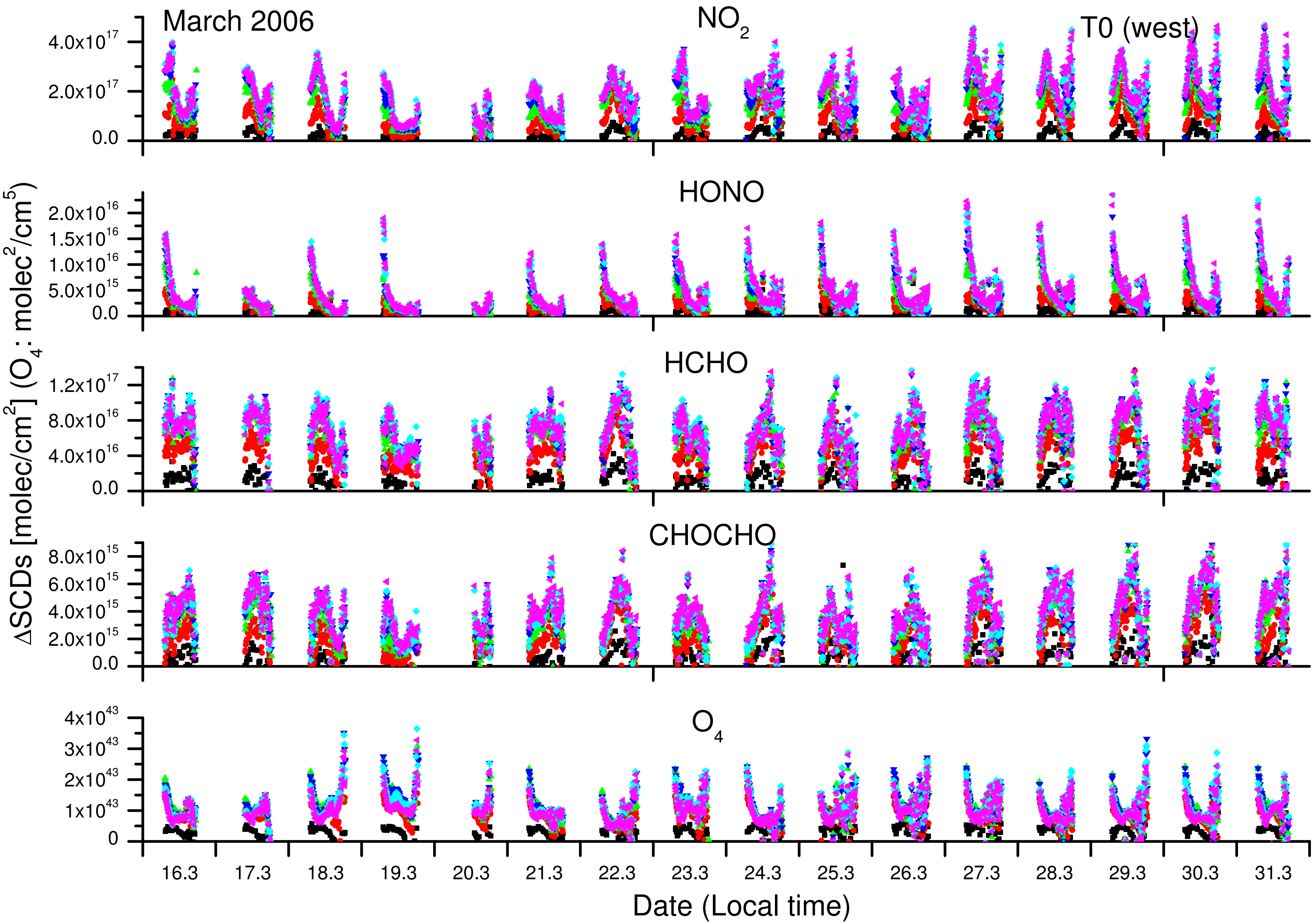
March 2006
NO$_2$
T0 (west)
4.0x10^{17}
2.0x10^{17}
0.0
HONO
2.0x10^{16}
1.5x10^{16}
1.0x10^{16}
5.0x10^{15}
0.0
HCHO
1.2x10^{17}
8.0x10^{16}
4.0x10^{16}
0.0
CHOCHO
8.0x10^{15}
6.0x10^{15}
4.0x10^{15}
2.0x10^{15}
0.0
O$_4$
4x10^{43}
3x10^{43}
2x10^{43}
1x10^{43}
0
ΔSCDs [molec/cm^2] (O$_4$: molec^2/cm^5)
16.3
17.3
18.3
19.3
20.3
21.3
22.3
23.3
24.3
25.3
26.3
27.3
28.3
29.3
30.3
31.3
Date (Local time)

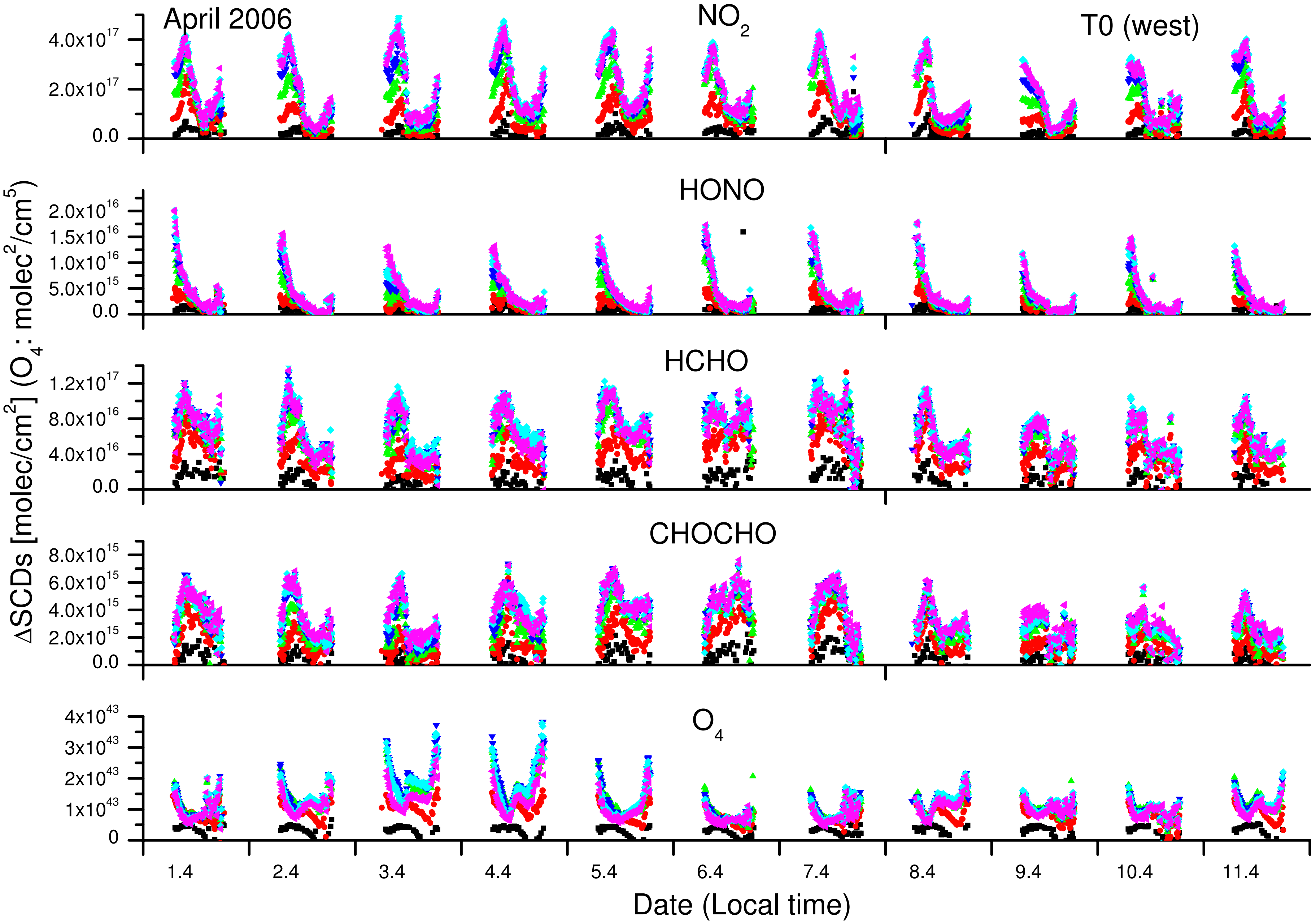
April 2006
NO$_2$
T0 (west)
HONO
HCHO
CHOCHO
O$_4$
ΔSCDs [molec/cm^2] (O$_4$: molec^2/cm^5)
4.0x10^{17}
2.0x10^{17}
0.0
2.0x10^{16}
1.5x10^{16}
1.0x10^{16}
5.0x10^{15}
0.0
1.2x10^{17}
8.0x10^{16}
4.0x10^{16}
0.0
8.0x10^{15}
6.0x10^{15}
4.0x10^{15}
2.0x10^{15}
0.0
4x10^{43}
3x10^{43}
2x10^{43}
1x10^{43}
0
1.4
2.4
3.4
4.4
5.4
6.4
7.4
8.4
9.4
10.4
11.4
Date (Local time)

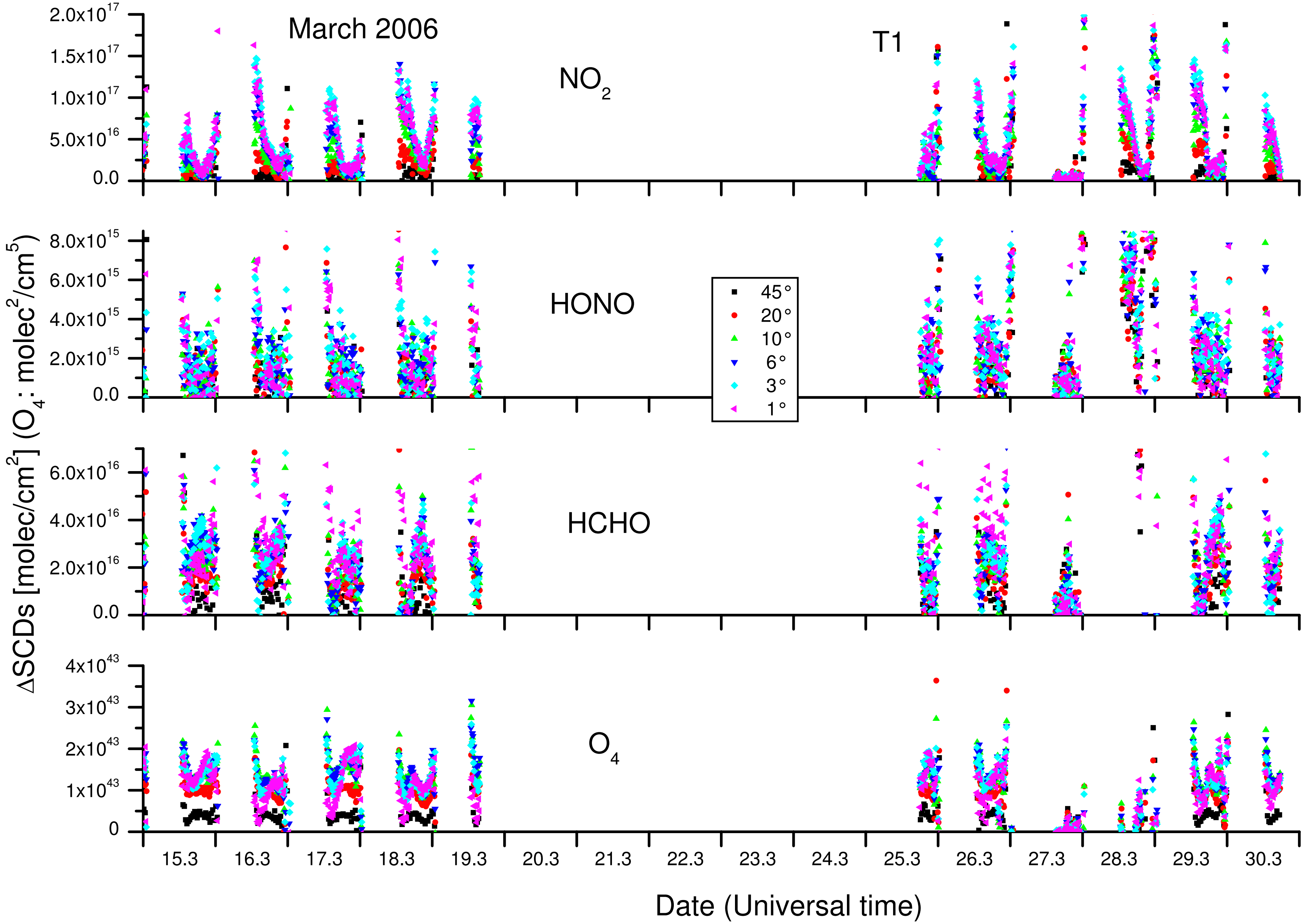
March 2006
T1
NO2
HONO
HCHO
O4
45°
20°
10°
6°
3°
1°
ΔSCDs [molec/cm²] (O4: molec²/cm⁵)
2.0x10^17
1.5x10^17
1.0x10^17
5.0x10^16
0.0
8.0x10^15
6.0x10^15
4.0x10^15
2.0x10^15
0.0
6.0x10^16
4.0x10^16
2.0x10^16
0.0
4x10^43
3x10^43
2x10^43
1x10^43
0
15.3
16.3
17.3
18.3
19.3
20.3
21.3
22.3
23.3
24.3
25.3
26.3
27.3
28.3
29.3
30.3
Date (Universal time)

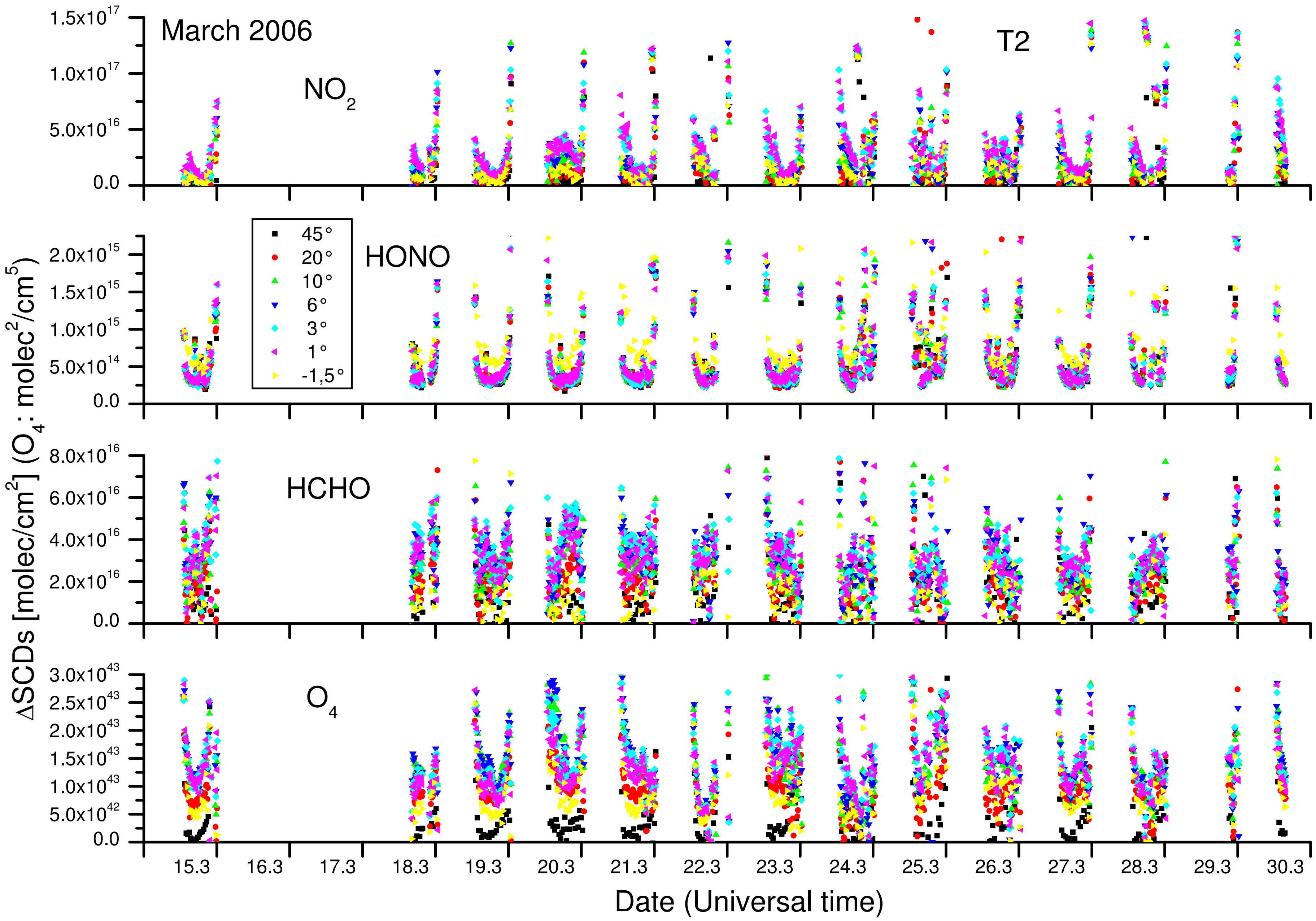
March 2006
T2
NO$_2$
HONO
HCHO
O$_4$
45°
20°
10°
6°
3°
1°
-1,5°
1.5x10^{17}
1.0x10^{17}
5.0x10^{16}
0.0
2.0x10^{15}
1.5x10^{15}
1.0x10^{15}
5.0x10^{14}
0.0
8.0x10^{16}
6.0x10^{16}
4.0x10^{16}
2.0x10^{16}
0.0
3.0x10^{43}
2.5x10^{43}
2.0x10^{43}
1.5x10^{43}
1.0x10^{43}
5.0x10^{42}
0.0
ΔSCDs [molec/cm^2] (O$_4$: molec^2/cm^5)
15.3
16.3
17.3
18.3
19.3
20.3
21.3
22.3
23.3
24.3
25.3
26.3
27.3
28.3
29.3
30.3
Date (Universal time)

List of Figures

List of Tables

Bibliography

Aben, I., D. M. Stam, and F. Helderman (2001). The Ring effect in skylight polarisation. *Geophys. Res. Lett. 28*, 519–522.

Acker, K., D. Möller, W. Wieprecht, F. Meixner, B. Bohn, S. Gilge, C. Plass-Dülmer, and H. Berresheim (2006). Strong daytime production of OH from HNO_2 at a rural mountain site. *Geophys. Res. Lett. 33*, L02809.

Albritton, D. L., A. L. Schmeltekopf, and R. N. Zare (1976). An introduction to the least-squares fitting of spectroscopic data. In R. K. Narahari and M. W. Weldon (Eds.), *Molecular Spectroscopy: Modern Research.* Orlando, Florida, USA: Academic Press.

Alicke, B. (2000). *The role of nitrous acid in the boundary layer.* Ph. D. thesis, University of Heidelberg.

Alicke, B., A. Geyer, A. Hofzumahaus, F. Holland, S. Konrad, H.-W. Pätz, J. Schäfer, J. Stutz, A. Volz-Thomas, and U. Platt (2003). OH formation by HONO photolysis during the BERLIOZ experiment. *J. Geophys. Res. 108 (D4)*, 8247.

Alicke, B., K. Hebestreit, J. Stutz, and U. Platt (1999). Iodine oxide in the marine boundary layer. *Nature 397*, 572 – 573.

Altshuller, A. P. (1993). Production of aldehydes as primary emissions and from secondary atmospheric reactions of alkenes and alkanes during the night and early morning hours. *Atmos. Environ. 27A*, 21–32.

Ammann, M., M. Kalberer, D. T. Jost, L. Tobler, E. Rössler, D. Piguet, H. W. Gäggeler, and U. Baltensperger (1998). Heterogeneous production of nitrous acid on soot in polluted air masses. *Nature 395*, 157 – 160.

Anderson, L. G., J. A. Lanning, R. Barrell, J. Miyagishima, R. H. Jones, and P. Wolfe (1996). Sources and sinks of formaldehyde and acetaldehyde: An analysis of Denver's ambient concentration data. *Atmos. Environ. 30*, 2113–2123.

Atkinson, R., D. L. Baulch, R. A. Cox, J. N. Crowley, R. F. Hampson, R. G. Hynes, M. E. Jenkin, M. J. Rossi, and J. Troe (2004). Evaluated kinetic and photochemical data for atmospheric chemistry: Volume I - gas phase reactions of O_x, HO_x, NO_x and SO_x species. *Atm. Chem. and Phys. 4*, 1461–1738.

Atkinson, R., E. C. Tuazon, and S. M. Aschmann (1995). Products of the gas-phase reactions of O_3 with alkenes. *Environ. Sci. Technol. 29*, 1860–1866.

Aumont, B., S. Madronich, M. Ammann, M. Kalberer, U. Baltensperger, D. Hauglustaine, and F. Brocheton (1999). On the NO_2 + soot reaction in the atmosphere. *J. Geophys. Res. 104*, 1729 – 1736.

Bates, T. S., R. J. Charlson, and R. H. Gammon (1987). Evidence for the climatic role of marine biogenic sulphur. *Nature 329*, 319 – 321.

Beirle, S., U. Platt, M. Wenig, and T. Wagner (2003). Weekly cycle of NO_2 by GOME measurements: a signature of anthropogenic sources. *Atm. Chem. and Phys. 3*, 2225–2232.

Beirle, S., R. Volkamer, F. Wittrock, A. Richter, J. Burrows, U. Platt, and T. Wagner (2006). DOAS Retrieval of Glyoxal from Space. In *Proceedings of the ESA Atmospheric Science Conference, 8-12 May 2006, Frascati.*

Bejan, I., Y. A. El Aal, I. Barnes, T. Benter, B. Bohn, P. Wiesen, and J. Kleffmann (2006). The photolysis of ortho-nitrophenols: A new gas phase source of HONO. *Phys. Chem. Chem. Phys. 8*, 2028–2035.

Bevington, P. (1969). *Data Reduction and Error Analysis for the Physical Sciences.* New York: McGraw-Hill.

Bogumil, K., J. O., T. Homann, S. Voigt, P. Spietz, O. Fleischmann, A. Vogel, M. Hartmann, H. Bovensmann, J. Frerik, and J. Burrows (2003). Measurements of Molecular Absorption Spectra with the SCIAMACHY Pre-Flight Model: Instrument Characterization and Reference Data for Atmospheric Remote-Sensing in the 230-2380 nm Region. *J. Photochem. Photobiol. A: Chem. 157*, 167–184.

Brasseur, G. P., J. J. Orlando, and G. S. Tyndall (1999). Chapter no. 5: Trace gas exchanges and biogeochemical sulfur cycles. Oxford University Press, Inc.

Brauer, M., P. Ryan, H. Suh, P. Koutrakis, J. Spengler, N. Leslie, and I. Billick (1990). Measurements of Nitrous Acid Inside 2 Research Houses. *Environmental Science & Technology 24 (10)*, 1521–1527.

Brinkmann, R. T. (1968). Rotational Raman scattering in planetary atmospheres. *Astrophys. J. 154*, 1087–1093.

Burrows, J., U. Platt, K. Chance, M. Vountas, V. Rozanov, A. Richter, H. Haug, and L. Marquard (1996). *Study of the Ring Effect.* Noordivijk, The Netherlands: European Space Agency.

Bussemer, M. (1993). Der Ring-Effekt: Ursachen und Einflußauf die spektroskopische Messung stratosphärischer Spurenstoffe. Diploma thesis, University of Heidelberg.

Calvert, J., R. Atkinson, K. Becker, R. Kamens, J. Seinfeld, T. Wallington, and G. Y. (Eds.) (2002). *The mechanisms of atmospheric oxidation of aromatic hydrocarbons.* Oxford Univ. Press, Oxford.

Calvert, J., R. Atkinson, J. Kerr, S. Madronich, G. Moortgat, T. Wallington, and G. Y. (Eds.) (2000). *The Mechanisms of Atmospheric Oxidation of the Alkenes.* Oxford Univ. Press, New York.

Calvert, J., G. Yarwood, and A. Dunker (1994). An Evaluation of the Mechanism of Nitrous Acid Formation in the Urban Atmosphere. *Research On Chemical Intermediates 20 (3-5)*, 463–502.

Carlier, P., H. Hannachi, and G. Mouvier (1986). The chemistry of carbonyl compounds in the atmosphere - a review. *Atmos. Environ. 20 (11)*, 2079–2099.

Chance, K., P. I. Palmer, R. J. D. Spurr, R. V. Martin, T. P. Kurosu, and D. J. Jacob (2000). Satellite observations of formaldehyde over North America from GOME. *Geophys. Res. Lett. 27 (21)*, 3461–3464.

Chance, K. and R. J. D. Spurr (1997). Ring effect studies; Rayleigh scattering, including molecular parameters for rotational Raman scattering and the Fraunhofer spectrum. *Appl. Opt. 36*, 5224–5230.

Charlson, R. J., J. E. Lovelock, M. O. Andreae, and S. G. Warren (1987). Oceanic phytoplankton, atmospheric sulphur, cloud albedo and climate. *Nature 326*, 655–661.

Crutzen, P. J. (2006). Albedo enhancement by stratospheric sulfur injections: A contribution to resolve a policy dilemma? *Climatic Change 77*, 211 – 219.

de Foy, B., E. Caetano, V. Magaa, A. Zitcuaro, B. Crdenas, A. Retama, R. Ramos, L. T. Molina, and M. J. Molina (2005). Mexico City basin wind circulation during the MCMA-2003 field campaign. *Atm. Chem. and Phys. 5*, 2267–2288.

Deutschmann, T. and T. Wagner (2006). *TRACY-II Users manual.* University of Heidelberg.

Diebel, D., J. Burrows, R. de Beek, R. Munro, B. Kerridge, L. Marquard, U. Platt, and H. Frank (1995). Detailed analysis of the retrieval algorithms selected for the level 1-2 processing of GOME data (Tracegas study). Technical report, ESA contract 10728/94/NL/CM, prepared by SERCO Europe Ltd., Southall, U.K.

Draxler, R. R. and G. D. Hess (1998). An Overview of the Hysplit 4 Modeling System for Trajectories, Dispersion, and Deposition. *Aust. Met. Mag. 47*, 295–308.

Eatough, D., C. Benner, J. Bayona, G. Richards, J. Lamb, M. Lee, E. Lewis, and L. Hansen (1989). Chemical Composition of Environmental Tobacco Smoke. 1. Gas-Phase Acids and Bases. *Environ. Sci. Technol. 23 (6)*, 679–687.

Eskes, H. J. and K. F. Boersma (2003). Averaging kernels for DOAS total-column satellite retrievals. *Atm. Chem. and Phys. 3*, 1285–1291.

Fast, J. D., B. de Foy, F. A. Rosas, E. Caetano, G. Carmichael, L. Emmons, D. McKenna, M. Mena, W. Skamarock, X. Tie, R. L. Coulter, J. C. Barnard, C. Wiedinmyer, and S. Madronich (2007). A meteorological overview of the MILAGRO field campaigns. *Atm. Chem. and Phys. 7*, 2233–2257.

Fayt, C. and M. van Roozendael (2001). Windoas 2.1. software user manual. ISAB/BIRA Belgium, http://www.oma.be/BIRA-IASB.

Finlayson-Pitts, B. J. and J. N. Pitts jr. (2000). *Chemistry of the upper and lower atmosphere: Theory, experiments and applications.* Academic Press, San Diego.

Fish, D. J. and R. L. Jones (1995). Rotational Raman scattering and the Ring effect in zenith-sky spectra. *Geophys. Res. Lett. 22*, 811–814.

Frankenberg, C., J. F. Meirik, M. van Weele, U. Platt, and T. Wagner (2005). Assessing methane emissions from global space-borne observations. *Science 308*, 1010 – 1014.

Frankenberg, C., U. Platt, and T. Wagner (2005). Iterative maximum a posteriori (imap)-doas for retrieval of strongly absorbing trace gases: Model studies for CH_4 and CO_2 retrieval from near infrared spectra of SCIAMACHY onboard ENVISAT. *Atm. Chem. and Phys. 5*, 9–22.

Frieß, U. (2001). *Spectroscopic Measurements of Atmospheric Trace Gases at Neumayer-Station, Antarctica.* Ph. D. thesis, University of Heidelberg.

Frieß, U., P. S. Monks, J. J. Remedios, A. Rozanov, R. Sinreich, T. Wagner, and U. Platt (2006). MAX-DOAS O_4 measurements: A new technique to derive information on atmospheric aerosols: 2. Modeling studies. *J. Geophys. Res. 111*, D14203.

García, A. R., R. Volkamer, L. T. Molina, M. J. Molina, J. Samuelson, J. Mellqvist, B. Galle, S. C. Herndon, and C. E. Kolb (2006). Separation of emitted and photochemical formaldehyde in Mexico City using a statistical analysis and a new pair of gas-phase tracers. *Atm. Chem. and Phys. 6*, 4545–4557.

George, C., R. S. Strekowski, J. Kleffmann, K. Stemmler, and M. Ammann (2005). Photoenhanced Uptake of Gaseous NO_2 on Solid Organic Compounds: A Photochemical Source of HONO. *Faraday Discussion 130*, 195–210.

Gerecke, A., A. Thielmann, L. Gutzwiller, and M. J. Rossi (1998). The chemical kinetics of HONO formation resulting from heterogeneous interaction of NO_2 with flame soot. *Geophys. Res. Lett. 25*, 2453 – 2456.

Geyer, A., K. Bächmann, A. Hofzumahaus, F. Holland, S. Konrad, T. Klüpfel, H. Pätz, D. Perner, D. Mihelcic, H. Schäfer, A. Volz-Thomas, and U. Platt (2003). Nighttime formation of peroxy and hydroxyl radicals during BERLIOZ – Observations and modeling studies. *J. Geophys. Res. 108 (D4)*, 8249.

Gomer, T., T. Brauers, F. Heintz, J. Stutz, and U. Platt (1993). *MFC User Manual, Vers. 1.98.* Institut für Umweltphysik, Universität Heidelberg.

Gomer, T., T. Brauers, F. Heintz, J. Stutz, and U. Platt (1995). MFC version 1.98 user manual. Technical report, University of Heidelberg.

Grainger, J. and J. Ring (1962). Anomalous Fraunhofer line profiles. *Nature 193*, 762.

Greenblatt, G. D., J. J. Orlando, J. B. Burkholder, and A. R. Ravishankara (1990). Absorption Measurements of Oxygen between 330 and 1140 nm. *J. Geophys. Res. 95*, 18577–18582.

Griffin, R. J., P. J. Beckman, R. W. Talbot, B. C. Sive, and R. K. Varner (2007). Deviations from ozone photostationary state during the International Consortium for Atmospheric Research on Transport and Transformation 2004 campaign: Use of measurements and photochemical modeling to assess potential causes. *J. Geophys. Res. 112*, D10S07.

Grosjean, D. (1991). Ambient levels of formaldehyde, acetaldehyde and formic acid in Southern California: Results of a one-year base-line study. *Environ. Sci. Technol. 25*, 710–715.

Hak, C. (2006). *Variability of formaldehyde in the polluted planetary boundary layer - measurements in the Milano metropolitan area, Italy (Po basin).* Ph. D. thesis, University of Karlsruhe.

Haug, H. (1996). Raman-Streuung von Sonnenlicht in der Erdatmosphäre. Diploma thesis, University of Heidelberg.

Hausmann, M., U. Brandenburger, T. Brauers, and H.-P. Dorn (1997). Detection of tropospheric OH radicals by long-path differential-optical-absorption spectroscopy: Experimental setup, accuracy, and precision. *J. Geophys. Res. 102*, 16011–16022.

Hausmann, M., U. Brandenburger, T. Brauers, and H.-P. Dorn (1999). Simple Monte Carlo methods to estimate the spectra evaluation error in differential-optical-absorption spectroscopy. *Appl. Opt. 38*(3), 462–475.

Hausmann, M. and U. Platt (1994). Spectroscopic measurement of bromine oxide and ozone in the high Arctic during Polar Sunrise Experiment 1992. *J. Geophys. Res. 99 (D12)*, 25399–25413, 10.1029/94JD01314.

Heckel, A., A. Richter, T. Tarsu, F. Wittrock, C. Hak, I. Pundt, W. Junkermann, and J. Burrows (2005). MAX-DOAS measurements of formaldehyde in the Po-Valley, atmos. chem. phys. 5, 909-918, 2005. *Atm. Chem. and Phys. 5*, 909–918.

Heintz, F. (1996). *Langzeitmessung von NO_3-Radikalen mittels DOAS in Kap Arkona (Insel Rügen).* Ph.D. thesis, University of Heidelberg.

Hendrick, F., B. Barret, M. V. Roozendael, H. Boesch, A. Butz, M. D. Mazière, F. Goutail, C. Hermans, J.-C. Lambert, K. Pfeilsticker, and J.-P. Pommereau (2004). Retrieval of nitrogen dioxide stratospheric profiles from ground-based zenith-sky UV-visible observations: validation of the technique through correlative comparisons. *Atm. Chem. and Phys. 4*, 2091–2106.

Henyey, L. and J. Greenstein (1941). Diffuse radiation in the Galaxy. *Astrophys. J. Vol. 93*, 70–83.

Hermans, C., A. C. Vandaele, M. Carleer, S. Fally, R. Colin, A. Jenouvrier, B. Coquart, and M.-F. Mérienne (1999). Absorption Cross-Sections of Atmospheric Constituents:NO_2, O_2, and H_2O. *Environ. Sci. & Pollut. Res. 6*(3), 151–158.

Hönninger, G. (2002). *Halogen Oxide Studies in the Boundary Layer by Multi Axis Differential Optical Absorption Spectroscopy and Active Longpath-DOAS*. Ph. D. thesis, University of Heidelberg.

Hönninger, G. and U. Platt (2002). Observations of BrO and its vertical distribution during surface ozone depletion at Alert. *Atmos. Environ. 36*, 2481–2489.

Hönninger, G., C. von Friedeburg, and U. Platt (2004). Multi axis differential optical absorption spectroscopy (MAX-DOAS). *Atm. Chem. and Phys. 4*, 231–254.

IPCC (2007). Intergovernmental Panel on Climate Change, 2007: Summary for Policymakers. In *Climate Change 2007: The Fourth Assessment Report of the Intergovernmental Panel on Climate Change*. Cambridge University Press, Cambridge, UK, 7-22.

Irie, H., Y. Kanaya, H. Akimoto, H. Iwabuch, A. Shimizu, and K. Aoki (2007). Performance of MAX-DOAS measurements of aerosols at Tsukuba, Japan: a comparison with lidar and sky radiometer measurements. *Atmos. Chem. Phys. Discuss. 7*, 9769–9793.

Johnston, P. (1996). Making uv/vis cross sections, reference fraunhofer and synthetic spectra. unpublished manuscript.

Kern, C., S. Trick, B. Rippel, and U. Platt (2006). Applicability of light-emitting diodes as light sources for active DOAS measurements. *Appl. Opt. 45*, 2077–2088.

Kesselmeier, J., K. Bode, U. Hofmann, H. Müller, L. Schäfer, A. Wolf, P. Ciccioli, E. Brancaleoni, A. Cecinato, M. Frattoni, P. Foster, C. Ferrari, V. Jacob, J. L. Fugit, L. Dutaur, V. Simun, and L. Torres (1997). Emission of short chained organic acids, aldehydes and monoterpenes from *Quercus ilex* L. and *Pinus pinea* L. in relation to physiological activities, carbon budget and emission algorithms. *Atmos. Environ. 31 (S1)*, 119–133.

Kessler, C. and U. Platt (1984). Nitrous acid in polluted air masses – Sources and formation pathways. In *Physiochemical behaviour of atmosperic pollutants.* Edited by B. Versino and G. Angeletti, D. Reidel, Varese, Italia.

Kirchstetter, T., R. Harley, and D. Littlejohn (1996). Measurement of Nitrous Acid in Motor Vehicle Exhaust. *Environmental Science & Technology 30 (9)*, 2843–2849.

Kleffmann, J., K. Becker, and P. Wiesen (1998). Heterogeneous NO_2 conversion processes on acid surfaces: possible atmospheric implications. *Atmos. Environ. 32*, 2721–2729.

Kleffmann, J., T. Benter, and P. Wiesen (2004). The Heterogeneous Reaction of Nitric Acid with Nitric Oxide on Glass Surfaces under Simulated Atmospheric Conditions. *J. Phys. Chem. 108*, 5793–5799.

Kleffmann, J., R. Kurtenbach, J. Lörzer, P. Wiesen, N. Kalthoff, B. Vogel, and H. Vogel (2003). Measured and simulated vertical profiles of nitrous acid - Part I: Field measurements. *Atmos. Environ. 37*, 2949–2955.

Kleffmann, J., J. Lörzer, P. Wiesen, C. Kern, S. Trick, R. Volkamer, M. Rodenas, and K.Wirtz (2006). Intercomparison of the DOAS and LOPAP techniques for the detection of nitrous acid (hono). *Atmos. Environ. 40*, 3640–3652.

Kraus, S. (2004). Doasis: Doas intelligent system. Software, copyright 2004 stefan kraus, Institute of Environmental Physics, University of Heidelberg, Heidelberg. In cooperation with Hoffmann Messtechnik GmbH.

Kurtenbach, D., K. H. Becker, J. A. G. Gomes, J. Kleffmann, J. C. Lörzer, M. Spittler, P. Wiesen, R. Ackermann, A. Geyer, and U. Platt (2001). Investigations of emissions and heterogeneous formation of HONO in a road traffic tunnel. *Atmos. Environ. 35*, 3385 – 3394.

Kurucz, R. L., I. Furenlid, J. Brault, and L. Testerman (1984). *Solar Flux Atlas from 296 to 1300 nm.* Sunspot, New Mexico, U.S.A.: National Solar Observatry.

Lammel, G. and J. Cape (1996). Nitrous acid and nitrite in the atmosphere. *Chem. Soc. Rev. 25 (5)*, 361+.

Lee, D., I. Köhler, E. Grobler, F. Rohrer, R. Sausen, L. Gallardo-Klenner, J. Olivier, F. Dentener, and A. Bouwman (1997). Estimates of global $\mathrm{NO_x}$ emissions and their uncertainties. *Atmos. Environ. 31 (12)*, 1735–1749.

Lee, K., J. Xue, A. Geyh, H. Ozkaynak, B. Leaderer, C. Weschler, and J. Spengler (2002). Nitrous acid, nitrogen dioxide, and ozone concentrations in residential environments. *Environmental Health Perspectives 110 (2)*, 145–150.

Leighton, P. A. (1961). Photochemistry of air pollution. Academic Press, New York.

Leser, H., G. Hönninger, and U. Platt (2003). MAX-DOAS Measurements of BrO and $\mathrm{NO_2}$ in the Marine Boundary Layer. *Geophys. Res. Lett. 30*, 1537, doi:10.1029/2002GL015811.

Leue, C., W. Wenig, T. Wagner, O. Klimm, U. Platt, and B. Jähne (2001, March). Quantitative analysis of $\mathrm{NO_x}$ emissions from Global Ozone Monitoring Experiment satellite image sequences. *J. Geophys. Res. 106*(D6), 5493–5505.

Levenberg, K. (1944). A method for the solution of certain non-linear problems in least squares. *Quart. Appl. Math. 2*, 164–168.

Logan, J. A., M. J. Prather, S. C. Wofsy, and M. B. McElroy (1981). Tropospheric chemistry: A global perspective. *J. Geophys. Res. 86 (C8)*, 7210–7254.

Marbach, T., S. Beirle, C. Frankenberg, U. Platt, and T. Wagner (2007). Identification of tropospheric trace gas sources: synergistic use of HCHO and other satellite observations. In *Proceedings to the ENVISAT Symposium 2007*.

Marchuk, G., G. Mikhailov, M. Nazaraliev, R. Darbinjan, B. Kargin, and B. Elepov (1980). *The Monte Carlo Methods in Atmospheric Optics*. Berlin, New York: Spinger.

Marquard, L., T. Wagner, and U. Platt (2000). Improved Air Mass Factor Concepts for Scattered Radiation Differential Optical Absorption Spectroscopy of Atmospheric Species. *J. Geophys. Res. 105*, 1315–1327.

Marquardt, D. W. (1963). An algorithm for least squares estimation of non-linear parameters. *Soc. Indust. Appl. Math 11*, 431–441.

Meller, R. and G. K. Moortgat (2000). Temperature dependence of the absorption cross sections of formaldehyde between 223 and 323 K in the wavelength range 225-375 nm. *J. Geophys. Res. 105*, 7089–7101.

Mentel, T. F., D. Bleilebens, and A. Wahner (1996). A study of nighttime nitrogen oxide oxidation in a large reaction chamber — The fate of NO_2, N_2O_5, HNO_3, and O_3 at different humidities. *Atmos. Environ. 30*, 4007–4020.

Molina, M. J. and L. T. Molina (2002). *Air Quality in the Mexico Megacity: An Integrated Assessment*, pp. 105–136. Kluwer Academic Publishers, Dordrecht,The Netherlands.

Notholt, J. and, J. H. and F. Raes (1992). Formation of HNO_2 on aerosol surfaces during foggy periods in the presence of NO and NO_2. *Atmos. Environ. 26A*, 211–217.

Noxon, J. F., E. C. Whipple, and R. S. Hyde (1979). Stratospheric NO_2. 1. Observational Method and Behavior at Midlatitudes. *J. Geophys. Res. 84*, 5047–5076.

Penndorf, R. (1957). Tables of the refractive index for standard air and the rayleigh scattering coefficient for the spectral region between 0.2 and 200 μ and their application to atmospheric optics. *J. Opt. Soc. Am. 47*(2), 176–182.

Perliski, L. M. and S. Solomon (1993). On the evaluation of air mass factors for atmospheric near-ultraviolet and visible absorption spectroscopy. *J. Geophys. Res. 98*, 10,363–10,374.

Perner, D., D. H. Ehhalt, H. W. Paetz, U. Platt, E. P. Roeth, and A. Volz (1976). OH radicals in the lower troposphere. *Geophys. Res. Lett. Vol. 3*, 466–468.

Perner, D. and U. Platt (1979). Detection of nitrous acid in the atmosphere by differential optical absorption. *Geophys. Res. Lett. Vol. 6*, 917–920.

Pitts, J., E. Sanhueza, R. Atkinson, W. Carter, A. Winer, G. Harris, and C. Plum (1984). An investigation of the dark formation of nitrous acid in environmental chambers. *Int. J. Chem. Kinet. XVI*, 919–939.

Platt, U. (1986). *The origin of nitrous and nitric acid in the atmosphere*, pp. 299–319. W. Jaeschke, Springer Verlag.

Platt, U. (1994). Differential Optical Absorption Spectroscopy (DOAS). In M. W. Sigrist (Ed.), *Air Monitoring by Spectoscopic Techniques*, Volume 127 of *Chemical Analysis*, New York. Wiley-Interscience.

Platt, U. (1999). Modern methods of the measurement of atmospheric trace gases - invited lecture. *Phys. Chem. Chem. Phys. 1*, 5409 – 5415.

Platt, U., L. Marquard, T. Wagner, and D. Perner (1997). Corrections for Zenith Scattered Light DOAS. *Geophys. Res. Lett. 24*(14), 1759–1762.

Platt, U. and D. Perner (1980). Direct Measurements of Atmospheric CH_2O, HNO_2, O_3, NO_2 and SO_2 by Differential Optical Absorption in the Near UV. *J. Geophys. Res. 85*, 7453–7458.

Platt, U., D. Perner, G. Harris, A. Winer, and J. Pitts (1980). Observations of nitrous acid in an urban atmosphere by differential optical absorption. *Nature 285*, 312–314.

Platt, U., D. Perner, G. W. Harris, A. M. Winer, and J. N. Pitts, Jr. (1980). Detection of NO_3 in the Polluted Troposphere by Differential Optical Absorption. *Geophys. Res. Lett. 7*, 89–92.

Platt, U., D. Perner, and H. W. Pätz (1979). Simultaneous measurements of atmospheric CH_2O, O_3 and NO_2 by differential optical absortion. *J. Geophys. Res. 84*, 6329–6335.

Reisinger, A. (2000). Observations of HNO_2 in the polluted winter atmosphere: possible heterogeneous production on aerosols. *Atmos. Environ. 34*, 3864–3874.

Richter, A. (1997). *Absorptionsspektroskopische Messungen stratosphärischer Spurengase über Bremen. 53° N.* Ph. D. thesis, University of Bremen, Bremen, Germany.

Rodgers, C. D. (1976). Retrieval of atmospheric temperature and composition from remote measurements of thermal radiation. *Rev. Geophys. 14*(4), 609–624.

Rodgers, C. D. (2000). *Inverse Methods for Atmospheric Sounding.* London: Worls Scientific.

Roedel, W. (2000). *Physik unserer Umwelt - Die Atmosphare.* Springer-Verlag, Berlin.

Rothman, L., C. P. Rinsland, A. Goldman, S. Massie, D. P. Edwards, J.-M. Flaud, A. Perrin, C. Camy-Peyret, V. Dana, J.-Y. Mandin, J. Schroeder, A. McCann, R. R. Gamache, R. B. Wattson, K. Yoshino, K. Chance, K. Jucks, L. Brown, V. Nemtchinov, and

P. Varanasi (1998). The HITRAN Molecular Spectroscopic Database and HAWKS (HITRAN Atmospheric Workstation): 1996 edition. *J. Quant. Spectrosc. Radiat. Transfer 60*, 665–710.

Rozanov, A., V.-V. Rozanov, and J. P. Burrows (2000). Combined differential-integral approach for the radiation field computation in a spherical shell atmosphere: Nonlimb geometry. *J. Geophys. Res. 105, D18*, 22937.

Rozanov, A., V.-V. Rozanov, and J. P. Burrows (2001). A numerical radiative transfer model for a spherical planetary atmosphere: combined differential-integral approach involving the Picard iterative approximation. *J. Quant. Spectrosc. Radiat. Transfer 69*, 491.

Saliba, N., M. Mochida, and B. Finlayson-Pitts (2000). Laboratory studies of sources ofHONO in polluted urban atmospheres. *Geophys. Res. Lett. 27 (19)*, 3229–3232.

Sander, S. P., R. R. Friedl, D. M. Golden, M. J. Kurylo, R. E. Huie, V. L. Orkin, G. K. Moortgat, A. R. Ravishankara, C. E. Kolb, M. J. Molina, and B. J. Finlayson-Pitts (2003). Chemical kinetics and photochemical data for use in atmospheric studies. *Tech. Rep. JPL Publication 02-25, Jet Propulsion Laboratory, Pasadena, CA.*

Sanders, R. W., S. Solomon, M. A. Carroll, and A. L. Schmeltekopf (1988). Ground based measurements of O_3, NO_2, OClO and BrO during the Antarctic Ozone Depletion Event. In R. D. Bjokov and P. Fabian (Eds.), *Ozone in the Atmosphere, Quadrennial Ozone Symposium 1988*, pp. 65–70. Hampton, Va.: Deepak Publishing.

Sanghavi, S. (2003). An effcient Mie theory implementation to investigate the influence of aerosols on radiative transfer. Diploma thesis, University of Heidelberg.

Schneider, W., G. Moortgat, G. Tyndall, and J. Burrows (1987). Absorption cross-sections of NO_2 in the UV and visible region (200 - 700 nm) at 298 K. *J. Photochem. Photobiol. 40*, 195–217.

Schofield, R., B. J. Connor, K. Kreher, P. V. Johnston, and C. D. Rodgers (2004). The retrieval of profile and chemical information from ground-based UV-visible spectroscopic measurements. *J. Quant. Spectrosc. Radiat. Transfer 86*, 115–131.

Schwab, J., Y.-Q. Li, and K. Demerjian (2004). Semi-Continuous Formaldehyde Measurements with a Diffusion Scrubber/Liquid Fluorescence Analyzer. In *Symposium on Air Quality Measurement Methods and Technology 2004 VIP-126-CD*. Air and Waste Management Association, Pittsburgh, PA, USA, ISBN 0-923204-62-8.

Sihler, H. (2007). Light-Emitting Diodes as Light Sources in Spectroscopic Measurements of Atmospheric Trace Gases. Diploma thesis, University of Jena.

Sillman, S., J. Logan, and S. Wofsy (1990). The sensitivity of ozone to nitrogen oxides and hydrocarbons in regional ozone episodes. *J. Geophys. Res. 95*, 1837–1852.

Sinreich, R., U. Frieß, T. Wagner, and U. Platt (2005). Multi axis differential optical absorption spectroscopy (MAX-DOAS) of gas and aerosol distributions. *Faraday Discuss. 130*, 153–164.

Sinreich, R., R. Volkamer, F. Filsinger, U. Frieß, C. Kern, U. Platt, O. Sebastián, and T. Wagner (2007). MAX-DOAS detection of glyoxal during ICARTT 2004. *Atm. Chem. and Phys. 7*, 1293–1303.

Sioris, C. E. and W. F. J. Evans (1999). Filling in of Fraunhofer and gas-absorption lines in sky spectra as caused by rotational Raman scattering. *Appl. Opt. 38*(12), 2706–2713.

Solomon, S., H. L. Miller, J. P. Smith, R. W. Sanders, G. H. Mount, A. L. Schmeltekopf, and J. F. Noxon (1989). Atmospheric NO_3 1. measurement technique and the annual cycle at 40°N. *J. Geophys. Res. 94(D8)*, 11041–11048.

Solomon, S., A. L. Schmeltekopf, and R. W. Sanders (1987). On the interpretation of zenith sky absorption measurements. *J. Geophys. Res. 92*, 8311–8319.

Stemmler, K., M. Ammann, C. Dondors, J. Kleffmann, and C. George (2006). Photosensitized Reduction of Nitrogen Dioxide on Humic Acid as a Source of Nitrous Acid. *Nature 440*, 195–198.

Stockwell, W. and J. Calvert (1983). The Mechanism of the HO-SO_2 Reaction atmos. envir., 17, 2231 - 2235, 1983. *Atmos. Environ. 17*, 2231–2235.

Stutz, J. (1991). Charakterisierung von Photodiodenzeilen zur Messung stratosphärischer Spurenstoffe. Diploma thesis, University of Heidelberg.

Stutz, J., B. Alicke, R. Ackermann, A. Geyer, S. Wang, A. B. White, E. J. Williams, C. W. Spicer, and J. D. Fast (2004). Relative humidity dependence of HONO chemistry in urban areas. *J. Geophys. Res. 109*, D03307.

Stutz, J., E. Kim, U. Platt, P. Bruno, C. Perrino, and A. Febo (2000). UV-visible absorption cross section of nitrous acid. *J. Geophys. Res. 105 (D11)*, 14858–14592.

Stutz, J. and U. Platt (1996). Numerical analysis and estimation of the statistical error of Differential Optical Absorption Spectroscopy measurements with least-squares methods. *Appl. Opt. 35*(30), 6041–6053.

Svensson, R., E. Ljungström, and O. Lindqvist (1987). Kinetics of the reaction between nitrogen dioxide and water vapour. *Atmos. Environ. 21*, 1529–1539.

Trick, S. (2004). *Formation of Nitrous Acid on Urban Surfaces – A physical-chemical perspective.* Dissertation, University of Heidelberg.

Ulshöfer, V., G. Uher, and M. Andreae (1995). Evidence for a winter sink of atmospheric carbonyl sulfide in the northeast Atlantic Ocean. *Geophys. Res. Lett. 22*, 2601–2604.

Van de Hulst, H. (1981). *Light scattering by small particles.* New York: Dover publication.

Van Roozendael, M., S. R. Alliwell, P. V. Johnston, A. Richter, M. V. Roozendael, T. Wagner, D. W.Arlander, J. P. Burrows, D. J. Fish, R. L. Jones, K. K. Tørnkvist, J. C. Lambert, K. Pfeilsticker, and I. Pundt (1999). Analysis for BrO in zenith-sky spectra - an intercomparison exercise for analysis improvement. *J. Geophys. Res.*. in preparation.

van Roozendael, M., C. Fayt, P. Post, C. Hermans, and J.-C. Lambert (2003). Retrieval of BrO and NO_2 from UV-Visible Observations. In P. Borell, P. Borell, J. Burrows, and U. Platt (Eds.), *Sounding the troposphere from space: a new era for atmospheric chemistry*. Springer-Verlag, ISBN 3-540-40873-8.

Vandaele, A., P. Simon, M. Guilmot, M. Carleer, and R. Colin (1994). SO_2 absorption cross section measurement in the UV using a Fourier transform spectrometer. *J. Geophys. Res. 99*, 25599–25605.

Vandaele, A. C., C. Hermans, P. C. Simon, M. Carleer, R. Colin, S. Fally, M.-F. Mérienne, A. Jenouvrier, and B. Coquart (1998). Measurements of the NO_2 Absorption Cross-section from 42000 cm^{-1} to 10000 cm^{-1} (238-1000 nm) at 220 k and 294 k. *J. Quant. Spectrosc. Radiat. Transfer 59*(D18), 171–184.

Veitel, H. (2002). *Vertical profiles of NO_2 and HONO in the planetary boundary layer*. Ph. D. thesis, University of Heidelberg.

Veitel, H., B. Kromer, M. Mößner, and U. Platt (2002). New techniques for measurements of atmospheric vertical trace gas profiles using DOAS. *Environ. Sci. Pollut. Res. special issue 4*, 17–26.

Vogel, B., H. Vogel, J. Kleffmann, and R. Kurtenbach (2003). Measured and simulated vertical profiles of nitrous acid – Part II. Model simulations and indications for a photolytic source. *Atmos. Environ. 37*, 2957–2966.

Voigt, S., J. Orphal, and J. P. Burrows (2002). The temperature- and pressure dependence of the absorption cross sections of NO_2 in the 250-800 nm region measured by Fourier-transform spectroscopy. *J. Photochem. Photobiol. A: Chem. 149*, 1–7.

Volkamer, R., L. T. Molina, M. J. Molina, T. Shirley, and W. H. Brune (2005). DOAS measurement of glyoxal as an indicator for fast VOC chemistry in urban air. *Geophys. Res. Lett. 32*, L08806.

Volkamer, R., U. Platt, M. Rodenas, K. Wirtz, and W. Junkermann (2005). Comparison of calibration standards for the measurement of HCHO via UV-, IR absorption spectroscopy and the Hantzsch technique. Technical report, EUPHORE annual report 2002. Fachbereich 9, BUGH Wuppertal: http://www.physchem.uni-wuppertal.de.

Volkamer, R., U. Platt, and K. Wirtz (2001). Primary and Secondary Glyoxal Formation from Aromatics: Experimental Evidence for the Bicycloalkyl-Radical Pathway from Benzene, Toluene, and p-Xylene. *J. Phys. Chem. 105*, 7865–7874.

Volkamer, R., P.Sheehy, L. Molina, and M. Molina (2007). Oxidative Capacity of the Mexico City Atmosphere. Part 1: A Radical Source Perspective. *Atmos. Chem. Phys. Discuss. 7*, 5365–5412.

Volkamer, R., P. Spietz, J. P. Burrows, and U. Platt (2005). High-resolution absorption cross-sections of glyoxal in the UV-vis and IR spectral ranges. *J. Photochem. Photobiol. A: Chem. 172*, 35–36.

von Friedeburg, C. (2003). *Derivation of Trace Gas Information combining Differential Optical Absorption Spectroscopy with Radiative Transfer Modelling.* Ph.D. thesis, Combined Faculties for the Natural Sciences and for Mathematics, Universität Heidelberg.

von Friedeburg, C., I. Pundt, K.-U. Mettendorf, T. Wagner, and U. Platt (2005). Multi-Axis-(MAX) DOAS Measurements of NO_2 during the BAB II Motorway Emission Campaign, (BAB II special issue). *Atmos. Environ. 39, 5, 977-985 5*, 977–985.

Wagner, T. (1999). *Satellite observations of atmospheric halogen oxides.* Ph. D. thesis, University of Heidelberg, Heidelberg, Germany.

Wagner, T., J. P. Burrows, T. Deutschmann, B. Dix, C. von Friedeburg, U. Frieß, F. Hendrick, K.-P. Heue, H. Irie, H. Iwabuchi, Y. Kanaya, J. Keller, C. A. McLinden, H. Oetjen, E. Palazzi, A. Petritoli, U. Platt, O. Postylyakov, J. Pukite, A. Richter, M. van Roozendael, A. Rozanov, V. Rozanov, R. Sinreich, S. Sanghavi, and F. Wittrock (2007). Comparison of box-air-mass-factors and radiances for Multiple-Axis Differential Optical Absorption Spectroscopy (MAX-DOAS) geometries calculated from different UV/visible radiative transfer models. *Atm. Chem. and Phys. 7*, 1809–1833.

Wagner, T., B. Dix, C. v. Friedeburg, U. Frieß, S. Sanghavi, R. Sinreich, and U. Platt (2004). MAX-DOAS O_4 measurements: A new technique to derive information on atmospheric aerosols - Principles and information content. *J. Geophys. Res. 109*, D22205.

Wagner, T., C. Otten, K. Pfeilsticker, I. Pundt, and U. Platt (2000). DOAS moonlight observation of atmospheric NO_3 in the Arctic winter. *Geophys. Res. Lett. 27(21)*, 3441–3444.

Warneke, C., J. A. de Gouw, P. D. Goldan, W. C. Kuster, E. J. Williams, B. M. Lerner, R. Jakoubek, S. S. Brown, H. Stark, M. Aldener, A. R. Ravishankara, J. M. Roberts, M. Marchewka, S. Bertman, D. T. Sueper, S. A. McKeen, J. F. Meagher, and F. C. Fehsenfeld (2004). Comparison of daytime and nighttime oxidation of biogenic and anthropogenic VOCs along the New England coast in summer during New England Air Quality Study 2002. *J. Geophys. Res. 109(D10)*, D10309.

Watts, S. (2000). The mass budgets of carbonyl sulfide, dimethyl sulfide, carbon disulfide, and hydrogen sulfide. *Atmos. Environ. 34*, 761–779.

Weidner, F. (2005). *Development and Application of a Versatile Balloon-Borne DOAS Spectrometer for Skylight Radiance and Atmospheric Trace Gas Profile Measurements.* Ph. D. thesis, University of Heidelberg.

Weidner, F., H. Bösch, H. Bovensmann, J. P. Burrows, A. Butz, C. Camy-Peyret, M. Dorf, K. Gerilowski, W. Gurlit, U. Platt, C. v. Friedeburg, T. Wagner, and K. Pfeilsticker (2005). Balloon-borne limb profiling of UV/vis skylight radiances, O_3, NO_2, and BrO: technical set-up and validation of the method. *Atm. Chem. and Phys. 5*, 1409–1422.

WHO (2000). *Air quality guidelines for Europe* (Second ed.). World Health Organisation, WHO Regional Publications, European Series, No. 91, WHO Copenhagen.

Wilmouth, D. M., T. F. Hanisco, N. M. Donahue, and J. G. Anderson (1999). Fourier transform ultraviolet spectroscopy of the $A^2\Pi_{3/2} \leftarrow X^2\Pi_{3/2}$ transition of BrO. *J. Phys. Chem. 103*, 8935–8945.

Winer, A. and H. Biermann (1994). Long Pathlength Differential Optical Absorption Spectroscopy (DOAS) Measurements of Gaseous HONO, NO_2 and HCHO in the California South Coast Air Basin. *Research On Chemical Intermediates 20 (3-5)*, 423–445.

Wiscombe, W. J. (1980). Improved Mie scattering algorithms. *Appl. Opt. 19*, 1505–1509.

Wittrock, F., H. Oetjen, A. Richter, S. Fietkau, T. Medeke, A. Rozanov, and J. P. Burrows (2004). MAX-DOAS measurements of atmospheric trace gases in Ny-Alesund - Radiative transfer studies and their application. *Atm. Chem. and Phys. 4*, 955–966.

Wittrock, F., A. Richter, J. Burrows, M. Kanakidou, R. Volkamer, S. Beirle, U. Platt, and T. Wagner (2006). Simultaneous Global Observations of Glyoxal and Formaldehyde from Space. *Geophys. Res. Lett. 33*, L16804.

Woyde, M. (2007). Erprobung einer InGaAs-Photodiodenzeile zur Detektion von Methan im NIR-Bereich. Diploma thesis, University of Heidelberg.

Acknowledgements

Mein erster Dank geht an Prof. Dr. Ulrich Platt, daß er mir diese interessante Arbeit ermöglicht hat, mit vielen Herausforderungen und Inspirationen.

Ein herzliches Dankeschön auch an Thomas, meinem Betreuer und zweiten Gutachter, der mir immer mit Rat und Tat zur Seite stand und mir auch in schwierigen Phasen Anstößе geben konnte.

Udo danke ich für die andauernde Unterstützung in allen DOAS-Fragen, Strahlungstransportproblemen und Optimal Estimation Berechnungen.

Vielen Dank auch an Rainer für immer wieder spannende Diskussionen und die Einführung in photochemisches Neuland.

In Roland hatte ich einen steten Ansprechpartner in allen chemischen Fragen. Danke.

Ich danke der ganzen Arbeitsgruppe, die sich im Laufe der Jahre immer wieder neu zusammengesetzt hat, für freundschaftliche Unterstützung und kollegiale Zusammenarbeit jedes einzelnen. Ganz besonderer Dank gilt Barbara, die mich vor allem in der Endphase zum nötigen Durchhaltevermögen anspornte.

Ein Dankeschön an Thomas, Udo, Thomas L., Jamie und Barbara fürs Korrektur lesen meiner Arbeit und die diesbezüglichen Tips.

Tim war dankenswerter Ansprechpartner für Fragen der Strahlungstransportberechnung und Handhabung von Tracy-II und McArtim.

Ein Dank auch an Holger, Thomas L. und Matthias für die Hilfe rund um Latex.

Thomas, Clemens, Steffen, Jessica und Ossama danke ich für die angenehme Arbeitsatmosphäre in unserem Büro mit vielen interessanten Diskussionen, auch jenseits der Physik und auf unserer roten Couch.

Für die große Hilfe vor Ort während der ICARTT Meßkampagne danke ich Oli, Christoph, Frank und Thomas, der sich zusätzlich auch in Mexico City verdient gemacht hat.

I thank Michael Trainer and Gerhard Hübler for the assistence in the ICARTT campaign and the possibility for an internship at NOAA.

Many thanks to Mark Twickler, Pieter Beckman and Don Troop (all UNH), Rainer (MIT), Eric Williams (RV Ron Brown), John Merrill and Brian Heikes (both URI), Peter Daum, Stephen Springston, Linda Bowerman and Art Sedlacek (all Brookhaven NL), J.

William Munger (Harvard) and Kenneth Demerjian, Jim Schwab and Yongquan Li (all UAlbany) who kindly provided access to the measurement sites during the ICARTT campaign and assisted in the MAX-DOAS measurements.

Thanks to NOAA which funded the MAX-DOAS measurements during ICARTT 2004.

I am grateful to Rainer for the possibility of taking part in the MILAGRO campaign in Mexico City.

Many thanks to Telma Castro (UNAM) and Zahra Chaudhry as well as Dominik Cieslak (both Univ. of Maryland) for taking care of the MAX-DOAS measurements at T1 and T2, respectively.

I thank Luisa Molina and the Molina Center for funding the MAX-DOAS measurements in Mexico City.

Vielen Dank an Thomas Schramm vom Reparaturpool, der mir in der Schlußphase meiner Arbeit zweimal meinen Computer gerettet hat.

Ein Dankeschön auch an die Werkstatt, das Sekretariat und die Verwaltung für ihre Unterstützung.